DISS. ETH NO. 29541

A seasonal weather perspective on forest vitality, vapor pressure deficit, and Greenland melt in a warming climate

A thesis submitted to attain the degree of
DOCTOR OF SCIENCES OF ETH ZURICH
(DR. SC. ETH ZURICH)

presented by

MAURO HERMANN
MSc in Environmental Sciences, ETH Zurich
born on 14 November 1994

accepted on the recommendation of

Prof. Dr. Heini Wernli, examiner
Dr. Matthias Röthlisberger, co-examiner
Prof. Dr. Stefan Brönnimann, co-examiner

2023

"In conclusion it may be said that the combustion of fossil fuel ...
is likely to prove beneficial to mankind in several ways ...

Small increases of mean temperature would be important at the northern margin of cultivation, and the growth of favourably situated plants is directly proportional to the carbon dioxide ... In any case the return of the deadly glaciers should be delayed indefinitely."

Guy Callendar (1938)

Line plot and data of atmospheric CO_2 from NOAA Global Monitoring Laboratory (2023).

Contents

Abstract

A wide range of meteorological and climatological phenomena shape atmospheric variability on different timescales. For example, convection in thunderstorms leads to intense precipitation within minutes, while stationary anticyclones often cause multi-day heat waves. In contrast, only few atmospheric phenomena operate on the seasonal timescale, where climate variability has a very strong impact on many natural and socioeconomic systems. Moreover, seasonal climate variability is relatively more affected by global warming than shorter-term variability, making these systems particularly vulnerable to ongoing global warming.

Therefore, the aim of this thesis is to improve our understanding of seasonal climate variability, which is crucial for the development of timely adaptation and preparedness strategies. To achieve this goal, our approach adopts a "weather perspective", i.e., we investigate how shorter-term atmospheric variability aggregates to form seasonal anomalies and extremes. We also focus on three selected components of the climate system that show remarkable sensitivity to seasonal variability. First, we examine the meteorological precursors of low forest vitality events in Europe during summer (June–August; JJA) using satellite observations of forest greenness. Although these events are indicative of the observed drought-related forest dieback, they have not been systematically assessed from the weather perspective yet. Second, we examine extremely high vapor pressure deficit (VPD) in JJA, which is a major contributor to plant water stress and thus crop failure and wildfire risk. Extreme seasonal VPD can be caused by a combination of air temperature anomalies (T') and humidity anomalies (q'), which we investigate for the first time over the northern mid-latitudes. Finally, we examine the increase in summer melt of the Greenland Ice Sheet (GrIS) over the 21st century, which is expected to contribute significantly to global sea-level rise. In particular, we quantify the role of melt expansion and intensification, and changes in synoptic circulation patterns.

In Chapter 3, low-forest-greenness events in 2002–2022 are identified separately for the European temperate and Mediterranean forest biomes as widespread (on spatial scales of $50 \times 50\,\mathrm{km}^2$) negative anomalies of the Normalized Difference Vegetation Index (NDVI) over most of JJA. First and foremost, according to these criteria, forest greenness was negatively affected in the summer of 2022 (the hottest on record) to an extent unprecedented in the study period. Low-NDVI events covered 37% of the forests in both biomes, exceeding previous records of around 24% coverage. Meteorological precursors to all events are then identified as 90-day meteorological signals that are statistically significantly different from climatology and shared among the events occurring in a biome. The summers of the low-NDVI events were unusually hot and dry. Negative precipitation anomalies (P') reached statistically significant

levels already in the winter preceding Mediterranean events. In temperate forests, the previous summer was also anomalously warm and dry, indicating potential negative legacy effects of drought. Notably, the persistence of dry periods ($P' < 0$) was significantly increased for at least ~2 and ~3 years before low-NDVI events in the temperate and Mediterranean biomes, respectively. However, the persistence of hot periods ($T' > 0$) was significantly increased only in the temperate biome, but not in the Mediterranean biome, over about the same 2-year period. Unusually large T' and P' were associated with significant changes in the frequency of weather systems, with less frequent cyclones relevant for dry periods in Mediterranean forests and more frequent anticyclones for dry periods in temperate forests. The analyses take into account the uneven distribution of events over the study period, and further shed light on spatial variations in the importance of the two weather systems for low-NDVI events.

In Chapter 4, we apply a novel framework to identify spatial objects of extremely high VPD in JJA ($\text{VPD}_{\text{JJA+}}$) from the exceedance of the local 40-year return level, and decompose their intensity (I) into contributions from seasonal mean T' and q'. After detrending seasonal mean VPD, we identify about 100 $\text{VPD}_{\text{JJA+}}$ with a center of mass in 30–60°N in ERA5 reanalysis covering the 1979–2020 period, and 2'500 such $\text{VPD}_{\text{JJA+}}$ in 105×10 years of large-ensemble CESM1 simulations. The decomposition of I in the mid-latitudes shows a high agreement between the two datasets. On average, positive T' makes a significant contribution of ~75% to the $I \approx 0.3\,\text{kPa}$. However, this warm anomaly also leads to a moistening resulting from the climatological co-variability of T and q, which reduces the I. Anomalous circulation dynamics causing negative q' during $\text{VPD}_{\text{JJA+}}$ are responsible for the remaining ~31% of I. Furthermore, we reveal robust spatial variations in these three contributions in the large set of CESM1 $\text{VPD}_{\text{JJA+}}$. Chapter 4 also demonstrates the consequences of the nonlinear dependence of VPD on T. First, VPD is underestimated when calculated from seasonal mean T and q compared to instantaneous values. However, this underestimation does not affect the VPD anomaly and thus the I of $\text{VPD}_{\text{JJA+}}$. Second, the contribution of T' to I is expected to increase in a warmer climate, which is confirmed by ERA5 $\text{VPD}_{\text{JJA+}}$. A final analysis of six observed high-impact $\text{VPD}_{\text{JJA+}}$ illustrates how individual heat waves and dry spells aggregate over a JJA season, and how periods of high VPD thereby interact with partly extreme drought conditions.

In Chapter 5, we attribute the summer melt increase of the GrIS from 2005–2015 to 2085–2095 to changes in melt area, melt intensity, and atmospheric circulation. The latter is quantified using the Self-Organizing Map method to identify specific synoptic circulation patterns and changes in their occurrence frequency. We consider the $\Delta\overline{m}_s = +501\,\text{Gt}\,\text{JJA}^{-1}$ summer melt increase in the upper-elevation zone ($\geq 1'200\,\text{m}$), where melt estimates from the surface energy balance of our CESM2 ensemble can be considered adequate. The $\Delta\overline{m}_s$ can fully be attributed to melt expansion (51%) and intensification (17%), their concurrent change (24%), and an increase in the daily covariance of melt area and intensity (8%). Changes in mid-tropospheric circulation occur mainly between synoptic flow patterns with a similar melt increase and thus do not contribute to the projected melt increase. Despite its irrelevance for mean melt changes, daily atmospheric variability will become more important for the inter-annual and intra-seasonal variability of melt and hence for the temporal evolution of mass loss from the GrIS.

Taken together, the results presented in the three chapters demonstrate the diversity of processes that can shape the climate system on the seasonal timescale. We present novel tools that are useful for systematically studying the impact of short-term weather variability on seasonal climate anomalies. Moreover, the thesis highlights how terrestrial ecosystems and the cryosphere are currently undergoing profound changes due to global warming. The insights gained into the forest-meteorology interaction, on the characteristics of extreme VPD seasons, and on the processes leading to the projected increase in GrIS melt not only represent progress at the weather-climate interface, but it is hoped that this thesis will also stimulate new research that benefits from the methodological advances developed here.

Zusammenfassung

Ein breites Spektrum meteorologischer und klimatologischer Phänomene prägt die atmosphärische Variabilität auf unterschiedlichen Zeitskalen. So führt beispielsweise Konvektion in Gewittern innerhalb von Minuten zu intensiven Niederschlägen, während stationäre Hochdrucksysteme oft mehrtägige Hitzewellen verursachen. Auf der saisonalen Zeitskala beeinflussen nur wenige atmosphärische Phänomene die Klimavariabilität, welche einen sehr grossen Einfluss auf viele natürliche und sozioökonomische Systeme hat. Darüber hinaus ändert sich die saisonale Klimavariabilität relativ gesehen stärker durch die globalen Erwärmung als kurzfristigere Variabilität, was die betroffenen Systeme besonders anfällig für die fortschreitende Klimaerwärmung macht.

Ziel dieser Arbeit ist es daher, unser Verständnis der saisonalen Klimavariabilität zu verbessern, was für die Entwicklung frühzeitiger Anpassungs- und Bereitschaftsstrategien von entscheidender Bedeutung ist. Um dieses Ziel zu erreichen, wählen wir eine "Wetterperspektive", d.h. wir untersuchen, wie kurzlebige atmosphärische Prozesse zu saisonalen Anomalien und Extremen beitragen. Ausserdem konzentrieren wir uns auf drei ausgewählte Komponenten des Klimasystems, die besonders sensitiv gegenüber saisonalen Schwankungen sind. Zunächst untersuchen wir die meteorologischen Vorläufer von Ereignissen reduzierter Waldgesundheit in Europa während des Sommers (Juni–August; JJA) anhand von Satellitenbeobachtungen des Waldgrüns. Obwohl diese Ereignisse ein Zeichen der beobachteten erhöhten Waldsterblichkeit sind, wurden sie bisher noch nicht systematisch aus der Wetterperspektive ausgewertet. Zweitens untersuchen wir extrem grosses Dampfdruckdefizit (vapor pressure deficit; VPD) im Sommer, das wesentlich zum Wasserstress von Pflanzen und damit zu Ernteausfällen und erhöhter Waldbrandgefahr beiträgt. Extremes saisonales VPD kann durch eine Kombination von Temperatur- (T') und Feuchteanomalien (q') verursacht werden, deren Beiträge wir zum ersten Mal über die nördlichen mittleren Breiten hinweg quantifizieren. Schliesslich untersuchen wir die Zunahme der sommerlichen Schmelze des grönländischen Eisschildes (GrIS) im Laufe des 21. Jahrhunderts, die erheblich zum globalen Meeresspiegelanstieg beitragen wird. Insbesondere quantifizieren wir die Rolle der räumlichen Ausdehnung und Intensivierung der Schmelze, sowie die von Veränderungen der synoptischen Zirkulation.

In Kapitel 3 werden Ereignisse geringen Waldgrüns von 2002 bis 2022 getrennt für die europäischen gemässigten und mediterranen Biome identifiziert, als weit verbreitete (auf räumlichen Skalen von $50 \times 50\,\mathrm{km}^2$) negative Anomalien des Normalized Difference Vegetation Index (NDVI) über den grössten Teil des Sommers. Nach diesen Kriterien war das Waldgrün im Sommer 2022 (der heisseste seit Beginn der Aufzeichnungen) in einem für den Unter-

suchungszeitraum noch nie dagewesenen Ausmass beeinträchtigt. Sogenannte low-NDVI-Ereignisse bedeckten 37% der Wälder in beiden Biomen und übertrafen damit frühere Rekorde mit einer Ausdehnung von rund 24%. Meteorologische Vorläufer aller Ereignisse werden als 90-tägige meteorologische Signale identifiziert, welche sich statistisch signifikant von der Klimatologie unterscheiden und welche die Ereignisse in einem Biom gemeinsam haben. Die Sommer der low-NDVI-Ereignisse waren ungewöhnlich heiss und trocken. Negative Niederschlagsanomalien (P') erreichten bereits im Winter vor mediterranen Ereignissen statistisch signifikante Werte. In den Wäldern des gemässigten Bioms war der vorangegangene Sommer ebenfalls ungewöhnlich warm und trocken, was auf einen negativen Legacy-Effekt ("Erbe") früherer Trockenperioden hindeutet. Bemerkenswert ist, dass Trockenperioden ($P' < 0$) im gemässigten Biom über ~2, und im mediterranen über rund 3 Jahre vor low-NDVI-Ereignissen unüblich lange andauerten. Die Persistenz von Hitzeperioden ($T' > 0$) war jedoch nur im gemässigten Biom signifikant erhöht, nicht aber im mediterranen, und zwar über rund denselben Zweijahreszeitraum. Besonders grosse T' und P' gingen mit signifikanten Änderungen der Häufigkeit der Wettersysteme einher. Dabei waren weniger häufige Tiefdruckgeiebte für Trockenheit in mediterranen Wäldern und häufigere Hochdruckgeiebte für solche in den gemässigten Wäldern ausschlaggebend. Die Analysen berücksichtigen u. a. das unregelmässige Auftreten der Ereignisse zwischen 2002 und 2022 und geben Aufschluss über räumliche Variationen in der Bedeutung der beiden Wettersysteme für low-NDVI-Ereignisse.

In Kapitel 4 wenden wir eine neuartige Methode an, um räumliche Objekte mit extrem grossem VPD in JJA ($\text{VPD}_{\text{JJA+}}$) aus der Überschreitung des lokalen 40-Jahres-Wiederkehrniveaus zu identifizieren, und orden deren Intensität (I) den Beiträgen von saisonal gemittelten T' und q' zu. Nach der Trendbereinigung von saisonalem VPD identifizieren wir etwa 100 $\text{VPD}_{\text{JJA+}}$ mit einem Massenzentrum in 30–60°N in der ERA5-Reanalys (Zeitraum 1979–2020), und 2'500 solcher $\text{VPD}_{\text{JJA+}}$ in 105×10 Jahren von large-ensemble CESM1-Simulationen. Die Zuordnung von I in den mittleren Breiten zeigt eine hohe Übereinstimmung zwischen den beiden Datensätzen. Durchschnittlich trägt positives T' mit ~75% signifikant zu $I \approx 0,3\,\text{kPa}$ bei. Diese Warmanomalie führt jedoch auch zu einer Anfeuchtung, die sich aus der klimatologischen Kovariabilität von T und q ergibt, welche somit I teils reduziert. Anomale Strömungsdynamik, die zu negativer q' führen, sind für die restlichen 31% von I verantwortlich. Ausserdem zeigen wir robuste räumliche Variationen dieser drei Beiträge im grossen Set von $\text{VPD}_{\text{JJA+}}$ in CESM1. Kapitel 4 zeigt auch die Folgen der nichtlinearen Abhängigkeit des VPD von T. Erstens wird VPD unterschätzt, wenn es aus saisonal gemittelten statt zeitlich höher aufgelösten Werten von T und q berechnet wird. Diese Unterschätzung beeinflusst die VPD-Anomalie der $\text{VPD}_{\text{JJA+}}$ und damit I jedoch nicht. Zweitens wird erwartet, dass der Beitrag von T' zu I in einem wärmeren Klima zunehmen wird, was unsere ERA5 $\text{VPD}_{\text{JJA+}}$ bestätigen. Eine abschliessende Analyse von sechs beobachteten $\text{VPD}_{\text{JJA+}}$ mit grossen sozioökonomischen Auswirkungen veranschaulicht, wie sich einzelne Hitzewellen und Trockenperioden über eine JJA-Saison summieren können und wie Perioden hohen VPDs dabei mit Dürre interagieren.

In Kapitel 5 ordnen wir die erwartete Zunahme der Sommerschmelze des GrIS von 2005–2015 bis 2085–2095 der Veränderung der Abschmelzfläche, der Schmelzintensität und der

atmosphärischen Zirkulation zu. Letztere wird mit Hilfe der Self-Organizing Map Methode quantifiziert, um spezifische synoptische Zirkulationsmuster und Veränderungen in deren Häufigkeit zu identifizieren. Wir betrachten die Schmelzzunahme von $\Delta\overline{m}_s = +501\,\mathrm{Gt\,JJA^{-1}}$ welche in Eisregionen über 1′200 m Höhe anfällt, da dort unsere Schätzungen der Schmelze aus der Enenergiebilanz des verwendeten CESM2-Ensembles als adäquat angesehen werden können. Das $\Delta\overline{m}_s$ kann vollständig auf die räumliche Ausdehnung (51%) und Intensivierung (17%) der Schmelze, deren gleichzeitige Änderung (24%) und eine Zunahme der täglichen Kovarianz von Abschmelzfläche und Intensität (8%) zurückgeführt werden. Änderungen in der mittel-troposphärischen Zirkulation treten hauptsächlich zwischen Strömungsmustern mit einer ähnlichen Schmelzzunahme auf und tragen daher nicht zum vorhergesagten Gesamtanstieg bei. Trotz ihrer Irrelevanz für die durchschnittliche Schmelzzunahme wird tägliche atmosphärische Variabilität für die interannuelle und intra-saisonale Schmelzvariabilität und somit für den zeitlichen Verlauf des grönländischen Massenverlusts an Wichtigkeit gewinnen.
Zusammengenommen zeigen die vorgestellten Ergebnisse die Vielfalt der Prozesse, die das Klimasystem auf der saisonalen Zeitskala beeinflussen. Wir stellen neue Methoden vor, die für die systematische Untersuchung der Auswirkungen kurzfristiger Wetterschwankungen auf die saisonale Zeitskala nützlich sind. Darüber hinaus zeigt die Dissertation auf, wie sich terrestrische Ökosysteme und die Kryosphäre aufgrund der globalen Erwärmung derzeit tiefgreifend verändern. Die gewonnenen Erkenntnisse über die Wechselwirkung zwischen Wald und Meteorologie, über die Eigenschaften extremen saisonalen VPDs und über die Prozesse, die zum erwarteten Anstieg der Grönland-Schmelze führen, stellen nicht nur einen Fortschritt an der Schnittstelle zwischen Wetter und Klima dar. Es ist auch zu hoffen, dass diese Dissertation neue Forschung anregen wird, die von den hier entwickelten methodischen Fortschritten profitieren kann.

Chapter 1

Background and introduction

1.1 An example of atmospheric variability

Atmospheric variability results from a variety of meteorological and climatological phenomena operating over a wide range of timescales (e.g., Wallace and Hobbs, 2006). Meehl et al. (2001) described a "continuum of process-related interactions" in which phenomena at longer timescales set the stage for shorter timescale phenomena, which, in turn, influence and modify the longer timescales again. For an exemplary demonstration of the range of phenomena involved, we consider the temperature T in Zurich, Switzerland (Fig.1.1). During summer, the diurnal cycle of T is driven by solar radiation, with additional short-lived fluctuations due to turbulence at the scale of seconds and local wind systems (Fig.1.1a). A convective cell developed over the course of the afternoon due to strong solar surface heating and an approaching upper-level shortwave trough (not shown), resulting in a rapid 10°C T drop after 18:00 local time of the exemplary day (Fig.1.1a). The days preceding the approach of the upper-level disturbance were notably warm (Fig.1.1b) due to strong solar heating and adiabatic warming associated with a blocking anticyclone located over Switzerland (not shown; Zschenderlein et al., 2020). This example demonstrates how synoptic-scale weather systems such as anticyclones (Pfahl and Wernli, 2012a; Zschenderlein et al., 2019) and cyclones (Wernli and Schwierz, 2006; Pfahl and Wernli, 2012b) determine the extratropical atmospheric variability on the daily to weekly timescale. The change of T from season to season primarily stems from the seasonal solar cycle (Earth's axial tilt), while inter-annual T variability in Zurich is shaped by various factors, including the sum of shorter-term phenomena as well as more slowly varying components of the climate system such as regional soil moisture, winter snow cover, and sea surface temperature (SST) patterns in the North Atlantic (Fig.1.1c). The combination of multiple processes and phenomena can lead to extreme events at one or the other timescale, such as the extremely hot summer experienced in (mostly northern) Europe in 2018 (NE2018). It arose due to a combination of SST preconditioning, a positive phase of the North Atlantic Oscillation (NAO), dry soils, and persistent anticyclones (Rousi et al., 2023). Both NE2018 and the summer of 2022 were exceptionally hot over much of Europe (e.g., Peters et al., 2020; Copernicus Climate Change

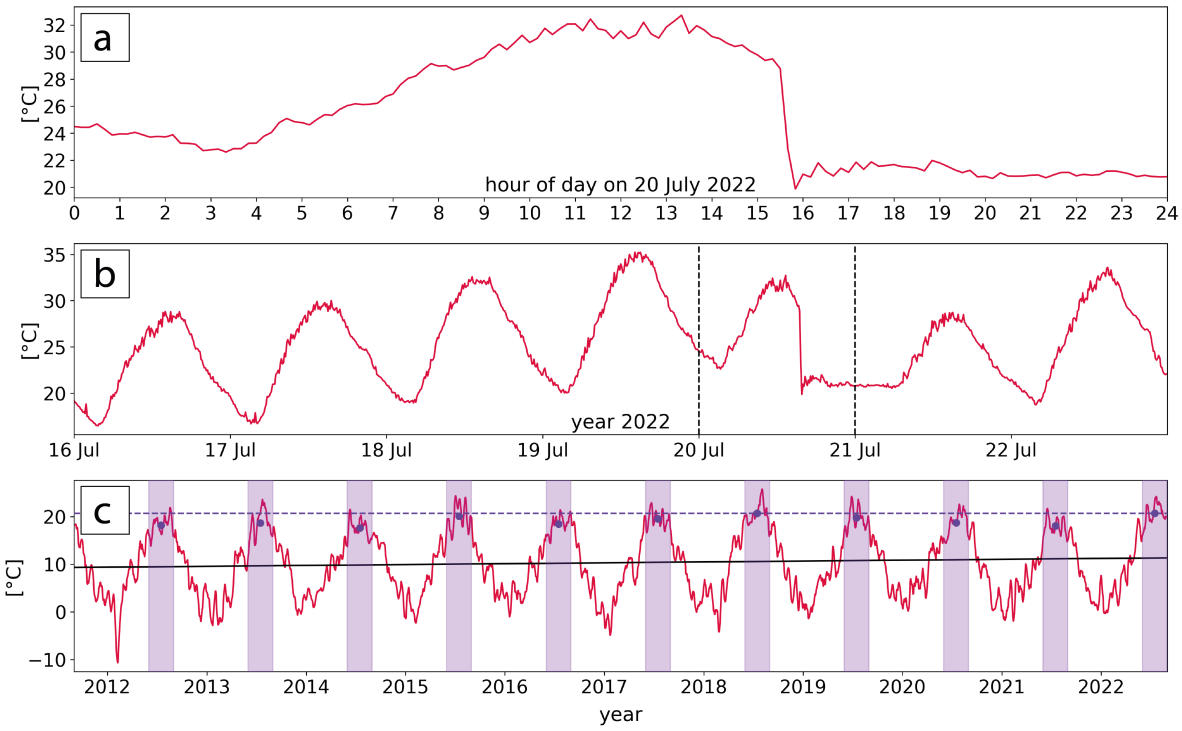

Figure 1.1: The red lines denote 10-minute temperature (T) on the CHN building of ETH Zürich on (a) 20 July 2022, and (b) on 16–22 July 2022. The red line in (c) shows 10-day running mean T from ERA5 in the Zurich region (47.5°N, 8.5°E) from 1 September 2011 to 31 August 2022. Vertical lines in (b) enclose the 20th July. Purple shading in (c) mark the summer season. Purple dots (dashed purple line) denote the summer mean T (in 2022). The solid black line shows the trend in daily T (linear fit).

Service, 2022; Rousi et al., 2023), including Zurich (Fig.1.1c). Lastly, on longer timescales, we observe a trend in T that is predominantly driven by the radiative effect of anthropogenic greenhouse gas (GHG) emissions (black line in Fig. 1.1c).

In summary, atmospheric variability at a single location is shaped by a wide range of phenomena from turbulence to rising atmospheric GHG concentration, each operating on a distinct timescale. When these phenomena are strongly pronounced or occur in combination or sequence, they can give rise to extreme events at different timescales, as exemplified by the extremely hot summer seasons in 2018 and 2022. Ultimately, at longer timescales, anthropogenic global warming becomes the dominant signal of variability. In this thesis, we will study three selected cases of seasonal variability and extremes, partly including their response to global warming. The cases are selected based on (i) their impact at the seasonal timescale (Sect. 1.4), and (b) as they are rapidly affected by global warming (see next section), and include (1) recent events of low summer forest greenness in Europe, (2) summers of extremely high vapor pressure deficit in reanalysis and climate model data, and (3) mechanisms governing the increase in Greenland summer melt over the course of this century. Our analyses will, thereby, focus specifically on how shorter-term variability forms such seasonal (extreme) anomalies, as will be introduced in Sect. 1.3.

1.2 Global warming

The unequivocally human-caused global warming (+1.1°C in 2011–2020 compared to pre-industrial levels) has amongst others increased the severity of weather and climate extremes, and led to numerous adverse impacts on human health, food production, and natural ecosystems (IPCC, 2021). One way to identify human-caused changes in the climate system, and regions that will be affected earliest by anthropogenic global warming is by detection and attribution (National Academies of Science Engineering and Medicine, 2016). Specifically, the robust identification of systematic changes in the climate system in the context of the internal climate variability is a matter of identifying a (forced) signal emerging from the noise (e.g., Hasselmann, 1979). Nowadays, this framework is also frequently used to detect and quantify the human influence on individual extreme events, such as in the European heatwave in summer 2003 (Stott et al., 2004). Early efforts successfully attributed the increase in global mean surface temperature to anthropogenic GHGs (Barnett and Schlesinger, 1987; Hegerl et al., 1996). With continued anthropogenic GHG emissions the temperature signal also emerged from the noise at regional scales (e.g., Stott, 2003). With increasing availability of climate projections and historical reference simulations, the level of global warming necessary to reveal anthropogenic influence could be identified for longer-term mean T and precipitation (P), and the corresponding extreme events at different temporal scales, as elaborated in the following. The emergence of climate from its historical variability is a matter of great concern, indicating that it no longer encompasses the niche in which numerous natural and social systems have evolved, and is thus a critical process regarding the required pace of their adaptation (e.g., Williams et al., 2007). Moreover, as specified in the following, the emergence of a new climate typically occurs earlier in low-income countries, whose adaptive capacity is also below average (Mahlstein et al., 2011; Mora et al., 2013).

The time of emergence (ToE) denotes the initial period when a given climatic change emerges from the noise of its (historical) internal variability (Hawkins and Sutton, 2012). Figure 1.2 shows an illustrative example of the ToE from Tan et al. (2018) for the annual maximum daily maximum T (TXx) at a single grid cell in the North Atlantic. The noise (N) is estimated from the standard deviation of TXx in the reference period (1971–2005), and the signal (S) is equal to the trend of TXx relative to a historical reference year, which was chosen as 2000 by the authors (Tan et al., 2018). Another commonly used approach including climate modeling infers the historical noise and reference value of a given climate index from simulations without anthropogenic GHG forcing, often pre-industrial control runs (e.g., Hawkins and Sutton, 2012). In our illustrative case (Fig. 1.2), the signal emerges from the noise between ToE1 = 2016 (84% confidence) and ToE2 = 2031 (98% confidence). The ToE is thus an estimate of how early climate change can be detected in a given variable of interest, and also represents the level of anthropogenic warming necessary to robustly detect and attribute the respective effect.

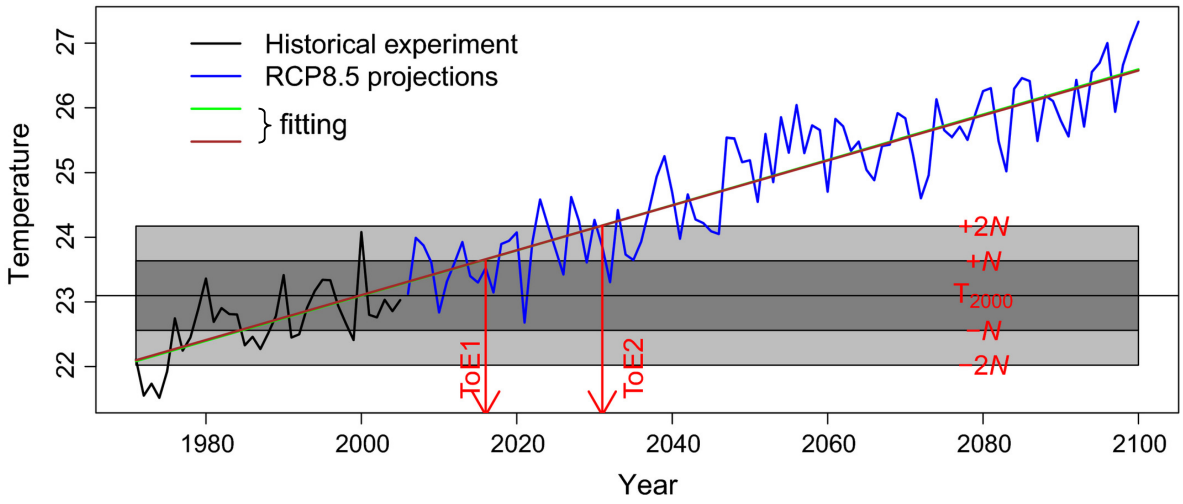

Figure 1.2: Example of the time of emergence (ToE) for the annual maximum daily maximum T (TXx) for a grid cell in the North Atlantic. The black (blue) line denotes the historical (projected) TXx. The green and pink lines denote TXx trend estimates (differences are neglected here). The TXx signal (S) is the magnitude of change of the TXx trend relative to the historical reference (year 2000). The noise (N) is derived from the historical internal variability, i.e., standard deviation, of TXx. The ToE1 and ToE2 denote times when S/N exceed 1 and 2, respectively. Figure adapted from Tan et al. (2018).

Estimation of the exact ToE is often hampered by short observational records (Mahlstein et al., 2011), and inter-model differences in simulating internal variability, resulting in a typical ToE uncertainty of 30 to 60 years (Hawkins and Sutton, 2012). The identified patterns, however, are largely consistent for a given metric, and imply that the ToE of boreal summer mean T (Mahlstein et al., 2011), monthly T (Mora et al., 2013), annual maximum daily T (Kirchmeier-Young et al., 2019), and of other magnitude-based T extreme indices (Fischer and Knutti, 2015; Tan et al., 2018) is earliest in the tropics, where internal variability is comparatively small. Moreover, high latitudes show an earlier ToE than mid-latitudes because of a strongly amplified T increase, especially for cold extreme events (Tan et al., 2018). Changes in P associated with the observed and projected external forcing (until 2100) show – regardless of the direction of change – a much smaller signal-to-noise ratio S/N and hence a later ToE than for changes of T – if emerging at all from the noise (Fischer and Knutti, 2015; Angélil et al., 2018; Tan et al., 2018; Kirchmeier-Young et al., 2019; IPCC, 2021). So, relatively low levels of global warming can be robustly detected in T-based metrics and in regions with low internal variability, such as the tropics, while anthropogenically induced trends in P are mostly detectable at higher levels of anthropogenic GHG forcing.

For extreme climate indices and events, and also mean T and P, the spatial and temporal scale under consideration is of great relevance for the ToE (Fischer and Knutti, 2015; Angélil et al., 2018; Kirchmeier-Young et al., 2019). The S/N increases due to the damping of the "weather noise" at larger spatial and longer temporal scales, especially so for P (Kirchmeier-Young et al., 2019). The fundamental reason for this effect is that the historical distribution is narrower, e.g., for monthly or seasonal mean values compared to daily values (Fischer and Knutti, 2015).

Consequently, an imprint of anthropogenic warming can be detected and attributed earlier for longer-term variables such as seasonal or annual mean T and P (Mora et al., 2013; Kirchmeier-Young et al., 2019). In this context, frequency-based climate metrics, which often relate to profound adverse impacts, pose an interesting contrast to the above-mentioned global patterns of magnitude-based indices. For example, the annual maximum number of consecutive dry days, and the longest heatwave per year can be detected earlier for many parts of the mid-latitudes compared to high and low latitudes (Tan et al., 2018). In summary, climate change manifests itself in a variety of ways, with distinct global patterns, but generally earlier at larger spatial and temporal scales.

This section highlighted the regions and metrics where global warming is most pronounced. Particularly prominent is global warming in the tropics due to small N, polar regions due to large S, frequency-based metrics in the mid-latitudes, and T-influenced metrics as compared to P. In addition, seasonal atmospheric variability emerges relatively early from the historical range compared to shorter-term variability. It is, therefore, of great interest to understand the mechanisms that shape these metrics and signals, as they require adaptation measures at the earliest.

1.3 A weather perspective on (extreme) seasonal anomalies

The previous section discussed how global warming exhibits pronounced effects at the seasonal timescale, which meteorologically spans a 90-day period and, thereby, falls between the commonly recognized timescales of weather (shorter) and climate (longer). However, as introduced in Sect. 1.1, it is important to note that the segregation of these timescales is artificial, as the phenomena in the climate system occur seamlessly across all timescales (Hoskins, 2013). Right at the seasonal timescale, however, there are very few meteorological phenomena to understand variability on that timescale – mainly the land surface-atmosphere coupling between precipitation and soil moisture (e.g., Betts et al., 1996). Therefore, investigating seasonal atmospheric variability from either a shorter or longer timescale perspective serves as two equally valuable starting points for research. The "climate perspective" primarily focuses on inter-annual to multi-decadal climate variability, encompassing phenomena like the NAO, the El Niño-Southern Oscillation (ENSO), and the Atlantic Multi-decadal Oscillation (AMO). On the other hand, the "weather perspective" encompasses sub-daily to weekly phenomena such as atmospheric convection, synoptic-scale weather systems like extratropical cyclones, and recurrent Rossby-wave packets (see also Sect. 1.1). In this thesis, we investigate seasonal atmospheric variability mostly from the "weather perspective" while fully acknowledging and partly addressing the value and additional insights of the "climate perspective".

The "weather perspective" on seasonal anomalies is concerned with how shorter-term variability aggregates to seasonal anomalies, and how weather systems thereby interact with other climatic processes. Due to their profound socioeconomic impact, most research has focused on

case studies of exceptionally anomalous seasons, i.e., of extreme seasons. The study of individual extreme seasons (storyline approach) is further motivated by the existence of numerous potential substructures that lead to the same seasonal mean anomaly (Röthlisberger et al., 2020). A pioneering study by Namias (1978) found not only El Niño and specific SST patterns in the vicinity of North America to be responsible for the "abnormal" winter 1976/77, but also stronger fronts and cyclones. Further, the clustering of cyclones resulted in an extremely stormy winter in Europe in 1999/2000 (Ulbrich et al., 2001), an recurrent cyclones and upper-level troughs led to the extremely wet winter in the UK in 2013/14 (Davies, 2015). On the other hand, blocking anticyclones are responsible for multi-day heatwaves by bringing about adiabatic warming and clear-sky conditions (Pfahl and Wernli, 2012a; Zschenderlein et al., 2020; Kautz et al., 2022; Röthlisberger and Papritz, 2023), which can be further amplified by enhanced sensible heating owing to the soil moisture-atmosphere feedback (Seneviratne et al., 2010). These two phenomena led to sequentially occurring and long-lived heatwaves that culminated in the extremely hot summers in Central Europe in 2003 (Fischer et al., 2007), in Russia in 2010 (Dole et al., 2011), and NE2018 (Rousi et al., 2023). These case studies illustrate how particularly strong or recurrent weather phenomena can result in an extreme event at the seasonal timescale, hereafter referred to as an extreme season.

Recently, the substructure of extreme seasons has been studied more systematically and revealed substantial diversity across regions. Röthlisberger et al. (2020) showed that in many parts of the globe extremely hot summers are sensitive to that part of their substructure that exerts the greatest climatological variability. So, that is, hot summers in India arise when the warmest days are particularly hot (i.e., a late monsoon onset), while summers in California become extremely hot due to a suppression of cold days (i.e., less cold air advection from slow-moving upper-level troughs). Moreover, extremely wet seasons are formed by the presence (and sometimes absence) of weather phenomena such as cyclones, warm conveyor belts, and tropical moisture exports (Flaounas et al., 2021). In the Arctic, weather systems shape extreme seasons with regard to T, P, and the surface energy balance, e.g., the positioning and persistence of cyclones (Hartmuth et al., 2022). Moreover, as discussed in Sect. 1.2, extreme seasons in the Arctic are rapidly moving out of their historical niche, i.e., show a strong and early imprint of global warming (Hartmuth et al., 2023). As indicated earlier, the term "niche" designates the range of historical climate variability in the absence of pronounced anthropogenic changes, which local communities and ecosystems are adapted to. Given the relevance of global warming for extreme seasons, the methodological framework by Röthlisberger et al. (2021) provides a valuable tool for investigating how the extreme seasons' substructure and dynamics more generally – i.e., also from a "climate perspective" – will change towards a warmer climate. So far, the framework has been comprehensively applied to reanalysis data to globally identify extremely hot, cold, windy, calm, wet, and dry seasons from 1950 to present (Boettcher et al., 2023). In summary, weather systems and short-term variability are key to understanding extreme seasons, and offer a vast potential for further research when put into the perspective of climatic change.

Lastly, one has to keep in mind that the definition and quantification of "extremeness" is non-trivial due to several reasons. In general, a meteorological or climatological extreme event is characterized at least by its spatial extent, duration, and intensity (Cattiaux and Ribes, 2018). While our focus on extreme seasons sets the duration to approximately 90 days, the spatial extent and intensity is subjectively chosen and, therefore, not consistent among the above-cited literature. As the spatial extent is affecting the S/N (Sect. 1.2), it also matters for the identification of extremes and has to be chosen carefully with regard to the research question. In terms of intensity, a seasonal mean value can be deemed extreme when exceeding a certain threshold (e.g., $T > 20°C$ in Fig. 1.1c), as one of the n largest observed values in a given period (e.g., Röthlisberger et al., 2020; Flaounas et al., 2021), or when exceeding a given return period estimated from its climatological distribution (e.g., Röthlisberger et al., 2021; Boettcher et al., 2023). The latter approach specifying "extremeness" by rarity is particularly valuable as it is established in relation to the local climate and allows for comparisons across different spatial and temporal contexts. However, accurately estimating the return period of seasonal mean values in observational data poses considerable challenges, as the estimates based on a small sample (with only one value per season and year) suffer from to the so-called "regression to the mean" or "conditional bias" (e.g., Stigler, 1997). A further consequence of the very few observed extreme seasons is that regional pooling (Fischer et al., 2013), and/or extensive climate model simulations (Röthlisberger et al., 2021; Hartmuth et al., 2023) are frequently used to more robustly and more systematically study extreme seasons. Lastly, a season can also be regarded extreme in terms of its socioeconomic impact (impact-oriented extreme season) instead of its meteorological anomaly (meteorological extreme season). For example, the winter 1976/77 can be regarded extreme as it "dramatically illuminated Man's vulnerability" (Namias, 1978), and the growing season in 2015 was extreme in terms of vegetation greening (Bastos et al., 2017). Also, the cold and rainy summer in western Europe in 1816 can, irrespective of meteorological anomalies, be seen extreme as it led to famine and potentially mass migration (Luterbacher and Pfister, 2015; Brönnimann and Krämer, 2016). So while there is no rigorous protocol to identify extreme seasons, the applied definition crucially determines the subsequent analyses and conclusions drawn.

1.4 Three hotspots of seasonal meteorology and global warming

In this section, we build upon the previous two sections and highlight three (partly related) components of the Earth system that are (i) profoundly affected by global warming, and (ii) particularly sensitive to the seasonal aggregation of shorter-term atmospheric variability. We, thereby, introduce the central motivation for the three research foci of this thesis. Each overview is further detailed in the introductory sections of Chapters 3–5.

1.4.1 Reduced forest vitality in Europe

The aforementioned hot-dry extreme season NE2018 has impaired forest ecosystems in an unprecedented extent. Stem dehydration (Salomón et al., 2022), reduced forest growth (Trotsiuk

et al., 2020), and hydraulic failure (Schuldt et al., 2020) were reported and contributed to the ongoing trend of increasing tree mortality in Europe (Allen et al., 2010; Hansen et al., 2013). Forests in Europe are typically able to tolerate multi-day heatwaves and dry periods, but the sequencing and persistence thereof over an entire season can mark the onset of tree mortality (Allen et al., 2010). While persistent heat drives the loss of soil and plant water due to an increased atmospheric water demand, i.e., vapor pressure deficit (VPD; Grossiord et al., 2020), low precipitation not sufficiently replenishes the soil water storage, and the combined effect of so-called hot droughts is particularly damaging (Allen et al., 2015). Secondary disturbances like bark beetles (Biedermann et al., 2019; Jakoby et al., 2019) and fire (Turco et al., 2017) are fostered by hot and dry conditions, thereby aggravating the impact of such extreme seasons over the following months to years (Seidl et al., 2014). Furthermore, by reducing tree resilience, hot-dry extreme seasons can have a negative legacy effect on trees in a following drought period, thereby enhancing the impact of the second drought period (Anderegg et al., 2020; Bose et al., 2020). Although forests in parts of Europe are adapted to low water availability, e.g., in the summer-dry Mediterranean, their vitality and mortality are also adversely affected by more frequent, longer, and hotter droughts (Tague et al., 2019; Ogaya et al., 2020).

With global warming, more intense heat waves (Meehl and Tebaldi, 2004; IPCC, 2021), meteorological droughts (Trenberth et al., 2014), and hot droughts (Allen et al., 2015) are expected to strengthen future forest dieback (Brodribb et al., 2020). In analogy to Sect. 1.2, as forests are long-lived organisms that are used to the climate of the past decades, their decreasing vitality could be an early warning of the climate moving out of its niche, i.e., of an emerging climate change signal (Seidl et al., 2017; McDowell et al., 2020). Altogether, the meteorological conditions of NE2018 as well as their impact on forests were in many regards unprecedented (Schuldt et al., 2020; Bastos et al., 2020b; Peters et al., 2020; Rousi et al., 2023), and hence designate a meteorological as well as impact-oriented extreme season. As discussed in Sects. 1.1 & 1.3, there is a multitude of meteorological processes that are able to cause extreme seasons relevant for forest dieback. It is, therefore, of great importance to better and more systematically understand the meteorological history of the observed dieback events.

1.4.2 Seasons of extremely high vapor pressure deficit

A second focus of this thesis lies on VPD, which is a central quantity in plant hydrology and thus a major control of the terrestrial water balance. It is defined as the difference between saturation (e_s) and actual water vapor pressure (e_a), respectively, in air at the leaf interface (e.g., Grossiord et al., 2020):

$$\mathrm{VPD} = e_s - e_a \tag{1.1}$$

The importance of VPD arises from its impact on surface evapotranspiration, more specifically on plant transpiration, which is the water loss of plants through leaf stomata that necessarily accompanies the uptake of carbon dioxide for plant growth. Particularly, increasing VPD first

boosts water loss from transpiration, and then limits the conductance of leaf stomata and thus transpiration to prevent the plant from water stress (Franks et al., 1997; Oren et al., 1999). Given this protection mechanism that limits the gas exchange across leaf stomata, extremely high VPD increases the risk of carbon starvation and growth reduction independent of other climatic variables (Breshears et al., 2013; Grossiord et al., 2020). Hence, VPD in the summer season has been identified as the most important meteorological predictor of global (wheat) crop failure (Vogel et al., 2021). Moreover, extremely high VPD fosters bark beetle outbreaks (Williams et al., 2013), and reduces the moisture content of fuel available for wildfires (Dios et al., 2021), therefore increasing wildfire activity (Williams et al., 2013; Seager et al., 2015; Williams et al., 2019). The importance of summer VPD has also been evident in NE2018, which constituted a meteorological extreme season in terms of high VPD (Schuldt et al., 2020).

The variability of VPD is highly important on impact-relevant timescales such as the summer (growing) season. Further, as VPD depends nonlinearly on T, its variability strongly responds to global warming. The short-term variability is driven by processes that determine T (thus e_s) and specific humidity (q thus e_a), i.e., mainly ocean evaporation and the atmospheric circulation (Wallace and Hobbs, 2006; Byrne and O'Gorman, 2016). The past warming trend has increased VPD mainly through a larger e_s, which has negatively affected the drought sensitivity of maize crops (Lobell et al., 2014). With the ongoing increase of T globally, the negative impact of high VPD on soy bean (Sun et al., 2023) and maize crop yields (Hsiao et al., 2019), as well as on forest water stress (Williams et al., 2013; Brodribb et al., 2020) are expected to become stronger. While a few studies have addressed the effect of short-term variability in e_a and e_s on VPD (Seager et al., 2015; Ficklin and Novick, 2017), an understanding of summer mean VPD from a weather perspective is lacking. This is clearly unsatisfactory given the increasing importance of VPD in a warming climate (Yuan et al., 2019), and the pronounced impact of extremely high seasonal VPD on terrestrial ecosystems and crops (Lesk et al., 2022).

1.4.3 Future increase of Greenland surface melt

The third focus of this thesis lies on melt of the Greenland Ice Sheet (GrIS), whose mass loss has been accelerating since the mid 1990s and has led to a total of ~11 mm of global sea-level rise (IMBIE Team, 2020). Global warming is thus not only emerging quickly in Greenland, but might also lead to the crossing of the tipping point beyond which the GrIS becomes unstable (Boers and Rypdal, 2021; Noël et al., 2021). The most important contributors to the total mass balance (TMB) of the GrIS are composed in the following way:

$$\mathrm{TMB} = \mathrm{SMB} - D \tag{1.2}$$

$$\mathrm{SMB} = P - M \tag{1.3}$$

where SMB and D denote the surface mass balance and ice discharge, i.e., mass loss by calving of ocean-terminating glaciers, respectively. The SMB is composed of the GrIS-integrated precipitation (P) minus melt-water runoff (M), whereby we neglect the smaller mass fluxes

from sublimation, evaporation, and dew/hoar formation (Eq. 1.3). Besides GrIS surface melt, M includes the effect of melt-water refreezing and retention in the GrIS firn layer (e.g., van den Broeke et al., 2016). The recent decrease in TMB was largely due to increasing D (Enderlin et al., 2014; Mouginot et al., 2019), and a decreasing SMB (van den Broeke et al., 2016). Recently, the TMB as well as its inter-annual variability has been increasingly dominated by the SMB, specifically, surface melt (Fettweis et al., 2013a; van den Broeke et al., 2016).

Atmospheric variability dictates surface melt of the GrIS, which occurs almost exclusively in the summer season. In the past two decades, a series of summers with positive geopotential height anomalies over and around Greenland have fostered surface melt (Fettweis et al., 2013b), mainly by stronger down-welling shortwave radiation (Hofer et al., 2017) and anomalous horizontal air mass transport (Hermann et al., 2020). During atmospheric blocking over Greenland, downward shortwave radiation is enhanced in the eastern GrIS, while in the central and western GrIS melt intensifies due to enhanced longwave cloud forcing (Bennartz et al., 2013; Wang et al., 2019; Izeboud et al., 2020). From the 1980s to 2005–2014, 17% in the melt increase was attributed a shift in atmospheric circulation, 75% to an intensification of melt during the same synoptic circulation, and the remainder to a concurrent change of both (Mioduszewski et al., 2016). Strong anticyclonic circulation, low GrIS albedo, and little snowfall caused extremely widespread melt events in the summers of 2012 (Nghiem et al., 2012) and of 2019 (Tedesco and Fettweis, 2020; Velicogna et al., 2020). In contrast, little melt was observed in the cold summers of 2017 and 2018 (Velicogna et al., 2020). Thus, in the current climate, daily to weekly atmospheric variability is a key factor determining the inter-annual variability in mass loss from the GrIS. Thereby, surface melt is determined by the interplay of atmospheric circulation and associated melt intensity.

Mass loss from the GrIS is expected to increase strongly in the coming decades, whereby the occurrence frequency of different synoptic circulation patterns is among the largest sources of uncertainty (Delhasse et al., 2018; Hofer et al., 2019; IPCC, 2021). In general, the synoptic drivers of strong melt are well-understood (Mioduszewski et al., 2016; Hermann et al., 2020; Preece et al., 2022). However, the change in their occurrence frequency over this century is a matter of debate, as recent observations are not in line with climate model simulations (Belleflamme et al., 2013; Hanna et al., 2018; Delhasse et al., 2021). This is amongst the reasons why climate model predictions are not yet settled on the future SMB, e.g., CMIP6 (SSP5-8.5) models project an almost two-fold lower SMB (and thus greater sea-level rise contribution) over the course of this century compared to previous CMIP5 (RCP8.5) estimates (Hofer et al., 2020). A main challenge regarding future mass loss from the GrIS is, therefore, to understand how the impact of short-term atmospheric variability on summer surface melt responds to global warming.

1.5 Research questions

This chapter has motivated three research foci that deserve special attention when using a seasonal weather perspective in a warming climate. First, we examined global warming, which,

among other things, is particularly early on the seasonal timescale. We also highlighted the enormous range of timescales and processes of atmospheric variability that shape seasonal anomalies and their extremes. The thematic focus of this thesis is on components of the Earth system that are highly sensitive to seasonal meteorology and are profoundly affected by global warming. Terrestrial ecosystems and crops grow over time and are, thereby, affected by weather over several months to years. In this context, we identified two topics of interest: (1) the increasing dieback and disturbance of European forests on a large scale, which are related to the magnitude and sequence of hot and dry conditions, and (2) extremely high VPD in the summer season, which is of great relevance for forest water stress and crop yields. The final topic of interest is (3) the increase in summer melt of the GrIS in this century, especially also the role of potential shifts in synoptic circulation patterns. To this end, we pose overarching research questions here, while more specific research questions are raised in the following chapters. The three overarching research questions addressed in this thesis from a seasonal weather perspective are as follows:

1. What were meteorological precursors of reduced forest vitality in Europe in the summers of the past two decades?

2. What is the meteorological composition of extremely high summer mean VPD in the present-day climate?

3. Which mechanisms govern the summer melt increase of the GrIS in this century?

This thesis is organized as follows: Chapter 2 introduces the data used for many of the following chapters, in particular introducing the climate model simulations performed. The following chapters are thematically distinct and each addresses one of the above research questions, while also introducing chapter-specific datasets. First, Chapter 3 identifies widespread events of low forest vitality in Europe in summers 2002–2022 using a remote-sensing vegetation index, and systematically analyzes their meteorological history. Next, we identify seasons of extremely high VPD in reanalysis and climate model data to examine and evaluate their meteorological composition and substructure (Chapter 4). The final result chapter applies and extends a framework to attribute the large increase in GrIS surface melt in this century to various processes, including the change in occurrence frequency of certain synoptic circulation patterns (Chapter 5). We conclude the thesis with a summary and by putting our results into context in Chapter 6.

Chapter 2

Reanalyses and climate model data

2.1 ERA5 reanalysis

To analyze the state of the atmosphere over about the past four decades, we use the fifth generation reanalysis (ERA5) from the European Centre for Medium-Range Weather Forecasts (ECMWF; Hersbach et al., 2020). Like any modern reanalysis, the ERA5 data represents the three-dimensional state of the atmosphere in a spatiotemporally complete manner, resulting from the assimilation of vast amounts of observations across the globe using the ECMWF Integrated Forecast System (IFS). The horizontal resolution of the IFS used in the ERA5 data assimilation is 31 km. Here we use hourly output on a horizontal 0.5° grid and on 137 vertical hybrid sigma/pressure levels with an atmosphere top at 0.01 hPa (≈ 80 km). ERA5 data used in this thesis dates back to 1979 and is considered a "full-input" reanalysis. It uses, amongst others, also observations from radiosondes, aircraft, and satellites, which is why ERA5 used here is limited to roughly the satellite era. In contrast, so-called "surface-input" reanalyses such as the Twentieth Century Reanalysis (20CR; Compo et al., 2011) use only surface observations (no upper-air observations) and, therefore, date back nearly 200 years (Fujiwara et al., 2017). Both are extremely valuable resources for investigating the atmospheric variability of the recent past.

Based on ERA5 sea-level pressure (SLP), we identify cyclones and anticyclones as the two most fundamental weather systems (Fig. 2.1). These two not only determine vertical and horizontal atmospheric transport of heat, momentum, and moisture but are also of great importance to the temperature and humidity structure of the atmosphere. Cyclones (anticyclones) are identified according to Wernli and Schwierz (2006) and Sprenger et al. (2017) as objects of low (high) SLP and are thus identified from the outermost closed SLP isoline around local SLP minima (maxima). Minima (maxima) of SLP are excluded if the outermost SLP isoline has a length outside the range 100–7'500 km (1'500–15'000 km) to account for the typical size of cyclones (anticyclones). Further, we exclude minima (maxima) over orography exceeding 1'500 m due to substantial artefacts arising from extrapolating temperature from the surface to sea-level,

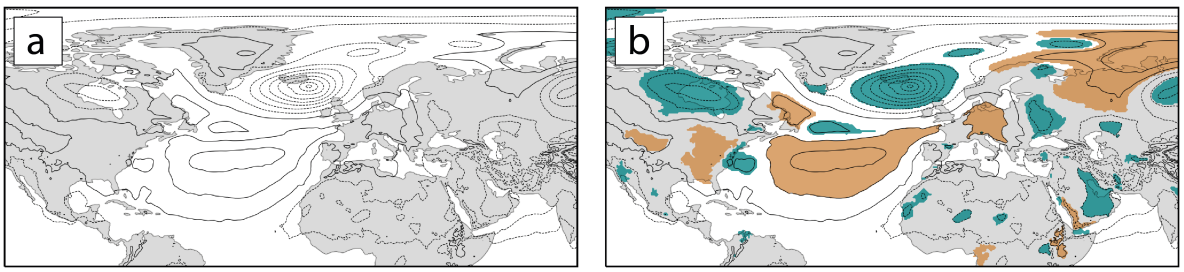

Figure 2.1: Contours denote ERA5 sea-level pressure (*SLP*) at 18 UTC on 7 July 2010. The dashed (solid) contours denote *SLP* in 5 hPa intervals below (above) 1'013 hPa. Beige (turquoise) shading in (b) denote the identified anticyclones (cyclones).

used in computing *SLP* in ERA5. The identification is illustrated at an exemplary time at 18 UTC on 7 July 2010 in Fig. 2.1. By and large, we see that the two weather systems mainly occur in the extra-tropics (Fig. 2.1b). There is high *SLP* over most of Europe and the central North Atlantic with two distinct *SLP* maxima that are identified as separate anticyclones. Several *SLP* minima are identified as cyclones, e.g., one over the Canadian Arctic and another one over Iceland. In addition to extratropical weather systems, there are some surface heat lows identified as cyclones over the Sahara (Fig. 2.1b). Moreover, the extrapolation of temperature to sea-level leads to some artefacts over elevated orography, e.g., the anticyclone identified over the Asir Mountains in the southwestern Arabian Peninsula (Fig. 2.1b). Although we exclude *SLP* minima and maxima above 1'500 m, cyclones and anticyclones might still cover such areas if their centers lie below 1'500 m, and the extrapolation in regions up to 1'500 m elevation is potentially still spurious. Due to these artefacts, orography has to be kept in mind when interpreting the two weather systems.

A summary of the basic ERA5 variables used in the following chapters is provided in Table 2.1. Furthermore, the temporal scale as well as the further processing of the variables used are typically unique to each chapter and are thus introduced there.

2.2 Community Earth System Model climate simulations

We use two versions of the Community Earth System Model (CESM), a widely recognized general circulation model (GCM) developed by the U. S. National Center for Atmospheric Research (NCAR; Hurrell et al., 2013). Both model versions used in this study, version 1.12 (CESM1; Hurrell et al., 2013) and version 2.1 (CESM2; Danabasoglu et al., 2020), are used in the respective large-ensemble projects by NCAR (e.g., Kay et al., 2015) and are also part of the Coupled Model Intercomparison Project 5 and 6 (CMIP5/CMIP6). For both model versions, 6-hourly output is generated with a horizontal resolution of 1.25° longitude $\times$ ~0.9° latitude on 30 vertical levels. These GCM simulations are freely running except for the external radiative forcing. The radiative forcing is determined based on observations for a specific historical period and subsequently relies on future scenarios, predominantly influenced by the projections of anthropogenic GHG emissions (e.g., O'Neill et al., 2014). A highly valuable application

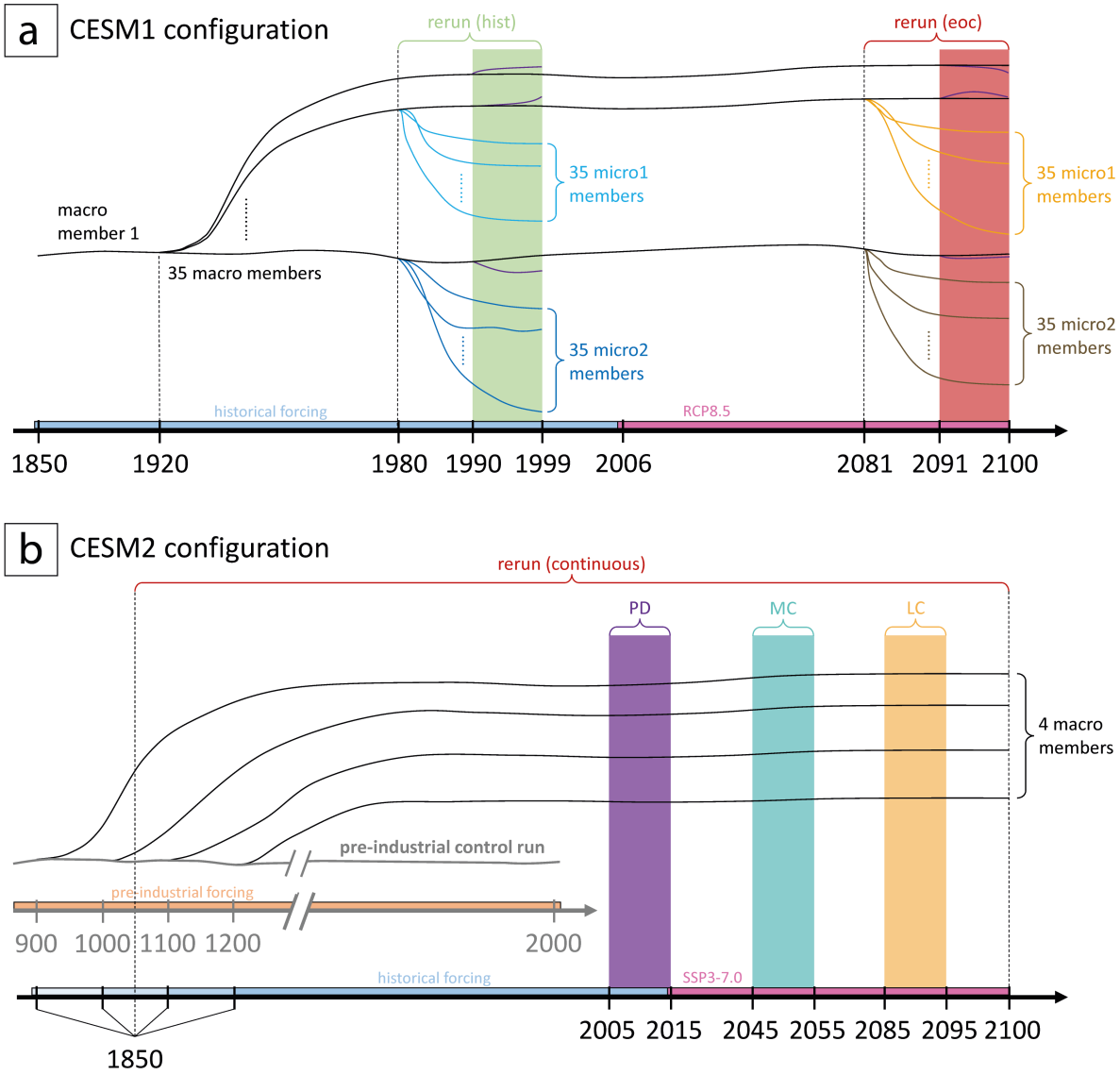

Figure 2.2: Each line denotes a single CESM member. In (a) CESM1, black lines denote the CESM-LENS macro ensemble and colored lines denote the simulations performed for this thesis. In (b) CESM2, the bold grey line denotes the pre-industrial control run (pre-industrial forcing from 1850) and black lines the individual macro ensembles computed for this thesis. The grey time axis in (b) refers to the control run. Colored vertical bars denote the study periods (a) historical (hist; 1990–1999) and end-of-century (eoc; 2091–2100), and (b) present-day (PD; 2005–2015), mid-century (MC; 2045–2055), and late-century (LC; 2085–2095). Colored horizontal bars show the forcing used in the respective period. More details are provided in the text.

of GCMs is to simulate multiple trajectories of the atmospheric evolution in a given climate, while we can only observe a single one in reality (reanalysis data). Through such ensemble simulations, we can explore and statistically assess the internal variability of the atmosphere (and the climate system as a whole). This capability is particularly crucial for investigating extremes at the seasonal timescale, as the limited number of such events in available reanalyses hinders robust statistical evaluation at the local scale. In this thesis, we will utilize CESM simulations based on two distinct approaches, each applied to one of the two model versions,

as outlined in the following two paragraphs.

The configuration of CESM1 (see Fig.2.2a) is designed to simulate a large number of realizations for both a historical (hist) period and an end-of-century (eoc) period, specifically the years 1990–1999 and 2091–2100. To achieve this, we use CESM1-LENS, which consists of an ensemble of 35 macro members spanning the years 1920–2100 (Kay et al., 2015). Macro member 1 was integrated from 1850 onwards, while macro members 2–35 were generated by introducing small perturbations at the round-off level in the oceanic (for macro member 2) and atmospheric conditions (for macro members 3–35) in 1920 (Fig. 2.2a; see Kay et al., 2015). These minute perturbations occurring at branch-off typically lead to distinct atmospheric states within a few weeks (Lorenz, 1963; Kay et al., 2015). Additionally, however, a part of climate variability, mostly that due to different oceanic states, responds only at the timescale of years to centuries and is hence not fully represented in this ensemble configuration (e.g., Meehl et al., 2001). These 35 macro members were integrated using historical forcing until 2005, followed by RCP8.5 forcing thereafter. Atmospheric fields are available either at sub-daily temporal resolution (on a few vertical levels) or in the full vertical column (with lower temporal resolution), but not both. Thus, for our study, these 35 members were rerun for the period 1 January 1990 to 31 December 1999 (hist), and 1 January 2091 to 31 December 2100 (eoc), in order to obtain spatiotemporally high-resolution model output. Two separate micro ensembles were created, each consisting of 35 micro members, by re-running the original macro members 1 and 2 with perturbed (by $O(10^{-13})$ K) atmospheric temperature fields from 1 January 1980 and at 1 January 2081 onward (Fig. 2.2a). As a result, our CESM1 data essentially includes 105 members each covering the 10-year-long hist and eoc periods. By employing a combination of micro and macro members initialized several years and decades before the study periods, respectively, this configuration captures a large part of atmospheric internal variability – the degree to which it captures atmospheric internal variability related to more slowly varying ocean dynamics is questionable. In summary, the CESM1 configuration provides three-dimensional and 6-hourly output spanning 1050 years in both hist and eoc climates. This setup is particularly valuable for assessing seasonal extremes as in Chapter 4, as it includes 1050 realizations of each season in both climates.

The configuration of CESM2 (see Fig.2.2b) aims at assessing internal variability continuously over the course of the 21st century and with different macro members (having variable oceanic states). Therefore, as for CESM2-LENS (Rodgers et al., 2021), several macro members were branched of from a 2'000-year long pre-industrial (PI) control run that constantly uses the radiative forcing of 1850 and thus is in a stable climate (Danabasoglu et al., 2020). Four macro members were computed with restart files provided by NCAR, which were branched off from the PI control run at time instances that are 100 years apart (Fig.2.2b). Hence, they were initialized with different atmospheric and oceanic states, and were integrated forward using the historical forcing until 2014, and that of the SSP3-7.0 scenario thereafter. In contrast to our CESM1 dataset, there are much fewer members, whose output is available continuously in 1850–2100. The CESM2 simulations were further designed to allow better opportunities for

Table 2.1: Name, description, and unit(s) used of the variables used from ERA5, CESM1, and CESM2.

Name	Description (respective dataset)	Unit
T	2-meter temperature (ERA5) temperature at reference height (CESM1)	[K], [°C]
T_s	surface temperature (CESM2)	[K]
q	2-meter specific humidity (ERA5) specific humidity at reference height (CESM1)	[g kg^{-1}]
P	convective plus large-scale precipitation (ERA5, CESM1)	[mm]
p	(surface) pressure (ERA5, CESM1)	[hPa]
SLP	sea-level pressure (ERA5)	[hPa]
$Z500$	geopotential height at 500 hPa (CESM2)	[m]
SH	surface sensible heat flux (CESM2)	[W m^{-2}]
LH	surface latent heat flux (CESM2)	[W m^{-2}]
SW_{net}	net surface shortwave radiation (CESM2)	[W m^{-2}]
LW_{net}	net surface longwave radiation (CESM2)	[W m^{-2}]

model evaluation and hence have a long temporal overlap with ERA5. Moreover, the CESM2 output covers almost the entire time range of internal variability, because (a) the individual macro ensembles were each initialized with different oceanic states, and (b) the branching-off of the members happened more than 100 years before the time period we consider here. In Chapter 5, we make use of the CESM2 setup and use its output in three time windows referred to as present-day (PD; 2005–2015), mid-century (MC; 2045–2055), and late-century (LC; 2085–2095).

Overall, both CESM configurations provide valuable insights for our research goals. First, they allow us to analyze the future climate, and, second, they provide a more comprehensive exploration of the internal atmospheric variability compared to ERA5, thanks to multiple realizations of the atmospheric evolution within a given climate. Specifically, the CESM1 data is highly advantageous for the identification of extreme VPD seasons, as we will demonstrate in the analysis of the hist climate simulations (Chapter 4). On the other hand, CESM2 data will be crucial for assessing the rate of change in Greenland surface melt throughout this century and has the advantage of covering the full range of climate variability (Chapter 5). The availability of 6-hourly output in both datasets is pivotal for our research, as this thesis focuses on capturing atmospheric variability on the sub-daily to daily timescale, which is strongly influenced by weather systems. As for ERA5, Table 2.1 provides the nomenclature of the basic CESM variables used in the following chapters, with all further processing introduced in the respective chapters.

Chapter 3

Meteorological history of low-forest-greenness events in Europe in 2002–2022

3.1 Introduction

European forest ecosystems have typically been in balance with their climatic environment and are thus largely adapted and acclimated to meteorological variability on a larger scale. This balance is increasingly disturbed by anthropogenic climate change, and expected to be further affected by pervasive shifts in forest dynamics (see furher elaborations in Sect. 1.4.1; Seidl et al., 2017; McDowell et al., 2020). This trend manifested in the recent two decades (Seidl et al., 2014), when forests have been affected on up to the continental scale, e.g., in the summer of 2018 (Bastos et al., 2020b), whereby drought was continuously linked to such excess forest mortality (Senf et al., 2020). In the context of drought, forest greenness as measured by satellites is an effective measure of forest vitality in order to monitor the drought-related forest dieback in Europe (Orth et al., 2016; Buras et al., 2020, 2021).

While forests can endure short-term weather extremes (e.g., an individual multi-day heat wave), they are more susceptible to longer-term extreme conditions. Particularly harmful long-term extremes include persisting or sequentially occurring droughts, whereby additional negative legacy effects are mediated through reduced tree resilience (Anderegg et al., 2015, 2020; Bose et al., 2020). However, drought legacy effects have also been suggested to provide acclimation to following droughts (Gessler et al., 2020). Furthermore, a stormy winter followed by a hot-dry growing season allows bark beetles to spread out and attack damaged and dying trees (Temperli et al., 2013; Biedermann et al., 2019; Jakoby et al., 2019). Additionally, persisting heat and/or precipitation deficits can – given fuel availability – trigger forest fires year-round, occurring most intensely in the Mediterranean (Turco et al., 2017). In strongly fuel-limited regions, however, forest fires can in the long run negatively feed back on fire activity (Pausas and Ribeiro, 2013). Lastly, beneficial conditions in the past can exert a negative legacy on forest

Parts of this chapter have been published in Hermann et al. (2023).

vitality in following dry periods through soil moisture depletion and structural overshoot, i.e., an excessive canopy buildup relative to average climatic conditions (Bastos et al., 2020a; Zhang et al., 2021). These examples highlight that in addition to the (co-)occurrence, magnitude, and duration of heat and drought, the position of such meteorological precursors in the longer-term history likely modulates their impact on forest greenness.

In the context of interaction and legacy effects the point in time when such meteorological precursors are relevant to forest greenness is intensively discussed in the literature. Meteorological impact has often been investigated by considering the mean over the current growing season (e.g., Hlásny et al., 2017; Seftigen et al., 2018; Seidl et al., 2020). Senf et al. (2020) revealed that hot-dry conditions are particularly harmful for canopy mortality in March to July. Neumann et al. (2017) identified warm summer temperatures and high variability in seasonal precipitation as meteorological drivers of tree mortality. In a drought-prone region, forest drought stress was about equally determined by temperature in summer and the previous autumn, and precipitation during the cold season (Williams et al., 2013). More generally, drought-induced partial or complete tree mortality shows a threshold behavior (Brodribb et al., 2020; Senf et al., 2020); however, water stress is not equally harmful at all times. Especially outside or at the bounds of the growing season there are complicating factors such as growth compensation, soil moisture coupling, and snowmelt (e.g., Harpold et al., 2015; Bastos et al., 2020a).

The meteorological processes that are relevant for low forest-greenness cover a wide range of timescales, whereby short-term variability can aggregate to longer-term extremes (see Sects. 1.3 & 1.4.1). In addition to blocking (Sect. 1.3) and on somewhat longer timescales, recurrent and quasi-stationary Rossby wave patterns may lead to co-occurring hot and dry conditions (Wolf et al., 2018; Röthlisberger and Martius, 2019; Ali et al., 2021). In central Europe, summer heat waves can also arise from weak synoptic forcing, which, in combination with a Scandinavian blocking, allowed for widespread hot-dry conditions in 2018 (Spensberger et al., 2020). During heat waves with no or reduced precipitation, the soil moisture-atmosphere coupling exacerbates the near-surface warming over drying soils (Fischer et al., 2007; Seneviratne et al., 2010). Accordingly, and especially in the Mediterranean, an extremely hot summer is more likely in years of a winter/spring precipitation deficit (Russo et al., 2019). As Europe hardly experiences drought over a longer (multi-annual) timescale (Schubert et al., 2016), seasonal meteorology, which is strongly linked to weather system dynamics, is of particular interest for forest greenness, and, therefore, in the focus of the present study.

Despite great progress in understanding the eco-hydraulic mechanisms linking drought to events of reduced forest greenness (Brodribb et al., 2020), a systematic analysis of the meteorological history of such events is still lacking (see also Sect. 1.4.1). The purpose of this study is to systematically document and characterize significant aspects of these meteorological histories in Europe's temperate and Mediterranean forests. Specifically, this study seeks to identify meteorological precursors over the 3 years prior to reduced forest greenness in Europe. Hereby

"precursors" are features in the meteorological histories that occur at a statistically significantly higher rate preceding reduced forest greenness events than in climatology, and that are shared among many events. We focus on the evolution of 90 d moving average 2-m temperature (T_{90d}) and precipitation (P_{90d}) as key variables and quantitatively address the following research questions:

1. When and how did T_{90d} and P_{90d} deviate significantly from climatology during the meteorological history of low-forest-greenness events in Europe?

2. Which anomalies in weather system frequencies went along with the meteorological precursors identified in (1)?

To identify low-forest-greenness events, generally characteristic for low productivity, crown defoliation and tree mortality (Buras et al., 2021), we use persistently low values of the Normalized Difference Vegetation Index (NDVI) in the summer of 2002−2022 (Sects. 3.2.2 & 3.2.3). Based on a sub-sampling of the resulting low-NDVI events in combination with a bootstrapping test, we then identify meteorological precursors along their meteorological history, and further investigate the spatial variation of weather system frequencies in Sect. 3.3. Finally, we critically discuss our results and the limitations of our analyses in Sect. 3.4.

3.2 Data and methods

We differentiate broadly between the temperate and Mediterranean biome according to Schultz (2005) in the domain extending from 10°W to 45°E and 35°N to 65°N, excluding all boreal forests (Fig. 3.1a).

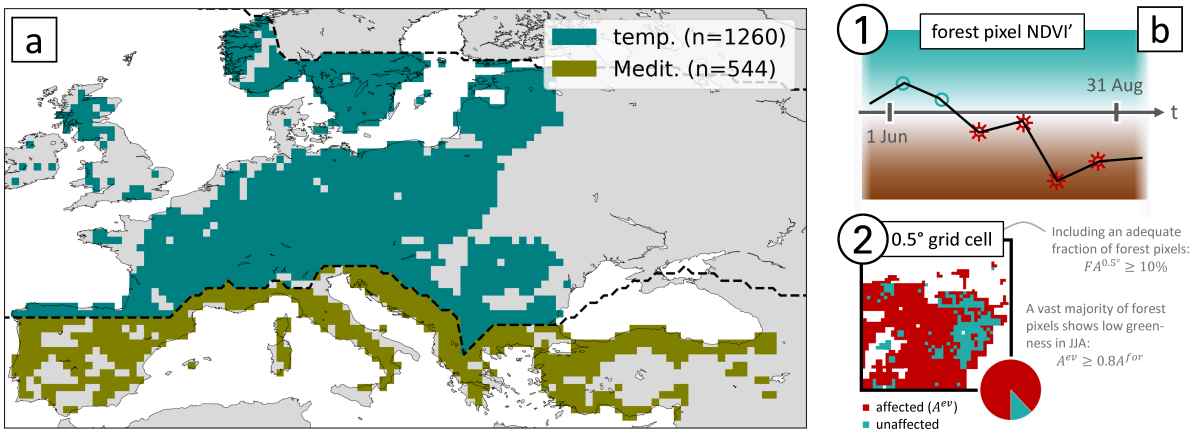

Figure 3.1: (a) Forest grid cells ($FA^{0.5} \geq 10\%$) in the study domain, separated into temperate and Mediterranean forests by the dashed black line. The boreal biome is cropped by the second dashed line in northern Europe. (b) An example of the identification of low-NDVI grid cells, where (1) forest pixels are flagged if at least four out of six time steps show negative NDVI', and (2) 0.5° × 0.5° forest grid cells are flagged if more than 80% of the forest pixels within are flagged (details provided in the text).

3.2.1 Forest cover data

Land surface cover observations are available from the Corine Land Cover (CLC) dataset from the Copernicus Land Monitoring Service at 100 m horizontal resolution from the year 2012 (Büttner et al., 2004). For comparison with the other datasets introduced below, we first interpolate the surface cover to 250 m resolution by nearest-neighbor interpolation. Following that, we mask all pixels except forest land cover classes (coniferous, broad-leaved, and mixed forest) to retain only forest pixels. We then coarse-grain fractional forest area to $0.5^\circ \times 0.5^\circ$ grid cells, which is the spatial resolution of the meteorological dataset used here (ERA5, see Sect. 2.1), hereafter denoted as $FA^{0.5}$. For our analysis we only consider grid cells with a significant fraction of forest cover, defined here as $FA^{0.5} \geq FA^{min} = 10\%$, and hereafter refer to these grid cells as "forest grid cells". According to this definition, there are 1'260 and 544 forest grid cells in the temperate and Mediterranean biome, respectively (Fig. 3.1a).

3.2.2 Normalized Difference Vegetation Index

We use the 16-day Normalized Difference Vegetation Index (NDVI) at ~250 m horizontal resolution from March 2002 to August 2022 from NASA MODIS Terra (Didan, 2015). As mentioned in Sect. 3.2.1, we only use NDVI at forest pixels according to CLC in order to minimize noise from other land cover types. The NDVI is based on the red (RED) and near-infrared (NIR) spectral irradiance:

$$\mathrm{NDVI} = \frac{\mathrm{NIR} - \mathrm{RED}}{\mathrm{NIR} + \mathrm{RED}} \tag{3.1}$$

The greener a forest pixel is, the closer its NDVI is to +1 (Tucker, 1979). The NDVI serves as a measure of vegetation greenness and has previously been used to assess drought impact on ecosystems (Anyamba and Tucker, 2012; Orth et al., 2016; Buras et al., 2020). The Application for Extracting and Exploring Analysis Ready Samples (AppEEARS; `https://appeears.earthdatacloud.nasa.gov`, last accessed 26-September-2022) additionally provides MODIS pixel quality. In addition to masking non-forest land cover, we mask NDVI values that are of poor quality due to snow and clouds, and only retain NDVI values with good and marginal quality according to MODIS pixel quality. The resulting NDVI time series contain missing values, which we linearly interpolate from neighboring time steps as in Buras et al. (2021). Finally, we perform a linear detrending of the entire time series as in Buras et al. (2020) due to a detected greening trend (Bastos et al., 2017).

After this post-processing, at every pixel j at time step t in year n we consider NDVI anomalies ($\mathrm{NDVI'}_{j,t,n}$) from the median in June−August (JJA). To later compare anomalies at different pixels, we standardize the anomalies by the local interquartile range $\mathrm{IQR}_j(\mathrm{NDVI})$:

$$\mathrm{NDVI'}_{j,t,n} = \frac{\mathrm{NDVI}_{j,t,n} - \overline{\mathrm{NDVI}_j}}{\mathrm{IQR}_j(\mathrm{NDVI})} \tag{3.2}$$

The climatological median $\overline{\text{NDVI}_j}$ and IQR_j(NDVI) are both calculated from all 126 NDVI anomalies in JJA 2002−2022.

3.2.3 Identification of low-NDVI grid cells

The aim of the approach presented here is to identify persistently low NDVI in JJA at the relatively large 0.5° scale of the meteorological reanalysis data, i.e., widespread low NDVI. In essence, the approach (1) considers all forest pixels j within a forest grid cell J and flags them if at least four out of the six NDVI' values in JJA are negative, and (2) identifies an event at forest grid cell J (i.e., a 0.5° × 0.5° grid cell with at least 10% forest cover) if at least 80% of forest pixels inside J are flagged (Fig. 3.1b). Our identification scheme thus features 3 tuning parameters: (1) the FA^{min}, (2) the minimum count of negative NDVI' per JJA at the pixel level (c_{ev}^{min}), and (3) the fraction of affected forest pixels per forest grid cell. An extensive sensitivity analysis to reasonable variations in these parameters is presented in Appendix A.1. Hereafter we detail the technical implementation of the approach.

In the first step (1 in Fig. 3.1b), we count the number of negative $\text{NDVI}'_{j,t,n}$ values for the six 16 d values during JJA in year n ($c_{n,ev}$). At every forest pixel j, an event flag $ev_{j,n}$ is determined according to the following criterion:

$$ev_{j,n} = \begin{cases} 1 & \text{if NDVI}'_{j,t,n} < 0 \text{ for } c_{n,ev} \geq c_{ev}^{min} = 4, \\ 0 & \text{otherwise.} \end{cases} \tag{3.3}$$

In the second step (2 in Fig. 3.1b), the total area of forest pixels with $ev_{j,n} = 1$ in J ($A_{J,n}^{ev}$) has to be at least 80% of the total forest pixel area in J (A_J^{for}) – for which we use the term minimum affected ratio $AR^{min} = 80\%$ hereafter:

$$EV_{J,n} = \begin{cases} 1 & \text{if } A_{J,n}^{ev} \geq 0.8 \cdot A_J^{for}, \\ 0 & \text{otherwise.} \end{cases} \tag{3.4}$$

Lastly, for the identified low-NDVI grid cells, we calculate a measure of event intensity as the average of JJA minimum $\text{NDVI}'_{j,t,n}$ over all flagged forest pixels ($ev_{j,n} = 1$), hereafter termed $\text{NDVI}'^{\text{min}}_{J,n}$. Subscripts are omitted whenever possible without loss of clarity.

The resulting low-NDVI grid cells ($EV_{J,n} = 1$) are publicly available (Hermann, 2022) and were tested for their sensitivity to the 3 threshold parameters AR^{min}, FA^{min}, and c_{ev}^{min} in Appendix A.1. Our choice of $AR^{min} = 80\%$ and $FA^{min} = 10\%$ was guided by compromising between sufficient low-NDVI grid cells for statistical evaluation and reasonable peculiarity of the low-NDVI events, which represent a form of extreme event. Furthermore, the main results of this study demonstrate a very low sensitivity to variation in these two threshold parameters, as to a reduction in c_{ev}^{min}. A substantial change of the identified low-NDVI grid cells results only when increasing c_{ev}^{min} to 5, i.e., almost uninterruptedly negative NDVI in JJA. While these most extreme

events would be worth studying, a robust statistical evaluation thereof would not be possible as the number of low-NDVI grid cells diminishes drastically (by almost a factor of 10).

3.2.4 ERA5 data

Atmospheric fields are used from the ERA5 reanalysis (Hersbach et al., 2020) at 0.5°horizontal resolution as described in Sect. 2.1.

a) Normalized meteorological 90 d anomalies

Our analyses focus on 90 d moving average values of 2-m temperature (T_{90d}), total precipitation (P_{90d}), cyclone frequency ($f_{90d}(C)$), and anticyclone frequency ($f_{90d}(A)$). The T_{90d} and P_{90d} can directly be averaged from T and P, while cyclones and anticyclones are identified from hourly sea-level pressure (SLP) fields as described in Sect. 2.1. These two most central weather systems are of interest to the low-NDVI events' meteorological history as they are of great importance to the temperature and humidity structure of the atmosphere. For all four variables, we calculate 90 d mean values as a right-aligned moving average. Each 90 d mean value, therefore, is labelled by the time step of the last value that contributes to the average. Leap days are discarded from the analysis to maintain consistency in each calendar day's climatology and the length of the meteorological histories. The climatologies of the four variables cover 90 d moving averages from 1 September 2001 to 31 August 2022.

Based on these 90 d mean values, we compute normalized anomalies at every forest grid cell for variables $X \in \{T_{90d}, P_{90d}, f_{90d}(C), f_{90d}(A)\}$ as follows:

$$X' = \frac{X - \overline{X}}{\sigma_X} \tag{3.5}$$

where X' denotes the normalized anomaly, and $\overline{X}$ and σ_X denote the climatological seasonal mean and standard deviation in the considered 21 years, respectively, i.e., are calculated over 21 values. Note that the normalization of X anomalies is used merely for scaling with local variability. The scaling enables the spatiotemporal comparison of these anomalies and is not used to estimate the anomalies' return period or likelihood.

For better interpretability of individual meteorological histories, we express $f_{90d}(C)$ and $f_{90d}(A)$ also as anomalies relative to the climatological mean. These relative anomalies are calculated as follows, e.g.,

$$f'^{rel}_{90d}(C) = \frac{f_{90d}(C) - \overline{f_{90d}}(C)}{\overline{f_{90d}}(C)} \tag{3.6}$$

b) Significance assessment

We conduct a bootstrapping test to identify statistically significant meteorological precursors that are shared among the low-NDVI grid cells. The details of how the test is conducted are

described in Appendix A.2. Broadly, the bootstrapping produces 1'000 synthetic samples of meteorological histories with a sample size equal to the number of low-NDVI grid cells under consideration. These samples correspond to many realizations of meteorological histories that are expected in the climatological reference period of 2002−2022, and are used to construct the null distributions for our statistical tests. We test the following null hypothesis $H_{0,EV}$ at different time lags Δt prior to the event time t_{ev} with a significance level of $\alpha = 5\%$:

> $H_{0,EV}$: The meteorological history at $t_{ev} - \Delta t$ is equal to a randomly sampled meteorological history.

We use different test statistics (with corresponding null distributions) to investigate different aspects of the meteorological history under consideration. These statistics are the sample mean T'_{90d}, P'_{90d}, $f'_{90d}(C)$ and $f'_{90d}(A)$ and the fraction of Δt that is on average covered by warm ($T'_{90d} > 0$) and dry periods ($P'_{90d} < 0$). Moreover, our statistical procedure is designed to retain the spatial correlation of the original meteorological fields (for details see Appendix A.2). In the bootstrapping test, p values are estimated from the percentiles of the 1'000 reference values. Values of the meteorological history under consideration that lie outside the range of the 1'000 corresponding synthetic values of the reference meteorological histories receive a p value of 0 (Röthlisberger et al., 2016). We reject the above null hypothesis if an observed value lies outside the 2.5^{th} to 97.5^{th} percentile of the null distribution (defined by the 1'000 values obtained from the bootstrapping). That is, we reject the null hypothesis at the 5% significance level. At time lags Δt when the meteorological history of the low-NDVI grid cells lies outside the confidence interval, $H_{0,EV}$ is rejected for time lag Δt.

3.3 Results

3.3.1 Low-NDVI events in JJA 2002–2022

Low-NDVI events covered substantial parts of both biomes in JJA 2002−2022, and were by far the most frequent in 2022 (Fig. 3.2a,d; Appendix A.3). In the temperate biome, the years with most low-NDVI grid cells – in descending order – were 2022, 2019, 2018, and 2020 (Fig. 3.2a,d). It is noteworthy that these 4 years all lie in the last 5 years of the study period. In 2022, 37% of temperate forests were affected by the low-NDVI event, which far exceeded the previous record years 2019 and 2018 by 13% and 15%, respectively (Fig. 3.2d). The top years in terms of affected forest grid cells in the Mediterranean biome were 2022, 2008, 2005, and 2007, again sorted by decreasing area affected. Low-NDVI grid cells were on average almost twice as frequent in the Mediterranean biome (9% yr^{-1}) compared to the temperate biome (5% yr^{-1}; Fig. 3.2d). Lastly, most low-NDVI events in each biome go along with increased disturbance area as measured by forest canopy mortality according to Senf and Seidl (2021a, Appendix A.4). More specifically, in the overlap period of the two datasets, most low-NDVI grid cells are among the top 4 and five 5 regarding the disturbance area in temperate and Mediterranean forests, respectively.

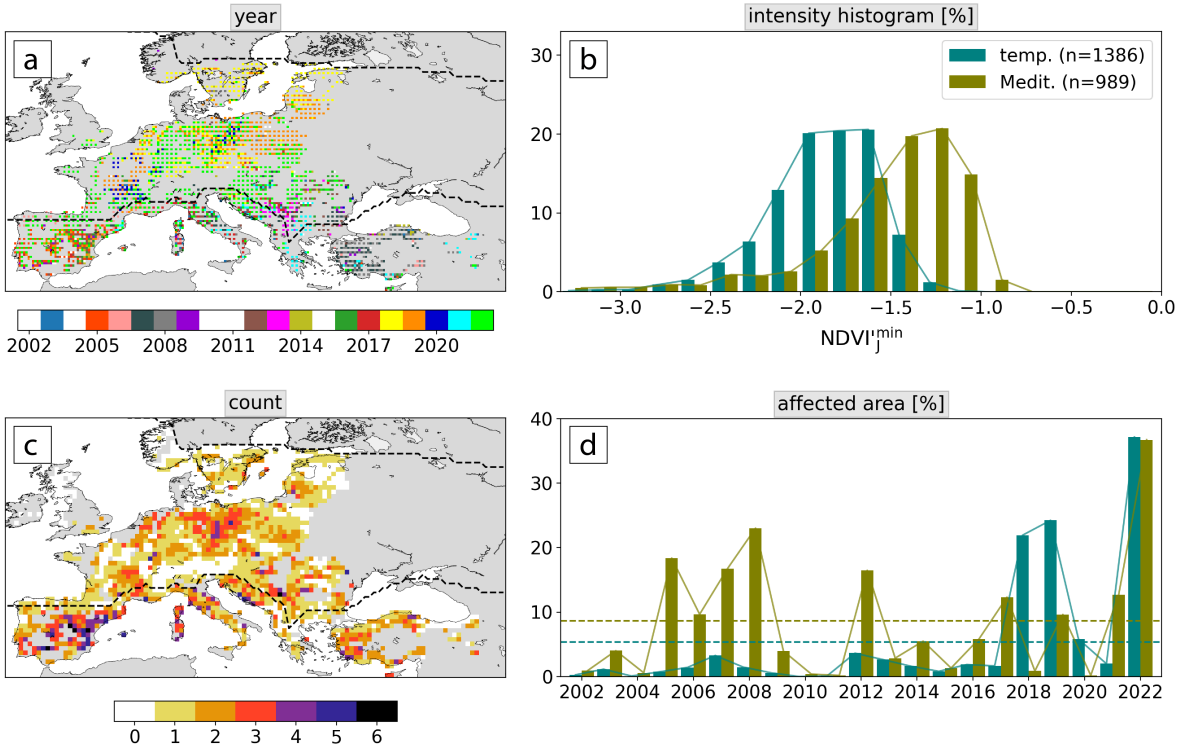

Figure 3.2: Maps of (a) years with a low-NDVI event (Appendix A.3), and (c) total number of events. (b) Histogram of event intensity as measured by $\text{NDVI}'^{\text{min}}_{J}$ in the two biomes, and (d) time series of the biome-integrated area of low-NDVI grid cells relative to all forest grid cells (in %). Years with few low-NDVI grid cells are shown in white in (a). In (a) each grid cell is split into four quads, showing the event year of up to the four most intense events. Dashed lines in (d) show the average over all years. Dashed lines in (a,c) delineate the temperate and Mediterranean biome.

Mediterranean forests faced more but typically less intense events, as measured by the grid-cell-wide average of summer minimum NDVI' (Fig. 3.2b, Sect. 3.2.3). $\text{NDVI}'^{\text{min}}_{J}$ was usually between -1 and -2, whereas it was about 0.5 lower for temperate forests. Hotspot regions with 3 or more events during the 21 years were northeastern Germany, the Balkans, and large parts of the Mediterranean biome (Fig. 3.2c). In the latter, we find many low-NDVI grid cells in Spain in 2005, in Turkey in 2007 and 2008, in Italy in 2017, and in 2022 in the northern Mediterranean (Appendix A.3). Central Europe was largely affected in the past 5 years, while the 2018−2019 events extended further to Scandinavia and the Baltic, and 2020 and 2022 affected also parts of southern France and eastern Europe, respectively. Note that 26% of the forest regions in the study domain never experienced an event in JJA 2002−2022 (Fig. 3.2c). These grid cells are in northeastern Europe or in mountainous regions including the Alps, the Carpathians, the southern Dinaric Alps, and the Eastern Black Sea Mountains.

3.3.2 Examples of meteorological histories

Low-NDVI events affected different forest regions all over Europe with varying intensity, each with its own meteorological history. We first present 3 examples of low-NDVI events that affected regions in Spain in 2005 (SPA05), in the Balkans in 2013 (BAL13), and in France in

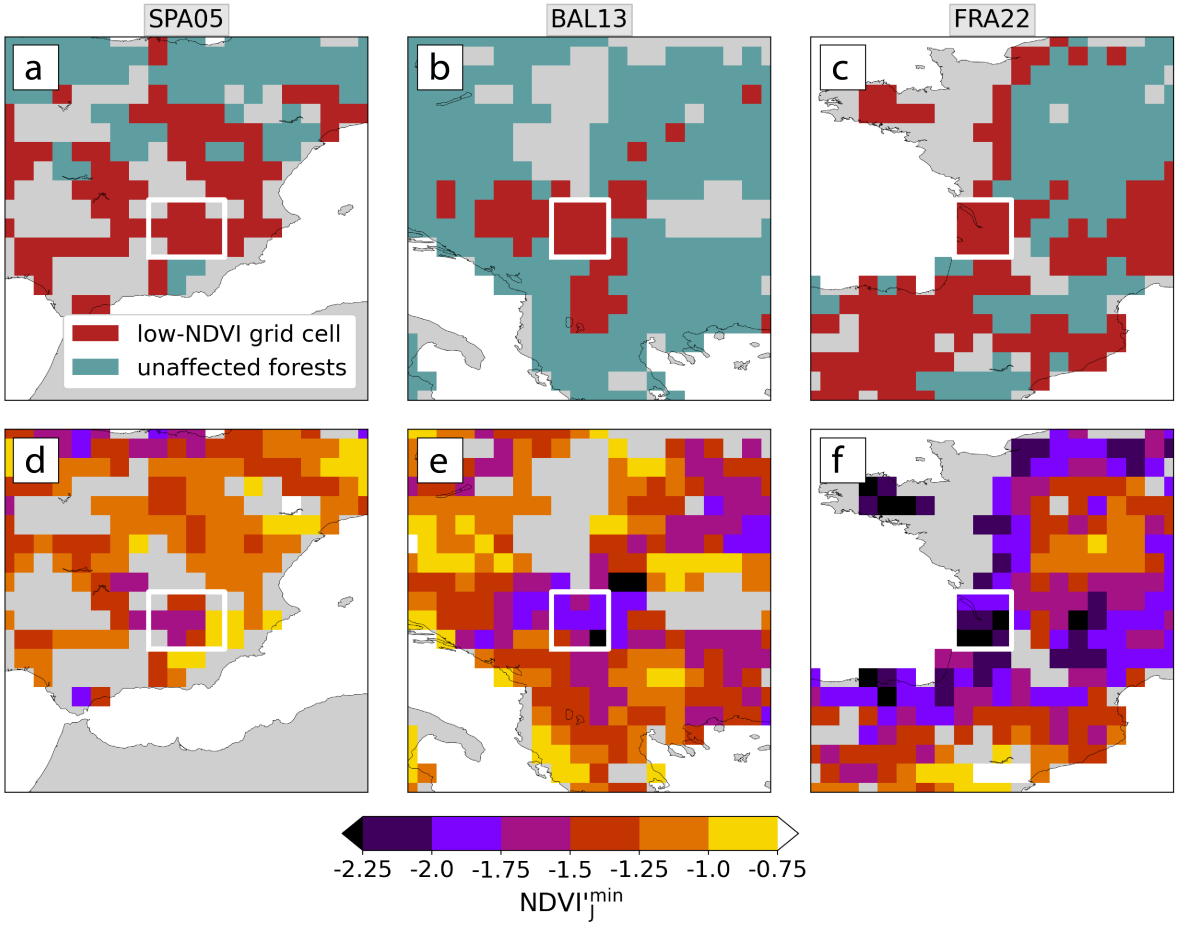

Figure 3.3: (a-c) Low-NDVI grid cells and (d-f) the event intensity measured by NDVI'$_J^{min}$ in (a,d) Spain in 2005, (b,e) the Balkans in 2013, and (c,f) France in 2022. The focus regions of SPA05, BAL13, and FRA22 are framed with white boxes.

2022 (FRA22; Fig. 3.3). First, these examples illustrate that the low-NDVI events identified in this study not necessarily featured a very low NDVI'$_J^{min}$, i.e., a strong magnitude of negative NDVI'. For example, some grid cells of the SPA05 region were identified as low-NDVI grid cells with NDVI'$_J^{min}$ just above -1, while others with NDVI'$_J^{min} < -1.75$ in northern Spain were not identified (Fig. 3.3a,d). In fact, this is an expected behavior of our identification scheme as low-NDVI grid cells are meant to indicate that a very large fraction of forest pixels in that grid cell experienced persistently low NDVI (Sect. 3.2.3). In many cases, however, event intensity as a JJA-integrated quantity was increased at low-NDVI grid cells, compared to their event-unaffected surrounding, illustrated in the example of France in 2022 (Fig. 3.3c,f). Lastly, another interesting case (not shown) occurred in 2014 in Slovenia, where an ice storm in the previous winter caused a few low-NDVI grid cells (Appendix A.3; Buras et al., 2021; Senf and Seidl, 2021c).

We now introduce the concept of a 3-year meteorological history prior to low-NDVI events for these 3 examples. For SPA05, the meteorological history was characterized by a shift from a precipitation surplus during SON-21m to JJA-12m to a precipitation deficit during the year

prior to the low-NDVI event (Fig. 3.4a). Note that seasons MAM, SON, and DJF refer to the periods March–May, September–November, and December–February, respectively, and that we here use a notation for seasons (e.g., SON-21m) that indicates their negative time lag to the events (i.e., SON-21m is the autumn 21 months prior to the low-NDVI event summer, termed JJA-ev). While the cyclone frequency was more than doubled during the former wet period, the period with negative P'_{90d} featured almost no cyclones at all. The relative cyclone frequency anomaly $f'^{rel}_{90d}(C)$ was most negative (-50% to -100%) in the climatological cyclone season from SON to MAM (Fig. 3.4a). For example in early MAM-3m, $P'_{90d} = -1.5$ coincided with $f'^{rel}_{90d}(C)$ of close to -75%. The meteorological history of SPA05 further featured strong cold spells in MAM-15m to JJA-12m and in DJF-6m to MAM-3m with T'_{90d} as low as -2.6 (Fig. 3.4b). Warm periods occurred in JJA-ev and DJF-18m and coincided with an increased frequency of anticyclones, i.e., positive $f'^{rel}_{90d}(A)$. In the second example, BAL13, the magnitude of negative P'_{90d} was also a dominant feature of the meteorological history with even more distinctive persistence over the 3 years (Fig. 3.4c). Similarly to SPA05, a precipitation deficit was often related to negative $f'^{rel}_{90d}(C)$ with some exceptions, e.g., in SON-9m. JJA-12m was characterized by the largest $T'_{90d} = +2.9$ of all examples and did not coincide with substantial changes in $f'^{rel}_{90d}(A)$ or in $f'^{rel}_{90d}(C)$ (Fig. 3.4c,d). Despite continuously positive T'_{90d} from JJA-12m to JJA-ev, the meteorological conditions became less dry and less hot than in JJA-12m, when, interestingly, the BAL13 region was mostly unaffected by low-NDVI events (Appendix A.3). The most recent event FRA22 had again a different meteorological history. It stands out with anomalously high T'_{90d} over the 6 months preceding the event that was related to negative $f'^{rel}_{90d}(A)$ over considerable portions of that period (Fig. 3.4f). Moreover, P'_{90d} during most of these 6 months was only slightly negative, and strongly positive when going further back in the meteorological history, e.g., in JJA-12m (+2.6; Fig. 3.4e). One last noteworthy disparity of FRA22 compared to BAL13 is that JJA-12m was persistently colder alongside negative $f'^{rel}_{90d}(A)$.

While they are illustrative, these exemplary meteorological histories of SPA05, BAL13, and FRA22 reveal great variability and clearly do not allow to draw any causal inferences about how certain aspects of these histories alter the likelihood of low-NDVI events. The events' meteorological histories share certain characteristics but clear disparities also emerge, for example, P'_{90d} in JJA-ev or T'_{90d} in the last year before the event. Thus, in the next section, we systematically analyze the meteorological history of all identified low-NDVI events, and use our sub-sampling and bootstrapping procedure to identify statistically significant meteorological precursors to these events. Again recall that these precursors are features of the low-NDVI events' meteorological histories that were significantly more frequent than during any random meteorological history in the climatology.

3.3.3 Meteorological precursors of low-NDVI events

The previous two sections have illustrated that (i) low-NDVI events were unequally distributed over the study period – especially in temperate forests –, and (ii) a more systematic analysis of meteorological histories is needed to assess their relevance for the low-NDVI grid cells.

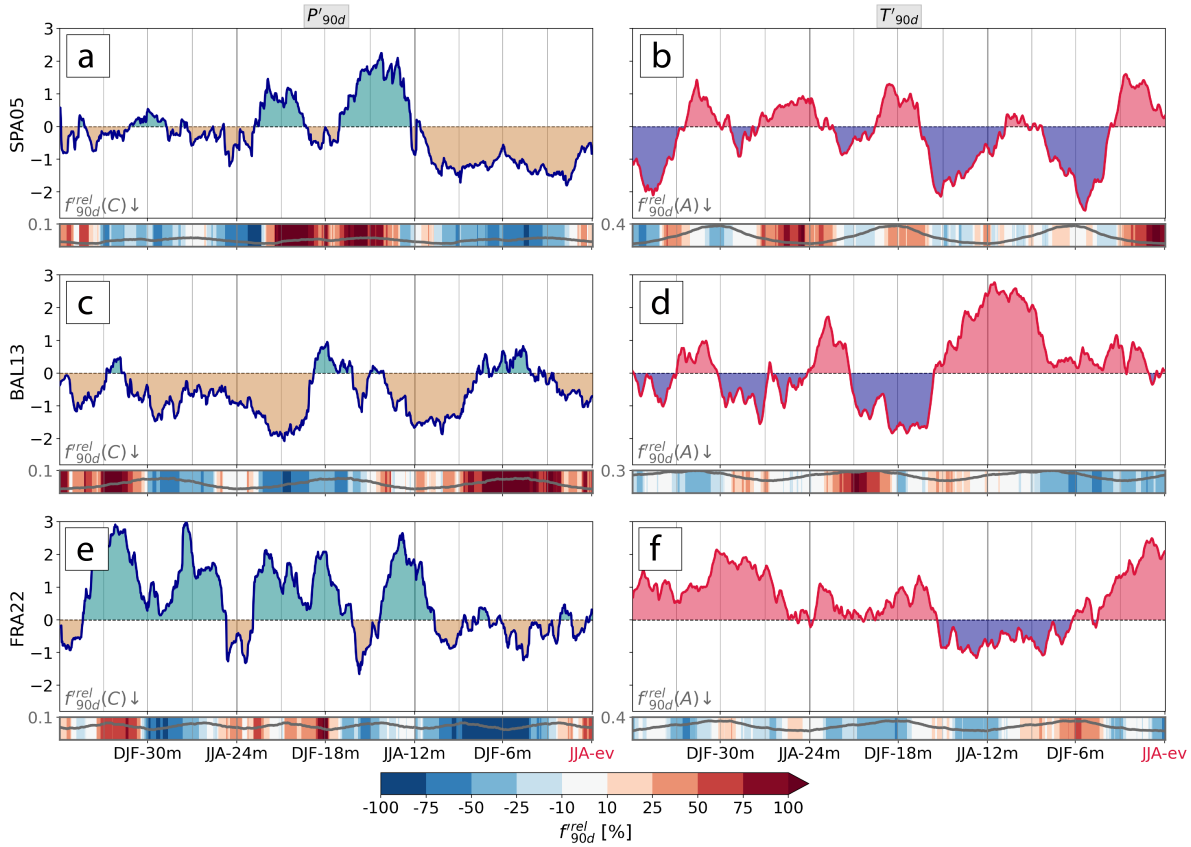

Figure 3.4: The 3-year evolution of (a,c,e) P'_{90d} and (b,d,f) T'_{90d} leading up to low-NDVI events in (a,b) Spain in 2005, (c,d) the Balkans in 2013, and (e,f) France in 2022. The relative anomaly of (a,c,e) cyclone frequency, and of (b,d,f) anticyclone frequency is shaded and their climatological mean is shown as grey line in the heatmap panels.

To account for the uneven distribution of events across years, we investigate the average meteorological history of a random sub-sample of low-NDVI grid cells in the temperate and Mediterranean biome separately. The sub-sample includes a maximum of 10 randomly selected low-NDVI grid cells per year. Given the 21-year-long study period, there is a maximum of 210 contributing low-NDVI grid cells. For years with fewer than or exactly 10 low-NDVI grid cells, all events of the respective year contribute to the sub-sample. The resulting average meteorological history of the temperate and Mediterranean biome is a mean over 170 and 164 low-NDVI grid cells, respectively (see Appendix A.1). Due to the randomness involved in the sub-sampling, we repeat the procedure $n_{samp} = 10$ times to create a variety of average meteorological histories that account for the variability in years when many low-NDVI grid cells were identified. Our bootstrapping test (significance level $\alpha = 5\%$) is then applied to the anomalies of the averaged meteorological histories to identify statistically significant meteorological precursors of the low-NDVI events in 2002−2022 (Sect. 3.2.4b). In the first part of this section, we analyze the magnitude of T'_{90d}, P'_{90d}, $f'_{90d}(C)$, and $f'_{90d}(A)$ during the 3 years leading to low-NDVI events – similarly to Fig. 3.4. Second, we investigate the persistence of dry ($P'_{90d} < 0$) and hot ($T'_{90d} > 0$) meteorological anomalies.

a) Magnitude of meteorological anomalies

The most remarkable meteorological precursors of low-NDVI events in the temperate biome are significantly negative P'_{90d} and positive T'_{90d} during the 4 months preceding the events (bold lines in Fig. 3.5a,c). Note that the 90 d anomaly 4 months prior to the event represents the conditions during the 6 to 4 months prior to JJA-ev: i.e., the time instances denoted here and in the following mark the end of the anomalous time periods. Furthermore, the meteorological history of low-NDVI events in temperate forests showed significantly reduced P'_{90d} in JJA-12m (Fig. 3.5a). In between JJA-12m and JJA-ev, P'_{90d} remained mostly negative but not with a statistically significant magnitude. Similarly to P'_{90d}, also for T'_{90d} significant signals along the meteorological history were always of the same sign (positive in the case of T'_{90d}). Further warm peaks occurred in MAM-3m, SON-9m, JJA-12m, SON-21m, and DJF-30m (Fig. 3.5c). Many of the highlighted periods when the magnitude of meteorological conditions were unusual coincided with larger spread of the ten low-NDVI grid cell sub-samples. For example, P'_{90d} in JJA-12m ranged between $-0{,}2$ and -0.4, indicating that the years with many low-NDVI grid cells (e.g., 2022, 2019, and 2018) showed increased variability at that point in time (Fig. 3.5a). That is, some NDVI grid cells showed a stronger, and others a weaker or no precipitation deficit in JJA-12m, respectively.

In Mediterranean forests, the magnitude of hot and dry anomalies in JJA-ev was comparable to that in temperate forests, with the difference that significantly negative P'_{90d} emerged already 8 months before low-NDVI events during DJF-6m (Fig. 3.5b,d). One more dry period in DJF-18m was significantly different from climatology, as was a wet and warm anomaly in DJF-30m (Fig. 3.5b). Apart from the few mentioned anomalies, the meteorological anomalies further back than 3 seasons (before SON-9m) were within the variability expected from the climatology. Similar to temperate forests, the uncertainty induced by the random sub-sampling is larger when anomalies were of greater magnitude. This applies in particular for the anomalies preceding the low-NDVI events by more than 1 year.

Most of the highlighted anomalies in surface meteorology went along with significant anomalies in the occurrence frequency of weather systems (Fig. 3.5e-h). Note that we here explore the median history of $f'_{90d}(C)$ and $f'_{90d}(A)$, i.e., of normalized anomalies that are comparable across space and time, and not of $f'^{rel}_{90d}(C)$ and $f'^{rel}_{90d}(A)$ as in Sect. 3.3.2, which are more meaningful in a local context (Sect. 3.2.4). In the temperate biome, the hot-dry conditions leading up to JJA-ev related to a concurrent positive $f'_{90d}(A)$ (Fig. 3.5g). Already in JJA-12m, negative P'_{90d} went along with significantly increased $f_{90d}(A)$. These positive anomalies thereby occurred in the season when anticyclones are climatologically the least frequent. Further back in time, negative $f'_{90d}(C)$ in MAM-15m had no direct connection to anomalies in surface meteorology, and the DJF-30m warm anomaly related to persistently negative $f'_{90d}(A)$. In the Mediterranean biome, there were 4 periods of significantly negative $f'_{90d}(C)$: two of them, in DJF-18m and during the 8-month long dry period before the event, coincided with $P'_{90d} < 0$ (Fig. 3.5f). Note that these were during periods when cyclones are climatologically the most frequent. Moreover,

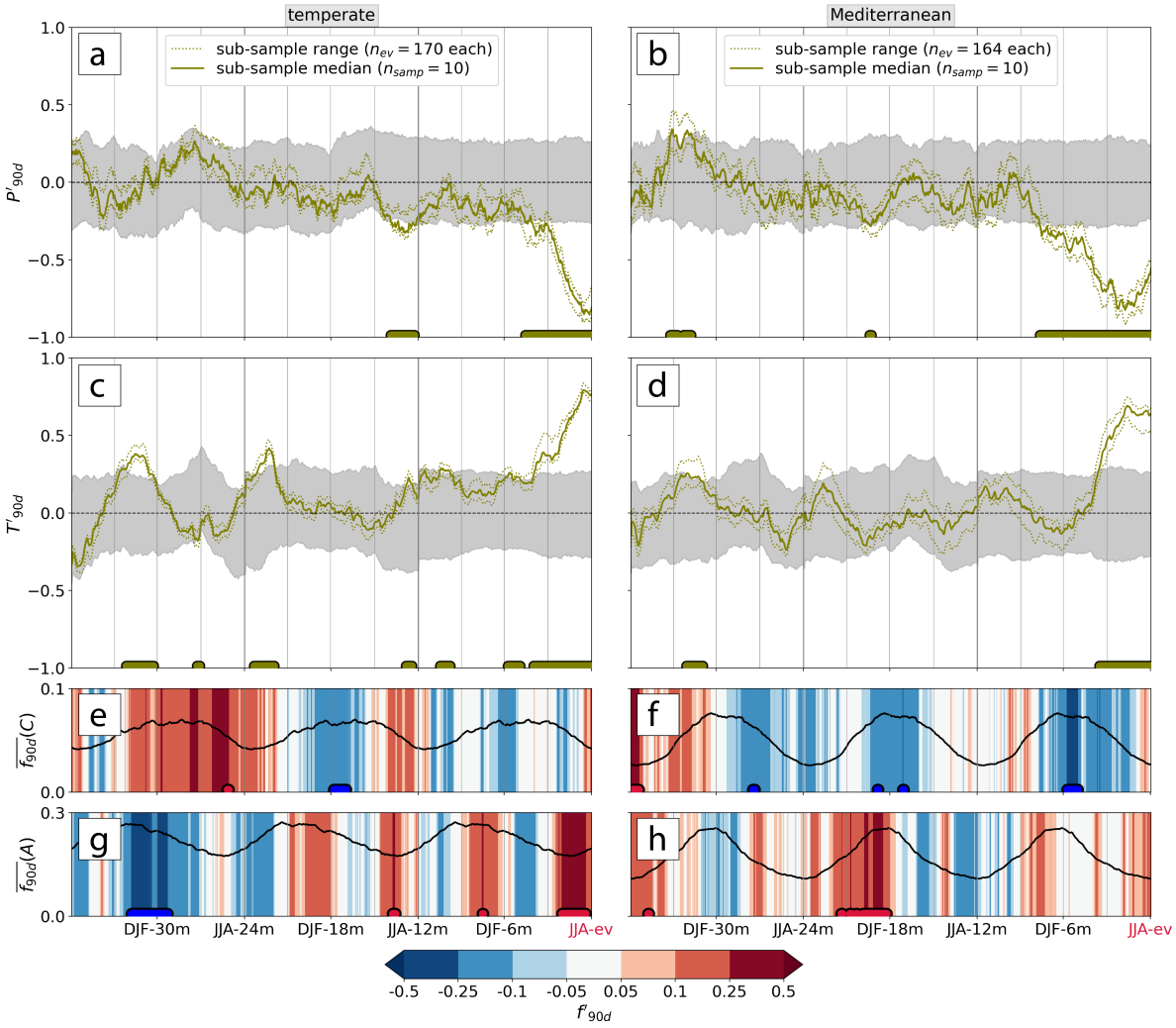

Figure 3.5: Average 3-year evolution of (a,c) P'_{90d} and (b,d) T'_{90d} at low-NDVI grid cells (olive lines). The range spanned up by the $n_{samp} = 10$ sub-samples (of n_{ev} low-NDVI grid cells each) is dotted, their median is solid. The confidence interval (CI), i.e., the $2.5^{\text{th}} - 97.5^{\text{th}}$ percentile of the reference climatology is shaded in grey (see Sect. 3.2.4b). The normalized (e,f) cyclone and (g,h) anticyclone frequency anomalies $f'_{90d}(C)$ and $f'_{90d}(A)$, respectively, as median over the 10 samples are shaded in colors. The 90 d climatology of the weather system frequencies is displayed as a solid line. Plots apply to events in the (a,c,e,g) temperate and (b,d,f,h) Mediterranean biome. Statistically significant median values outside the 95% CI are marked by colored dots at the bottom of each panel.

in the drier than usual DJF-18m, $f'_{90d}(A)$ was persistently positive (Fig. 3.5h). To summarize, significant changes in weather system frequencies often occurred simultaneously with the time periods when the magnitude of P'_{90d} and T'_{90d} were identified as meteorological precursors of low-NDVI grid cells.

The systematic assessment of meteorological histories across all low-NDVI grid cells in 2002−2022 has revealed several meteorological precursors of low-NDVI events in temperate and Mediterranean forests. In addition to the mere magnitude of T'_{90d} and P'_{90d}, some of these anomalies have co-occurred with a significantly altered frequency of cyclones and/or

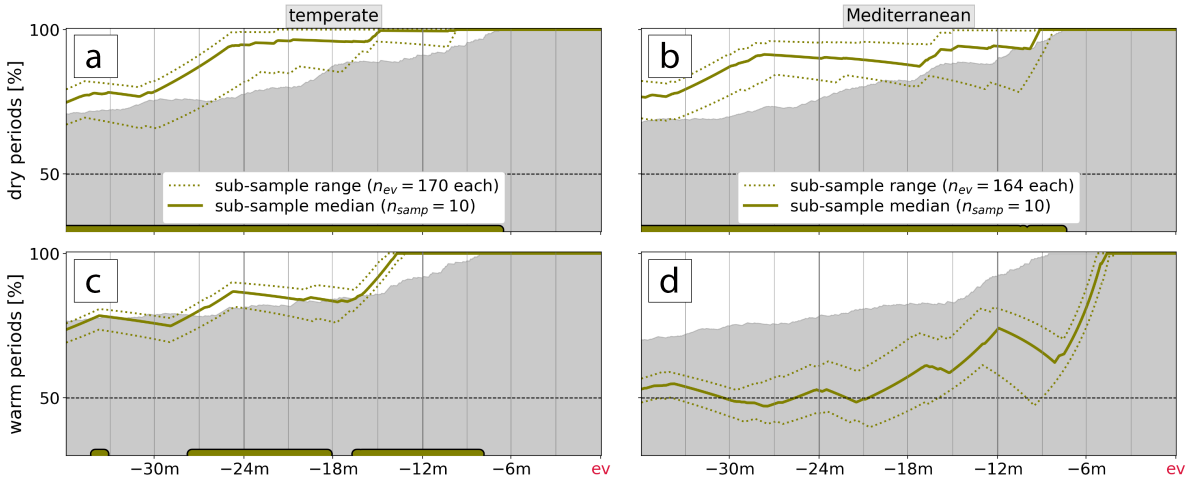

Figure 3.6: The average fraction of the integration period with a (a,c) dry ($P'_{90d} < 0$) and (b,d) warm period ($T'_{90d} > 0$) for decreasing integration period Δt prior to low-NDVI events. The range spanned by the $n_{samp} = 10$ sub-samples (of n_{ev} low-NDVI grid cells per biome) is dotted, and their median is solid. The grey shading displays the 95% confidence interval (CI) of the reference climatology. Statistically significant median values outside the 95% CI are marked by colored dots at the bottom of each panel.

anticyclones. At the biome scale, anticyclones went along with locally drier conditions across all low-NDVI grid cells, e.g., in JJA-ev and in JJA-12m (temperate), and in DJF-18m (Mediterranean). Further, the lack of cyclones in the Mediterranean in their climatological peak season was linked to significantly reduced P'_{90d}. Figure 3.5 reveals that some T'_{90d} and P'_{90d} signals were not significantly unusual in their magnitude; however, seem to have been of unusual persistence. For example, warm anomalies in temperate forests were hardly ever interrupted during the entire meteorological history (Fig. 3.5c). Therefore, we next analyze the persistence of dry and warm anomalies.

b) Persistence of dry and warm periods

The previous subsection pointed to not necessarily intense but unusually persistent dry and warm periods, which we investigate in more detail in Fig. 3.6. To do so we take the data displayed in Fig. 3.5 and compute the fraction of positive and negative T'_{90d} and P'_{90d}, respectively, from a single 90 d average to 3 years prior to the low-NDVI events. This is done, again, for the 10 sub-samples individually, for which we calculate a median time series. Moreover, analogously to Fig. 3.5, we contrast the respective fractions to values expected under the null hypothesis $H_{0,EV}$ that the fraction of dry/warm periods preceding the low-NDVI events (i.e., during Δt) was not different from a randomly sampled meteorological history (grey shading in Fig. 3.6; Sect. 3.2.4b).

In the temperate biome, when going back more than 8 months prior to low-NDVI events, the persistence of warm and dry anomalies was each a statistically significant meteorological precursor to low-NDVI grid cells in 2002−2022 (Fig. 3.6a,c). While T'_{90d} and P'_{90d} prior to this period were only briefly of significant magnitude (Fig. 3.5a,c), their persistence was unusually farther back along the meteorological history. When considering 2 years before events, dry

periods accounted for 82−99% of that time period, where the range is spanned up by the 10 random sub-samples, which is significantly more than the climatological expectation (Fig. 3.6a). Similarly, the persistence of warm anomalies during 81−90% of the preceding 2 years were significantly anomalous (Fig. 3.6c) for 9 out of the 10 sub-sample meteorological histories (not shown). When considering all 10 sub-samples separately, we find that the persistence of dry periods and warm periods was significantly different from climatology at least over 26 and 25 months prior to low-NDVI events, respectively. This is also the integration period when these two meteorological precursors were most distinct – i.e., when $H_{0,EV}$ is most clearly rejected. So an accumulation of both warm and dry periods over the approximately 2 previous years comprised peculiarities of events in the temperate biome.

In the Mediterranean biome, warm periods were more frequent than usual but not significantly so compared to the reference climatology (Fig. 3.6d), which is an interesting contrast to the temperate biome. None of the 10 sub-samples indicate that positive T'_{90d} values were unusually persistent for any Δt during the meteorological history. Similarly to the temperate biome, dry periods accumulate to a highly unusual degree when going back more than 8 months (Fig. 3.6b). The lowest p value is reached 28 months prior to events, when dry periods persisted over 81−95% of the time afterwards. Again considering each of the 10 sub-samples individually, we conclude that the persistence of dry periods was increased over at least 34 months preceding low-NDVI events, which is longer than for low-NDVI events in temperate forests. In contrast, the persistence of warm conditions does not emerge as a significant precursor to low-NDVI events in the Mediterranean.

3.3.4 Spatial patterns of weather system anomalies

Additionally to the biome-wide averages shown in Fig. 3.5e-h, anomalies in weather system frequencies exert some typical spatial patterns along the meteorological history, which we illustrate in the example of the past year prior to JJA-ev. Based on our set of low-NDVI grid cells, we identify common patterns in the anomalies of weather system frequencies in the grid cells' meteorological history. Note, however, that the robustness of such an analysis is inherently low at the local scale due to the rarity of low-NDVI events (Sect. 3.3.1). Figure 3.7 shows the consistency in the sign of $f'^{rel}_{90d}(A)$ and $f'^{rel}_{90d}(C)$ for the 90 d periods of approximately JJA-ev (Fig. 3.7a,b) and MAM-3m (Fig. 3.7c,d), respectively, for all forest grid cells that experienced at least two low-NDVI events in 2002−2022. The results for DJF-6m and SON-9m are shown in Appendix A.5.

In the temperate biome, changes in weather system frequencies that were consistent among most or all low-NDVI events at one location occurred in 66−81% and in 54−64% of the considered forest grid cells in JJA-ev and MAM-3m, respectively. Most prominently, northeastern Europe showed a consistent increase of anticyclones and decrease of cyclones in JJA-ev (Fig. 3.7a,b). Negative $f'^{rel}_{90d}(C)$ was consistent among all low-NDVI events at the southern edge of the storm track, i.e., south of the region of climatologically high $\overline{f_{90d}}(C)$ (Fig. 3.7b). In MAM-3m, how-

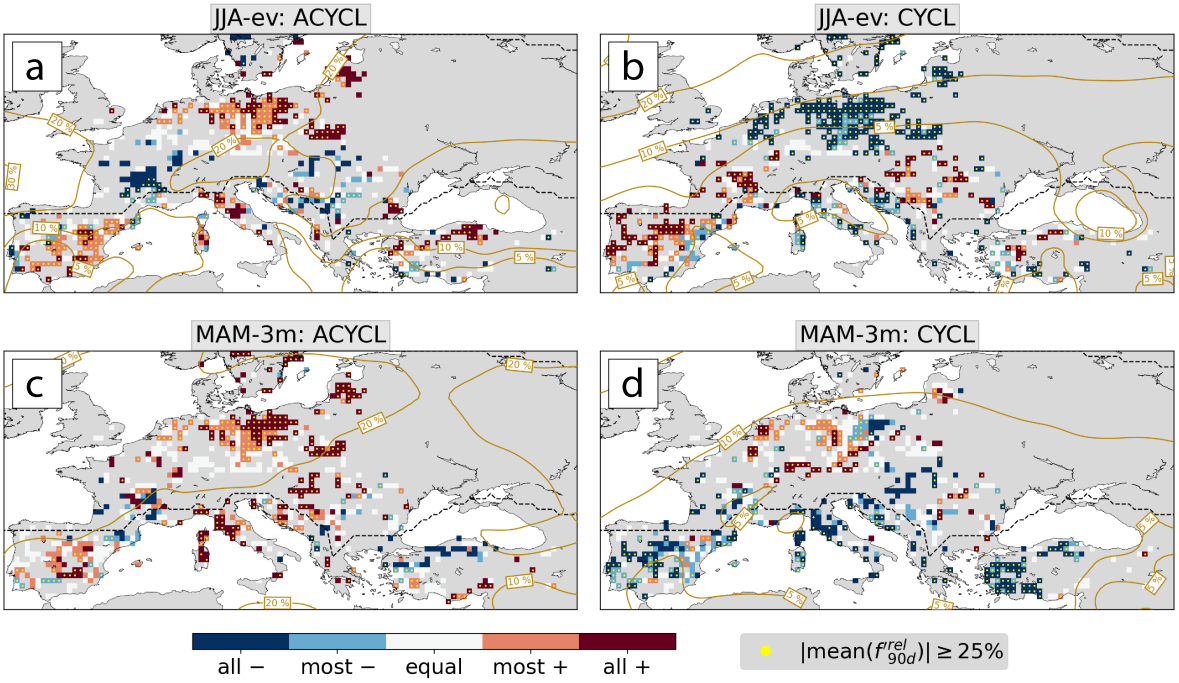

Figure 3.7: The consistency in the sign of (a,c) $f'^{rel}_{90d}(A)$, and (b,d) $f'^{rel}_{90d}(C)$ for all forest grid cells with at least two low-NDVI events in 2002−2022. Maps are shown for the last day of (a,b) JJA-ev, and (c,d) MAM-3m. Stippling indicates absolute averages over all anomalies of the same sign of $\geq$ 25%. Two-dimensional Gaussian-smoothed (2σ) climatological $\overline{f_{90d}}(A)$ and $\overline{f_{90d}}(C)$ are shown in beige contours.

ever, positive $f'^{rel}_{90d}(C)$ occurred simultaneously with positive $f'^{rel}_{90d}(A)$ in Germany and parts of northwestern Europe. Positive $f'^{rel}_{90d}(A)$ in northern Europe was prevalent not only in JJA-ev, but also in MAM-3m (Fig. 3.7a), in DJF-6m, and partly in SON-9m (Appendix Fig. A.5). In MAM-3m this signal further extended towards the Balkans (Fig. 3.7b). Southern France showed an opposite signal of increased cyclone frequency and negative $f'^{rel}_{90d}(A)$ in JJA-ev. Farther back in the meteorological history in DJF-6m and SON-9m $f'^{rel}_{90d}(C)$ was negative for most or all of the low-NDVI events in 56−58% of the considered forest grid cells (Fig. A.6). To summarize, positive $f'^{rel}_{90d}(A)$ and negative $f'^{rel}_{90d}(C)$ were prominent features in northern Europe in the warm and cold season, respectively. Other regions, such as southern France, show interesting differences from this prominent signal.

The Mediterranean showed overall greater spatial coherence than its temperate counterpart. First of all, as with Germany in MAM-3m, the Iberian Peninsula was a region of generally increased weather system activity in JJA-ev. There was a dipole pattern of consistently positive $f'^{rel}_{90d}(C)$ in the West, and a mostly to consistently positive $f'^{rel}_{90d}(A)$ in the East (Fig. 3.7a,b). This synoptic pattern fosters more frequent southerly advection. Note that the Iberian Peninsula was also a hotspot of low-NDVI events, i.e., results there were consistent among up to six events (Fig. 3.2c). The typical signal of positive $f'^{rel}_{90d}(A)$ and negative $f'^{rel}_{90d}(C)$ occurred in the central Mediterranean in JJA-ev and in most Mediterranean forest grid cells in MAM-3m (Fig. 3.7c,d) and in DJF-6m (Figs. A.5 & A.6). In these two seasons, only 5% and 6% of considered forest grid cells showed mostly or consistently positive $f'^{rel}_{90d}(C)$. Also in SON-9m, cyclones were

mostly less frequent than usual (Fig. A.6). Thus, Mediterranean low-NDVI grid cells very often experienced negative $f^{rel}_{90d}(C)$ in the past year of the meteorological history, consistent with the results in Fig. 3.5f. Low-NDVI events in the western Iberian Peninsula hotspot region, however, experienced the opposite change in cyclone frequency in JJA-ev, which might be a signal of intensified Iberian thermal lows (Santos et al., 2015).

3.4 Discussion

3.4.1 Low-NDVI events

The low-NDVI grid cells identified in this study typically represented summers with a heat- and/or drought-induced loss of forest greenness (Anyamba and Tucker, 2012; Orth et al., 2016; Buras et al., 2020). Known drought and heat events were identified as low-NDVI events, e.g., the Iberian drought in 2005 (Gouveia et al., 2009), a 2-year-long drought in 2007−2008 in Turkey (Varol and Ertuğrul, 2016), the 2011−2013 drought in the Balkans (Cindrić et al., 2016), the hot summer of 2017 in Italy (Rita et al., 2020), and the Central European hot drought in 2018 (Schuldt et al., 2020; Senf and Seidl, 2021b). Additionally, we identify 2022 as record-breaking year of the most widespread low-NDVI events covering 37% of the Mediterranean and temperate forest biome each. In 2022, Europe experienced its hottest JJA on record alongside dry soils (Copernicus Climate Change Service, 2022), and the largest carbon emissions from wildfires since 2007 were recorded (Copernicus Atmosphere Monitoring Service, 2022). Specifically, among the countries with most low-NDVI grid cells were also those that faced extreme anomalies in wildfire activity: the burned area in Romania, Germany, France, Spain, and Croatia was 11, 10, 7, 4, and 3 times larger in 2022, respectively, than the 2006−2021 average (EFFIS, 2022). First observations of early leaf senescence as in 2018 are mentioned by Kittl (2022). The regions spared by the low-NDVI event in 2022 – mainly Scandinavia, parts of France, and a belt from the Austrian Alps to the Baltic – were the only regions that showed a surplus in surface soil moisture compared to 1991−2020 conditions (Copernicus Climate Change Service, 2022). Our approach to identify low-NDVI events, therefore, identifies not only events due to heat and drought but also events due to positively interacting disturbances such as fire and insect outbreaks. Finally, however, there was at least one example of a drought-unrelated low-NDVI event, namely an ice storm that hit Slovenia in February 2014 (Senf and Seidl, 2021c; Buras et al., 2021). Consequently, we cannot rule out that other disturbances that were not necessarily linked to heat or drought, e.g., also late frost (Bascietto et al., 2018; Vitasse et al., 2019), have impacted some of the low-NDVI grid cells.

As our approach identifies persistent and widespread NDVI losses, more localized and potentially more extreme reductions in forest greenness are often not captured (Appendix A.3), e.g., logging in France in 2009 (Senf and Seidl, 2021a), or low NDVI following the winter windstorm Gudrun in southern Sweden in 2005 (Buras et al., 2021). Interestingly, the hot drought in 2003 also hardly lead to low-NDVI grid cells in Europe. The NDVI reduction in that summer was

most prominent for grassland and crops but less so for forests (Buras et al., 2020). Forests are capable of resisting a temporally limited drought much better than grassland, as they can respond with reduced evapotranspiration and increased water use efficiency (Wolf et al., 2013). Note, however, that grassland typically recovers better after long-lasting droughts than forests (Stuart-Haëntjens et al., 2018). The only forest regions that were affected by a low-NDVI event in 2003 are in southern France and Italy, where strongest growth reductions in forests were observed (Ciais et al., 2005). Our results, therefore, suggest that – compared to the events since 2018 – the impact of the 2003 drought on forest greenness was generally limited and scattered in space.

3.4.2 Meteorological histories and their inter-biome differences

The purpose of systematically analyzing meteorological histories of low-NDVI events was to identify statistically significant meteorological precursors to these events. Hereby, it should be noted that this statistical analysis alone does not allow to infer causation between the precursors and the low-NDVI events, but identifies unusual co-occurrence of these precursors and the low-NDVI events. The causation surmised in our interpretation of these precursors below is inferred from the large body of process-focused literature we cite. We neither identify a universally valid meteorological history leading to low-NDVI events nor establish hitherto unknown causal links between seasonal timescale meteorology and low-NDVI events. Rather, the value of our approach is that we can systematically examine which aspects of the meteorological history stand out of the noise and variability that are invariably present across the large set of meteorological histories (e.g., Fig. 3.4) identified here.

The case study of low-NDVI grid cells in Spain in 2005 (SPA05) is one example that illustrates this value of our approach (Sect. 3.3.2). The meteorological history of SPA05 showed a precipitation surplus in the previous spring and summer, which was not a significant meteorological precursor to low-NDVI events in the Mediterranean in general (Sect. 3.3.3a). A preceding surplus in precipitation in a water-limited region such as Spain could cause structural overshoot, i.e., the buildup of large crowns with high water demand, which was suggested to worsen the following drought impact (Zhang et al., 2021). Long-term irrigation experiments at dry sites revealed reduced tree growth over several years as a response to ceasing irrigation (Rigling et al., 2003; Feichtinger et al., 2014). Furthermore, short-term irrigation causes more pronounced responses in tree growth than long-term irrigation, while both potentially increase the sensitivity to drought in the following years indirectly via increased leaf area and tree height (Feichtinger et al., 2015). So while there is strong evidence for lagged responses to a previous precipitation surplus due to structural overshoot, our approach shows that this process does not translate to a systematic meteorological precursor at the biome scale in the Mediterranean.

The most striking meteorological precursors of low-NDVI grid cells were the persistence of a precipitation deficit (both biomes) and of positive temperature anomalies (temperate biome) over at least 2 years. Continuously dry conditions reached farther back in Mediterranean than

in temperate forests, respectively, which might be an important difference due to year-round growth of widespread evergreen tree species in the Mediterranean (Camarero et al., 2021). Also, these conditions play an important role for forest fires, which likely aggravated the meteorological impact on NDVI indirectly (Nagel et al., 2017; Turco et al., 2017). The identified extremely unusual accumulation of warm periods over around 25 months prior to events in the temperate biome points to its indirect effects on insect populations and fire, as well as to the joint amplification of drought impacts (Seidl et al., 2017; Sommerfeld et al., 2018; Seidl et al., 2020; Forzieri et al., 2021). Also, because the significantly pronounced warm periods occurred in the (late) growing season of all 3 preceding years, continuously increased temperatures might have worsened the impact of the event-concurrent hot drought through structural overshoot and soil moisture depletion (Bastos et al., 2020a; Zhang et al., 2021). This 4-month-long hot drought in JJA-ev was of significant magnitude for both meteorological anomalies in the studied low-NDVI grid cells. In the Mediterranean, a large precipitation deficit preceded positive T'_{90d} by another 4 months, which could follow from the fact that winter/spring drought in southern Europe increases the likelihood of a hot JJA through an enhanced soil moisture-atmosphere feedback (Seneviratne et al., 2010; Russo et al., 2019). More generally and in both biomes, the emergence of an unusually strong 90 d precipitation deficit already in spring can be particularly damaging (Senf et al., 2020; Bigler and Vitasse, 2021; Bose et al., 2021).

Apart from the accumulation of dry periods reaching far back in time in both biomes, primarily temperate forests show meteorological precursors that occurred more than 1 year in the past. Significantly reduced P_{90d} and increased T_{90d} occurred during the previous JJA, which points towards drought legacy effects (Anderegg et al., 2015). This legacy might not always be reflected in NDVI (Kannenberg et al., 2019), however, it can indirectly affect future forest vitality via reduced tree resilience (Bose et al., 2020). Moreover, the succession of drought in consecutive summers is particularly harmful for temperate forests, while Mediterranean forests show a decreased sensitivity to the second drought (Anderegg et al., 2020). To summarize, the systematic meteorological histories of low-NDVI events and differences between the two biomes can be linked to much of the current mechanistic understanding of forest vitality in the two bioclimatic regions.

3.4.3 The role of weather systems

Our results highlight that the timing and positioning of weather systems are crucially determining their impact on surface meteorology relevant for low-NDVI grid cells. At the biome scale, the at least 34-month-long dry period in the Mediterranean is accompanied by reduced 90 d cyclone frequency, mostly so in DJF and MAM when cyclones are climatologically most frequent (Wernli and Schwierz, 2006). Cyclones are the main contributor to cold season precipitation in these forest regions (Rüdisühli et al., 2020), and also to extreme precipitation (Pfahl and Wernli, 2012b). Other water-limited forest regions show a similar sensitivity to cold season precipitation (Williams et al., 2013), and therefore, to the precipitation-causing weather phenomenon. More frequent anticyclones were typical in JJA-ev and MAM-3m and relate to an upper-level sub-

tropical ridge extending into the Mediterranean – a known driver of heat extremes in southern Europe (Sousa et al., 2018; Zschenderlein et al., 2019). Over the western Iberian Peninsula in JJA-ev, specifically, more frequent cyclones likely occurred as Iberian thermal lows that favor summer heat extremes through increased diabatic heating over the continent (Santos et al., 2015). Thus, reduced cyclone activity all along the meteorological history of the Mediterranean low-NDVI events appears to have been the main contributor to the hot-dry meteorological precursors – with the exception of Iberian thermal lows in JJA.

In temperate forests, the JJA-ev and JJA-12m hot-dry conditions were both accompanied by more frequent anticyclones, especially in regions at the southern edge of the storm track. The accompanying reduction in cyclone frequency in northern Europe corresponds to a northward shift of the jet stream, which can lead to reduced forest greenness in these regions (Messori et al., 2022). More frequent anticyclones, on the other hand, often relate to an upper-level blocking that causes heat and precipitation suppression in central to northern Europe (Pfahl and Wernli, 2012a; Zschenderlein et al., 2019). A few regions in western Europe show an opposite signal, i.e., reduced anticyclone frequency in JJA-ev. This relates to the fact that summer precipitation there frequently occurs within high-pressure systems (Rüdisühli et al., 2020). In these cases, convective precipitation occurs in the moist and unstable inflow west of the anticyclone center (Mohr et al., 2020). So while in JJA a European-centered anticyclone can favor low-NDVI grid cells in northern Europe, it might be unfavorable for low-NDVI grid cells in western Europe. All in all, these considerations highlight the importance of weather systems and the necessity of considering their spatiotemporally varying impact on surface meteorology, also when interested in events of substantial forest impact.

3.4.4 Caveats

The two main caveats of this study are (i) the event aggregation to the comparably large scale, and (ii) the relatively short data record. The former implies that our analyses can account neither for species-specific drought responses (Scherrer et al., 2011; Vanoni et al., 2016), nor for the multidimensional nature of tree mortality (Allen et al., 2015; Etzold et al., 2016; Schuldt et al., 2020). The link between drought, drought response, and tree mortality is mediated by site, stand, and tree properties (Etzold et al., 2019; Vitasse et al., 2019; Frei et al., 2022), and can further be shaped by tree species diversity within a forest (Grossiord et al., 2014), its microclimate (Buras et al., 2018), and legacies of changing environmental conditions due to, e.g., past forest management (Thom et al., 2018). This aggregation, however, is a central element of this study as we aimed to investigate the link of synoptic atmospheric variability with variability in forest NDVI, which both act on very different spatial scales. The event identification is, therefore, targeted to identify only spatially coherent losses of forest NDVI, which are meaningful to aggregate to the larger scale. Also, the sub-sampling of the identified low-NDVI grid cells ascertains that our results do not highlight meteorological precursors that are unique to very few events or regions. Nevertheless, the results of this study should be confronted with more

specific and local impact assessments.

The main consequence of the relatively short data record is that the normalization of meteorological anomalies suffers from significant sampling uncertainty, which renders any comparison over space and time rather difficult. The normalized P'_{90d} and T'_{90d} then do not necessarily represent the actual site-level temperature and precipitation values and their interpretation requires care (Zang et al., 2020). This specifically applies when comparing the meteorological history of the temperate with the Mediterranean biome, respectively, as the latter climatologically receives little precipitation during summer (Schultz, 2005). The normalization, however, is a way to use basic meteorological variables that can readily be interpreted and linked to weather system dynamics, which is of great importance to the novelty of this study.

3.5 Conclusions

This study identified specific aspects of the meteorological history (the 3-year evolution of 90 d temperature, T'_{90d}, and precipitation anomalies, P'_{90d}), which are systematically shared characteristics of events of persistently low summer forest greenness at the 50 km scale in Europe in 2002−2022. Forest greenness as measured by the NDVI is also used as an early warning metric for forest dieback (Buras et al., 2021). First and foremost, in the temperate and Mediterranean biomes, the regions with low-NDVI events in 2022 far exceeded the previous record summers 2018 (temperate) and 2008 (Mediterranean) in terms of spatial extent. During the hottest summer on record in Europe, 37% of both forest biomes were affected by persistently low NDVI, which is about +13% more than during the previous records. In contrast, our approach classifies the impact of the hot-dry summer of 2003 on forests as very limited and, if so, scattered in space.

The approach used in this study identifies and quantifies the meteorological features that preceded many of the events in the same way, and reveals significant differences between biomes. The persistence of dry periods was significantly increased for at least 26 and 34 months prior to low-NDVI events in the temperate and Mediterranean biome, respectively. In contrast, the persistence of hot periods was significantly increased (at least for 25 months prior to the events) only in the temperate biome, but not the Mediterranean biome. Closer to the event summer, negative P'_{90d} and positive T'_{90d} were significantly anomalous in magnitude. In the temperate biome, both anomalies acquired statistically significant magnitudes in spring, 4 months before the low-NDVI event. In the Mediterranean biome, negative P'_{90d} arose another 4 months earlier, i.e., 8 months prior to low summer NDVI. Note that a single P'_{90d} value that was anomalous, e.g., 8 months prior to the low summer NDVI, denotes an anomaly that refers to a 90 d period, i.e., to the 8 to 10 months prior to the event. Finally, the systematic meteorological histories can be used to test whether meteorologically related processes from local observations apply to an entire biome. We discuss structural overshoot (Zhang et al., 2021), which plausibly systematically affects low-NDVI events in the temperate biome through warmer or longer growing seasons. In

contrast, structural overshoot due to more precipitation in the previous year is highly plausible for a case study in the water-limited Mediterranean, but not at the biome scale.

Finally, we provide clear evidence of the spatially variable impact of synoptic-scale weather systems on key meteorological precursors. At the biome scale, the prominent dry periods are often caused by a significantly reduced cyclone frequency in the Mediterranean biome, and by increased anticyclone frequency in the temperate biome. This effect can, however, differ at a local scale, depending on which weather system is locally relevant for precipitation. For example, western Europe often receives summer precipitation from convective cells in anticyclones, and thus hot-dry conditions in the summer are associated with reduced anticyclone frequency.

The important differences between the meteorological histories affecting temperate and Mediterranean forests as identified in this study provide a better understanding of European forests' response to multi-seasonal meteorology. Moreover, we, for the first time, quantify and assess the impact of the extremely hot summer of 2022 and compare it with that of the previous 20 years. Finally, the presented systematic investigations bridge the gap between forest dynamics and atmospheric dynamics, and thus represent a step forward in linking expected forest dieback to changing meteorological and climatic conditions under global warming.

Chapter 4

Extreme vapor pressure deficit seasons and their meteorological contributions

4.1 Introduction

Section 1.4.2 has underlined the importance of vapor pressure deficit (VPD) in summer for crop yield, forest water stress, wildfire risk, and bark beetle outbreaks. As a central quantity in plant hydrology, VPD quantifies the ability of air to draw moisture from the (vegetated) Earth surface, and is defined as the difference between saturation (e_s) and actual water vapor pressure (e_a; see Eq. 1.1). In addition to aspects highlighted in Sect. 1.4.2, reduced evapotranspiration due to high VPD or low soil moisture can again increase VPD (Miralles et al., 2019), and promote the rapid intensification of so-called "flash droughts" (Williams et al., 2017). All in all, high VPD increases the land-atmosphere water vapor flux and directly alters plant functioning, further affecting the biogeophysical environment to the disadvantage of plant functioning.

VPD depends on the atmospheric humidity and temperature and, therefore, varies greatly across the globe and is subjected to change in the coming decades. While e_s is generally determined by the ambient air temperature (T), e_a depends mainly on specific humidity (q), i.e., the availability of moisture in the air, which is controlled by land and ocean evapotranspiration and by atmospheric transport (Fig. 4.1; Wallace and Hobbs, 2006; Byrne and O'Gorman, 2016). Consequently, VPD is highest in hot-dry regions such as large desert regions and in the summer season (Fig. 4.2a). The global trend in VPD has been increasing in the past four decades, and is expected to climb further throughout the 21^{st} century (Fig. 4.2c; Yuan et al., 2019), as expected from its strong dependence on T (Sect. 1.4.2). That is, by the Clausius-Clapeyron relationship, global warming causes a nonlinear increase of e_s of 7% per Kelvin of local warming (Fig. 4.1a; e.g., Wallace and Hobbs, 2006). The rate of change in e_a is more uncertain and spatially varying, but in many regions smaller compared to that in e_s (Held and Soden, 2006; Simmons et al., 2010; Vicente-Serrano et al., 2018). Limitations in e_a are due to limited atmospheric moisture

Small parts of this chapter have been published in Röthlisberger et al. (2021).

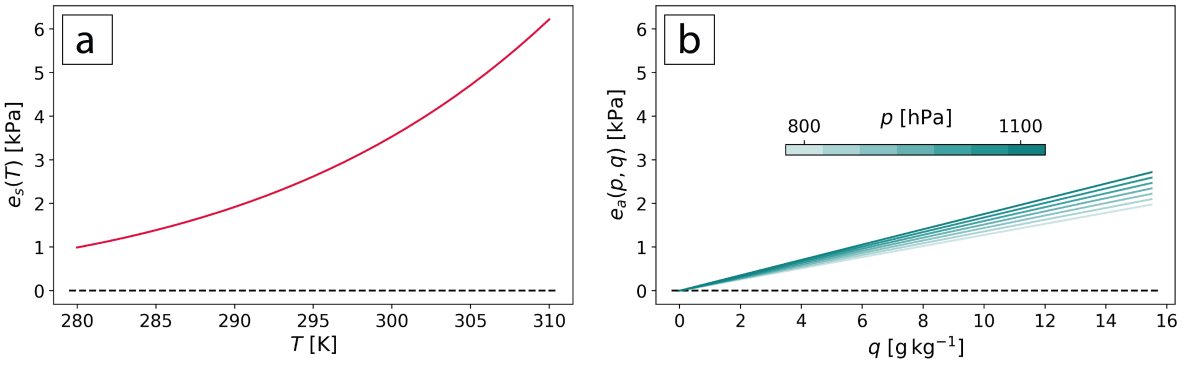

Figure 4.1: The dependence of (a) e_s on T and (b) e_a on q and p. The color of the lines in (b) denote p used to compute the respective $e_a(q)$. The respective equations will be introduced in Sect. 4.3.1.

transport and limited land evaporation (Byrne and O'Gorman, 2016; Vicente-Serrano et al., 2018). Long-term changes in VPD are, therefore, mainly attributed to changes in e_s, especially in regions such as the southwestern United States (U. S.), where e_a is expected to increase only weakly if at all (Ficklin and Novick, 2017).

While the long-term increase of VPD is strongly related to T, the meteorological processes leading to VPD extremes are more complex. On the one hand, variability in VPD is typically larger and more strongly temperature-dependent in climatologically warm regions (Fig. 4.2b), due to the increasing derivative $\frac{de_s}{dT}$ with T (Fig. 4.1a). On the other hand, circulation anomalies and land surface fluxes are also affecting q and, thus, e_a (Fig. 4.1b), which translates to shorter-term variability in VPD (Seager et al., 2015). Extreme VPD in a given climate is hence driven by T and q anomalies, both strongly coupled to atmospheric flow dynamics. Given the relevance of VPD for plant functioning and forest dynamics, longer-term extremes, e.g., of growing season mean VPD or seasonal VPD, are particularly interesting. So far, seasonally extreme VPD has been investigated in case studies (e.g., Schuldt et al., 2020), as identifying seasonal extremes in reanalysis data is inherently challenging given the shortness of these records (Sect. 1.3). In contrast, daily VPD extremes have been studied systematically and benefit from a more robust statistical modelling thanks to extreme value statistics (Gamelin et al., 2022). All in all, the analysis of seasonal VPD extremes regarding the importance of T and q anomalies is highly relevant and provides interesting linkages between ecosystem dynamics and weather and climate dynamics.

In this chapter, we investigate the contribution of anomalies of T and q to the intensity of extreme VPD seasons in the Northern Hemisphere mid-latitudes in June–August (JJA) of the historical climate. We apply a novel scheme for the identification of extremes on the seasonal timescale (Röthlisberger et al., 2021) to VPD in reanalysis and climate model data. This results in spatial objects of extremely high seasonal mean VPD in ERA5 in JJA 1979–2020 (Hersbach et al., 2020), and in a 1'050-year-large ensemble simulation with the Community Earth System

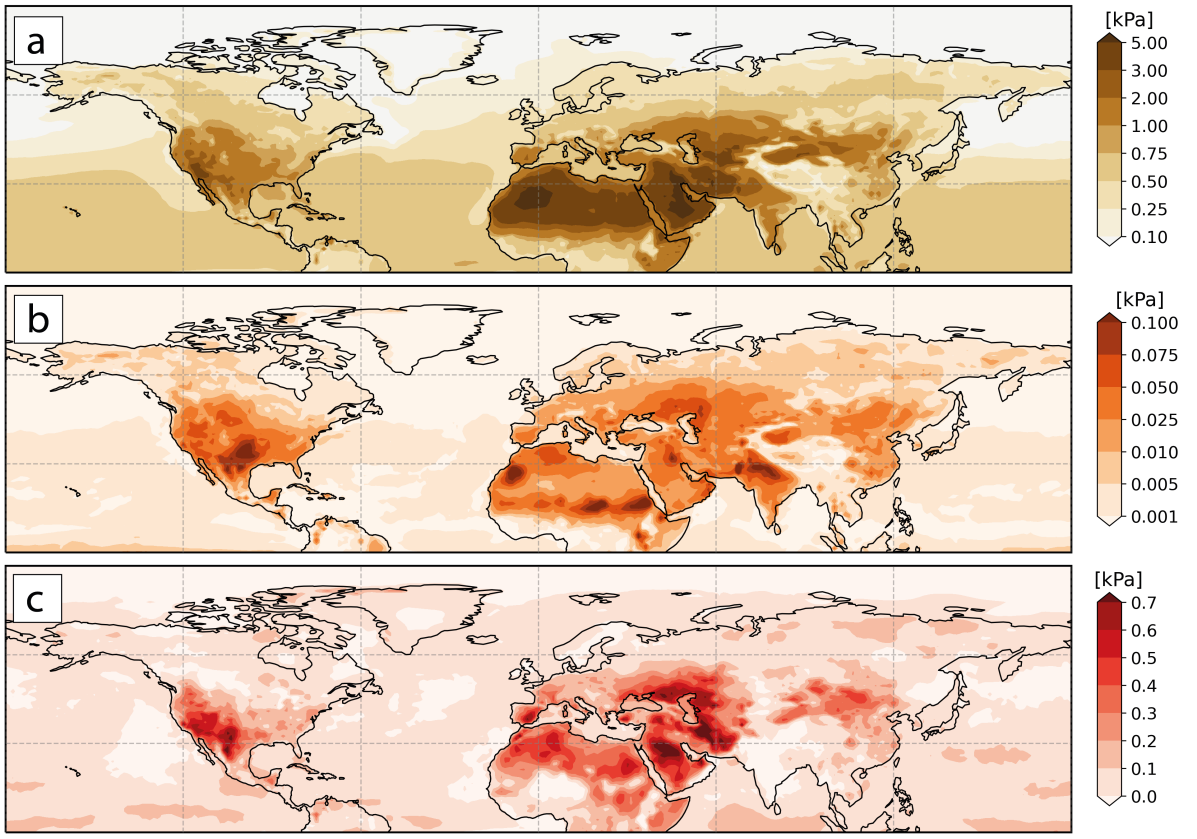

Figure 4.2: ERA5 (a) mean VPD in June–August (JJA) 1979–2020, (b) variance of detrended seasonal VPD anomalies in JJA 1979–2020, and (c) forced change estimate in JJA VPD between 1979 and 2020 (see Sect. 4.3.2) in the Northern Hemisphere.

Model version 1.12 (CESM1; Hurrell et al., 2013) simulations in the hist period (1990–1999; see Chapter 2). Thereby, we aim to answer the following research questions:

1. How can VPD be evaluated to identify extreme VPD season objects?
2. How do extreme positive VPD anomalies arise across the globe and what is the relative importance of T and q anomalies?

To study seasonal VPD extremes independent of the long-term VPD trend, we use detrended VPD anomalies, which are based on a regression of T with global mean temperature (Sect. 4.3.2). Moreover, while previous studies typically decomposed VPD into contributions from e_s and e_a (Seager et al., 2015; Ficklin and Novick, 2017), we, for the first time, decompose seasonal VPD anomalies into contributions from seasonal mean T and q, while discounting intra-seasonal VPD variability (Sect. 4.3.4). By identifying extreme VPD seasons in ERA5 and a large set of CESM1 simulations, we provide a starting point to study extreme VPD at the seasonal timescale systematically – under the premise that CESM1 is able to reasonably simulate VPD extreme seasons (Sect. 4.4). In Sect. 4.5, we compare the two datasets, and explore spatial patterns in q and T contributions to extreme VPD (in CESM1) and the daily substructure of some well-known high-impact VPD seasons (in ERA5). For these case studies, we additionally analyze the impact of the extreme VPD seasons on top-1-meter soil moisture from ERA5-Land (Muñoz-Sabater

et al., 2021) and on drought conditions as by the Standardized Precipitation Evapotranspiration Index (SPEI; Vicente-Serrano et al., 2010). There are several conceivable applications of the developed framework that go beyond the scope of this chapter, which we discuss together with the caveats of this chapter in Sect. 4.6.

4.2 Datasets

4.2.1 ERA5 and CESM1 data

Our analysis is based on JJA seasonal mean data from the ERA5 reanalysis and from historical CESM1 climate simulations, which both are introduced in Chapter 2. In short, the CESM1 data includes 105 different micro and macro members that were run for the period 1990–1999, resulting in a total of 1'050 years of data. From that data we calculate the seasonal mean values at the native spatial resolution of 1.25° longitude × ~0.9° latitude, yielding 1'050 seasonal mean values per grid point. Similarly, we compute 42 seasonal mean values from hourly ERA5 data in JJA 1979–2020, which we linearly interpolate to the CESM grid. More specifically, the variables used are surface pressure, 2-m temperature, and 2-m specific humidity calculated from the 2-m dew point temperature and surface pressure (ECMWF, 2016) from ERA5. From CESM1 we use surface pressure, as well as temperature and specific humidity at the CESM1 reference height. Hereafter, these variables are referred to as T, q, and p, respectively. To distinguish daily values studied in Sect. 4.5.3 from seasonal ones, we will use the subscript d for daily values; e.g., T_d denotes daily 2-m temperature in ERA5.

In order to process the 1'050 years of CESM1 data analogously to the 42 years of ERA5 data, we group CESM1 data into 25 subsets (C1–C25) of 42 years each (without replacement). The years are attributed to the subsets such that each subset contains 4 × 10 years in 1990–1999 from four randomly selected CESM1 members plus two random years from another member.

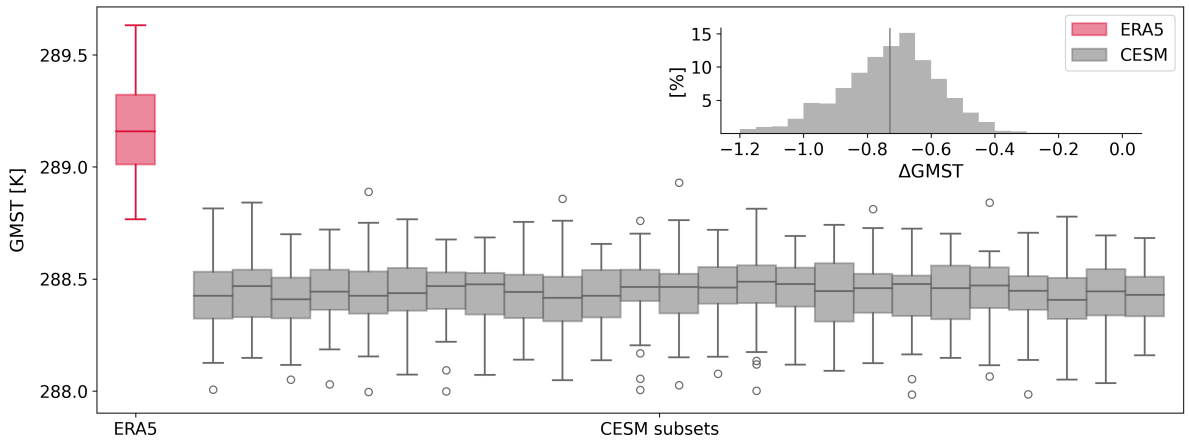

Figure 4.3: Boxplots of non-detrended global mean T in JJA (GMST) in ERA5 (red), and in the 25 CESM1 subsets (grey). The inset panel displays the distribution of deviations of GMST in all 1'050 years of CESM1 data from the ERA5 mean GMST. The vertical line denotes the mean deviation.

The JJA global mean T (GMST), calculated from (non-detrended) T values, is on average 0.73 K higher in ERA5 than in CESM1 (Fig. 4.3). Despite ERA5 data extending further back than our considered CESM1 period, the coldest GMST of ERA5 in 1984 is above the GMST range of most CESM1 subsets. As expected from the longer ERA5 data record, which thus sees more of the warming trend of the last 40 years compared to the CESM1 data (which only experienced 1990–1999 radiative forcing), variability in ERA5 GMST is slightly larger than in the CESM1 subsets (Fig. 4.3). All further data processing, e.g., trend estimation, climatologies, and anomalies of CESM1 data, are always computed for each subset separately in order to exclude effects from conditional bias (Sect. 1.3; Röthlisberger et al., 2021).

4.2.2 Volumetric soil water content

We use daily volumetric water content of the top 1 meter of soil (θ_d) in JJA 1979–2020 from ERA5-Land (Muñoz-Sabater et al., 2021). The θ_d values result from a depth-weighted average of the volumetric water content in the top three ERA5-Land soil layers covering 0–7 cm, 7–28 cm, and 28–100 cm, respectively. Furthermore, we compute seasonal averages over JJA (θ) and a seasonal climatology as mean over θ in JJA 1979–2020 ($\overline{\theta}$). This data is only used for the ERA5 case studies (Sect. 4.5.3). Daily anomalies (θ'_d) are computed similarly to the other variables in this section as $\theta'_d = \theta_d - \overline{\theta}$. Moreover, the data is not interpolated to the CESM1 grid, as it covers only land grid cells and its interpolation would result in the loss of information along the coastlines.

4.2.3 Standardized Precipitation Evapotranspiration Index

We use weekly Standardized Precipitation Evapotranspiration Index (SPEI_w) data available from Vicente-Serrano et al. (2022). This dataset is used for congruence with other studies and is based on T and P data from ERA5 as used in this study, i.e., at 0.5° horizontal resolution. The SPEI is a widely used drought index that is based on the surface water balance, i.e., on the difference between P and potential evapotranspiration (PET), integrated over different time periods (Vicente-Serrano et al., 2010). The water balance is modelled with a three parameters log-logistic distribution, whose parameters are estimated in the study period 1979–2020. For further details regarding the computation of SPEI see Vicente-Serrano et al. (2010). The SPEI is standardized with a mean value of 0 and a standard deviation of 1, and the severity of drought can be inferred from the cumulative distribution function. For example, the probability of an SPEI smaller than approximately -1.65 is 5%, which is why $\text{SPEI} \leq -1.65$ are also referred to as extreme drought conditions (Vicente-Serrano et al., 2022). In this chapter, we use the SPEI calculated at the timescales of 1, 3, and 12 months, hence representing the accumulated water balance of the previous 1, 3, and 12 months, respectively. We refer to the three time series as SPEI_w-1, SPEI_w-3, and SPEI_w-12. As for θ, SPEI data is merely available over land and thus used at its original horizontal resolution of 0.5° to avoid the loss of information during interpolation (Sect. 4.5.3).

4.3 Evaluation and processing of VPD data

The computation of VPD on the seasonal timescale is challenging due to the nonlinear dependence of VPD on the meteorological variables. This section, therefore, not only describes the methods required to compute detrended VPD anomalies consistently in both datasets, but also evaluates the inherent assumptions and consequences. Furthermore, before focusing on the northern mid-latitude land regions, we investigate seasonal mean VPD in the entire Northern Hemisphere to get a more comprehensive understanding.

4.3.1 Deriving a suitable formulation of VPD

We derive a formulation of VPD [Pa] in terms of T, q, and p, starting with the fundamental definition of VPD (Eq. 1.1; Grossiord et al., 2020). For e_s we use the formulation by Murray (1967), which is valid over a wide range of T [K]:

$$e_s = 610.78 \cdot \exp\left(\frac{17.2694 \cdot (T - 273.16)}{T - 35.86}\right) \tag{4.1}$$

Specific humidity can be expressed as the ratio of water density (ρ_w) and (moist) air density ($\rho_d + \rho_w$). To derive an expression $q(e_a, p)$, we use the ideal gas law for dry air and for water vapor to reformulate as follows (Wallace and Hobbs, 2006):

$$q(e_a) = \frac{\rho_w}{\rho_d + \rho_w} = \frac{\frac{e_a}{R_w \cdot T}}{\frac{p - e_a}{R_d \cdot T} + \frac{e_a}{R_w \cdot T}} = \frac{e_a \cdot \frac{M_w}{M_d}}{p - e_a \cdot \left(1 - \frac{M_w}{M_d}\right)} \approx \frac{0.622 \cdot e_a}{p - 0.378 \cdot e_a} \tag{4.2}$$

where $R_w = 461.5\,\mathrm{J\,kg^{-1}\,K^{-1}}$ and $R_d = 287.1\,\mathrm{J\,kg^{-1}\,K^{-1}}$ are the gas constants for water vapor and dry air, respectively, and $M_w = 18.0\,\mathrm{g\,mol^{-1}}$ and $M_d = 29.0\,\mathrm{g\,mol^{-1}}$ are the molar mass of water and dry air. VPD can now be expressed as a function of T, q, and p by combining Eqs. 1.1, 4.1,& 4.2:

$$\mathrm{VPD} \overset{(1.1)}{=} e_s - e_a \overset{(4.2),(4.1)}{=} 610.78 \cdot \exp\left(\frac{17.2694 \cdot (T - 273.16)}{T - 35.86}\right) - \frac{q \cdot p}{0.622 + 0.378 \cdot q} \tag{4.3}$$

The dependence of VPD on the three meteorological variables is nonlinear (Fig. 4.1), strongly so with respect to T, which has various consequences for the work presented in this chapter, in particular also for the timescale used to compute VPD (Sects. 4.3.3 & 4.3.4). Before addressing this issue in greater detail, we estimate the forced trend in seasonal mean VPD in the next subsection.

4.3.2 Detecting and removing the forced trend in seasonal mean VPD

In our statistical modelling of seasonal mean VPD (hereafter simply VPD) anomalies, we assume a stationary VPD time series. Therefore, we first have to detect and account for the forced trend due to increasing atmospheric CO_2 concentration in CESM1 and ERA5 data. That is, we estimate a trend value for each season, which is changing over time due to the external forcing. At the same time, we aim at retaining most of the unforced internal climate variability

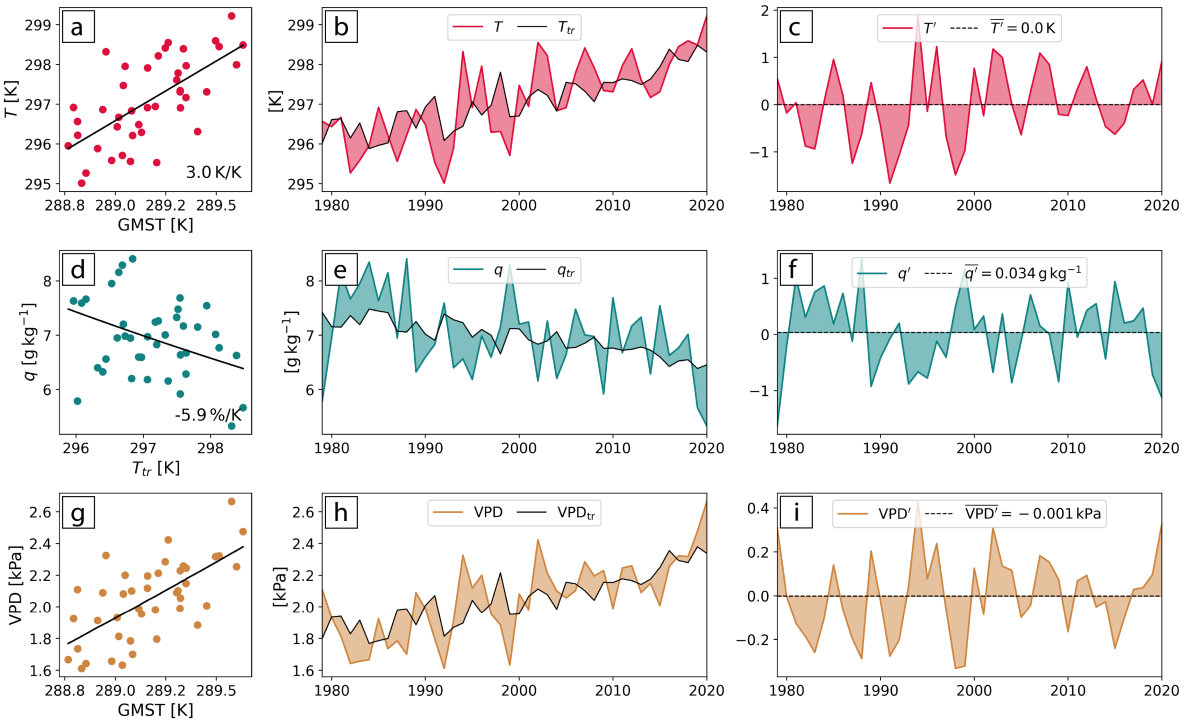

Figure 4.4: Estimation of the forced trend in ERA5 seasonal mean values in JJA of (a-c) T, (d-f) q, and (g-i) VPD near Phoenix, U. S. (35.34°N, 111.25°W). Scatter plots show (a) T vs. GMST, (d) q vs. T_{tr}, and (g) VPD vs. GMST, including the respective trend curves in black. Inset numbers in (a,d) mark the slope of the trend line. (b,e,h) Evolution of the respective values (colored lines) including their trend estimate (black line) in 1979–2020. (c,f,i) Detrended anomalies, i.e., deviations from the trend line, T', q', and VPD′. Their respective climatological mean values are indicated in the legend.

in the individual CESM1 members as well as in ERA5, which is important as internal variability conceivably plays an important role in the occurrence of extreme seasons.

To identify VPD anomalies in ERA5 we first estimate a spatially varying trend that is physically consistent among the variables used – shown at the example grid point Phoenix, U. S. (35.34°N, 111.25°W) in Fig. 4.4. For local T we compute a least square regression with GMST as predictor, because GMST variability is considered predominantly externally forced (e.g., van Oldenborgh et al., 2009; Sutton et al., 2015) and ranges from 288.8 K to 289.6 K (Fig. 4.4a). The resulting trend evolution $T_{tr}(\text{GMST})$ (Fig. 4.4b) is then computed as follows:

$$T = \alpha_1 + \alpha_2 \cdot \text{GMST} + \epsilon \tag{4.4}$$

$$T_{tr} = \alpha_1 + \alpha_2 \cdot \text{GMST} \tag{4.5}$$

where α_1 and α_2 are intercept and slope of the linear regression estimate with residuals ϵ. The T_{tr} is used as an estimate for the evolution in T that occurs as a response to the long-term increase in GMST – not due to inter-annual climate variability. As physics-based scaling arguments suggest an exponential relationship between q and T (Dai, 2006), we estimate the forced trend

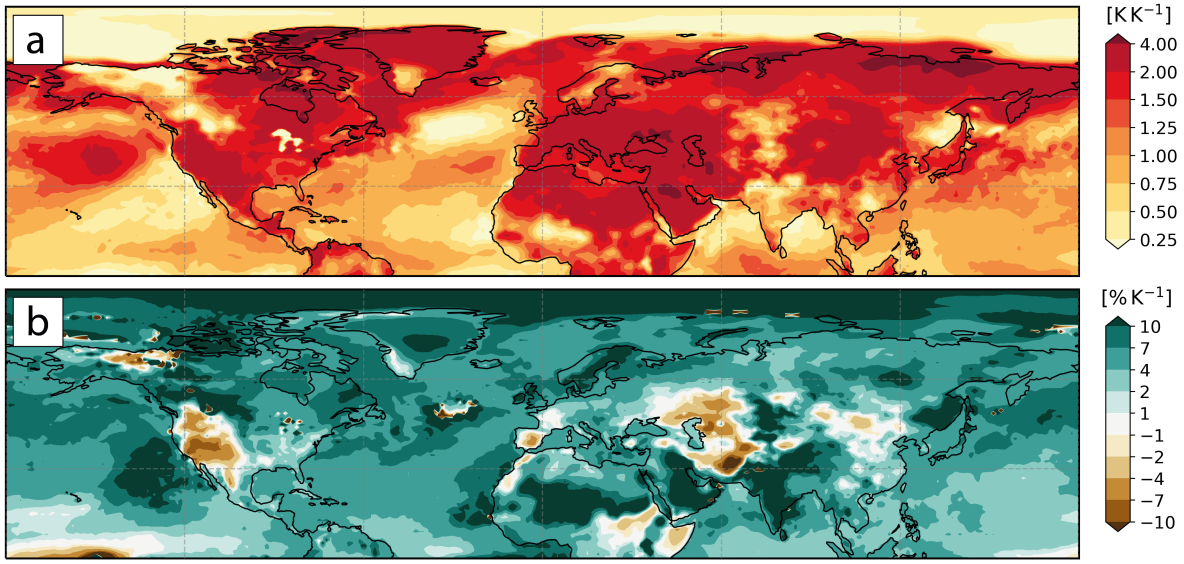

Figure 4.5: Trend parameters estimated from seasonal mean T, q, and GMST values in JJA in ERA5. (a) Trend parameter α_2, i.e., the local warming relative to global mean warming, and (b) $100{\cdot}(\exp(\beta_2) - 1)\,\mathrm{K}^{-1}$, which is the relative moistening wrt. the local forced warming.

in q (q_{tr}) based on an exponential fit of q on T_{tr}. To do so we fit a linear least square regression to $\ln(q)$ with T_{tr} as predictor (Fig. 4.4d,e):

$$\ln(q) = \beta_1 + \beta_2{\cdot}T_{tr} + \epsilon \tag{4.6}$$

$$q_{tr} = \exp(\beta_1 + \beta_2{\cdot}T_{tr}) \tag{4.7}$$

where β_1 and β_2 are intercept and slope of the linear regression estimate with residuals ϵ. The parameter α_2 in Eq. 4.5 denotes the local warming relative to the global mean in $\mathrm{K\,K}^{-1}$, and $100{\cdot}(\exp(\beta_2) - 1)\,\mathrm{K}^{-1}$ is the local trend in q per Kelvin of local warming in $\%\,\mathrm{K}^{-1}$ (Fig. 4.5). The α_2 is considerably larger over land than over ocean, and typically increases towards the pole. One exception is the Arctic sea ice region, where apparently the ice surface keeps T almost constant in JJA, i.e., $\alpha_2 \approx 0$ (Fig. 4.5a). Although GMST has increased by about 0.7 K in 1979–2020, some regions have experienced a forced warming of around 2–3 K. Furthermore, the forced warming typically goes along with a moistening of below +7% expected from the Clausius-Clapeyron relationship (Fig. 4.5b). Strong relative increases in q per Kelvin increase in T_{tr} can be found in the Arctic (with almost no near-surface warming) and very dry regions (with low climatological q). In some regions, namely continental Asia, the southwestern U. S., and the Iberian Peninsula, the forced warming causes a negative trend in q (e.g., Fig. 4.4d).

Given the identified forced signals in T and q, we compute the trend evolution in VPD using Eq. 4.3 (Fig. 4.4g,h):

$$\mathrm{VPD_{tr}} = \mathrm{VPD}(T_{tr}, q_{tr}, p) \tag{4.8}$$

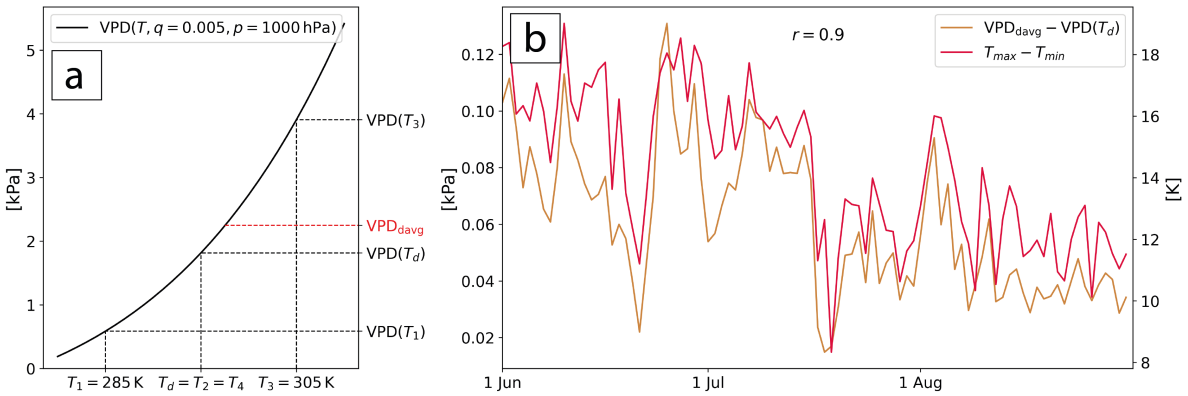

Figure 4.6: (a) VPD as a function of T for constant $q = 5\,\mathrm{g\,kg^{-1}}$ and $p = 1'000\,\mathrm{hPa}$. Temperatures T_1, T_2, T_3, T_4, and T_d are highlighted along with their corresponding VPD, as well as the daily average $\mathrm{VPD_{davg}}$. (b) The difference $\mathrm{VPD_{davg}} - \mathrm{VPD}(T_d)$ (brown) and the daily temperature amplitude (red) over the course of JJA 1994 at Phoenix. The r indicates the Pearson correlation coefficient of the two curves. Note the two different y-axes.

We, thereby, assume no trend in p with respect to GMST due to the lack of physical evidence and the weak dependence of VPD on p. The temporally evolving trend values $\mathrm{VPD_{tr}}$, T_{tr}, and q_{tr} can be interpreted as a reference value in a given year. Deviations from these reference values are assumed to be entirely due to internal variability. Hence, for every variable $X \in \{\mathrm{VPD}, T, q\}$ we compute the seasonal mean anomaly (X') as follows:

$$X' = X - X_{tr} \tag{4.9}$$

Note that only for T, the mean anomaly $\overline{T'}$ is equal to zero because the trend estimate of T is linear (Fig. 4.4a,c). The trend estimates for q and VPD are, by construction, nonlinear, however, are intended to be physically consistent with the forced warming T_{tr}. Therefore, $\overline{\mathrm{VPD}'}$ and $\overline{q'}$ are different from zero but only marginally so, as in the example of Phoenix (Fig. 4.4f,i). Globally, the mean anomalies $\overline{\mathrm{VPD}'}$ are virtually zero with an average of $-3.9{\cdot}10^{-5}$ kPa and a maximum absolute value of 0.011 kPa in the Northern Hemisphere mid-latitudes (30–60°N). A mean anomaly around zero is a desirable characteristic of detrended anomalies, as the remaining internal variability is expected to cancel out over a sufficiently long time series.

The trends and anomalies in CESM1 data are calculated analogously to ERA5, while not the entire dataset containing 1'050 years is used at once. Instead, to ensure equal treatment of CESM1 and ERA5 data, we compute the trend estimates separately for each of the 25 subsets including 42 years of data (Sect. 4.2.1). As for ERA5 data, this procedure results in seasonal mean anomalies (X') that are computed to exclude any externally forced change in $X \in \{\mathrm{VPD}, T, q\}$.

4.3.3 Timescale-dependence of VPD and its intra-seasonal variability

The nonlinearity of Eq. 4.3 implies that sesasonal mean values of VPD will differ depending on whether VPD is first calculated from hourly, daily, or seasonal mean values of T, q, and p (see

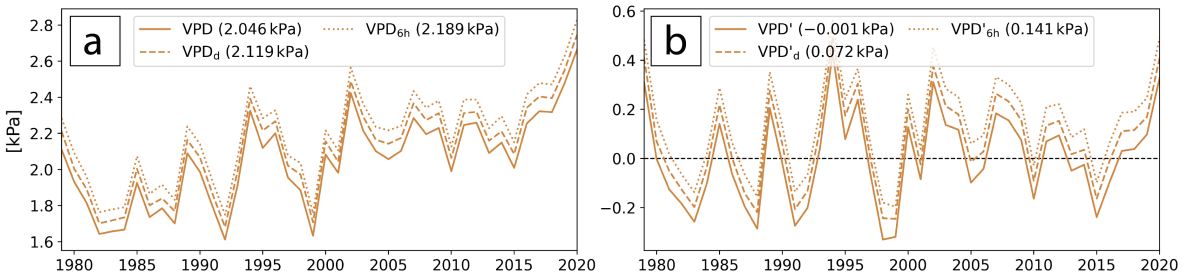

Figure 4.7: Values of (a) VPD, VPD$_d$, and VPD$_{6h}$, which are based on seasonal, daily, and 6-hourly VPD calculations, respectively. (b) Anomalies of the three time series in (a) from VPD$_{tr}$ (Fig. 4.4h). The legends indicate climatological mean values of all time series.

also Appendix in Williams et al., 2013). We first illustrate the effect of sampling frequency for the sub-daily and daily timescale with a simple synthetic example. Let's assume that we compute daily VPD from four 6-hourly mean values. The 6-hourly temperature values are $T_1 ... T_4$, which represent a daily cycle with $T_1 = 285\,\mathrm{K}$, $T_2 = T_4 = 295\,\mathrm{K}$, and $T_3 = 305\,\mathrm{K}$ (Fig. 4.6a). Their average results in the daily temperature $T_d = 295\,\mathrm{K}$. For all five T values, we compute the corresponding VPD(T). Thereby, we focus on the effect of T, which is also the most dominant dependence of VPD (see Sect. 4.3.4), and assume constant $q = 5\,\mathrm{g\,kg^{-1}}$ and $p = 1000\,\mathrm{hPa}$ during the day. Note that $\frac{\partial \mathrm{VPD}}{\partial T}$ is independent of q and p. As $\frac{\partial \mathrm{VPD}}{\partial T}$ is a monotonically increasing function of T, the change in VPD is larger for larger T (Fig. 4.6a). As a consequence, the VPD corresponding to T_3 deviates more from that corresponding to T_d compared to the VPD corresponding to T_1, i.e., VPD$(T_3)-$VPD$(T_d) >$ VPD$(T_d)-$VPD(T_1) (Fig. 4.6a). Therefore, the daily average VPD$_{\mathrm{davg}}$, computed as the average of VPD(T_1), VPD(T_2), VPD(T_3), and VPD(T_4), is larger than VPD(T_d).

Now using ERA5 data at the example grid point near Phoneix in JJA 1994, the underestimation of VPD$_{\mathrm{davg}}$ when using daily instead of 6-hourly T, q, and p is on the order of a few percent (Fig. 4.6b). Furthermore, the difference VPD(T_d) − VPD$_{\mathrm{davg}}$ is strongly correlated ($r = 0.9$) with the amplitude of the diurnal cycle of T, computed as the difference of daily maximum and minimum T, i.e., $T_{max} - T_{min}$. To summarize, the use of lower-frequency daily average T_d necessarily causes an underestimation of VPD compared to VPD$_{\mathrm{davg}}$, which is calculated from sub-daily values.

This behaviour of VPD can be summarized more generally: The more frequently T is sampled, the larger and the more realistic are the resulting long-term mean VPD values. We investigate this effect again on the seasonal timescale by comparing seasonal VPD as in the previous section with those computed from daily (VPD$_{\mathrm{d}}$) and 6-hourly values of T, q, and p (VPD$_{6h}$), respectively in Fig. 4.7a. Furthermore, we compare their anomalies VPD', VPD'$_{\mathrm{d}}$, and VPD'$_{6h}$ in Fig. 4.7b, whereby VPD'$_{\mathrm{d}}$ and VPD'$_{6h}$ are also computed wrt. VPD$_{tr}$, i.e., trend values deduced from seasonally calculated VPD. The VPD$_{6h}$ values are, as expected, largely underestimated by VPD with a root mean square deviation normalized by the mean ($nRMSD$) of ~9% (Fig 4.7a).

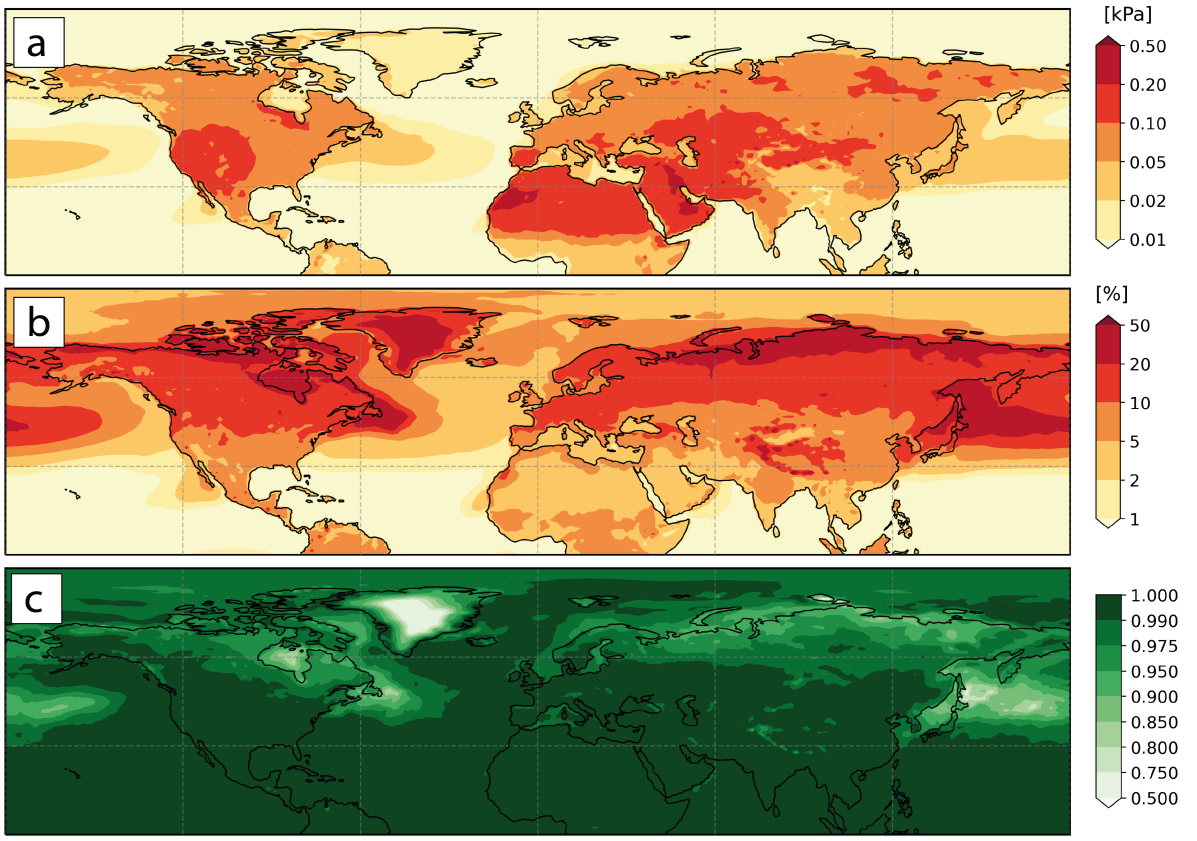

Figure 4.8: (a) Mean absolute difference VPD_{6h} minus VPD, (b) normalized RMSD of VPD_{6h} and VPD, and (c) Pearson correlation coefficient between the anomalies VPD′ and VPD'_{6h} all in JJA 1979–2020.

The underestimation is about half ($nRMSD \approx 5\%$) when using VPD_d to approximate VPD'_{6h}. Interestingly, the underestimation by VPD and VPD_d at this grid point hardly varies from season to season. This means that daily as well as sub-daily variability, which is only captured by VPD_d and VPD_{6h}, respectively, are about the same in every season. As a consequence, VPD′ as well as VPD'_d agree extremely well with VPD'_{6h} except for an approximately constant offset (Fig 4.7b). The offset of VPD′ and VPD'_{6h} quantifies the average contribution of intra-seasonal variability to VPD_{6h}, which, in the example of Phoenix, equals 0.141 kPa or about 7%. Furthermore, the offset between VPD′ and VPD'_d and that between VPD'_d and VPD'_{6h} separately quantify the effects of day-to-day and of sub-daily variability, respectively. At this grid point, the intra-seasonal variability is on average composed of 51% day-to-day variability and 49% sub-daily variability.

Across the Northern Hemisphere, while the average underestimation of VPD_{6h} by VPD differs, the co-variability of their anomalies is very high (Fig. 4.8). In absolute terms, intra-seasonal variability increases VPD by on average 0.094 kPa in mid-latitude land regions, with the largest effect in dry land regions where absolute VPD is largest (Fig. 4.8a). Relatively speaking, the $nRMSD$ between VPD and VPD_{6h} is around 5–20% over mid-latitude land. The $nRMSD$ is largest in regions with a pronounced intra-seasonal variability of T, q, and/or p, e.g., in the storm tracks and in particular in high latitudes (Fig. 4.8b). There, the effect of intra-seasonal

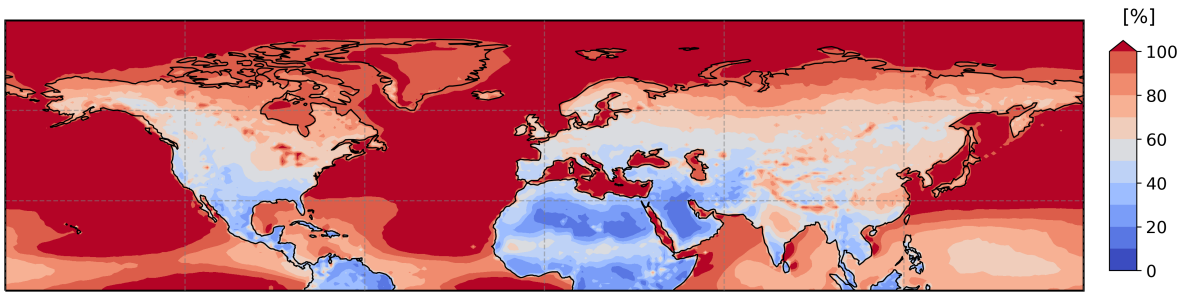

Figure 4.9: The effect of day-to-day variability on VPD (computed as mean difference between VPD_d and VPD) relative to the effect of total intra-seasonal variability (computed as mean difference between VPD_{6h} and VPD) in JJA 1979–2020. Values of 0% (100%) indicate that the entire effect on VPD is owed to sub-daily (day-to-day) variability.

variability on VPD is dominated by day-to-day variability, which originates from, e.g., changing solar insolation, synoptic weather systems, and variable soil moisture and snow cover (Fig. 4.9). In contrast, in more arid and sub-tropical regions day-to-day VPD variability is smaller and/or has a minor effect on VPD (Fig. 4.9), which is why the underestimation of VPD_{6h} by VPD is much smaller (Fig. 4.8b). There, the daily cycle (of mainly T) contributes to sub-daily VPD variability, which is larger than day-to-day variability. In both cases, the absolute values of VPD as used in the previous section are systematically lower than the values derived from data with higher temporal resolution, due to the nonlinear dependence of VPD on T. Note, however, that importantly, the agreement between VPD′ and VPD'_{6h} – and also VPD'_d (not shown) – is extremely high and the Pearson correlation coefficient between the two exceeds 0.95 in most mid-latitude land regions (Fig. 4.8c). That is, even though the absolute values of VPD used here underestimate the seasonal VPD computed from temporally higher resolution data, this underestimation seems to be roughly constant in time. Moreover, across all mid-latitude land regions, this underestimation arises from the effect of 58% day-to-day and 42% sub-daily VPD variability (Fig. 4.9). Based on the results in this subsection, we hereafter assume that the magnitude of VPD′ is not affected substantially by the investigated underestimation.

All in all, the previously deduced VPD′ (Sect. 4.3.2) are particularly well-suited for the purpose of this chapter. Firstly, as we will see in the following section, VPD′ is the preferred quantity to assess VPD-contributions of q' and T' independent of intra-seasonal VPD variability, which would not be possible when using seasonal mean values based on temporally higher resolved VPD data. Secondly, and of equal importance, we can use VPD′ to identify extreme VPD seasons as they capture VPD variability but not any forced trend. Still, one has to bear in mind that the absolute VPD values used here underestimate the more realistic and plant-relevant VPD_{6h}.

4.3.4 Decomposition of VPD′

In order to better understand VPD′ from a meteorological perspective, we decompose each VPD′ value into contributions from T' and q' according to $VPD(T, q, p)$ (Eq. 4.3). In a second step, the contribution of q' is split into a reference part, which captures the effect of locally and

climatologically expected moistening or drying on VPD′ for a given T', and a particular part that represents the deviation of q from the reference part.

In the first step, we use a multivariable linearization of VPD from the trend evolution, i.e., we approximate any value $\mathrm{VPD}(T, q, p)$ tangentially from $\mathrm{VPD}(T_{tr}, q_{tr}, p)$. Therefore, according to e.g., Stewart (2012):

$$\mathrm{VPD}(T, q, p) \approx \mathrm{VPD}(T_{tr}, q_{tr}, p) + (T - T_{tr}) \cdot \frac{\partial \mathrm{VPD}}{\partial T}\bigg|_{T_{tr}, q_{tr}, p} + (q - q_{tr}) \cdot \frac{\partial \mathrm{VPD}}{\partial q}\bigg|_{T_{tr}, q_{tr}, p} \tag{4.10}$$

which can be formulated as:

$$\mathrm{VPD}(T, q, p) = \mathrm{VPD}_{\mathrm{tr}} + T' \cdot \frac{\partial \mathrm{VPD}}{\partial T}\bigg|_{T_{tr}, q_{tr}, p} + q' \cdot \frac{\partial \mathrm{VPD}}{\partial q}\bigg|_{T_{tr}, q_{tr}, p} + \epsilon \tag{4.11}$$

where ϵ marks a residual term containing higher-order terms, and the derivatives of $\mathrm{VPD}(T, q, p)$ wrt. T and q are evaluated at $(T, q, p) = (T_{tr}, q_{tr}, p)$ (Eq. 4.3.). We rewrite the above equation to:

$$\mathrm{VPD}' = \underbrace{T' \cdot \frac{\partial \mathrm{VPD}}{\partial T}\bigg|_{T_{tr}, q_{tr}, p}}_{\mathrm{VPD}'_{T'}} + \underbrace{q' \cdot \frac{\partial \mathrm{VPD}}{\partial q}\bigg|_{T_{tr}, q_{tr}, p}}_{\mathrm{VPD}'_{q'}} + \epsilon \tag{4.12}$$

where $\mathrm{VPD}'_{T'}$ and $\mathrm{VPD}'_{q'}$ denote the contributions of T' and q' to VPD′, respectively.

The steps from Eq. 4.10 to Eq. 4.12 refer back to ideas outlined in the previous sections in several ways. We introduced anomalies X' as the difference of X and X_{tr}, i.e., an anomaly independent of the forced trend, which enables the decomposition in the first place (see Eq. 4.9). Moreover, as the trend estimates are physically consistent, i.e., not independent, $\mathrm{VPD}(T_{tr}, q_{tr}, p) = VPD_{tr}$ (see Eq. 4.8). And finally, the effect of the nonlinear dependence of VPD on T, which leads to larger seasonal mean VPD when first computing VPD from temporally high-resolution data and then averaging over time than the converse, does not affect the VPD′ in Eq. 4.12. This is because we computed VPD from seasonal mean T and q, which allows a decomposition consistent with (seasonal mean) T and q (Sect.4.3.3). All in all, this decomposition as well as the trend estimates of Sect. 4.3.2 constitute a robust framework tailored to the aims of this chapter, namely (i) statistically identifying regions with extreme VPD and (ii) explaining VPD′ with q' and T' – both at the seasonal timescale.

In a second step, we account for the fact that the above decomposition does not yet take into account climatological co-variability of T and q. We know from Sect. 4.3.2 that many regions show a long-term increase of q_{tr} due to increasing T_{tr} (Fig. 4.5b). Also regarding inter-annual variability, we expect a given T' to induce a change in q (and so in VPD) that is indirectly related to warmer T, e.g., due to typically limited moisture supply in warm conditions ($q \searrow$ when $T \nearrow$) or due to the fact that warm air can hold more moisture ($q \nearrow$ when $T \nearrow$). To estimate the climatological co-variability of T and q, we compute the same regression as in Eq. 4.6 but now for absolute values T:

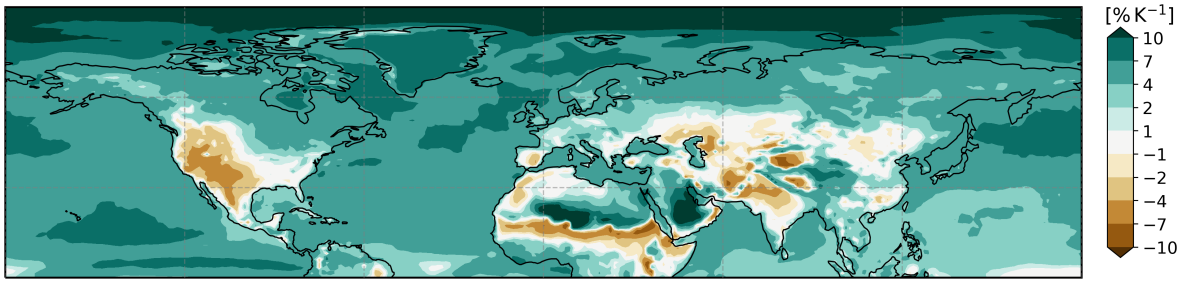

Figure 4.10: Climatological co-variability between T and q expressed as $\Delta q_T = \left(\exp(\gamma_2 \cdot 1\,\mathrm{K}) - 1\right) \mathrm{K}^{-1}$, which describes the expected relative increase in q_{ref} per Kelvin increase in T.

$$\ln(q) = \gamma_1 + \gamma_2 \cdot T + \epsilon \tag{4.13}$$

$$q_{ref} = \exp(\gamma_1 + \gamma_2 \cdot T) \tag{4.14}$$

$$q'_{ref} = q_{ref} - q_{tr} \tag{4.15}$$

$$q'_{par} = q - q_{ref} \tag{4.16}$$

The four equations denote the linear regression that quantifies the inter-annual co-variability of T and q (Eq. 4.13), the resulting estimate of the expected q for a given T (q_{ref}; Eq. 4.14), the anomaly of q_{ref} (q'_{ref}; Eq. 4.15), and the introduction of the particular anomaly q'_{par}, which is not explained by T' (Eq. 4.16). Note that the two anomalies add up to the full anomaly, i.e., $q' = q'_{ref} + q'_{par}$. Based on Equation 4.14, we can define the relative increase in q_{ref} per Kelvin of temperature change, i.e., the change in q expected from the climatological q-T-correlation. It is a function of γ_2 and hereafter referred to as Δq_T in [% K^{-1}]:

$$\Delta q_T = \frac{q_{ref}(T_0 + 1\,\mathrm{K}) - q_{ref}(T_0)}{q_{ref}(T_0) \cdot 1\,\mathrm{K}} \overset{(4.14)}{=} \left(\exp(\gamma_2 \cdot 1\,\mathrm{K}) - 1\right) \mathrm{K}^{-1} \tag{4.17}$$

The separation of q' into two components accounts for the climatological co-variability between T and q, by means of Δq_T, which can be considerable (Fig. 4.10). For ERA5 data, the pattern of inter-annual q-T-relationship (Fig. 4.10) is similar to that of the long-term trend (Fig. 4.5b) but of lower magnitude. Differences in sign between the two estimates occur in regions that exert a weak or negative forced warming and a pronounced inter-annual variability in T, e.g., in parts of western Canada and of Central Asia (Figs. 4.5 & 4.10). In these regions, q_{tr} is estimated relative to small changes in T_{tr} and hence shows a different sensitivity than q to T on the inter-annual timescale. Given q'_{ref} and q'_{par}, we can combine Eq. 4.12 with Eqs. 4.15 & 4.16 to separate VPD$'_{q'}$ in contributions of q'_{ref} and q'_{par}:

$$\mathrm{VPD}' = \mathrm{VPD}'_{T'} + \mathrm{VPD}'_{q',par} + \mathrm{VPD}'_{q',ref} + \epsilon \tag{4.18}$$

where, e.g., $\mathrm{VPD}'_{q',par} = q'_{par} \cdot \frac{\partial \mathrm{VPD}}{\partial q}\big|_{T_{tr},q_{tr},p}$. For every grid point, this equation quantifies the contributions of T' (VPD$'_{T'}$) and q' (VPD$'_{q',par}$ + VPD$'_{q',ref}$) to any VPD$'$. The separation of VPD$'_{q',par}$ and VPD$'_{q',ref}$ further enables us to compute a particular contribution VPD$'_{q',par}$ that is linked to anomalous climate dynamics and that is not related to changes in q expected from

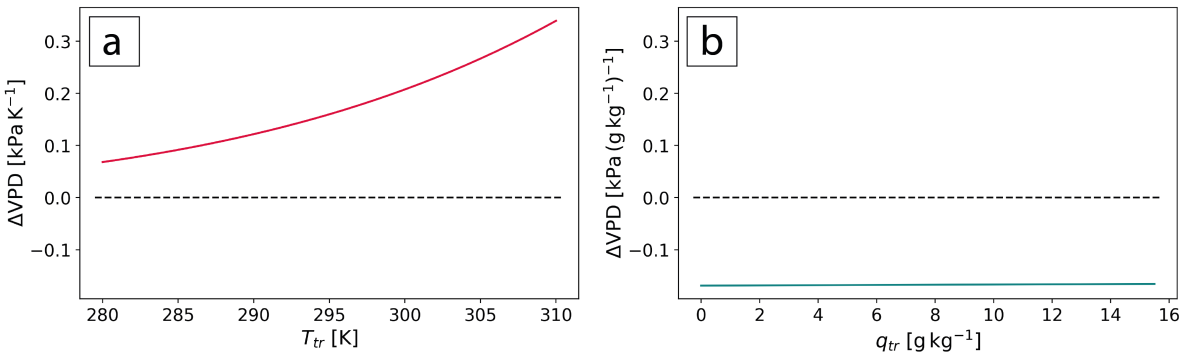

Figure 4.11: The change in VPD(T, q, p) for (a) $T' = 1$ K, and (b) $q' = 1\,\mathrm{g\,kg^{-1}}$ as a function of T_{tr} and q_{tr}, respectively. Note that the curve in (b) is shown for $p = 1'000$ hPa.

the climatological co-variability between T and q.

Lastly, we note that the point $(T, q, p) = (T_{tr}, q_{tr}, p)$, i.e., the current and local climate characterized by (T_{tr}, q_{tr}, p), over which the linearization in Eq. 4.10 is performed, is crucial for the potential of meteorological anomalies to cause a certain magnitude of VPD′, in particular due to the nonlinear dependence of VPD on T. Figure 4.11 shows the change in VPD (ΔVPD) that goes along with a $T' = 1$ K and a $q' = 1\,\mathrm{g\,kg^{-1}}$ at different levels of T_{tr} and q_{tr}, respectively. Clearly, ΔVPD(T_{tr}), i.e., VPD′$_{T'}$ related to a 1 K warm anomaly, increases drastically at higher T_{tr}, i.e., in a warmer climate (Fig. 4.11a). For example, $T' = +1$ K at $T_{tr} = 290$ K and at $T_{tr} = 300$ K causes VPD′$_{T'} = 0.12$ kPa and VPD′$_{T'} = 0.21$ kPa, respectively, i.e., contributes almost twice as much to VPD′ when going to a 10 K warmer climate. Note that this increase is independent of q and p. The ΔVPD(q_{tr}) becomes slightly less negative at higher q_{tr} (Fig. 4.11b). Note that this term additionally depends on p (not shown). As we assume no trend in p, VPD(q_{tr}, p) is mainly changing due to spatiotemporal variations in p related to surface elevation and atmospheric circulation. Overall, however, a reasonable trend in q of around $1 - 2\,\mathrm{g\,kg^{-1}}$ over the ERA5 period of 42 years does hardly change the VPD′$_{q'}$ related to a given q'. In stark contrast, the forced trend in T, which is locally on the order of a few Kelvin (Fig. 4.5a), potentially substantially altered VPD′$_{T'}$ per K temperature anomaly over the course of the study period 1979–2020. These considerations again illustrate the strong nonlinear dependence of VPD on T, whose consequences on the timescale used to compute VPD were already illustrated in Sect. 4.3.3.

4.4 Identification of extreme VPD seasons

Given detrended VPD′, we use an identification scheme to find spatially coherent objects of extremely positive VPD′ in ERA5 data as well as in the much more extensive CESM1 data. In this subsection, we summarize the most important aspects of the identification scheme and discuss particular challenges arising from applying this scheme to VPD′ data. Please see Röthlisberger et al. (2021) for further details about the identification scheme. The scheme consists of three steps:

1. Estimate at each grid point the distribution of VPD′ by statistical modelling, then calculate the local return period (LRP) of each VPD′ value.

2. Identify locally extreme VPD′ based on exceedances of an LRP threshold τ.

3. Form spatially coherent objects within which LRP $> \tau$, and quantify their characteristics.

As in Röthlisberger et al. (2021), we choose $\tau = 40$ y, but theoretically every threshold for LRP could be used as long as it can be reasonably estimated from the two datasets. We, therefore, identify extreme VPD seasons that affect a given region about every 40 y. For this, the use of detrended VPD′ is crucial, as the statistical fitting of a distribution to estimate LRPs is based on the assumption of a stationary time series, i.e., that VPD′ at one grid point come from a climate without forced trend.

4.4.1 Statistical modelling of VPD′

Estimation of the LRP is performed by statistically modelling the distribution of VPD′. The absolute VPD values follow a bounded distribution, with a lower bound of zero, and thus also the distributions of VPD′ are typically positively skewed. To account for this skew we combine the normal distribution with a parameterized data transformation to allow for modelling skewed distributions. Specifically, we assume that VPD′ follow a Yeo–Johnson transformed normal distribution N^{YJ} with the three parameters μ (mean), σ^2 (variance), and λ (transform parameter) according to Yeo and Johnson (2000). The three parameters are considered to vary between grid points and datasets (ERA5 and each of the 25 CESM1 subsets), and are estimated with a maximum likelihood estimation in a two step approach. First, VPD′ are transformed, which

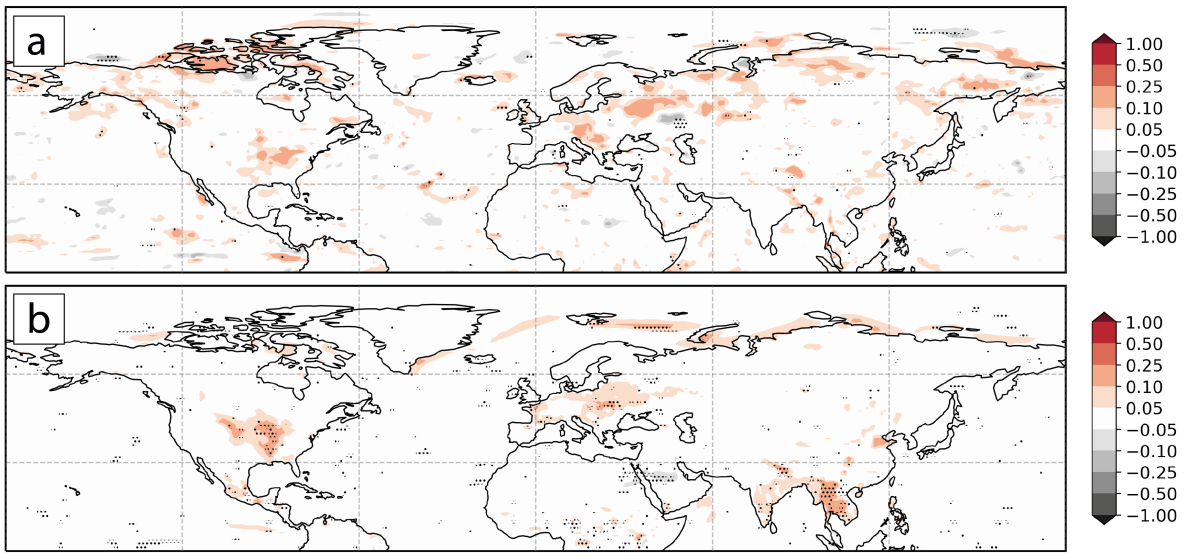

Figure 4.12: (a) Sample skewness of the transformed VPD′ in ERA5, and (b) the mean skewness of transformed VPD′ over all CESM1 subsets. Stippling in (a) indicates grid points where the ERA5 distribution of transformed VPD′ deviates from the normal distribution according to a Shapiro-Wilks test ($\alpha = 5\%$). Stippling in (b) indicates where this is the case for more than one CESM1 subset.

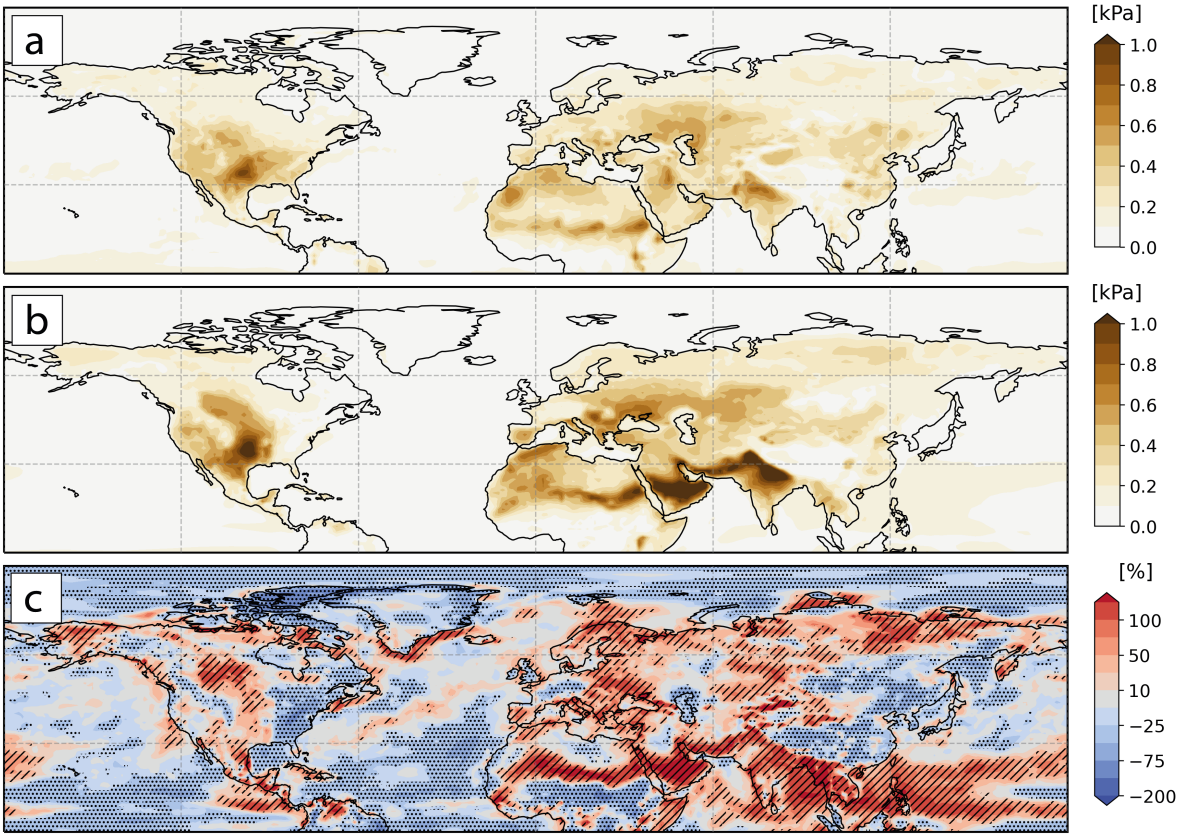

Figure 4.13: (a) The 40-year return level of VPD′ in ERA5, and (b) the mean 40-year return level over all CESM1 subsets. (c) The difference of (b) minus (a) relative to (a). Stippling (hatching) denote grid points where the ERA5 value lies above (below) all 25 CESM1 subset values.

results in an estimate for λ, and second, we estimate μ and σ^2 by fitting a normal distribution to the transformed anomalies. Details regarding the technical implementation of the parameter estimation can be found in Röthlisberger et al. (2021).

Figure 4.12 shows that all across the Northern Hemisphere the distribution of the transformed VPD′ values is not in contradiction with a normal distribution, which implies that the same statement holds for the (untransformed) VPD′ values and the N^{YJ}. Note, however, that the power of the goodness-of-fit test, with 42 observations per dataset and grid point, is relatively low. The skew of ERA5 data remaining after the transformation is mostly small in magnitude except for some regions in Siberia, eastern Europe, and the Central U. S. (Fig. 4.12a). If skewed, the transformed VPD′ show widely positive skew, as expected from the lower bound of VPD. In addition to the previously mentioned regions, the distribution of transformed VPD′ in CESM1 is positively skewed in parts of India and China (Fig. 4.12b). All in all, from the 42-year sets of VPD′ data, it seems appropriate to follow the approach of Röthlisberger et al. (2021) by using a N^{YJ} to globally model the distribution of VPD′, because we cannot reject the null hypothesis that YJ-transformed VPD′ values are normally distributed over almost the entire Northern Hemisphere.

4.4.2 Exceedance of 40-year return level

From the resulting distribution, we estimate the LRP of every seasonal mean VPD′ value, focusing on extremely positive VPD′. The LRP of a given VPD′ is defined as:

$$\mathrm{LRP}(\mathrm{VPD}') = \frac{1}{1 - G(\mathrm{VPD}'; \mu, \sigma^2, \lambda)} \tag{4.19}$$

where $G(\mathrm{VPD}'; \mu, \sigma^2, \lambda)$ is the cumulative distribution function of the N^{YJ} (Röthlisberger et al., 2021). Figure 4.13 compares the 40-year return levels of VPD′ between ERA5 and CESM1 data. In general, the 40-year return level in ERA5 is large in regions of pronounced inter-annual variability in VPD, e.g., the Great Plains in the U.S., the Sahel, and Central Asia (cf. Figs. 4.2b & 4.13a). These spatial patterns are largely reflected in the mean return level of the 25 CESM1 subsets (spatial Pearson correlation of $r = 0.84$, Fig. 4.13b). In many subtropical, continental, and high-latitude regions, CESM1 overestimates the 40-year return level wrt. ERA5 (Fig. 4.13c). In contrast, the eastern U.S., Central Europe, East Asia, the Arctic, and many ocean regions have a consistently lower VPD′ return level in CESM1 compared to ERA5. These discrepancies between the two datasets can be explained by biases in local absolute T and q and their inter-annual variability, as illustrated in Appendix B (Figs. B.1 – B.4). For example, the largely overestimated CESM1 return level in the African and Indian monsoon regions relate to an almost two times larger variance of T and q (Figs. B.2c & B.4c). In regions of low T, e.g., in the Arctic, the underestimation of T also implies an underestimation of $\frac{\partial \mathrm{VPD}}{\partial T}$ and $\mathrm{VPD}'_{T'}$ (Sect. 4.3.4), which – despite overestimated variance of T and q – leads to a lower 40-year return level (Fig. B.1c). Note that biases in absolute q (Fig. B.3) hardly affect the calculation of the 40-year return level, as the change in $\frac{\partial \mathrm{VPD}}{\partial q}$, i.e., the change in the potential of a given q' to cause VPD′, for different levels of q is extremely low (Eq. 4.3, Fig. 4.11). These results highlight that the spatial pattern of the 40-year return level is simulated well in CESM1. Regarding the magnitude of the 40-year return level, CESM1 model biases in T and variability of q and T are the causes of discrepancies between ERA5 and CESM1.

4.4.3 Forming and characterizing extreme VPD season objects

Lastly, grid points where $\mathrm{LRP} > \tau$ are connected in space to form spatially coherent objects. Each grid point is connected to those of all eight neighboring grid points that also exhibit a VPD′ with $\mathrm{LRP} > \tau$. The resulting objects are hereafter called "extreme VPD seasons" or in short $\mathrm{VPD}_{\mathrm{JJA+}}$. For each extreme VPD season, we calculate characteristics such as its size and its mean VPD′. A specific focus is on quantifying the object-mean contributions to VPD′ from T', q'_{ref}, and q'_{par}, respectively (Sect. 4.3.4). For all further analyses, we exclude all $\mathrm{VPD}_{\mathrm{JJA+}}$ that affect less than 10^5 km^2 of land area. Additionally, we select those with a center of mass – considering the affected land area only – in the mid-latitudes of the Northern Hemisphere (30–60°N). All discussed characteristics only consider land grid points of $\mathrm{VPD}_{\mathrm{JJA+}}$, which is motivated by their impact on terrestrial ecosystems. Note that, despite the focus on land grid points, the forming of $\mathrm{VPD}_{\mathrm{JJA+}}$ includes ocean/lake grid points to connect land regions that are affected by the same extreme season but are separated by a water body.

4.5 Results

4.5.1 Extreme VPD seasons in ERA5 and CESM1

In the Northern Hemisphere mid-latitudes (30–60°N) we identify 96 VPD_{JJA+} in 1979–2020 that are larger than 10^5 km^2, of which many are know as high-impact events. Figure 4.14 shows the ten largest according to their land area (A). The by far largest VPD_{JJA+} occurred in Russia in 2010 (RU2010) and strongly impaired net ecosystem productivity (Barriopedro et al., 2011; Bastos et al., 2020b). It was not only the largest VPD_{JJA+}, but also ranks third in terms of the land mean VPD′ (I), which we use as measure of intensity (Tables 4.1 & 4.2). The second-largest VPD_{JJA+} was in the Central U. S. in 1988 (US1988) and strongly reduced the vegetation's carbon sink capacity across the U. S. (Trenberth et al., 1988; Mekonnen et al., 2017). The extreme fire season linked to large VPD in the southwestern U. S. in 2011 coincides with the most intense VPD_{JJA+} (US2011), with $I = 0.78$ kPa (Table 4.2; Williams et al., 2014). Finally, also the summer of reduced ecosystem evapotranspiration and carbon uptake in Europe in 2003 (Ciais et al., 2005) is related to the largest VPD_{JJA+} in this region (Table 4.1). This identification scheme, however, also identifies less well-known events of exceptional size, e.g., the VPD_{JJA+} that occurred in Central Asia in 1984 (CA1984, Fig. 4.14, Table 4.1). Interestingly, several of the mentioned extreme VPD seasons, e.g., RU2010, US1988, and CA1984, have also ranked within the ten largest extremely hot summers (Röthlisberger et al., 2021). Also with respect to precipitation, e.g., RU2010 and CA1984 are know as the largest and fifth largest extremely dry summers, respectively, in 1979–2020 (Boettcher et al., 2023). These results underline the linkage between extreme VPD seasons and other seasonal meteorological extremes.

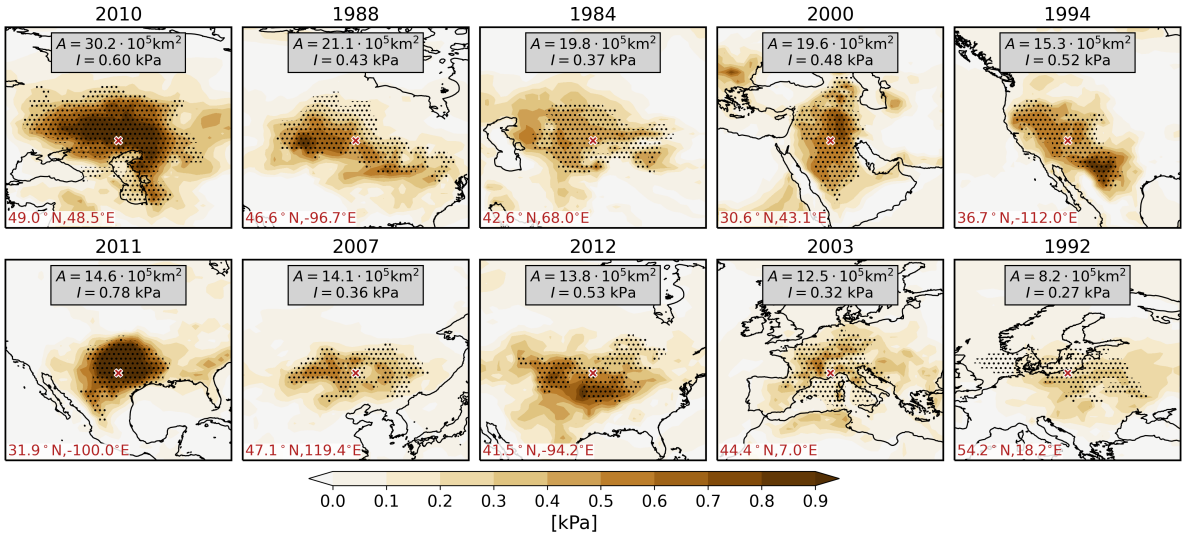

Figure 4.14: VPD′ of the ten largest VPD_{JJA+} in the northern mid-latitudes in 1979–2020 identified from ERA5. Stippling shows the entire region affected by VPD_{JJA+} (other VPD_{JJA+} are omitted). The geographical center (red crosses) of the VPD_{JJA+} are indicated in the bottom left. Text boxes indicate values of A and I, which refer to land grid cells only. Note that the panels cover variable lat/lon ranges.

Table 4.1: The ten largest (land area, A) VPD_{JJA+} in 1979–2020 shown in Fig. 4.14. The columns denote the intensity (I) and rarity (R) of VPD_{JJA+}. The R equals the land area mean LRP.

Year	Region	A [10^5 km^2]	I [kPa]	R [y]
2010	Western Russia	30.2	0.60	99
1988	Central U. S.	21.1	0.43	84
1984	Central Asia	19.8	0.37	98
2000	Arabian Peninsula	19.6	0.48	77
1994	Western U. S./Mexico	15.3	0.52	91
2011	Southern U. S./Mexico	14.6	0.78	104
2007	China/Mongolia	14.1	0.36	75
2012	Central U. S.	13.8	0.53	68
2003	Central Europe	12.5	0.32	99
1992	Eastern Europe	8.2	0.27	62

Table 4.2: The same as in Table 4.1 but ranked according to I.

Year	Region	A [10^5 km^2]	I [kPa]	R [y]
2011	Southern U. S./Mexico	14.6	0.78	104
1980	Southern U. S.	3.4	0.73	49
2010	Western Russia	30.2	0.60	99
2012	Pakistan	1.5	0.59	89
2012	Central U. S.	13.8	0.53	68
1994	Western U. S./Mexico	15.3	0.52	91
2000	Southeastern Europe	1.1	0.51	61
2006	Central Asia	1.1	0.51	54
1994	Morocco/Algeria	2.8	0.49	66
2000	Arabian Peninsula	19.6	0.48	77

In their respective local context, extreme VPD seasons with large I were not necessarily more extreme, i.e., rare, compared to less intense VPD_{JJA+}. First of all, note that the estimates of the mean LRP over land (R) are based on 42 observed VPD' per grid point only and thus inherently uncertain – particularly so for large R. They merely serve the purpose of putting I into the local climatic context and should not be interpreted as a fully accurate estimate of the VPD_{JJA+}'s recurrence. The most intense VPD_{JJA+} US2011 ($R = 104$ y) ranks behind the VPD_{JJA+} in China and Kazakhstan in 2008 (CK2008), which had lower $I = 0.33$ kPa but $R > 150$ y (Table B.1). Not surprisingly, intense VPD_{JJA+} preferentially occurred in hot-dry regions of large VPD variability, where also the 40-year return level is high, such as the southwestern U. S. and southeastern Europe. Moreover, if the much less intense events CK2008 or CA1984 ($I = 0.37$ kPa,) had occurred in the southwestern U. S., where the 40-year return level widely exceeds 0.5 kPa (Fig. 4.13a),

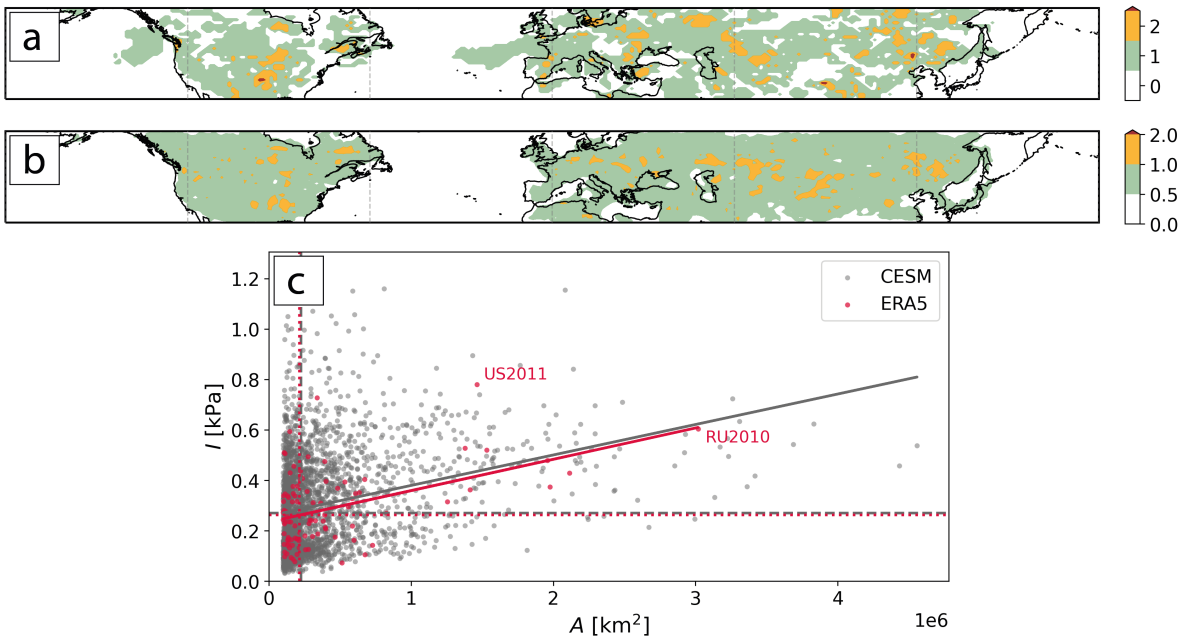

Figure 4.15: Number of VPD_{JJA+} per grid point (a) in 1979–2020 in ERA5, and (b) on average in each CESM1 subset (42 years). Note the slightly different color scales. (c) Scatter plot of I and A for VPD_{JJA+} in 30–60°N in ERA5 (red) and CESM1 (grey). Linear regression lines are shown in solid, the median I and A are marked by dashed lines. The VPD_{JJA+} US2011 and RU2010 are highlighted.

they would not have been identified as a local 40-year extreme. These considerations highlight the importance of assessing the "extremeness" – often referring to the rarity – of each VPD' in its local climatic context. Whether an intense VPD_{JJA+} (with very strong atmospheric water demand) or a rare VPD_{JJA+} (which vegetation is not adapted to) causes a greater impact on ecosystems is a point of discussion and could be addressed in future work.

The occurrence of VPD_{JJA+} as well as the two central characteristics A and I are all well-represented by the 2'507 VPD_{JJA+} identified in CESM1 data. Most land regions on average experience slightly less than one VPD_{JJA+} per 42 years (Fig. 4.15b), as expected from the LRP threshold $\tau = 40\,y$ used to identify the extreme seasons (Sect. 4.4). Thus, the CESM1 data provides much more VPD_{JJA+} for systematic studies, whereas in many regions only one VPD_{JJA+} has been observed in the ERA5 period (Fig. 4.15a). The median (and mean) $A = 2.26{\cdot}10^5$ km^2 ($3.92{\cdot}10^5$ km^2) and $I = 0.27$ kPa (0.31 kPa) in CESM1 correspond well to the respective values in ERA5: $A = 2.14{\cdot}10^5$ km^2 ($4.08{\cdot}10^5$ km^2) and $I = 0.26$ kPa (0.29 kPa) (Fig. 4.15c). As for the largest and most intense VPD_{JJA+} in ERA5, there is also a pronounced correlation between A and I for large and intense VPD_{JJA+} in CESM1. The intensity of VPD_{JJA+} larger than $\sim 5{\cdot}10^5$ km^2 increases for larger A (Fig. 4.15c). Thus, in addition to the typical A and I of VPD_{JJA+}, also this positive relationship between the two characteristics is well-simulated in CESM1. Moreover, the phase space of A and I illustrates that for every observed VPD_{JJA+}, even the most intense and largest ones, several CESM1 analogs exist that are of similar (or even larger) size and intensity (Fig. 4.15c). The potential of systematically studying CESM1 analogs to a given extreme season

is illustrated in Röthlisberger et al. (2021).

All in all, the presented set of extreme VPD seasons in ERA5 includes several well-known high-impact events as well as unstudied VPD_{JJA+} in most regions of the mid-latitudes. All of them could be studied in greater detail with numerous analogs occurring in the same region in CESM1, which suggests that CESM1 is able to simulate the statistical characteristics of VPD_{JJA+} extremely well. In the next section, we specifically focus on the contributions of T' and q' to the intensity of extreme VPD seasons.

4.5.2 Decomposition of the intensity of extreme VPD seasons

The mean I of VPD_{JJA+} in ERA5 (0.29 kPa) is composed of contributions from T' as well as q'_{par} and q'_{ref}. Figure 4.16 shows the contributions of T', q'_{par}, q'_{ref}, and the residual, denoted as $I_{T'}$, $I_{q',par}$, $I_{q',ref}$, and I_{res}, which result from the spatial average of Eq. 4.18 over the land area of each VPD_{JJA+} (Sect. 4.3.4). Considering all VPD_{JJA+}, the largest part (77%) of I was due to T' (Fig. 4.16). All VPD_{JJA+} in 1979–2020 were warmer than usual within their respective local climate, and T' contributed at least 29% to I (not shown). Given that most mid-latitude land regions show a positive q-T-correlation (Fig. 4.10), this positive $I_{T'}$ on average went along with a negative $I_{q',ref}$. That is, we expect an increase in q in many regions during warm summers, which acted to dampen I by on average -13% (Fig. 4.16). The total of the two temperature-related contributions $I_{T'}$ and $I_{q',ref}$ accounted for about two thirds of I. Approximately one third was, therefore, due to q'_{par}, i.e., an unusually low q relative to what is expected in a warm summer of given T' (Fig. 4.16). So despite the dominant dependence of VPD on T, about 19% of I in VPD_{JJA+} were due to anomalous q, in a hemispherically aggregated sense, whose contribution was even more important when the effect of T' on q is subtracted. Finally, the

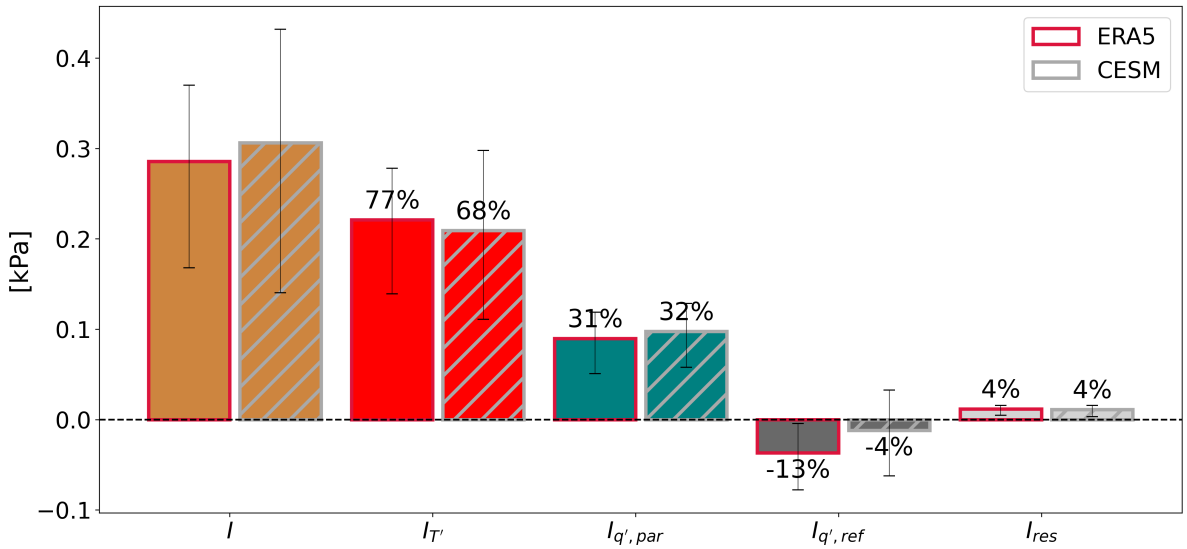

Figure 4.16: The mean I of all VPD_{JJA+} in 30–60°N including the contributions $I_{T'}$, $I_{q',par}$, $I_{q',ref}$, and I_{res} (Sect. 4.3.4) for ERA5 (red) and CESM1 (grey). The whiskers indicate the inter-quartile range and numbers above the bars denote the respective mean contribution relative to I.

residual term resulting from higher-order contributions to I is relatively small with only 4%.

The mean I as well as the contributions of the different meteorological anomalies are similar over all $\text{VPD}_{\text{JJA+}}$ in CESM1 (Fig. 4.16). The most notable difference to ERA5 arises from a smaller relative $I_{T'} = 68\%$ and, consequently, also a less negative $I_{q',ref}$. This is potentially related to the fact that the temperature dependence of VPD, and thus the potential of a given T' to cause large $I_{T'}$, is itself a function of T (Fig. 4.11a). Due to different time periods and model biases, absolute T is in numerous mid-latitude regions lower in CESM1 than in ERA5 data (Fig. B.1). At lower T, $\frac{\partial \text{VPD}}{\partial T}$ is smaller and, consequently, the same T' in CESM1 produces a smaller VPD′ than it would in ERA5. Not only mean values but also variability in T and q are potential sources of disagreement (see Sect. 4.4.2). And lastly, the more positive $I_{q',ref}$ in CESM1 compared to ERA5 also implies an overall weaker co-variability of T and q. The many potential sources of disagreement between CESM1 and ERA5 likely cause local discrepancies between the discussed $\text{VPD}_{\text{JJA+}}$ characteristics. However, the agreement between CESM1 and ERA5 I as well as its meteorological decomposition of $\text{VPD}_{\text{JJA+}}$ on a hemispheric scale are extremely high.

An interesting aspect is that about 3% of CESM1 $\text{VPD}_{\text{JJA+}}$ objects arise despite a cold anomaly and thus negative $I_{T'}$. In these colder than usual summers, the VPD′ large enough to constitute a 40-year event entirely comes from negative q'. Interestingly, these $\text{VPD}_{\text{JJA+}}$ are concentrated in two distinct regions, namely along the east coasts of North America and Northeast Asia (Fig. B.5). There, the q-T-correlation is positive (Fig. 4.10), with 4–7% reduction in q per Kelvin of cooling, and thus (locally) extremely large VPD′ can occur during colder than usual conditions. This is only possible if T' is not so low that the negative $I_{T'}$ overcompensates the total $I_{q',ref} + I_{q',par}$. Consequently, $\text{VPD}_{\text{JJA+}}$ with these characteristics are further constrained to the regions with a rather low 40-year return level, i.e., low variability in VPD (Fig. 4.13b).

We next assess the temperature-dependence of I and its contributions in the light of global warming, which overall increases the ability of inter-annual variability to produce large VPD (Fig. 4.11, Sect. 4.3.4). Figure 4.17 illustrates the contributions to I of ERA5 $\text{VPD}_{\text{JJA+}}$ wrt. GMST, which increased from 288.8 K to 289.6 K in 1979–2020. A linear regression of all contributions with GMST as predictor shows, first of all, that I increased by about 0.06 kPa (+23%) between the coldest (1984) and the warmest (2019) year (Fig. 4.17a). This intensification comes from an increase in $I_{T'}$ and of $I_{q',ref}$. As mentioned above, the increase in $I_{T'}$ is at least partly owed to a larger VPD′ resulting from the same T' in a warmer climate. Changes in the two q'-contributions are more difficult to attribute to a phenomenon, as they additionally depend on the local relationship between q and T, which varies across the globe. Still, we note a strong reduction of $I_{q',par}$ in absolute, but especially in relative terms (Fig. 4.17a,b). The relative importance of q'_{par} for I decreased with the observed global warming from 41% to 23%. All in all, the importance of q'_{par}, i.e., q' related to anomalous climate dynamics, for the intensity of $\text{VPD}_{\text{JJA+}}$ was reduced with the observed global warming in 1979–2020. Instead, $I_{T'}$ and $I_{q',ref}$, i.e., processes mostly related to T', contributed more positively to I at higher GMST. The robustness, however, over a

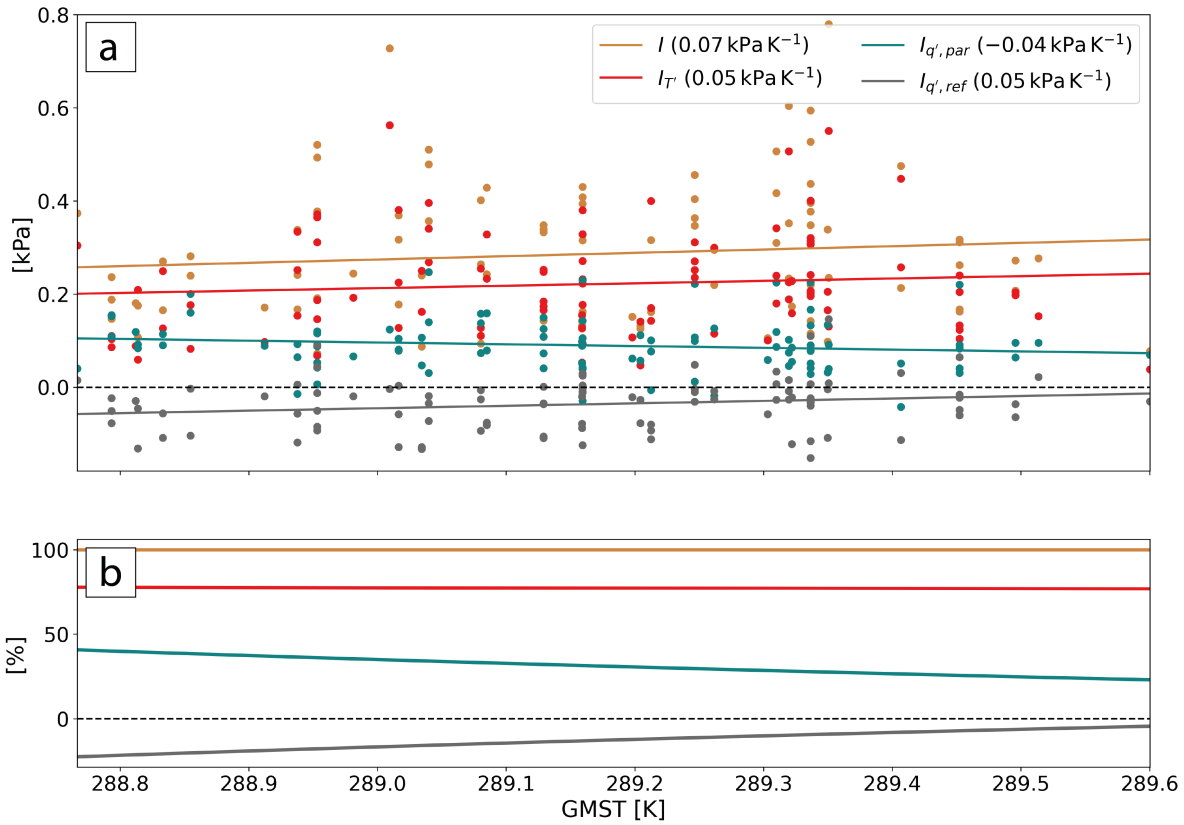

Figure 4.17: (a) Scatter plot of I (brown), $I_{T'}$ (red), $I_{q',par}$ (teal), and $I_{q',ref}$ (grey) of all ERA5 $\text{VPD}_{\text{JJA+}}$ in 30–60°N with respect to GMST. Linear regression lines are shown in solid lines of the respective color. (b) All regression lines relative to that of I in %.

relatively narrow range of GMST and slightly less than 100 $\text{VPD}_{\text{JJA+}}$ is relatively low. Consequently, all four assessed trends are insignificant at a significance level of $\alpha = 5\%$. Nevertheless, these results are indicative of what is to be expected with ongoing global warming, which could be investigated when applying the presented framework to future climate simulations.

Lastly, given the good performance of modelling the contributions to $\text{VPD}_{\text{JJA+}}$ intensity across the mid-latitudes, we use the much more extensive set of CESM1 $\text{VPD}_{\text{JJA+}}$ to assess the spatial patterns of I and the three contributions. In CESM1, the most intense $\text{VPD}_{\text{JJA+}}$ with $I > 0.8$ kPa occur in the Great Plains in the Central U. S., and the Indus River Basin in Pakistan (Fig. 4.18a). These large I on average consist of more than 50% $I_{T'}$, while the larger part of the remainder comes from $I_{q',ref}$ and only up to 10% from $I_{q',par}$ (Fig. 4.18b-d). Very low I is found for $\text{VPD}_{\text{JJA+}}$ that affect the eastern continents, higher latitudes, and northwestern Europe. A typical characteristic of $\text{VPD}_{\text{JJA+}}$ in these and adjacent regions are negative $I_{q',ref}$, i.e., a moistening during the warmer than usual $\text{VPD}_{\text{JJA+}}$ (Fig. 4.18c). Consequently, the share of $I_{q',par}$ is widely above 25% (Fig. 4.18d). The previously-mentioned $\text{VPD}_{\text{JJA+}}$ with negative $I_{T'}$, occurring at the east coasts of North America and Asia, belong to those with $I < 0.2$ kPa (Fig. 4.18a). On average over all $\text{VPD}_{\text{JJA+}}$ there, $I_{T'}$ is still positive (Fig. 4.18b). Still, more than 75% of I are on average attributed to $I_{q',par}$ (Fig. 4.18d). In contrast, other $\text{VPD}_{\text{JJA+}}$ with typical $I < 0.2$ kPa are first and

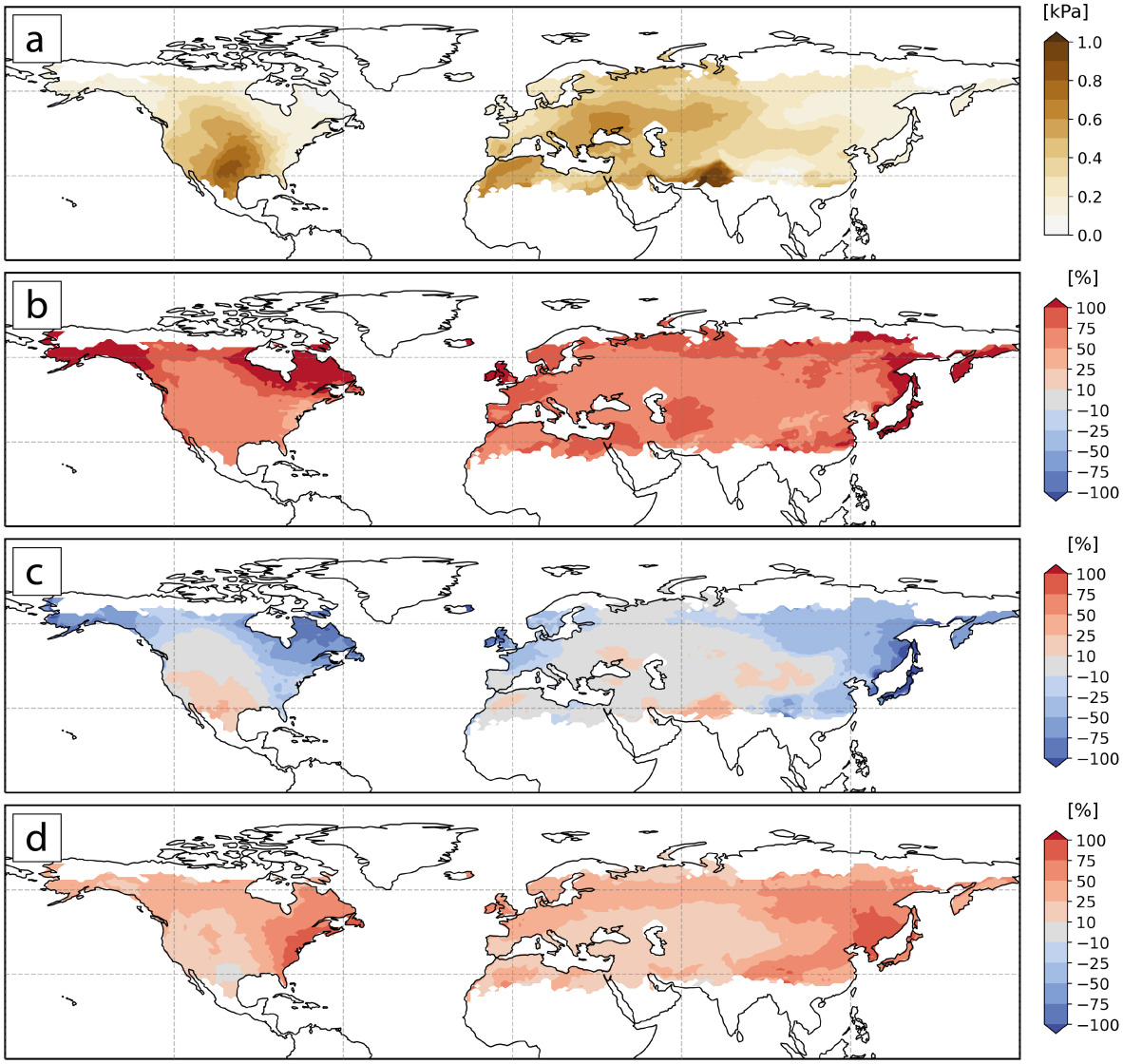

Figure 4.18: Maps of (a) the intensity I, and its relative contributions (b) $I_{T'}$, (c) $I_{q',ref}$, and (d) $I_{q',par}$ averaged over all CESM1 $\text{VPD}_{\text{JJA+}}$ in 30–60°N. At each grid cell we average over the respective object-land-mean values of all $\text{VPD}_{\text{JJA+}}$ that cover the respective grid cell.

foremost composed of $I_{T'}$ with a relative contribution of $> 100\%$, and occur, e.g., in Alaska, Newfoundland, the British Isles, and Japan (Fig. 4.18a,b). In the remaining regions, mostly over mid-latitude continents, the typical $I_{T'}$ and $I_{q',par}$ are around 70% and 20%, respectively, while $I_{q',ref}$ does not contribute substantially to the intensity of $\text{VPD}_{\text{JJA+}}$ (Fig. 4.18b-d). We conclude that the key factors contributing to I are very diverse across the mid-latitudes. There are some characteristic patterns, of which the majority – but not all – show the largest fraction of I related to T'. Moreover, the decomposition of I into the different contribution seems to be affected by the absolute level of I itself. While lower I can sometimes be attributed largely to q'_{par}, $\text{VPD}_{\text{JJA+}}$ with high values of I seem to rely on a sufficiently large $I_{T'}$.

4.5.3 Case studies: substructure and drought impact

To illustrate the meteorological conditions leading to extreme VPD_{JJA+} in different regions, we qualitatively investigate daily meteorological time series over JJA for a diverse set of exemplary VPD_{JJA+} in 1979–2020. This so-called temporal substructure of VPD_{JJA+} provides insight into the meteorological composition of an entire JJA season and reveals shorter-term phenomena, e.g., individual heat waves, droughts, or combinations thereof (see Sect. 1.3). We selected six VPD_{JJA+} that are diverse regarding their decomposition of I (Table 4.3). For each of the cases we use daily anomalies VPD'_d, T'_d, and q'_d – which are calculated as the deviation of the daily mean values from the seasonal trend value in that year (analogously to Eq. 4.9) – and daily accumulated precipitation P_d (convective plus large-scale). Moreover, we also discuss daily anomalies of the volumetric water content of the top 1 meter of soil (θ'_d) and weekly values of 1-, 3-, and 12-monthly Standardized Precipitation Evapotranspiration Index ($SPEI_w$-1, $SPEI_w$-3, and $SPEI_w$-12) to assess the interaction of VPD_{JJA+} with drought (see Sects. 4.2.2 & 4.2.3). Note that VPD'_d have a slight positive bias of approximately 0.05 kPa as VPD is slightly larger when calculated on shorter timescales (Sect. 4.3.3). Consequently, the average of VPD'_d over one season is slightly larger than its I, which is based on seasonally calculated VPD′. The qualitative assessment of the substructure presented in the following, however, is hardly impeded as typical VPD'_d are much larger than this offset.

The VPD_{JJA+} in Spain (SP1994) and in Morocco/Algeria (MA1994) in 1994 show a similar substructure, as they were less than two hundred kilometers apart (Fig. 4.19). They appear as separate extreme seasons, however, as the two VPD_{JJA+} objects were separated by one grid cell. SP1994 and MA1994 occurred in one of the most extreme hydrological years in northern Africa (Benassi, 2008), and the vast majority of Mediterranean woody flora in central and southern Spain was damaged, i.e., dry, completely decolorated or defoliated (Peñuelas et al., 2001; Lloret et al., 2004). The intensity of the two VPD_{JJA+} mostly comes from positive T', especially so for SP1994 with a relative $I_{T'}$ of 82% (Table 4.3). On the daily timescale, positive T'_d during virtually all of July and August caused positive VPD'_d of around 1 kPa (Fig. 4.19a,c). Nevertheless, q'_d played an important role, which becomes clear when contrasting the hot-moist period of ~+5 K in early August with the similarly warm dry period in early July: the latter

Table 4.3: VPD_{JJA+} examples in ERA5 including their intensity I and the four contributions relative to I.

Year	Region	I [kPa]	$I_{T'}$ [%]	$I_{q',par}$ [%]	$I_{q',ref}$ [%]	I_{res} [%]
1994	Morocco/Algeria	0.49	75	23	−3	4
1994	Spain	0.38	82	2	12	4
2000	Southeastern Europe	0.51	53	48	−4	3
2003	Central Europe	0.32	127	−2	−35	11
2011	Southern U. S./Mexico	0.78	71	5	19	6
2018	Northern Europe	0.21	95	31	−31	5

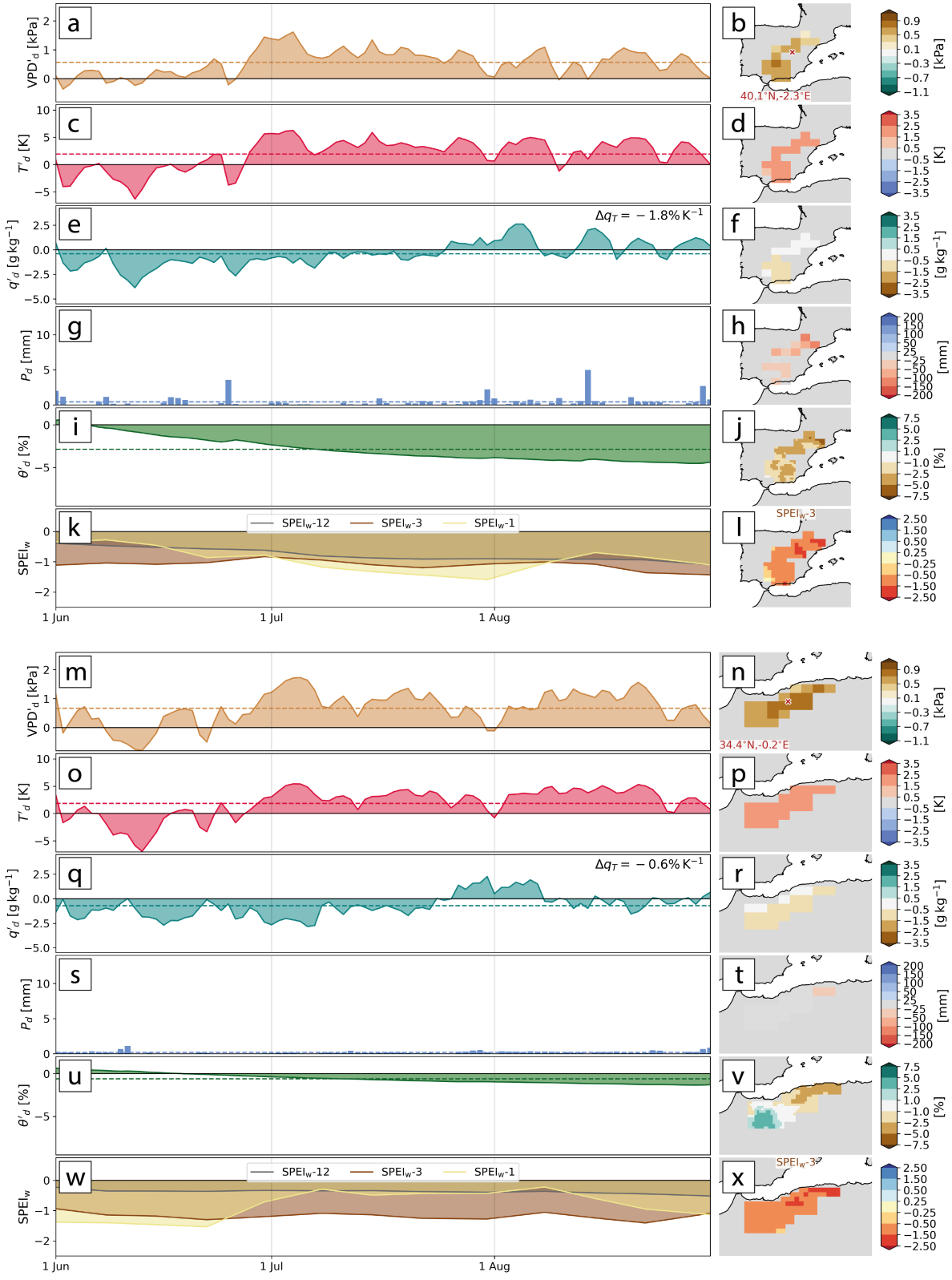

Figure 4.19: Time series of (a) VPD′$_d$, (c) T'_d, (e) q'_d, (g) P_d, (i) θ'_d, and (k) 1-, 3-, and 12-monthly SPEI$_w$ during SP1994. Maps (b,d,f,j,l) show the seasonal mean of the respective time series in (a,c,e,i,k), and (h) the mean anomaly of P from the 1979–2020 seasonal mean value. Dashed lines in (a,c,e,g,i) denote the time series' mean. The cross in (b) denotes the center of SP1994. (m-x) The same as (a-l) but for MA1994.

went along with a twice as large $\mathrm{VPD'_d} \approx 1.5\,\mathrm{kPa}$ (Fig. 4.19a,c,e). Moreover, the frequent cold periods in June went along with mostly positive $\mathrm{VPD'_d}$ due to q'_d as low as $-4\,\mathrm{g\,kg^{-1}}$. In that time, $\mathrm{SPEI_w}$-1 was the least negative in SP1994, and greatly decreased to below -1 during July (Fig. 4.19k). On the seasonal timescale, the region of SP1994 climatologically features decreased q during warm JJA, as indicated by the expected decrease in q_{ref} per Kelvin of T' ($\Delta q_T = -1.8\,\%\,\mathrm{K^{-1}}$), which is why the contribution of the mentioned periods of negative q'_d are mostly attributed to $I_{q',ref}$ (Table 4.3). The contribution of negative q' was mostly important in the southwest of SP1994, where VPD′ was larger than its northeast (Fig. 4.19b,d,f). In addition to the extremely large VPD, precipitation (P) was scarce and accumulated a seasonal deficit between 25 mm in the southwest and 150 mm in the northeast (Fig. 4.19h). The most negative seasonal anomalies in P also went along with a greatly reduced $\mathrm{SPEI_w}$-3 ≈ -2 and $\theta' < -5\%$ (Fig. 4.19j,l). A lack of P_d compared to climatology together with the intense periods of positive $\mathrm{VPD'_d}$ led to a declining θ'_d mostly throughout JJA, reaching its minimum at the end of August (Fig. 4.19i). The only larger differences of MA1994 compared to SP1994 arise from the fact that Morocco/Algeria are climatologically almost completely dry in most of JJA, i.e., the absence of P_d does not cause large anomalies in seasonal P (Fig. 4.19s,t). Consequently, θ'_d remains relatively small, as soils are climatologically dry during JJA, and $\mathrm{SPEI_w}$-1 partly increases over the course of JJA when the water balance is climatologically strongly negative (Fig. 4.19u,w). Nevertheless, there was a decrease of θ'_d over the course of JJA, mostly so in the northeast of MA1994, where in addition to extremely high VPD P' was reduced most strongly (Fig. 4.19t,u,v).

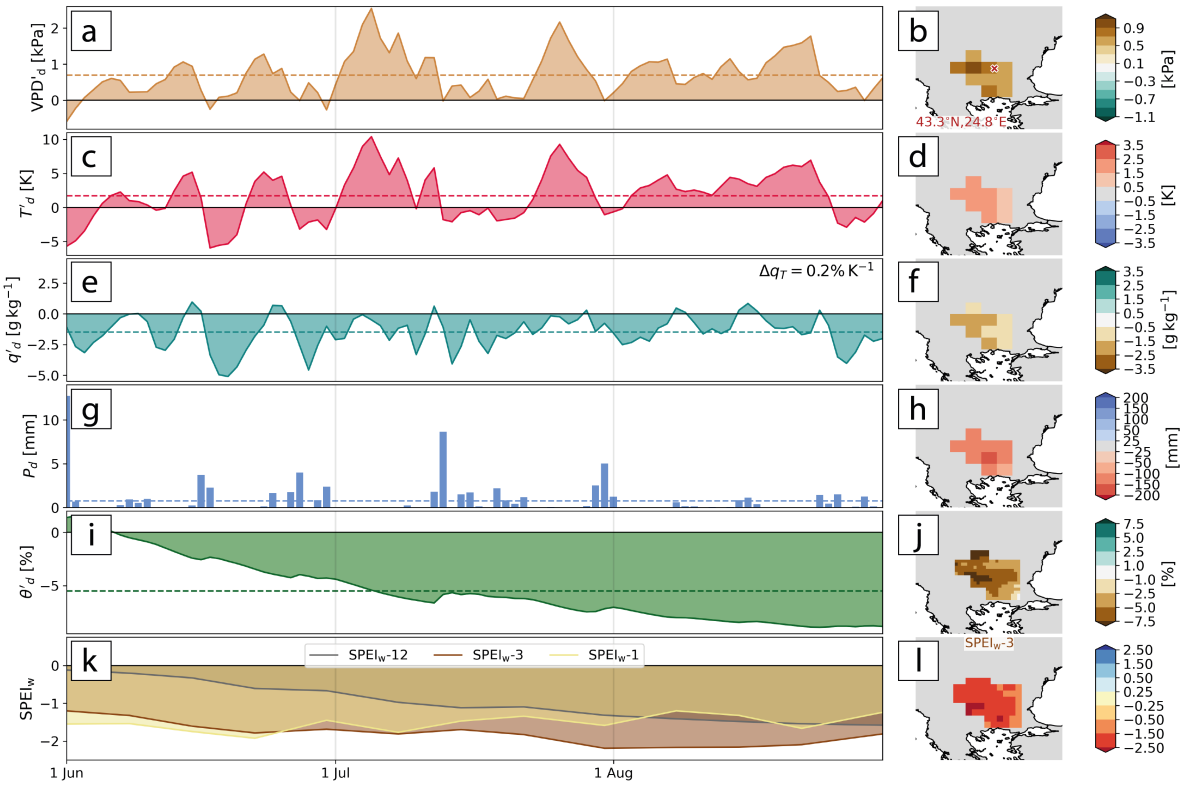

Figure 4.20: The same as Fig. 4.19a-l but for SE2000.

The extreme VPD season in southeastern Europe (SE2000) mainly affected northern Greece, Bulgaria, and Serbia. In some contrast to SP1994, the intensity of SE2000 was equally due to positive T' and negative q'_{par} (Table 4.3). Two very intense heat waves in July with T'_d of up to 10 K partly coincided with negative q'_d and thus caused VPD'$_d$ of more than 2 kPa (Fig. 4.20a,c,e). In these periods, the reduction in θ'_d was particularly strong (Fig. 4.20i). During the first one, the highest temperature in Bulgaria in 1979−2021 was recorded (Nojarov and Nikolova, 2022). In many Mediterranean countries such as Greece, temperatures above 48°C caused an extreme atmospheric water demand that led to extensive wildfires and anomalously low soil moisture (Fig. 4.20i,j; Demirtaş, 2017). The q'_d was negative during all but 12 days of the warmer than usual SE2000 with an average of $-1.5\,\mathrm{g\,kg^{-1}}$, especially during and after the two heat waves in July (Fig. 4.20c,e). Some very pronounced dry periods in June and August went along with negative $T'_d < -2$ K, which is why VPD'$_d$ then remained around zero and the almost continuously decreasing θ'_d stagnated (Fig. 4.20a,c,e,i). As the affected region shows hardly any climatological correlation between T and q, the anomalies in q contribute almost entirely to $I_{q',par}$ and not to $I_{q',ref}$ (Table 4.3). The few intermittent periods of positive q'_d were often accompanied by some rainfall that increased soil moisture anomalies, and which either resulted from increased q_d and/or which increased surface evapotranspiration in the moisture-limited period (causing larger q) (Fig. 4.20g,i). The SPEI$_w$-1 and SPEI$_w$-3 indicate that drought conditions were partly extreme (≤ -1.65) all throughout JJA of SE2000, with lowest seasonal mean values ($\theta' < -5\,\%$) in the center and northwest of SE2000. Over this summer season SPEI$_w$-12, i.e., drought conditions considering the previous 12 months, shifted from indicating almost normal conditions (SPEI$_w$-12 $= -0.11$) at 1 June to extreme drought at 31 August (SPEI$_w$-12 $= -1.79$). All in all, the intensity of SE2000 was shaped predominantly by the two heat waves and continuously less than climatological q. The reduced atmospheric moisture content also related to an accumulated P deficit of more than 100 mm (Fig. 4.20h). This both led to a great reduction in top-1-meter soil moisture and extreme drought conditions even on the 12-monthly timescale by the end of JJA.

The two most discussed summers regarding heat, drought, as well as impaired ecosystem functioning in Europe are related to the VPD$_{JJA+}$ in central and southwestern Europe in 2003 (CE2003) and to that in northern Europe in 2018 (NE2018; Bastos et al., 2020b). The most unusual conditions in NE2018 emerged earlier during the year – already in May – compared to CE2003, which had its most extreme hot period in August (Fig. 4.21; Buras et al., 2020). Therefore, VPD'$_d$ of up to 1.5 kPa in August contributed substantially to I of CE2003 (Fig. 4.21a), while VPD'$_d$ was often negative and P more abundant in August of NE2018 (Fig. 4.21m,s). Consequently, lowest θ'_d of around -8% occurred at the end of August and July in the case of CE2003 and NE2018, respectively (Fig. 4.21i,u). Contrary to the previous case studies, the central and northern European continent climatologically shows increased q during hot JJA, e.g., $\Delta q_T = +2.5\,\%\,\mathrm{K^{-1}}$ for CE2003 (Fig. 4.21c). Consequently, mostly positive q'_d during CE2003 caused I to be about 27% lower compared to the contribution from T' alone (Fig. 4.21e, Table 4.3). The moistening during CE2003 was at about the rate expected from the climatological q-T relationship, consequently $I_{q'par}$ was just around zero. Moisture availability seems to have

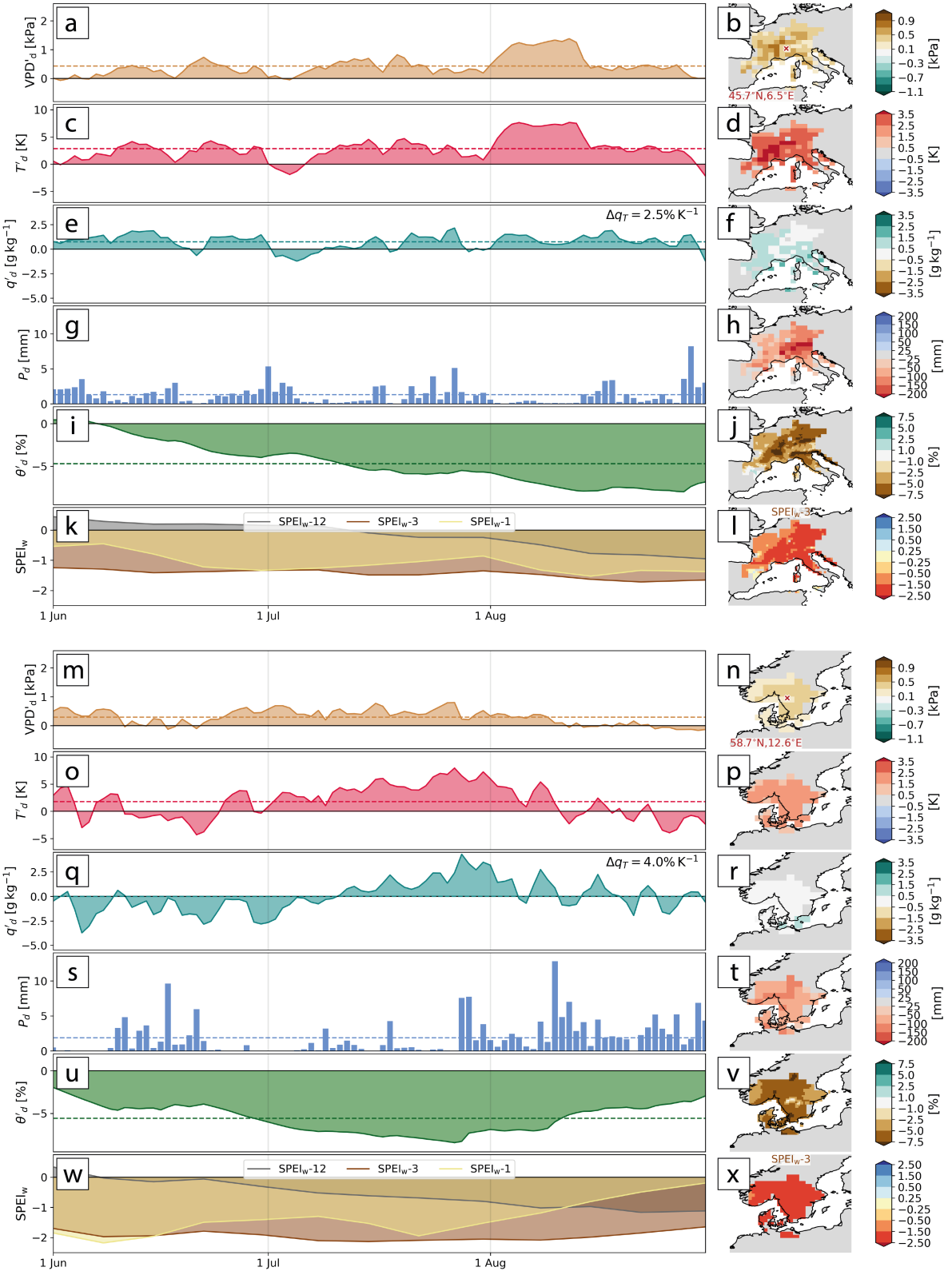

Figure 4.21: The same as Fig. 4.19 but for (a-l) CE2003 and (m-x) NE2018.

been an important factor for dampening I, as q' was most positive along the Mediterranean and Atlantic coasts (Fig. 4.21f). Hence, these were the only regions of CE2003 where $SPEI_w$-3 indicated mild instead of extreme drought conditions (Fig. 4.21l). Again, we cannot determine whether q'_d was positive due to P_d or vice-versa, due to the strong temporal correlation of the two variables (Fig. 4.21e,g). The deficit in accumulated P was greatest with < -100 mm in the continental regions affected by CE2003 and with < -200 mm in the Alps (Fig. 4.21h). The dampening of I due to larger q was not equally pronounced in NE2018 compared to CE2003 and weaker than expected climatologically. Mostly due to negative q'_d during the first half of JJA, q'_{par} contributed 30% to I of NE2018 (Table 4.3, Fig. 4.21q). Related to that, the longer-term impact on drought, i.e., on $SPEI_w$-3 and $SPEI_w$-12, was larger and regionally more consistent for NE2018 than for CE2003 (Fig. 4.21k,l,w,x). Nevertheless, regarding VPD in JJA, CE2003 was more exceptional in terms of intensity ($I = 0.32$ kPa) and rarity ($R = 99$ y) than NE2018 ($I = 0.21$ kPa; $R = 71$ y). Recall that R values are rough estimates of the recurrence and are only meant to contextualize I in the local climate. This difference most likely arises from the timing of most extreme periods of positive VPD'_d and below-average P_d, which in the case of NE2018 were shifted by about a month wrt. JJA – which is also reflected in the increasing θ'_d and $SPEI_w$-1 in August (Fig. 4.21u,w). When considering the entire growing seasons, that in 2018 featured stronger climatic impact on ecosystems than that in 2003 (Buras et al., 2020; Bastos et al., 2020b). In summary, for both VPD_{JJA+} the climatological dampening of I, occurring preferentially in coastal regions and manifesting in negative $I_{q'ref}$, was important but still outweighed by the large $I_{T'}$ (CE2003 and NE2018) and $I_{q'par}$ (NE2018).

Lastly, the most intense VPD_{JJA+} discussed earlier, US2011, was characterized by an extremely homogeneous substructure (Fig. 4.22). All but one day of US2011 showed positive VPD'_d and also positive T'_d of on average 2.6 K (Fig. 4.22a,c). This could be partly due to the dry soils at the beginning of summer, indicated by the already negative θ'_d and $SPEI_w$ values at all three timescales (Fig. 4.22i,k). The hot spot of positive T' and negative q' were the central and northern regions affected by US2011 (Fig. 4.22d,f). ERA5 P_d exceeded 5 mm on only one day in June, and the seasonal anomalies of P were so large that accumulated P in most regions was below 50 mm (Fig. 4.22g,h). These features of the substructure, especially also that of q'_d, were similar to those of SP1994, which occurred in a similarly arid region (Figs. 4.19 & 4.22). Also here, the largest part of I was due to T' (71%) but also $I_{q',par}$ contributed with 19% to I (Table 4.3). However, the region of the southern Great Plains is unique regarding the intensity of VPD_{JJA+}, which in the case of US2011 (and also US1980) was about twice that of SP1994. The spatial patterns of drought intensity show the aggregated nature of $SPEI_w$-3, which was extremely low where rainfall was anomalously scarce (in the southwest of US2011) and where extremely positive VPD′ occurred (in the north of US2011). Note that positive θ' in the southwest of US2011 has to be interpreted carefully, as it is situated in the climatologically dry area of the Chihuahua desert and might still indicate very low absolute θ (Fig. 4.22j). Lastly, in contrast to the case studies in non-arid regions (e.g., SE2000 and NE2018), θ'_d did not further decrease and was less negative for US2011 during JJA despite a more extreme atmospheric water demand reflected

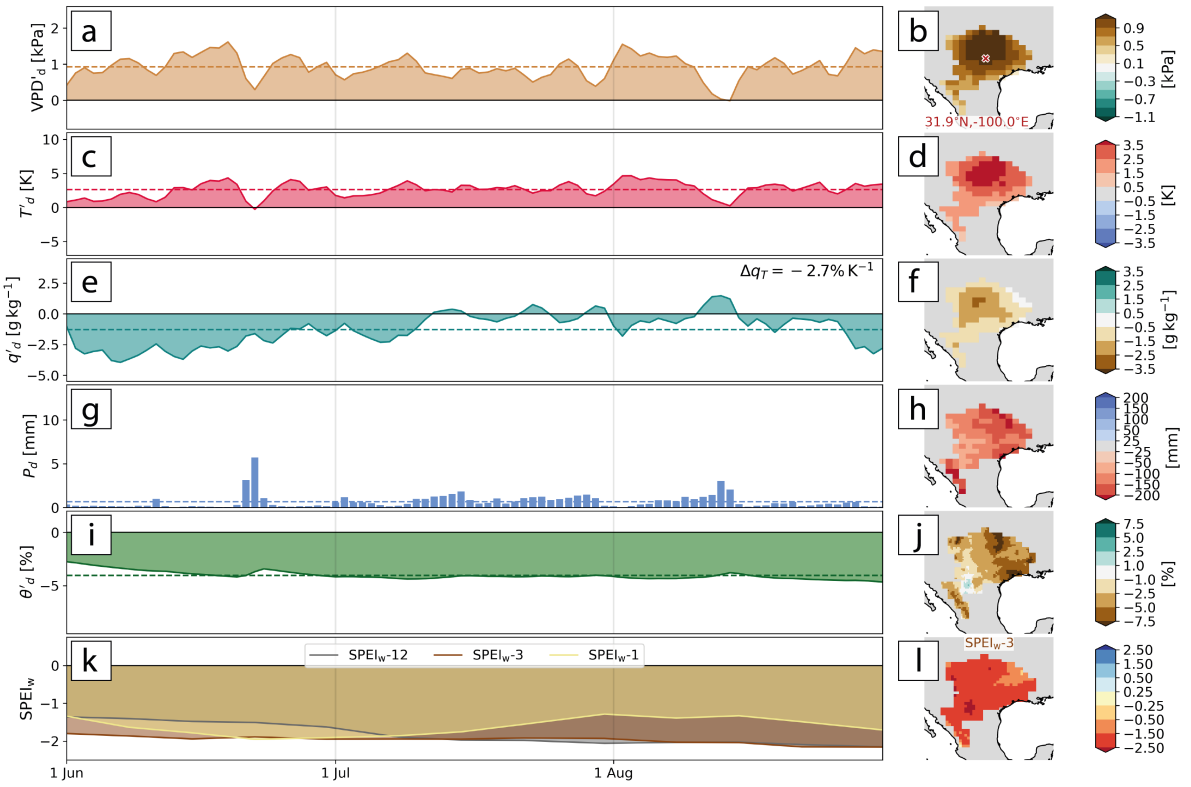

Figure 4.22: The same as Fig. 4.19a-l but for US2011.

in large VPD'$_d$ and low SPEI$_w$-1 (Fig. 4.22a,i,k). This means that virtually no soil water was available for evapotranspiration, i.e., actual evapotranspiration was well below PET, and all excess energy at the surface was converted into sensible heat to warm the (dry) air above. Thus, these water-limited conditions fed back on high T'_d, low q'_d and hence high VPD'$_d$, and were partly responsible for the extremely large I of US2011. In summary, US2011 is an example that illustrates how VPD$_{JJA+}$ can intensify in an arid region that reaches complete water limitation.

To conclude, the six cases of VPD$_{JJA+}$ illustrated the diversity of how extreme VPD on the seasonal timescale formed in 1979−2020, and how strongly it is linked to drought conditions, i.e., to soil water content and to the SPEI. While all of the six VPD$_{JJA+}$ shared extremely positive I, absolute values of I as well as the physical limits of individual meteorological anomalies to produce large VPD' varied with region. The combined potential of q_d and T_d to form large VPD'$_d$ becomes particularly obvious when contrasting the impact of individual cold-dry periods (e.g., in SP1994), hot-dry periods (e.g., in US2011), and hot-moist periods (e.g., in CE2003). Regarding the decomposition of I, (strongly) positive T' was important in all case studies, but $I_{q',par}$ and $I_{q',ref}$ were important contributions in exceptionally dry summer seasons (e.g., SE2000), and in specific regions such as the southern Great Plains (US2011). The latter illustrated the feedback mechanisms between extreme VPD reducing θ, and low θ fostering high VPD under arid conditions (Miralles et al., 2019). Similarly, the below-average θ and P often co-occur in space and time with negative q', as these anomalies are positively coupled in many regions (Betts et al., 1996).

4.6 Discussion

We have applied the scheme of Röthlisberger et al. (2021) to identify extreme VPD seasons in the Northern Hemisphere mid-latitudes in JJA 1979–2020 (ERA5) and in a 1'050-year-large set of climate simulations (CESM1) with 1990–1999 historical radiative forcing (see Chapter 2), and have decomposed the intensity of the resulting $\text{VPD}_{\text{JJA+}}$ into contributions from T', q'_{par}, and q'_{ref}. The evaluation of VPD on the seasonal timescale requires a careful methodological setup that allowed us to (i) statistically identify $\text{VPD}_{\text{JJA+}}$, and (ii) decompose I into seasonal mean contributions from the meteorological anomalies. Using seasonal mean T, q, and p leads to an underestimation of VPD compared to a more accurate computation based on sub-daily VPD values. This underestimation of the lower-frequency computation has been accounted for with empirical corrections (Williams et al., 2013), or with the use of long-time averaged daily minimum and maximum temperature, which, however, tends to overestimate VPD inferred from sub-daily values (Seager et al., 2015). As we find that the underestimation is approximately constant in time, it is merely the result of intra-seasonal VPD variability rather than of a process related to the intensity of one particular $\text{VPD}_{\text{JJA+}}$. Consequently, this fraction of VPD could not have been explained by seasonal mean anomalies of T and q. In summary, regarding the magnitude of VPD, our results have to be considered a conservative estimate, which, however, does neither impede the identification of $\text{VPD}_{\text{JJA+}}$ nor their I.

In both datasets analyzed here, the intensity of $\text{VPD}_{\text{JJA+}}$ is clearly dominated by $I_{T'}$, however, $I_{q',par}$ accounts for about a third of total I across all $\text{VPD}_{\text{JJA+}}$ in ERA5 and CESM1. Many recent studies on VPD, on its trend and variability, and particularly those that quantify future impacts of VPD on forests emphasized the role of T' (or e_s) for large VPD (Williams et al., 2013; McDowell et al., 2016; Ficklin and Novick, 2017). Only few studies, e.g., Seager et al. (2015), have investigated and highlighted the importance of e_a (i.e., q) variability for inter-annual VPD variability. Our results for ERA5 $\text{VPD}_{\text{JJA+}}$ indicate an increase of I with global warming, which is consistent with future projections of global VPD (Yuan et al., 2019), or regional analyses in the U. S. (Ficklin and Novick, 2017) and Europe (Balting et al., 2022). Interestingly, although insignificantly, $I_{T'}$ increases at about the same rate as I, while there is a strong shift of the q'-contribution from $I_{q',par}$ to $I_{q',ref}$ at the hemispheric scale (Fig. 4.17). The globally decreasing trend in relative humidity that accompanied the recent climate warming could explain that a larger share of q' is attributed to q'_{ref} instead of q'_{par} at warmer temperatures (Simmons et al., 2010; Vicente-Serrano et al., 2018). Projections of daily VPD extremes (Gamelin et al., 2022) and seasonal VPD (Ficklin and Novick, 2017) underline the increasing importance of T for large VPD towards the end of this century. It would, therefore, be of high interest to use the setup developed here to investigate $I_{T'}$, $I_{q',par}$, and $I_{q',ref}$ of $\text{VPD}_{\text{JJA+}}$ in CESM1 simulations for a future climate with larger radiative forcing than that used for our simulations.

We found that CESM1 is well able to model the typical $\text{VPD}_{\text{JJA+}}$ size and intensity, their positive correlation, and the decomposition of their I in the Northern Hemisphere mid-latitudes. First

of all, we use CESM1 in 1990–1999, a relatively short period during which the observed global trend in relative humidity was still small (Simmons et al., 2010; Blunden and Boyer, 2021). Consequently, the inability of many CMIP5 models to capture this trend (Dunn et al., 2017), which would have introduced an error in the decomposition of I, did not apply to our CESM1 setup. Furthermore, the climatological co-variability between q and T is well-simulated by the models in the historical period (Dunn et al., 2017). As a consequence of a well-simulated co-variability, the modelling of VPD can be better than that of q and T individually (Fischer and Knutti, 2013). Nevertheless, the high agreement of extreme VPD characteristics in CESM1 compared to ERA5 remains surprising, given the considerable uncertainties related to the land-atmosphere coupling (Berg and Sheffield, 2018). Therefore, further evaluation of $\text{VPD}_{\text{JJA+}}$ characteristics analogously to Röthlisberger et al. (2021) could consolidate and explain the ability of CESM1 to simulate $\text{VPD}_{\text{JJA+}}$.

Spatial patterns in the decomposition of I during extreme VPD seasons appear to be physically constrained by the observed q-T-correlation, i.e., Δq_T, which arises from the local climate, weather system dynamics, surface cover, and orography. On the one hand, Δq_T exhibits its largest negative values in dry regions of the southwestern U. S. and Pakistan (Dai, 2006), where negative q' contributes mainly to $I_{q',ref}$ as low q is expected in warm JJA. This could be strongly coupled to intra-seasonal weather system dynamics, which explain why most rainfall – which is inherently coupled to moist ($q' > 0$) conditions – falls on colder than normal days in the southwestern U. S. (Zschenderlein and Wernli, 2022). On the other hand, regions of highly positive Δq_T, such as northwestern Europe and the northeast of Asia and of North America (Dai, 2006), show typically negative $I_{q',ref}$ and large relative $I_{T'}$. Large contributions $I_{q',par}$ are found adjacent to the western ocean basins and in northern latitudes, where cyclones are climatologically the most abundant in JJA (Wernli and Schwierz, 2006). Cyclones are responsible for atmospheric (moisture) transport and for a large share of P in these regions (Pfahl and Wernli, 2012b; Zschenderlein and Wernli, 2022) and thus exceptionally low cyclone frequency could be the source of negative q'_{par} in $\text{VPD}_{\text{JJA+}}$. Related to that, in more confined areas within the coastal entrance regions of the Northern Hemisphere jet streams, CESM1 revealed a unique group of $\text{VPD}_{\text{JJA+}}$ with negative $I_{T'}$. They arise from a subtle balance between sufficiently negative T' (thsu negative q'_{ref}), which, however, are not too low to cause a substantially negative $I_{T'}$. A southward shifted Northeast Asian jet reduces the local cyclone frequency and hence precipitation in and north of North Korea, fostering a colder and more continental flow towards these regions (Zheng-Bin et al., 2014). Thus, the colder conditions relate to positive $I_{q',ref}$ and the particularly dry conditions further contribute to $I_{q',par}$. In the eastern U. S., a northward shifted North Atlantic jet stream reduces the moist southerly inflow towards the eastern U. S. (Coleman and Budikova, 2013) – a pattern which has been responsible for major droughts in that region (Seager et al., 2012). These situations disfavor atmospheric rivers and warm conveyor belts, which are two weather systems crucial for summer precipitation in the eastern U. S. (Zschenderlein and Wernli, 2022). The absence of the weather systems related to wet conditions during $\text{VPD}_{\text{JJA+}}$, in the eastern U. S. but also elsewhere in the mid-latitudes, is pre-

sumably compensated by the increased occurrence frequency of (blocking) anticyclones, which can favorably contribute to both positive $I_{T'}$ and $I_{q',par}$ (e.g., Zschenderlein et al., 2020). These considerations highlight how weather and climate dynamics can – amongst others – shape the identified $\text{VPD}_{\text{JJA+}}$ and how the interplay of T', q'_{ref}, and q'_{par} determines their intensity.

As already discussed in Sects. 4.5.1 & 4.5.3, many of the identified $\text{VPD}_{\text{JJA+}}$ have previously been related to adverse impacts on ecosystems and drought conditions indicated by θ and SPEI. As reduced P and dry soils often went along with $\text{VPD}_{\text{JJA+}}$, partly amplifying their intensity (Miralles et al., 2019; Lesk et al., 2022), it remains difficult to attribute the adverse ecosystem impact to the extremely high VPD or to dry soils alone (Sulman et al., 2016). Nevertheless, the extreme forest drought stress in Europe in 2018 has regionally been linked to the highest growing season mean VPD of the last 100 years (Schuldt et al., 2020). Also, specifically in the southwestern U. S., VPD has been highlighted as major factor determining forest drought stress and wildfire risk (Williams et al., 2013, 2014). Generally in arid and semi-arid regions, the intensification of drought stress by VPD is more straight-forward than in humid regions, where prevalent θ and P are more important for drought stress (Vicente-Serrano et al., 2020). This is evident from the temporal substructure of US2011, where almost completely dry soils from early on greatly limited evapotranspiration and thus fostered positive T'_d, negative q'_d, and high VPD'_{d} via enhanced sensible heat fluxes (Seneviratne et al., 2010; Lesk et al., 2022). Nevertheless, also in semi-arid to sub-humid regions of Europe, the case studies of $\text{VPD}_{\text{JJA+}}$ (SE2000, CE2003, and NE2018) went along with extreme SPEI_{w}-3 values below -1.65, which are strongly related to agricultural and forest drought impact (Bachmair et al., 2018). Finally, the set of $\text{VPD}_{\text{JJA+}}$ presented here constitutes a starting point to study the adverse impacts of extremely high VPD more systematically and to quantify the role of VPD for ecosystem drought stress in comparison with other climatic determinants.

Finally, and despite all efforts to develop a nuanced methodological setup that fits the purpose of this chapter, some limitations of the presented analyses remain. The first one is the short observational period of 42 summer seasons, which affects the estimation of VPD trends, the shares of q'_{ref} and q'_{par}, and the parameters of the N^{YJ} at each grid point. Using a longer reanalysis dataset, e.g., the backward extension of ERA5 from 1940 to 2022 (Hersbach et al., 2020), would make all statistical models used here more robust. Second, since the lower tail of any VPD distribution is bounded at zero, the forced warming trend potentially increases the variability of VPD in ERA5 over time, which would impede the assumptions made in the parameter estimation of the N^{YJ} distribution. Observations do not show a consistent change in VPD variability over the past 50 years, as it is locally influenced by additional factors of climate variability (Hansen et al., 2022). However, these first two limitations lead to a mutual trade-off: A longer observational period would increase the robustness of the parameter estimation, but at the same time, the undesirable effect of global warming on VPD variability would be larger and thus potentially call for substantial modifications in the statistical modelling of VPD compared to Röthlisberger et al. (2021). A last limitation concerns the use of ERA5 and CESM1 data

in different time periods, which goes along with different climatic reference states used to compute the $I_{T'}$ and alters the effect of a given T' on VPD′. From our results, which show a good agreement between ERA5 and CESM1 in terms of I and $I_{T'}$, we cannot infer whether these differences are of minor importance or compensated by CESM1 model biases. We, therefore, suggest additional model evaluations regarding $\text{VPD}_{\text{JJA+}}$.

4.7 Conclusions

High vapor pressure deficit (VPD) during the summer season results from hot and/or dry air and is, among other things, a key driver of ecosystem drought stress, crop failure, increased wildfire risk, and tree mortality in mid-latitude forests. This chapter presents the results of a sophisticated methodology that (i) identifies extremely high VPD on the seasonal timescale guided by Röthlisberger et al. (2021) based on the exceedance of the local 40-year return level, and (ii) decomposes the mean VPD′ of the resulting extreme season objects ($\text{VPD}_{\text{JJA+}}$) into meteorological contributions from seasonal anomalies of T and q (T' and q'). Both aspects constitute progress in the understanding of inter-annual VPD variability, as neither extremes of seasonal mean VPD have previously been identified on a hemispheric scale, nor have their intensities been attributed to T' and q'.

In the region from 30–60 °N in summer, we identify 96 $\text{VPD}_{\text{JJA+}}$ in ERA5 in 1979–2020, and 2′507 $\text{VPD}_{\text{JJA+}}$ in a 1′050-year-large set of CESM1 climate simulations with 1990–1999 radiative forcing. The most intense observed $\text{VPD}_{\text{JJA+}}$ occurred in the southern U. S. and Mexico in 2011 with an intensity of $I = 0.78\,\text{kPa}$, and the largest one affected $A = 30.2{\cdot}10^5\,\text{km}^2$ of land area in western Russia in 2010. Over all $\text{VPD}_{\text{JJA+}}$, approximately 75% of I are due to positive T' in both ERA5 and CESM1; a fraction that is likely to increase in a warming climate due to the exponential dependence of VPD on T. A minor fraction of this temperature contribution is offset by a moistening that can be attributed solely to the warming (q'_{ref}). The remaining ~31% can be attributed to a dry anomaly in q that is related to anomalous circulation dynamics during extreme VPD seasons (q'_{par}). According to CESM1, which simulates the main characteristics of $\text{VPD}_{\text{JJA+}}$ extremely well, the relative contributions of T', q'_{par}, and q'_{ref} vary across the mid-latitudes. In a few semi-arid and arid regions, all three terms contribute positively. In more northern regions, positive q'_{ref} acts to dampen the contributions of the hot and dry anomalies during $\text{VPD}_{\text{JJA+}}$. Very few regions along the east coasts were identified, where $\text{VPD}_{\text{JJA+}}$ can also occur in association with negative T' due to exceptionally large negative q'. Many of the presented relationships between T, q'_{ref}, and q'_{par} during $\text{VPD}_{\text{JJA+}}$ are potentially related to anomalous weather system dynamics on the daily to weekly timescales. A possible future extension of this work could examine the meteorological phenomena and processes that influence q' and T' in the first place.

Moreover, we explored the peculiarities of the nonlinear dependence of VPD on T, which causes an underestimation of the seasonal mean VPD computed from seasonal mean T, q, and

p compared to higher-frequency data of the same variables. This underestimation is due to intra-seasaonal VPD variability (58% day-to-day and 42% sub-daily variability), and hardly contributes to the rarity, i.e., extremeness, of the identified $\text{VPD}_{\text{JJA+}}$.

In a last analysis, we presented the substructure of a diverse set of exemplary $\text{VPD}_{\text{JJA+}}$ and their concurrence with (extreme) drought according to the SPEI and top-1-meter soil water content. They exemplify the importance of individual heat wave contributions to $\text{VPD}_{\text{JJA+}}$, and also illustrate the importance of extended periods of simultaneously low q and high T for large VPD and low SPEI.

Overall, this chapter presents a novel meteorological decomposition of extreme seasonal mean VPD to better understand how they are shaped by shorter-term atmospheric variability. Furthermore, the presented framework could be used in future work to investigate the impact of $\text{VPD}_{\text{JJA+}}$ more systematically and separately from other drivers of plant water stress, and also to investigate the relative importance of T' and q' in a warmer future climate.

Chapter 5

Assessment of the Greenland summer melt increase in the 21st century

5.1 Introduction

Short-term atmospheric variability in summer is a major determinant of the total mass balance (TMB; Eq. 1.2) of the Greenland Ice Sheet (GrIS) and thus of the GrIS's contribution to global sea-level rise (see a more elaborate introduction in Sect. 1.4.3). As a response to global warming, surface melt has contributed more and more to the decrease of TMB in the past decades (Fettweis et al., 2013a; van den Broeke et al., 2016). Future mass loss will be dominated by surface melt, as the contribution from dynamical ice loss (D) decreases due to the retreat and thinning of outlet glaciers (Muntjewerf et al., 2020). As a consequence, surface processes including the impact of atmospheric variability on melt remain the largest source of uncertainty regarding future GrIS mass loss (Delhasse et al., 2018; Hofer et al., 2019; IPCC, 2021; Delhasse et al., 2021).

While the increase in surface melt in the near future is unequivocal (Box et al., 2022b), the potential impact of changing atmospheric circulation patterns as a response to continued global warming is a matter of debate (Belleflamme et al., 2013; Hanna et al., 2018; Delhasse et al., 2021). Delhasse et al. (2018) suggested that more frequent anticyclonic circulation anomalies as in the early 2000s – which are not well-captured by current general circulation models (GCMs) – would cause a two times larger surface mass loss than currently estimated (see Eqs. 1.2 & 1.3). In addition to altered atmospheric circulation patterns, future changes in surface melt include an increasing melt area and a larger melt intensity (Q) in the melt area (Franco et al., 2013; Mioduszewski et al., 2016). The increase in Q results from spatially varying processes that cause an energy surplus at the GrIS surface, e.g., changes in cloud properties (Hofer et al., 2017, 2019), enhanced sensible heat fluxes from a warmer atmosphere (Wang et al., 2021), the melt-albedo feedback (Box et al., 2012), and the melt-elevation feedback (Muntjewerf et al., 2020). A main challenge regarding future mass loss from the GrIS is, therefore, to understand if and how strongly (i) the expanding melt area, (ii) intensified Q in the melt area, i.e., melt intensification,

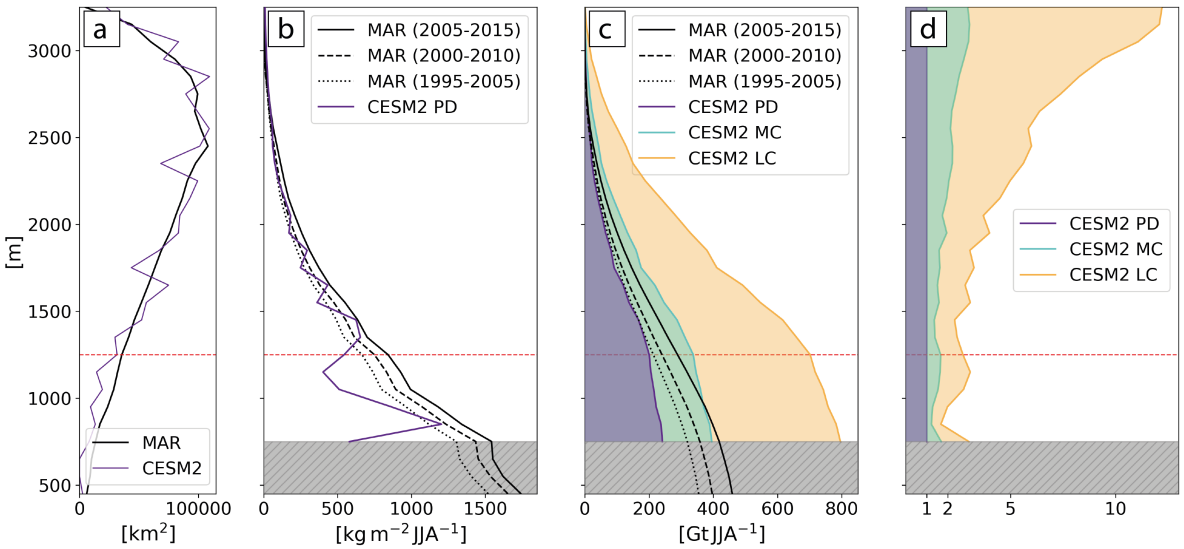

Figure 5.1: Vertical profiles of 100 m-binned (a) ice sheet area, (b) surface melt intensity, (c) accumulated melt above a certain elevation, and (d) ratio of accumulated melt relative to PD. Purple lines show CESM2 average values in PD. Dotted, hatched, and solid black lines in (a-c) show MAR average values in 1995–2005, 2000–2010, and 2005–2015 (PD), respectively. Cyan and yellow lines in (c,d) denote CESM2 average values in 2045–2055 (MC) and 2085–2095 (LC), respectively. The dashed red line denotes 1'250 m, i.e., values for the elevation bin 1'200–1'300 m. Grey shading in (b-d) shows blind spots of CESM2.

and (iii) shifts in the occurrence frequency of given circulation patterns determine the increase in summer melt. Moreover, it is worth investigating if atmospheric circulation anomalies remain an important driver of melt variability in a warmer future climate, or if the average conditions already lead to widespread and intense melt.

We use an ensemble of the Community Earth System Model version 2.1 (CESM2) with a static GrIS topography using radiative forcing from the SSP3-7.0 scenario to quantify melt and the three aforementioned contributing mechanisms (Danabasoglu et al., 2020). We consider the change in June–August (JJA) surface melt estimated from the surface energy balance between present-day (PD; 2005–2015), mid-century (MC; 2045–2055), and late-century (LC; 2085–2095), for details see Sect. 5.2.4. To motivate the use of a CESM2 at ~1°resolution to model surface melt, we first compare our melt estimates with those of the regional climate model (RCM) MAR v3.11 with 6 km horizontal resolution and ERA5 boundary conditions (Fig. 5.1; Fettweis et al., 2017). By and large, the GrIS area as well as the mean Q in PD are well-captured by CESM2 for regions above ~1'200 m (Fig. 5.1a,b). As expected from the coarse resolution, the increasingly steep ablation area is greatly underestimated by CESM2, and fully ice-covered regions below ~1'000 m hardly exist (Fig. 5.1a). Consequently, the accumulated melt in CESM2 deviates strongly from MAR estimates when including lower elevations (Fig. 5.1c). Above 1'200 m, however, the accumulated melt in CESM2 amounts to 201 Gt JJA^{-1} in PD, which is relatively close to MAR estimates in the same period (30% underestimation). The cause of the remaining discrepancy is unclear, but it is conceivable that internal variability and model biases both contribute. Note that the exceptional melt years in 2007, 2010, and 2012 are contained

in the MAR data but not in the freely running CESM2 simulations and thus likely contribute to this discrepancy (Fettweis et al., 2020). The underestimation of melt in CESM2 is smaller with 16% and 6% when compared to MAR values in 2000–2010 and 1995–2005, respectively (Fig. 5.1c). Thus in this study, we will consider only upper-elevation ($\geq 1'200$ m) surface melt for two reasons: Firstly, these regions will see an extremely large relative increase in melt of +68% and +249% towards MC and LC (Fig. 5.1c,d), respectively, and, secondly, the CESM2 melt is consistent with the MAR melt there.

In this chapter, we analyze melt from the upper-elevation zone ($\geq 1'200$ m), which is projected to contribute an additional 501 Gt JJA^{-1} (~1.4 mm JJA^{-1} of sea-level rise) to GrIS summer melt in the 2090s (assuming the SSP3-7.0 scenario). Thereby, we aim to answer:

1. How much of the change in GrIS surface melt in the 21st century can be attributed to changes in melt extent, melt intensity, and atmospheric circulation?
2. How does atmospheric circulation modulate this melt change across the GrIS?
3. How important is atmospheric variability for intra- and inter-seasonal variability of GrIS surface melt?

As mentioned above, we use a CESM2 ensemble including four members in the periods PD, MC, and LC, i.e., 44 years of simulated data in each time period (Sects. 2.2 & 5.2.2). To classify the GrIS atmospheric circulation, we use the Self-Organizing Map method on 500 hPa geopotential height anomalies in Sect. 5.2.3 (Kohonen, 1982). To attribute changes in surface melt to changing melt area, melt intensity, and circulation, we refine a decomposition introduced by Cassano et al. (2007, Sect. 5.2.5). We acknowledge that the use of a GCM might still underestimate atmospheric variability (Delhasse et al., 2021), which is discussed in Sect. 5.4. Nevertheless, CESM2 is one of the best evaluated GCMs, performing well in the GrIS region (van Kampenhout et al., 2020). Moreover, this chapter provides a framework to study the three main determinants of the enormous projected increase in surface melt, which are studied in Sect. 5.3, and advances our understanding of the atmospheric influence on GrIS mass loss and associated sea-level rise.

5.2 Data and methods

5.2.1 Regional climate model MAR

We used MAR data in 1995–2015 in Sect. 5.1 to evaluate the melt estimates from CESM2 data (Fettweis, 2007; Fettweis et al., 2017). Daily output on a 6 km horizontal grid was downloaded from `ftp://ftp.climato.be/fettweis/MAR/` (Fettweis, 2020). MAR is a widely used regional climate model targeted to high latitudes and includes a 1-dimensional multi-layered energy balance model that simulates the energy fluxes between the GrIS surface and the atmosphere. In v3.11, MAR is laterally forced with ERA5 reanalysis data (Sect. 2.1). We sum the melt-water production in JJA over the GrIS for several elevation bins to acquire the results shown in Fig. 5.1,

using the provided GrIS mask and GrIS topography. For further details with regard to MAR data see Fettweis (2007).

5.2.2 CESM2 data

We use 6-hourly output from four members of the Community Earth System Model 2.1 (CESM2) integrated from 1850 to 2100 using historical forcing up to 2014 and the SSP3-7.0 scenario thereafter (Sect. 2.2). CESM2 is one of the latest CMIP6 models and is among the currently best GCMs to simulate the climate of the GrIS (Noël et al., 2020; van Kampenhout et al., 2020). In our CESM2 setup ("noevolve"), the GrIS topography is static, however, the Community Land Model 5.0 (CLM5) does modify the GrIS surface albedo by modelling mass concentrations of atmospheric-deposited aerosols and ice effective grain size (Lawrence et al., 2019). We use the data in June–August (JJA) grouped into three 11-year periods termed present-day (PD; 2005–2015), mid-century (MC; 2045–2055), and late-century (LC; 2085–2095). The variables used include 6-hourly values of surface temperature (T_s), and daily mean values of 500 hPa geopotential height ($Z500$), net shortwave radiation (SW_{net}), net longwave radiation (LW_{net}), sensible heat flux (SH), and latent heat flux (LH). For the SOM analysis, we compute anomalies of $Z500$ ($Z500'$) from transient climatologies, which are defined as 11-day running mean $Z500$ over the 44 years of data in each period. Each $Z500'$, therefore, refers to the climatology of the period of its occurrence. We consider glaciated grid cells in Greenland as part of the GrIS – as elaborated in Sect. 5.1 – if they lie at least at 1'200 m (this yields a total area of $1.51 \cdot 10^6$ km^2, which is hereafter referred to as the "upper-elevation zone").

5.2.3 Self-Organizing Map

To classify the atmospheric circulation over the GrIS in the three time periods, we make use of the Self-Organizing Map (SOM) method (Kohonen, 1982). SOM is an unsupervised neural network that identifies similarities in high-dimensional data without prior knowledge of the resulting patterns. It is, therefore, well-suited to classify and visualize the synoptic circulation and has become a widely used tool in atmospheric sciences (Liu and Weisberg, 2011). Specifically in the Greenland region, SOM was applied to classify not only atmospheric circulation patterns (Mioduszewski et al., 2016; Gallagher et al., 2022), but also water vapor transport (Mattingly et al., 2018), and atmospheric blocking (Preece et al., 2022).

The SOM input data is daily mean $Z500'$ from all three time periods in the domain from 50–80°N, and 65–20°W at its southern edge and 90°W–5°E at its northern edge (see Fig. 5.2 below). The domain includes the GrIS, as well as the proximal North Atlantic storm track, the Davis and the Denmark Strait. The $Z500'$ data was first interpolated to an equidistant grid with $\Delta x = 100$ km to ensure that all latitude bands contribute equally. This results in $o = 12'144$ observation days and $n = 1'041$ equidistant grid points within the domain. Second, we normalize $Z500'$ at every equidistant grid point with the mean and standard deviation of all observations to account for spatial variations in $Z500'$ variability. Consequently, the input data consists of normalized

$Z500'$ as a two-dimensional (2D) $o \times n$ array. Note that we perform the SOM analysis on data that is pooled from all three periods, i.e., not separately for each period.

We tested different SOM setups, which are summarized in the Appendix C (Table C.1). The SOM user chooses the size of the SOM map, i.e., how many nodes or circulation patterns to identify, and a set of tuning parameters. The latter include the neighborhood function and the initial radius (r), which both determine how the input data adjusts the position of the closest and neighboring nodes in the data space during training, and the number of training iterations (I), i.e., how often the SOM is trained with the input data. We test different rectangular SOM sizes (5×4, 6×4, 6×5), whereby the trade-off is between a more accurate representation of circulation patterns (many nodes) and a stronger reduction in the dimensionality (fewer nodes). The number of iterations I, i.e., the "training length", was varied with $I \in \{1'000, 3'000, 5'000, 10'000\}$. Further, we test $r \in \{2, 3, 4\}$, which are in the range of about half the size of SOM side length, and which should ensure that the initialized nodes converge to a final SOM map. As advised by Liu et al. (2006), we chose the Epanechikov neighborhood function. Our final choice of parameters was guided by the ability of the final SOM map to adequately classify the GrIS circulation, i.e., by the quantization error (QE), and by the topographic error (see Liu et al. (2006) for details). We were primarily interested in sufficiently reducing dimensionality while still minimizing QE, which quantifies the similarity between the final SOM nodes and the observed daily $Z500'$. Considering all these aspects, we chose the setup of a 6×5 map with $r = 2$ and $I = 10'000$.

To perform SOM, we use the SOM Toolbox in Matlab, which is among the most flexible and frequently tested public-domain SOM tools (Vesanto et al., 2000). On the following lines we provide a brief and somewhat "heuristic" explanation of how the final SOM map is computed. For more details the interested reader is referred to Vesanto et al. (2000). The 30 nodes are initialized linearly in a mesh in a 2D plane along the two greatest eigenvectors of the input data. In the following batch training process, which describes the training with all input data at once, the nodes in the n-dimensional data space are modified according to the input observations. The training draws the nodes and its neighboring nodes towards regions of high data density, such that each node of the final SOM map is closest to about the same number of observations. The final nodes can be displayed as a 2D map, in which neighboring nodes are more similar than nodes that are further apart. Each daily $Z500'$ observation is allocated to the closest node in the data space – also called its best-matching unit.

5.2.4 Surface melt characteristics

In this subsection, we introduce several daily measures to arrive at a formulation for daily melt, which is then aggregated to one JJA season and also formulated in terms of the SOM node classification of the previous subsection. First of all, at each grid cell j and day d we define the daily melt energy ($Q_{d,j}$) according to the surface energy balance as,

$$Q_{d,j} = SW_{net,d,j} + LW_{net,d,j} - LH_{d,j} - SH_{d,j} \tag{5.1}$$

where $Q_{d,j}$ is approximated from the sum of radiative and turbulent fluxes with unit $\mathrm{W\,m^{-2}}$. Positive radiative fluxes point downwards while positive turbulent fluxes point upwards. Thereby, we assume that the entire energy surplus at the surface is available for melt, i.e., that all ice is at the melting point and that the subsurface conductive heat flux is zero. This assumption is justified during periods when the GrIS is melting (van den Broeke et al., 2016). Consequently, in a second step, we define the daily melt area (A_d) from 6-hourly surface temperature (T_s). A grid cell of the upper-elevation zone is considered to be melting at a given day if at any time of that day $T_s \geq 272.15\,\mathrm{K}$ (Nghiem et al., 2012). Finally, we compute the daily melt intensity as the spatial average of $Q_{d,j}$ over A_d (Q_d) and the daily melt total (m_d) as follows:

$$A_d = \sum_{j \in \mathbf{J_d}} a_j \tag{5.2}$$

$$Q_d = \frac{\sum_{j \in \mathbf{J_d}} a_j \cdot Q_{d,j}}{A_d} \tag{5.3}$$

$$m_d = A_d \cdot Q_d \tag{5.4}$$

where a_j is the area of grid cell j, and $\mathbf{J_d}$ is the set of melting grid cells at day d. Negative values of Q_d (and hence m_d) are set to zero. The m_d values are converted from W to $\mathrm{Gt\,d^{-1}}$ by using the heat of fusion to melt 1 g of ice at 0°C equal to $H_f = 334\,\mathrm{J\,g^{-1}}$ (e.g., Hofer et al., 2017). Aggregating the (daily) m_d to a seasonal melt total (m_s, in $\mathrm{Gt\,JJA^{-1}}$) equals:

$$m_s = \sum_{d=1}^{92} m_d = \sum_{i=1}^{30} \sum_{d \in \mathbf{D_i}} m_d \tag{5.5}$$

where i denotes the SOM node index and $\mathbf{D_i}$ the set of days in node i. The number of days in $\mathbb{D}_i$, i.e., the number of node days per JJA season, is hereafter termed $f_{s,i}$ [$\mathrm{d\,JJA^{-1}}$].

5.2.5 Decomposition of 21st century melt change

We use a framework similar to that introduced by Cassano et al. (2007) to decompose the changes in summer melt that occur during the 21st century into contributions from circulation changes, melt area changes, and melt intensity changes.

To apply the decomposition, we first compute node day averages of several quantities over all 44 years of data in one period. That is, daily variables A_d, Q_d, and m_d are averaged over all days in node i of period P, which are termed $\overline{A}_i^P$, $\overline{Q}_i^P$, and $\overline{m}_i^P$. As $f_{s,i}$ is a seasonally aggregated variable, $\overline{f}_i^P$ simply denotes the average of $f_{s,i}$ over all 44 years. Thus, the average summer melt in period P, which is the average of m_s over 44 years ($\overline{m}_s^P$), can be written as:

$$\overline{m}_s^P = \sum_{i=1}^{30} \overline{m}_{s,i}^P = \sum_{i=1}^{30} \overline{f}_i^P \cdot \overline{m}_i^P = \sum_{i=1}^{30} \overline{f}_i^P \cdot \left(\overline{A \cdot Q}\right)_i^P = \sum_{i=1}^{30} \overline{f}_i^P \cdot \left(\overline{A}_i^P \cdot \overline{Q}_i^P + C_i^P\right) \tag{5.6}$$

where $\overline{m}_{s,i}^{P}$ denotes the average JJA melt produced during days in node i, and $C_i^P = cov(A_d, Q_d)_i^P$ denotes the covariance of A_d and Q_d for all days of node i in period P. So $\overline{m}_s^P$ is (second equality in Eq. 5.6) the sum over all nodes of the average seasonal node occurrence [d JJA^{-1}] times the average melt per node day [Gt d^{-1}]. The latter can be expressed in terms of $\overline{A}_i^P$, $\overline{Q}_i^P$, and the covariance of A_d and Q_d, which arises due to the averaging of the nonlinear Eq. 5.4. Based on that, we formulate the change of $\overline{m}_s^P$ between two given time periods $P1$ and $P2$ ($\Delta\overline{m}_s$) as follows:

$$\Delta\overline{m}_s = \overline{m}_s^{P2} - \overline{m}_s^{P1} \overset{(5.6)}{=} \sum_{i=1}^{30} \left(\overline{f}_i^{P2} \cdot \overline{A}_i^{P2} \cdot \overline{Q}_i^{P2} + \overline{f}_i^{P2} \cdot C_i^{P2} - \overline{f}_i^{P1} \cdot \overline{A}_i^{P1} \cdot \overline{Q}_i^{P1} - \overline{f}_i^{P1} \cdot C_i^{P1}\right) \tag{5.7}$$

Further, we insert $X_i^{P2} = X_i^{P1} + \Delta X_i$ for all $X \in \{\overline{f}, \overline{A}, \overline{Q}, C\}$, where ΔX_i denotes the change of X_i between P1 and P2, and arrive at the following expression:

$$\Delta\overline{m}_s = \sum_{i=1}^{30} \Big(\underbrace{\Delta\overline{f}_i \cdot \left(\overline{A}_i^{P1} \cdot \overline{Q}_i^{P1} + C_i^{P1}\right)}_{\text{(i)}} + \underbrace{\Delta\overline{A}_i \cdot \overline{f}_i^{P1} \cdot \overline{Q}_i^{P1}}_{\text{(ii)}} + \underbrace{\Delta\overline{Q}_i \cdot \overline{A}_i^{P1} \cdot \overline{f}_i^{P1}}_{\text{(iii)}} + \underbrace{\Delta\overline{A}_i \cdot \Delta\overline{Q}_i \cdot \overline{f}_i^{P1}}_{\text{(iv)}} + \underbrace{\Delta\overline{C}_i \cdot \overline{f}_i^{P1}}_{\text{(v)}} + E_i \Big) \tag{5.8}$$

The sums of terms (i) to (v) over all nodes denote parts of $\Delta\overline{m}_s$ that are attributed to a change in (i) node day frequencies, i.e., atmospheric circulation, (ii) melt area, (iii) melt intensity, (iv) concurrent changes in (seasonal) melt intensity and area, and in (v) the covariance of daily melt area and intensity. The expression E_i summarizes four additional concurrent terms that are negligible when summed over all nodes as we will show a posteriori in Sect. 5.3.1. Term (iv) can be better understood with the example of positive $\Delta\overline{Q}_i$ and $\Delta\overline{A}_i$, i.e., of increasing average melt area and melt intensity in a given node. This necessarily causes also a nonlinear, positive contribution (iv), which quantifies the amount of melt that arises over the extension of the melt area ($\Delta\overline{A}_i$) by the extra melt intensity ($\Delta\overline{Q}_i$). In the following, we will refer to the five terms or their sums over all nodes by (i) the frequency term, (ii) the area term, (iii) the intensity term, (iv) the concurrent term, (v) the covariance term, and the residual. We use the decomposition (Eq. 5.8) to attribute melt changes occurring between PD and MC, and between PD and LC. Changes between MC and LC result from the difference of the two.

In summary, we decompose the change in the mean GrIS surface melt in JJA between periods PD, MC, and LC by using (1) a SOM classification of the mid-tropospheric circulation, and (2) a refined version of the decomposition introduced by Cassano et al. (2007), which attributes the melt change to altered atmospheric circulation, melt area, and melt intensity (Eq. 5.8).

5.3 Results

In the first part of this section, we present the attribution of the melt increase during the first and second half of the 21st to the individual processes (Sect. 5.3.1). Thereby, we first introduce the atmospheric circulation patterns derived from the SOM analysis, their frequency, and the associated melt, melt area, and melt intensity. In the second part, we present the melt change

decomposition for every node and further illustrate the spatial variability in how the extent and intensity of melt are modified during different circulation patterns (Sect. 5.3.2). Lastly, we examine to what extent circulation variability in the late 21st century still matters for melt (Sect. 5.3.3).

5.3.1 The 21st century summer melt increase

a) Mid-tropospheric circulation patterns

The 30 nodes (atmospheric circulation patterns) identified by the SOM method from daily $Z500'$ in PD (2005–2015), MC (2045–2055), and LC (2085–2095) demonstrate the great circulation variability over the GrIS (Fig. 5.2). Nodes in the upper left of the SOM map are characterized by cyclonic $Z500'$, with lowest GrIS-wide average $Z500'$ ($Z500'_{GrIS}$) of -163 ± 37 m for days in node (1,1). Diagonally opposed are nodes with anticyclonic $Z500'$ and anomalies of up to $Z500'_{GrIS} = +201 \pm 44$ m in node (5,6). The SOM nodes further vary according to the location of cyclonic and anticyclonic $Z500'$, which determine the mid-tropospheric flow anomaly in the GrIS region. Nodes in the lower left oft the SOM map, e.g., (4,1) and (5,2), exert southerly flow anomalies due to positive $Z500'$ to the Southeast of the GrIS. Nodes with negative $Z500'$ in that region are in the opposite corner of the SOM map, e.g., (1,5) and (1,6), and show more northerly flow over the GrIS. As a result, neighboring nodes differ due to a combination of a shift in location and in strength of the main mid-tropospheric flow anomalies. Finally, although the SOM method aims at distributing the 30 nodes equally in the data space (Sect. 5.2.3), the occurrence frequencies underline that nodes with most distinct $Z500'$ at the margins of the data space are less common than those in the center of the SOM map (Fig. 5.2).

b) Evolution of melt characteristics

In this subsection, we first discuss the quantities and changes that the decomposition is based on, before presenting the results of the actual decomposition in Sect. 5.3.1c. Average summer melt of a given node ($\overline{m}_{s,i}$) as well as the node occurrence frequency ($\overline{f}_i$), node-average melt extent ($\overline{A}_i$), and node-average melt intensity ($\overline{Q}_i$) reveal considerable variability between the three time periods (Fig. 5.3). By and large, the increase in $\overline{m}_{s,i}$ is larger in the second than in the first half of the century. On average over all nodes, summer melt per node increases from 6.7 Gt JJA^{-1} (PD) to 11.3 Gt JJA^{-1} (MC) to 23.4 Gt JJA^{-1} (LC; Fig. 5.3a). The partially weak melt increase from PD to MC is illustrated at the example of node (4,6), which is merely due to an increase in occurrence frequency (Fig. 5.3b), while $\Delta\overline{A}_{(4,6)}$ and $\Delta\overline{Q}_{(4,6)}$ are approximately zero (Fig. 5.3c,d). For many other nodes, only $\overline{A}_i$ is increasing between PD and MC, while $\overline{Q}_i$ is about constant or even decreasing (Fig. 5.3c,d). Hence, the average increase in daily melt intensity from MC to LC (+7.1 W m^2) is more than three times that from PD to MC (+2.0 W m^2). In short, there is a strong acceleration of the melt increase from the first to the second half of this century during most circulation patterns.

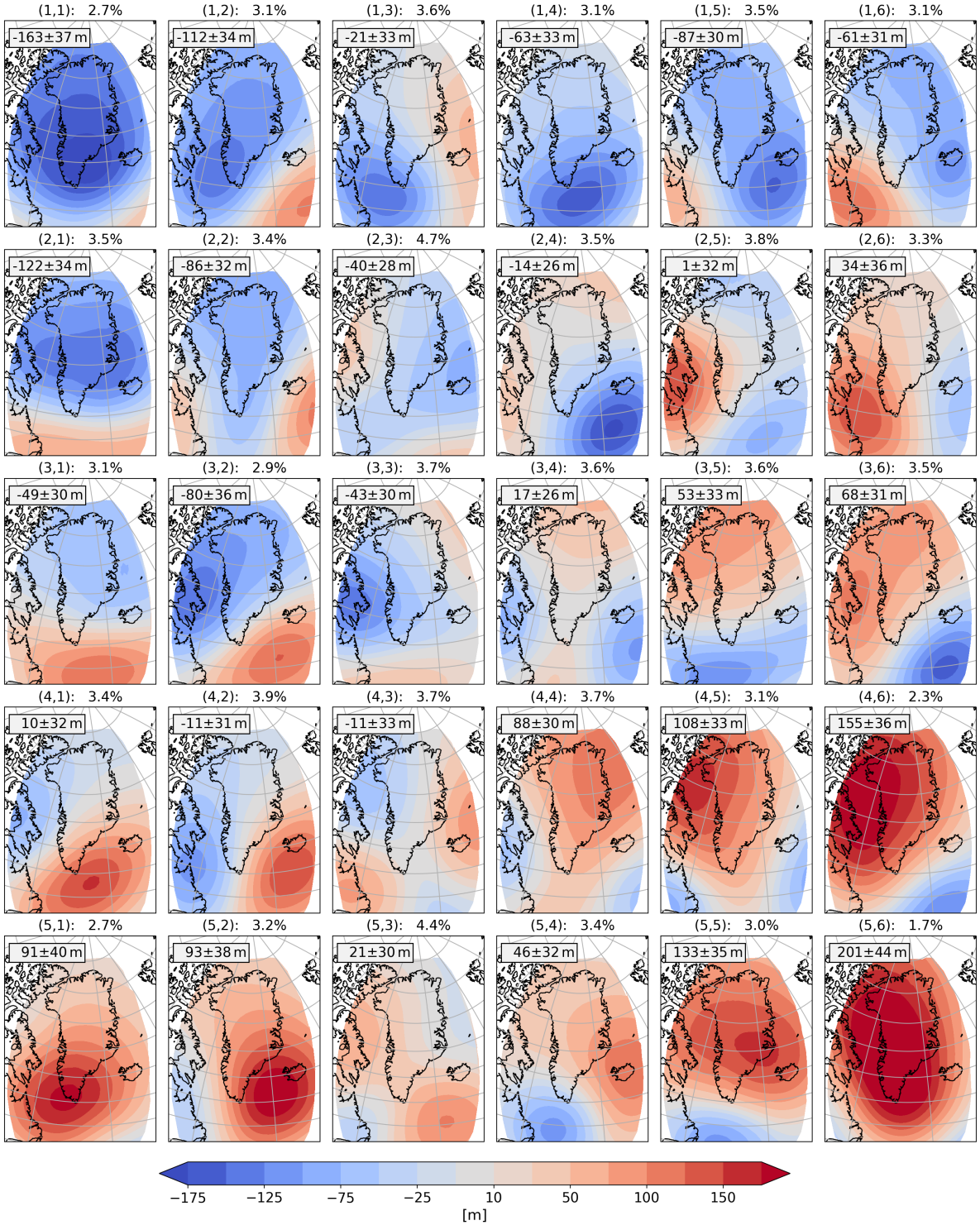

Figure 5.2: The 30 SOM nodes identified from daily $Z500'$ in JJA of the periods PD, MC, and LC (3×44 years). Shading shows $Z500'$. The title indicates the node number as (column,row) and the occurrence frequency over all 132 years. The mean and standard deviation of GrIS-wide average $Z500'$ ($Z500'_{GrIS}$) over all node days are indicated in the legend.

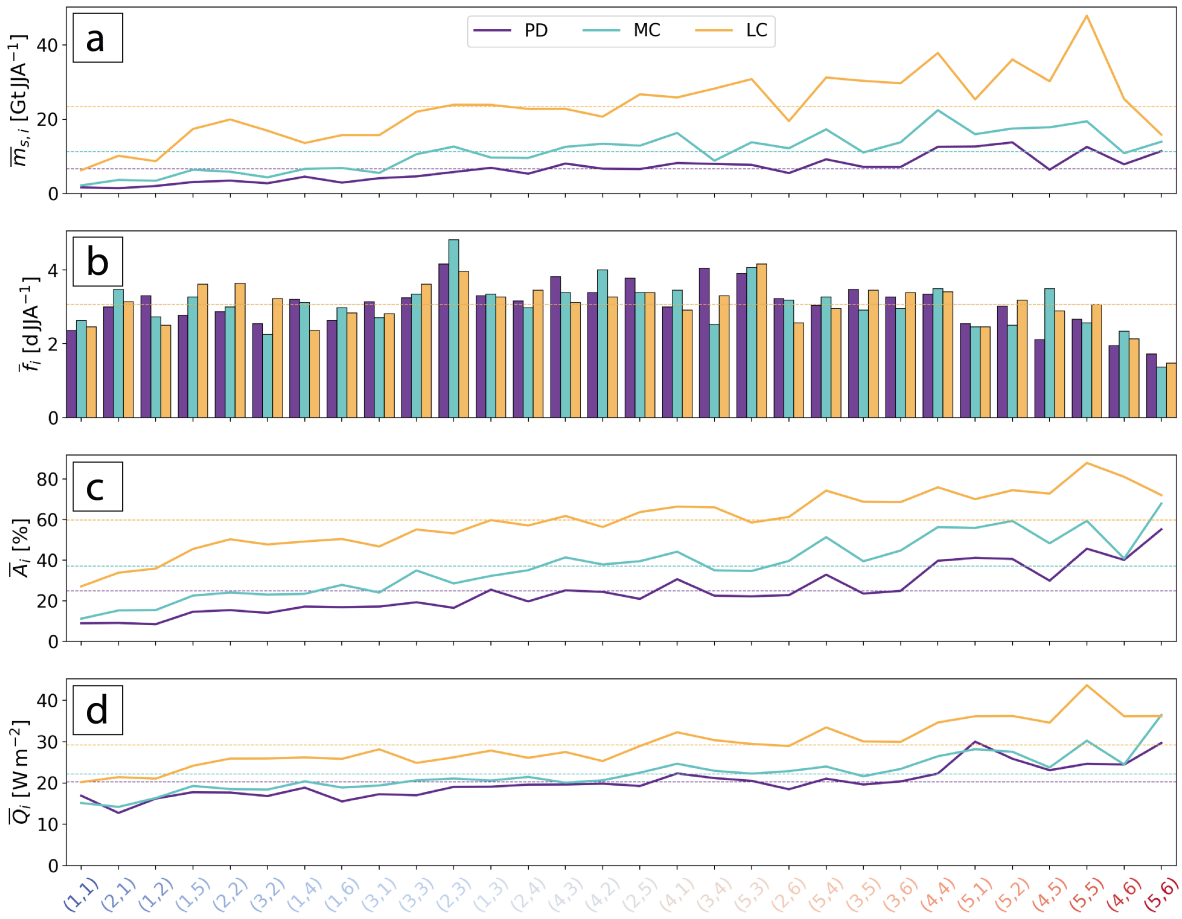

Figure 5.3: Node-average (a) summer melt ($\overline{m}_{s,i}$), (b) seasonal occurrence frequency ($\overline{f}_i$), (c) melt extent ($\overline{A}_i$), and (d) melt intensity ($\overline{Q}_i$) for node i in present-day (purple), mid-century (cyan), and late-century (yellow). The nodes are sorted from lowest (left) to highest (right) $Z500'_{GrIS}$. The respective $Z500'_{GrIS}$ is indicated by the label color (according to Fig. 5.2). Horizontal dashed lines denote (a,b) seasonal and (c,d) daily averages over all nodes.

The changing melt dynamics are strongly dependent on the SOM node. In PD, the node contributing most melt per season was (5,2) with $\overline{m}_s^{PD} = 13.8\,\mathrm{Gt\,JJA^{-1}}$ (Fig. 5.3a). In terms of $\overline{m}_{s,i}^{PD}$ scaled by $\overline{f}_{s,i}^{PD}$ (not shown), i.e., melt per node day, node (5,6) led to most melt in PD. Both nodes are characterized by positive $Z500'$ in the South of the GrIS and thus strong advection of air from lower latitudes directed towards the GrIS (Fig. 5.2). In LC, nodes (4,6) and (5,5) with the anticyclonic anomaly further north induce more melt per node day than (5,2) and (5,6), of which (5,5) is also responsible for the maximum summer total of $\overline{m}_s^{LC} = 47.9\,\mathrm{Gt\,JJA^{-1}}$ (Fig. 5.3a). More generally, circulation patterns with positive $Z500'_{GrIS}$ typically show a larger $\Delta\overline{A}_i$ and $\Delta\overline{Q}_i$ between PD and LC than cyclonically dominated nodes (Fig. 5.3c,d). Therefore, the importance of atmospheric circulation for variability in summer melt increases from PD (inter-node variability of $\sigma = 3.4\,\mathrm{Gt\,JJA^{-1}}$) to LC ($\sigma = 8.8\,\mathrm{Gt\,JJA^{-1}}$), which will be looked at further in Sect. 5.3.3. Interesting exceptions are (5,6) and (5,1), which are amongst those nodes with the highest $Z500'_{GrIS}$ and also with the highest $\overline{m}_{s,i}^{PD}$. The very weak increase in $\overline{m}_{s,(5,6)}$ is related to the low occurrence frequency of node (5,6), i.e., relatively few days contributing to

the summer melt total, and to a stagnation of $\overline{A}_{(5,6)}$ and $\overline{Q}_{(5,6)}$ between MC and LC (Fig. 5.3a-d). That is, during days in node (5,6) melt affects about the same fraction of the GrIS with the same average intensity in MC as in LC. The melt area becomes extensive for many nodes and exceptionally so for (5,5) and (4,6) with $\overline{A}^{LC}_{(5,5)} = 89\%$ and $\overline{A}^{LC}_{(4,6)} = 81\%$, i.e., almost the entire GrIS is melting during days in these nodes (Fig. 5.3c). Despite the smaller magnitude, the melt increase is also pronounced for nodes with mostly negative $Z500'$ over the GrIS (Fig. 5.3a). For example, node (1,1), which contributes the least melt in LC, still contributes $\overline{m}^{LC}_s = 6.3\,\mathrm{Gt\,JJA^{-1}}$. Lastly, changes in frequency are generally small and often opposing for neighboring nodes (Fig. 5.3b). For example, the decrease of node (1,2) from PD to LC ($\Delta\overline{f} = -0.8\,\mathrm{d\,JJA^{-1}}$) is counteracted by an increased occurrence frequency of neighboring, i.e., synoptically similar, nodes (1,1) and (2,2). We conclude that $\overline{m}^{LC}_{s,i}$ becomes large for all nodes, whereby nodes with high $Z500'_{GrIS}$ typically lead to most melt in PD and also in LC. Also, inter-node melt variability increases from PD to LC, i.e., atmospheric variability determines inter-annual variability in summer melt more strongly in LC (see also Sect. 5.3.3).

c) Decomposition of summer melt increase

We now combine the summed effects over all nodes on $\Delta\overline{m}_s$ of changes in node frequency (changing circulation), melt area, and melt intensity that were discussed above (using Eq. 5.8 in Sect. 5.2.5). The increase of $\Delta\overline{m}_s = +501\,\mathrm{Gt\,JJA^{-1}}$ from PD to LC is entirely attributable to changing melt area and melt intensity. The largest share of 50.9% to $\Delta\overline{m}_s$ comes from an increase in daily average melt area, which increases from 24% to 60% (Figs. 5.3c & 5.4c). At the same time, 16.6% of the melt increase ($+83\,\mathrm{Gt\,JJA^{-1}}$) is due to an intensification of melt, i.e., more melt energy available in the melt area of the GrIS (Fig 5.4c). As both quantities increase from PD to LC, there is a concurrent change, which contributes 23.6% to $\Delta\overline{m}_s$ and which quantifies the extra melt intensity over the additional melt area. These results can be understood better based on the following considerations. The increases in $\overline{Q}_i$ discussed in Fig. 5.3d contribute more strongly to the concurrent term (term (iv) in Eq. 5.8) than to the intensity term (term (iii)) because of the relatively large values of $\Delta\overline{A}_i$ compared to $\overline{A}^{PD}_i$ with which they are factorized, respectively (Sect. 5.2.5). Over all summer days, $\overline{A}$ increases from PD to LC by +147% (Fig. 5.3c,d). Hence, the concurrent area-intensity terms (iv) of the decomposition including $\Delta\overline{A}_i$ become larger than the intensity terms (iii) including $\overline{A}^{PD}_i$ (see Sect. 5.2.5). In contrast, $\overline{Q}$ over all node days increases only by +46% (Fig. 5.3d) and thus $\Delta\overline{A}_i$ more strongly contributes to melt induced by the area term than by the concurrent term (Fig 5.4c). Lastly, 8.3% of $\Delta\overline{m}_s$ can be attributed to an increasing covariance of A_d and Q_d. That is, large anomalies of A_d more often co-occur with large anomalies of Q_d. Reasons for this process are twofold: First, the variance of both quantities increases (not shown), likely because both quantities acquire larger values in LC compared to PD while still having daily values of zero. Therefore, larger anomalies occur in LC than in PD. Second, and possibly related to that, the correlation of A_d and Q_d increases as well (not shown). Lastly, changes in atmospheric circulation as well as all other contributions to $\Delta\overline{m}_s$ summarized in the residual E are negligible. That is, while atmospheric circulation is pivotal for the inter-annual variability of seasonal melt, circulation changes are largely irrelevant for its

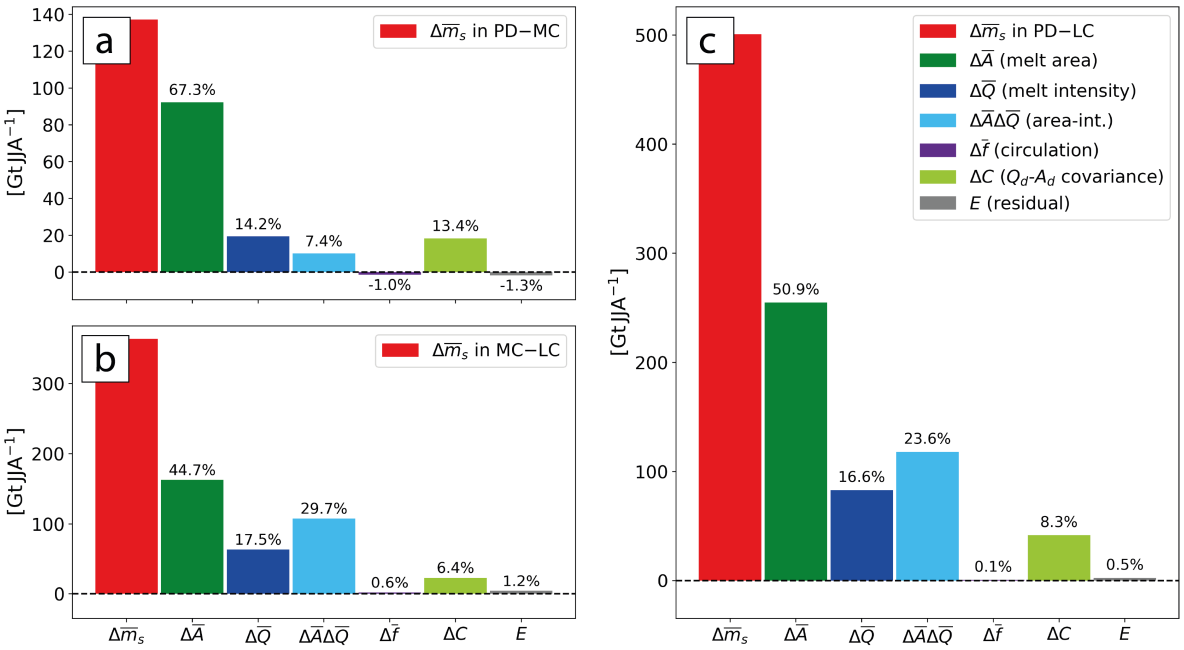

Figure 5.4: The decomposition of $\Delta\overline{m}_s$ from (a) PD to MC, (b) MC to LC, and (c) PD to LC into contributions from changes in melt area ($\Delta\overline{A}$), in melt intensity ($\Delta\overline{Q}$), in melt area and intensity combined ($\Delta\overline{A}\Delta\overline{Q}$), in atmospheric circulation ($\Delta\bar{f}$), in covariance between Q_d and A_d (ΔC), and in the residual E according to Eq. 5.8 (Sect. 5.2.5). Numbers indicate the contributions relative to the respective $\Delta\overline{m}_s$.

response to global warming. After further investigating the response of seasonal melt to global warming, we will revisit the role of inter-annual variability for seasonal melt in LC in Sect. 5.3.3.

The decomposition sheds further light on the previously mentioned acceleration of melt from the first to the second half of this century, as well as the changing importance of individual contributions to $\Delta\overline{m}_s$ (Fig 5.4a,b). First of all, $\Delta\overline{m}_s = +137\,\mathrm{Gt\,JJA^{-1}}$ between PD and MC increases to $\Delta\overline{m}_s = +364\,\mathrm{Gt\,JJA^{-1}}$ between MC and LC. Moreover, the relative contribution to $\Delta\overline{m}_s$ from the area term is larger from PD to MC (67.3%) than from MC to LC (44.7%; Fig 5.4a,b). Instead, the increase of the concurrent term becomes much more important in the second half of this century, causing 29.7% of the extra melt from MC to LC (Fig 5.4b). This is because the nonlinear effect of two strongly increasing quantities becomes disproportionally larger the larger the individual quantities are. Melt intensification further becomes more important in absolute and relative terms from MC to LC compared to from PD to MC, but contributes less than the concurrent term in the latter period (Fig 5.4a,b). As discussed in the previous paragraph, a large share of the concurrent term relates to melt intensification rather than an increase in melt area. This effect is illustrated in the Appendix (Fig. C.1): When computing the decomposition directly between MC and LC the share of melt intensification to $\Delta\overline{m}_s$ is 26.5% instead of 17.5% (Figs. C.1 & 5.4). The area term increases slightly when using this method (49.1% instead of 44.7%) but much less than the intensity term.

To summarize, GrIS melt will strongly increase, mainly due to an increase in melt area and an intensification of melt. While the increase in melt area is particularly important during the first half of this century, the melt intensification becomes more relevant during the second half of this century. Changes in atmospheric circulation, at least those simulated by CESM2, do not contribute significantly to changes of the mean melt between the periods. To better understand the decomposition, we will, in the following, investigate the melt contributions as well as their spatial patterns over the GrIS for all nodes individually.

5.3.2 Melt dynamics of different circulation patterns

a) Decomposition of summer melt increase

The contribution of all processes to $\Delta\overline{m}_s$ between PD and LC for every node individually are displayed in Fig. 5.5. The average increase in summer melt per node varies between $\Delta\overline{m}_{s,(5,6)} = +4.4\,\mathrm{Gt\,JJA^{-1}}$ and $\Delta\overline{m}_{s,(5,5)} = +35.3\,\mathrm{Gt\,JJA^{-1}}$ (see also Fig. 5.3a). As for their total, the main determinant of $\Delta\overline{m}_{s,i}$ is $\Delta\overline{A}_i$ for every node, especially for the cyclonically dominated nodes in the upper (left) part of the SOM map (Figs. 5.2 & 5.5). That is, the expanding melt area contributes most to the melt increase in this century, and particularly much during cyclonic circulation patterns. Melt intensification becomes almost equally important for nodes with southerly flow anomalies and/or large positive $Z500'_{GrIS}$, e.g., (4,4), (5,5), and (5,6). Recall from Figure 5.3a that the anticyclonic nodes (5,6) and (5,1) have unusual, below-average increases in melt. The slight reduction in occurrence frequency does not explain the smallest $\Delta\overline{m}_{s,(5,6)}$ (Fig. 5.5). Rather, the contributions of $\Delta\overline{A}_{(5,6)}$, $\Delta\overline{Q}_{(5,6)}$, and thus also of their concurrent change are limited compared to other nodes. So despite the prevalent anticyclonic conditions over Greenland in (5,6), neither the melt area increases significantly nor the melt intensity. Further, despite simulated circulation shifts of up to $\Delta\overline{f}_i \approx +0.8\,\mathrm{d\,JJA^{-1}}$, i.e., about a third of $\overline{f}_i^{PD}$ (Fig. 5.3b), the associated contributions to $\Delta\overline{m}_{s,i}$ are much smaller than those from the area and intensity terms for all nodes. Only for nodes (4,5) and (5,5), there is a noteworthy positive contribution to increasing melt by a larger occurrence frequency of $+2.4\,\mathrm{Gt\,JJA^{-1}}$ and $+1.9\,\mathrm{Gt\,JJA^{-1}}$, respectively (Fig. 5.5). This contribution of changing circulation, however, is offset by the reduced occurrence frequency of nodes that show similar increases in $\overline{m}_{s,i}$, namely (3,4), (4,3), and (5,6). Hence, the total effect of changing occurrence frequencies over all nodes is negligible (Sect. 5.3.1) because there is no shift from weak to strong melting nodes, or vice versa, but rather within nodes with similar melt increases. Lastly, a larger covariance between (daily) A_d and Q_d is contributing substantially for nodes with negative or near-zero $Z500'_{GrIS}$ (Figs. 5.2 & 5.5). The spread of A_d and Q_d increases, as flow anomalies of these nodes can go along with very extensive and intense melt while relatively low A_d and Q_d are still possible in these nodes during the LC period, e.g., early in JJA.

In summary, nodes with positive $Z500'$ over and near Greenland typically cause a larger $\Delta\overline{m}_{s,i}$ than those with negative $Z500'$. An exception to this rule are nodes (5,1) and (5,6), which feature intense melt already in PD, and which do not increase their melt as dramatically as other

anticyclonic nodes. The increases in melt area and intensity also dominate $\Delta\overline{m}_{s,i}$ at the node level, while the simulated circulation changes are only for a few nodes of relevance (but their effect cancels when summing over all nodes). We will, therefore, focus on the spatial patterns of the melt area and intensity changes over the GrIS to understand their varying importance for different nodes in the next subsection.

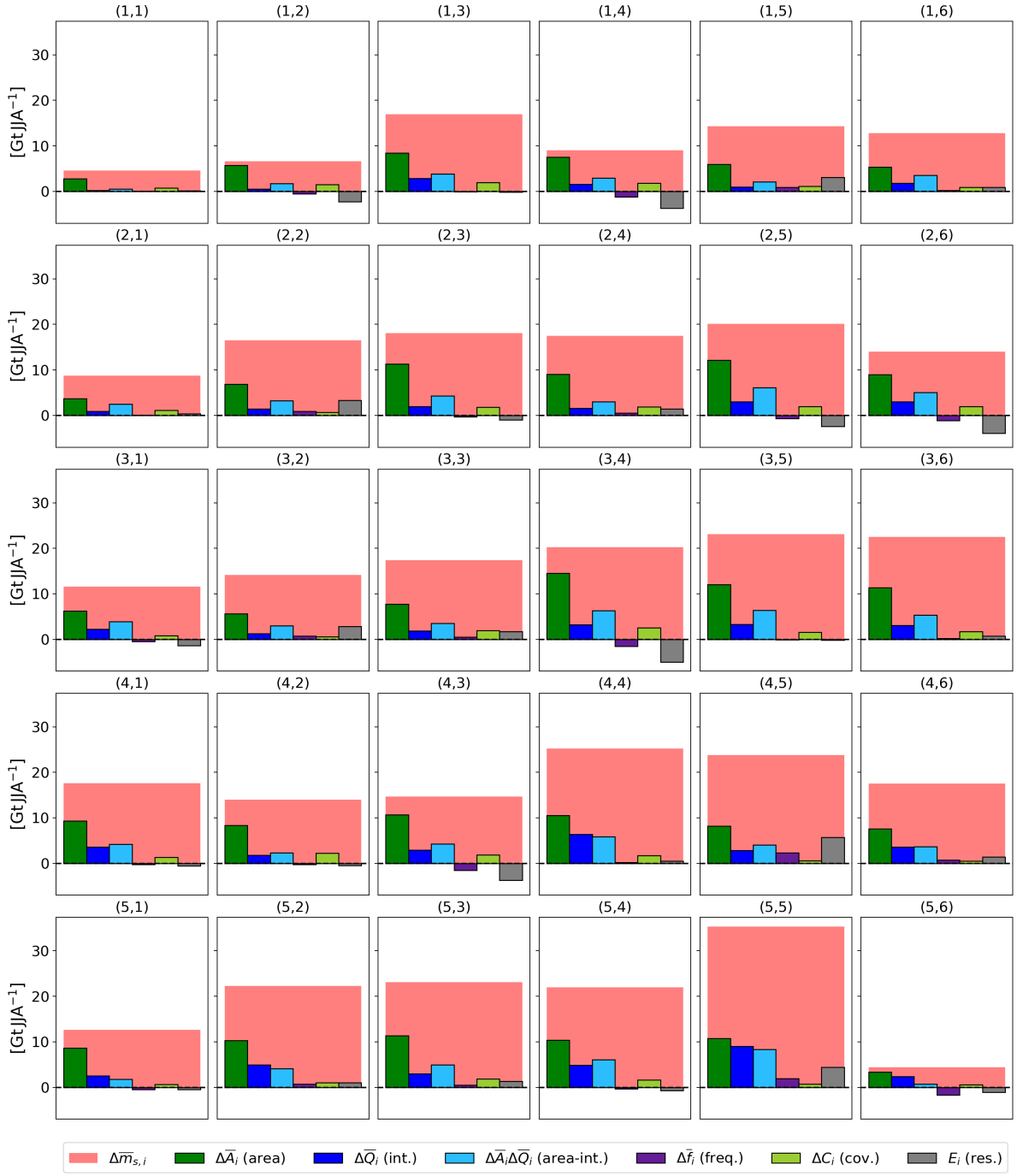

Figure 5.5: The decomposition of $\Delta\overline{m}_{s,i}$ for every node i between PD and LC. That is, the same decomposition as in Fig. 5.4c (for $\Delta\overline{m}_s$) but for the melt increase of every SOM node (Fig. 5.2) individually. The $\Delta\overline{m}_{s,i}$ is shown as wide red bar on top of the individual contributions.

b) Spatial patterns of increasing melt extent and intensity

To better understand the large differences in this century's melt increase for different SOM nodes, we investigate the spatial patterns of melt extent and intensity in each node as well as the changes in these spatial patterns (Figs. 5.6 & 5.7; Appendix Figs. C.2-C.7). To investigate the effect of an increasing melt area spatially, Fig. 5.6 shows maps of the change in average melt frequency in node i ($\Delta\overline{\omega}_i$) minus that in all days ($\Delta\overline{\omega}$). On average over all days, there is a pronounced increase in $\overline{\omega}$ everywhere, from 10% in the GrIS Summit region to 40–50% around 2'000 m (Fig. 5.6 top right panel). At the lowest elevations, $\overline{\omega}$ is again below 30% due to a "satuarion" effect, i.e., melt persists almost continuously throughout JJA in LC. Note that deviations for individual nodes from $\Delta\overline{\omega}$ are mostly smaller than $\Delta\overline{\omega}$ itself, i.e., there is a substantial change occurring irrespective of the atmospheric variability (Fig. C.4). Nevertheless, $\Delta\overline{\omega}_i$ is strongly pronounced at lower elevations for nodes with a northerly flow anomaly and such with mostly negative $Z500'$ – e.g., (1,2), (1,5), (2,1), (2,3), and (2,4). This pattern can be related to a uniform warming, which increases $\overline{\omega}_i$ values at and below the zero degree altitude, except for regions hit by the northerly flow anomaly, e.g., the northern GrIS in (1,6). For some cases, it seems that downslope Foehn winds additionally contribute to more positive $\Delta\overline{\omega}_i$ in the lee of the cyclonic flow anomaly, e.g., in the western GrIS for nodes (1,1), (1,2), and (1,3). Conversely, nodes with positive $Z500'_{GrIS}$ and/or with southerly flow anomalies increase $\overline{\omega}_i$ most strongly at higher elevations – for example (4,4) (4,6), (5,2), (5,4), and (5,5). In these nodes, melt reaches high elevations of the GrIS frequently and lower elevations partly reach the previously mentioned melt saturation. The exceptionally low increases in melt during nodes (5,1) and especially (5,6) can at least partially be explained by below average increase in $\overline{\omega}$ due to melt saturation at low elevations and on the southern GrIS (Fig. 5.6). Furthermore, $\overline{\omega}_{(5,6)}$ in LC remains at PD values of around 50% for large parts of the accumulation area, meaning that $\overline{\omega}_{(5,6)}$ is limited by other factors than climate warming during GrIS-centered positive $Z500'$ (Figs. C.2-C.4). Lastly, flow anomalies that advect air from lower latitudes cause above-average values of $\Delta\overline{\omega}_i$ in the regions hit by the respective flow direction, e.g., the central and northwestern GrIS in nodes (1,3) and (5,4). To summarize, $\Delta\overline{\omega}$ depends on the atmospheric circulation pattern ($Z500'$ and flow direction/origin) with the constraint of a melt saturation effect and a substantial increase that occurs irrespective of the circulation pattern.

While the increase in $\overline{\omega}_i$ is pronounced all over the GrIS and for every node, some parts of the GrIS experience a very weak increase or even slight decrease in $\overline{Q}_i$ for some nodes (Fig. 5.7). Over all days, the increase in $\overline{Q}$ is largest with up to +50 W m^{-2}, reaching more than 75 W m^{-2}, at the lowest elevations of the southwestern GrIS (top right panel in Figs. 5.7 & C.7). Further, considering all days, $\overline{Q}$ decreases nowhere on the GrIS. For some nodes, however, melt becomes regionally less intense, e.g., during node (1,6) with northwesterly flow anomalies. For this node, $\Delta\overline{Q}_{(1,6)} < 0$ over parts of the high accumulation area with values of around -10 W m^{-2} (Figs. C.5-C.7). Also for nodes (1,1), (1,3), (2,2), (2,4), and (3,2), there are highly elevated regions with negative $\Delta\overline{Q}_i$ (Figs. 5.2 & 5.7). However, note that, importantly, the composites of $Z500'$ for node days in PD and LC are different from the SOM nodes identified from all three time periods,

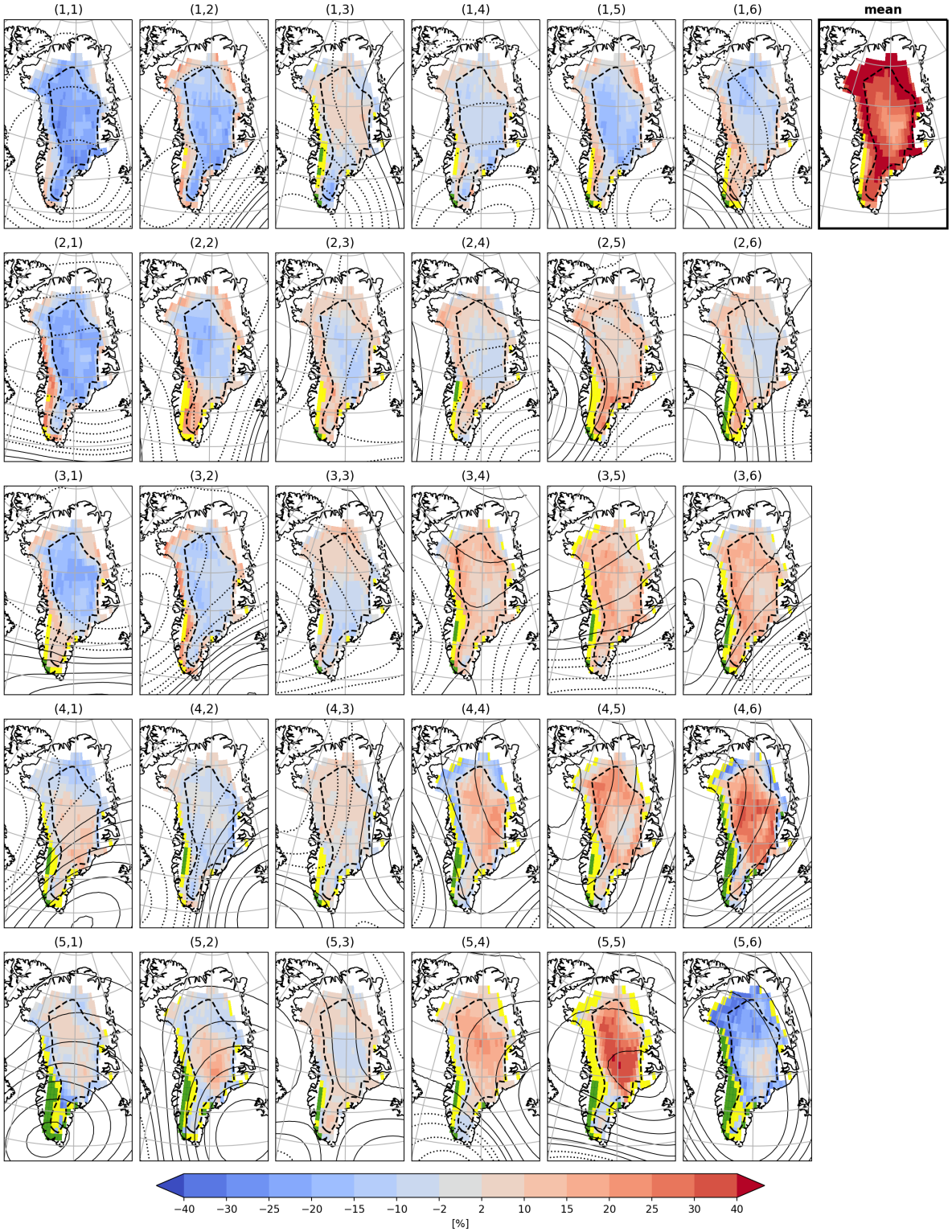

Figure 5.6: The top right panel shows the mean change in melt day frequency from PD to LC ($\Delta\overline{\omega}$). The other panels illustrate the change in each node relative to the mean change ($\Delta\overline{\omega}_i - \Delta\overline{\omega}$). Green (yellow) shading denotes grid cells with $\overline{\omega}^{PD} > 95\%$ ($\overline{\omega}^{LC} > 95\%$). Dotted (solid) black lines show negative (positive) $Z500'$ contours according to Fig. 5.2. The dashed line denotes 2'200 m elevation.

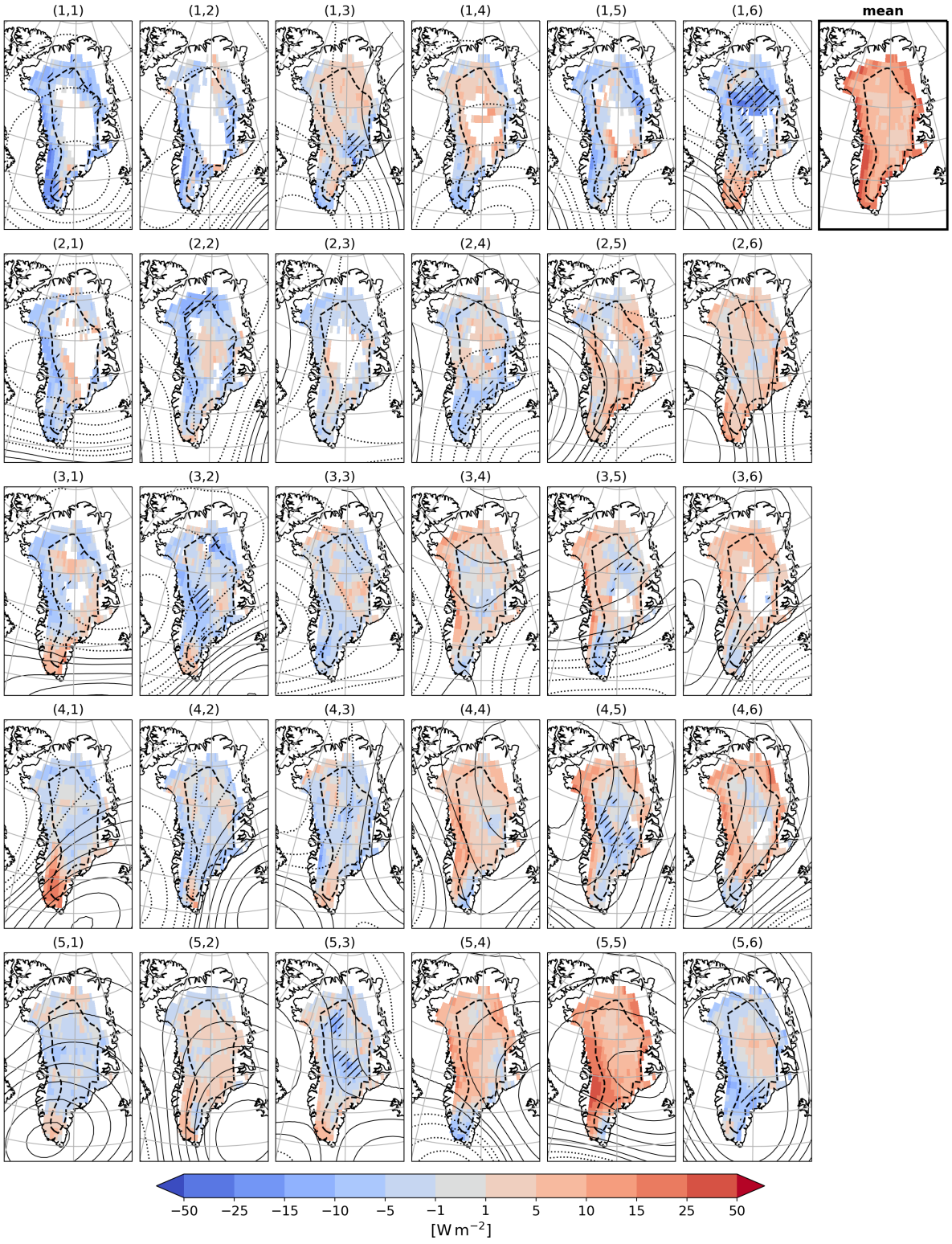

Figure 5.7: The same as Fig. 5.6 but for the change in node average melt intensity $\Delta\overline{Q}_i$ minus the overall average $\Delta\overline{Q}$ (shown in the top right panel) in PD to LC. Moreover, hatching denotes grid cells that show a negative $\Delta\overline{Q}_i$. Grid cells that never experience melt in PD and/or LC are masked. Dotted (solid) black lines show negative (positive) $Z500'$ contours according to Fig. 5.2.

which might explain some spatial shifts of weak melt intensity (Appendix Figs. C.8 & C.9). For example, the cyclonic flow anomaly east of the GrIS in node (1,6) is notably stronger in LC compared to PD, which might explain why stronger cold-dry northerly flow anomalies reduced the downward longwave radiation in LC compared to PD, as such radiative anomalies are the most important contribution to $\overline{Q}$ in the high accumulation area (e.g., Bennartz et al., 2013; Wang et al., 2019). Furthermore, some of the relevant $\overline{Q}_i^{PD}$ values at the highest elevations are based on comparably few days with melt, i.e., $T_s \geq 272.15\,\mathrm{K}$ (Fig. C.2). In contrast to negative $\Delta\overline{Q}_i$, wherever southerly flow anomalies impinge on the GrIS topography, e.g., in the Southwest for nodes (4,1) and (5,2), melt intensifies strongly from PD to LC (Fig. 5.7). Moreover, the two anticyclonic nodes with a relatively weak melt increase have below average $\Delta\overline{Q}_{(5,1)}$ and $\Delta\overline{Q}_{(5,6)}$ over large parts of the GrIS. This means that several other nodes show a larger $\overline{Q}_i^{LC}$ thanks to a more pronounced intensification over this century (Figs. C.5-C.7). These considerations highlight that the intensification of melt is not uniform over all nodes and thus those nodes with largest melt intensity today are not the most intense in the future (Fig. 5.3d). In contrast to the change in melt frequency, some regions show a decrease in melt intensity for some circulation patterns. The later, however, might be explained by methodologically induced intra-node differences between days in PD and LC rather than physical changes (see also Sect. 5.4).

5.3.3 Relevance of atmospheric variability for summer melt in the late-century

We conclude the result section by assessing the relevance of atmospheric variability for GrIS summer melt in LC. So far, we have discussed that (i) atmospheric variability is a strong determinant of $\overline{m}_s$ in PD (Sect. 5.1), and (ii) atmospheric circulation changes do not lead to significant $\Delta\overline{m}_s$ towards LC (Sect. 5.3.1c). The increase in $\overline{m}_s$ from $200.6\,\mathrm{Gt\,JJA^{-1}}$ in PD to $701.6\,\mathrm{Gt\,JJA^{-1}}$ in LC is accompanied by a more than two-fold increase in the standard deviation of $\sigma(m_s) = 61.4\,\mathrm{Gt\,JJA^{-1}}$ to $\sigma(m_s) = 130.6\,\mathrm{Gt\,JJA^{-1}}$. This increase in inter-annual melt variability is due to a larger spread in the melt produced by the different SOM nodes, i.e., during different atmospheric circulation patterns (Sect. 5.3.1b). Consequently, atmospheric variability becomes a more important determinant of seasonal m_s variability in LC.

Figure 5.8 illustrates the distribution of SOM nodes in four summers in LC, which exert the two lowest (Fig. 5.8a,b) and highest (Fig. 5.8c,d) m_s. This so-called substructure indicates that during the two summers with exceptionally low m_s^{LC}, nodes that cause little melt and that relate to strongly negative $Z500'_{GrIS}$ are particularly frequent. For example, node (1,1), which exerts the lowest $\overline{A}_i$ and $\overline{Q}_i$ among all nodes (Fig. 5.3c,d), is almost twice as frequent as all other nodes in the year with lowest m_s^{LC} (Fig. 5.8a). At the same time, there are only 17 out of 92 summer days with positive $Z500'_{GrIS}$, which are, however, attributed to anticyclonic nodes with comparably low $\overline{A}_i^{LC}$ and $\overline{Q}_i^{LC}$, e.g., (3,6), (4,5), and (5,3) (Fig. 5.3a). This is similar for the year with second-lowest m_s^{LC}, where anticyclonic nodes are slightly more frequent (Fig. 5.8b). Conversely, summers with very high m_s^{LC} can arise, e.g., due to the absence of cyclonic $Z500'_{GrIS}$ (Fig. 5.8c) or due to the high occurrence frequency of nodes with particularly intense and extensive melt (Fig. 5.8d). In the year with highest m_s^{LC}, nodes (4,4) and (5,2) with high $\overline{A}_i$ and

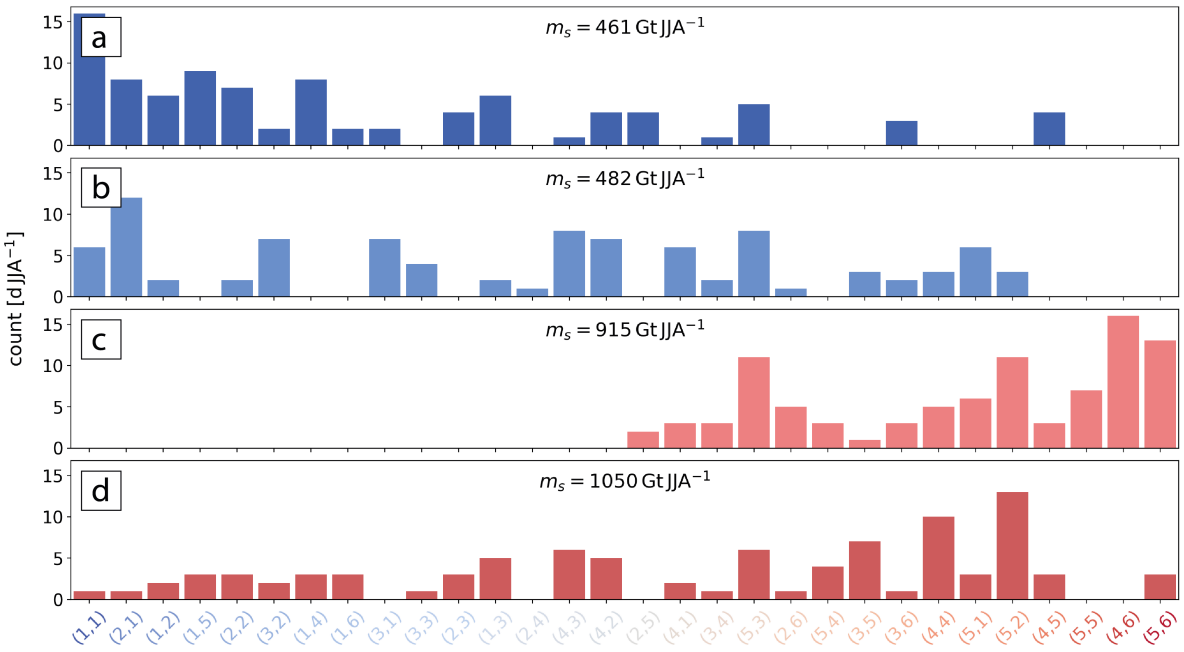

Figure 5.8: The count of days attributed to the 30 SOM nodes for the JJA with (a) lowest, (b) second-lowest, (c) second-highest, and (d) highest melt in LC (m_s^{LC}), which is indicated in the panel title. The nodes are sorted from lowest (left) to highest $Z500'_{GrIS}$ (right). The respective $Z500'_{GrIS}$ is indicated by the label color (according to Fig. 5.2).

$\overline{Q}_i$ account for a quarter of all summer days (Fig. 5.8d). Note that, importantly, the clustering of days in individual nodes does not change significantly between PD and LC (not shown), which thus is not the cause for the increasing $\sigma(m_s)$. In summary, these four examples clearly demonstrate how atmospheric variability shapes the JJA season's substructure at the example of summers with extremely low and high m_s^{LC}. Summer melt is greatly shaped by the absence and presence of individual circulation patterns in all three time periods, which are particular either in their occurrence frequency or in their melt characteristics. Due to the differential $\Delta\overline{m}_{s,i}$ with mostly stronger increases for anticyclonic nodes than for cyclonic nodes, the inter- as well as intra-annual variability of m_s increases from PD to LC.

5.4 Discussion

In this study we focus on the upper-elevation zone ($\geq 1'200$ m) of the GrIS and study the causes of changing melt. Even in the upper-elevation zone, the CESM2 underestimates $\overline{m}_s$ compared to 2005–2015 values obtained from the MAR RCM (Fig. 5.1). We hypothesize that this relates in part to the frequent high-melt years in the validation period (2007, 2010, and 2012), which are not captured by our free-running CESM2 simulations (Fettweis et al., 2020). This is supported by the fact that CESM2 realistically simulates the GrIS surface energy balance, which we use to compute $\overline{m}_s$, in 1979–1999 (van Kampenhout et al., 2020). Additionally, the computation of Q at 1° resolution is likely inferior to estimates from downscaled melt estimates using an RCM or an ice sheet model at higher resolution (e.g., Noël et al., 2020; van Kampenhout et al.,

2020). Finally, smaller parts of the melt underestimation could relate to melt that occurs at $T_s < 272.15\,\mathrm{K}$ throughout the day (which we do not consider part of the melt area) or that results from the rain heat flux (Fausto et al., 2016), which is ignored here and likely becomes more important with an upward extension of the zero degree altitude in MC and LC. Given our computation of Q, however, considering upper-elevation zone melt only is also advantageous as we exclude the regions that are increasingly affected by the melt-elevation feedback in this century (Muntjewerf et al., 2020), i.e., which call for a model with dynamic GrIS topography (Le clec'h et al., 2019). All in all, it is important to highlight that the results of this chapter are valid for a substantial share of the increase in $\overline{m}_s$ between PD and LC ($+501\,\mathrm{Gt\,JJA^{-1}}$), but extra melt from today's ablation area is not analyzed. Consequently, the results on the importance of changing melt extent, melt intensity, and atmospheric circulation most likely differ for the lower GrIS.

A key finding of this chapter is that changes in the atmospheric circulation (characterized by the frequencies of the 30 SOM nodes) contribute very little to changes in melt, despite the unequivocal importance of atmospheric circulation for inter-annual variability in melt. In fact, there are nodes that occur much more frequently in LC compared to PD and induce an above-average amount of melt in LC. For example, node (4,5) becomes +36% more frequent, however, this dynamical effect only contributes 10% to $\Delta\overline{m}_{s,(4,5)}$ (Figs. 5.3a,b & 5.5). Hence, even for circulation patterns that become more/less frequent, the frequency change effect on melt is outweighed by the extension and intensification of melt. Moreover, over all nodes, these partly substantial changes in node occurrence frequency occur between nodes with similar $\Delta\overline{m}_{s,i}$. Accordingly, Mioduszewski et al. (2016) found that 75% of the melt increase since the 1980s arose due to melt intensification and expansion, despite the exceptional anticyclonic conditions in the early 2000s. These and our results qualify the findings of, e.g., Delhasse et al. (2018) and Delhasse et al. (2021) to some extent, which underline the inability of current GCMs to accurately model atmospheric circulation relevant for GrIS melt. We rather highlight the comparably larger potential of Q and A modifications in this century as Hofer et al. (2019). Important changes with global warming that foster the strong extension and intensification of melt are the intensifying melt-albedo feedback (Box et al., 2012), increasing rainfall (Box et al., 2022a), and potential increases in sensible heat fluxes and downward longwave radiation from a warmer and moister atmosphere (Franco et al., 2013; Izeboud et al., 2020; Wang et al., 2021). Lastly, although simulated circulation changes do not contribute significantly to changes in $\overline{m}_s$, atmospheric variability becomes increasingly important for inter-annual variability in $\overline{m}_s$. This is because increases in $\overline{m}_{s,i}$ are node-dependent, and particularly pronounced for nodes that already exert large $\overline{m}_s^{PD}$. This indicates that not only the expansion of the ablation area becomes increasingly important for the GrIS surface mass balance (SMB) (Fyke et al., 2014), but also melt intensification in the upper-elevation zone. Therefore, it remains crucial to understand how atmospheric variability modifies the ongoing intensification of melt, i.e., to investigate how upper-elevation GrIS melt changes during different SOM nodes. Furthermore, in addition to the node day distribution in one JJA season (Sect. 5.3.3), future research should consider

different sequences of daily atmospheric circulation patterns, which greatly affect the impact on surface melt (Box et al., 2022a).

This chapter for the first time separates the so-called "thermodynamic" $\Delta\overline{m}_s$, i.e., that independent of circulation changes (Mioduszewski et al., 2016), directly into contributions from $\Delta\overline{A}$ and $\Delta\overline{Q}$ for different circulation patterns. The increasing melt extent is by and large elevation dependent: The lowest parts of the considered GrIS melts continuously in JJA in LC, while the GrIS interior remains spared from melt during several weeks. Melt intensification is strongest below 2'000 m and locally more dependent on the prevailing circulation than $\Delta\overline{A}$. The intensification is strongest during anticyclonic circulation regimes and over the southern and western GrIS, when warm air advection and enhanced solar radiation favor melt feedbacks (Bennartz et al., 2013; Fausto et al., 2016; Hermann et al., 2020; Box et al., 2022a). Studies considering the entire GrIS often attribute melt intensification to shortwave radiation and sensible heat fluxes (e.g., Franco et al., 2013), which is mainly due to their impact on ablation area melt (Wang et al., 2021). This likely differs for the upper-elevation zone considered here, where longwave forcing from liquid clouds and moist-warm air is highly relevant in PD (Bennartz et al., 2013; Mioduszewski et al., 2016; Wang et al., 2019). Below-average or even negative changes in melt intensity from PD to LC occur for some nodes and mainly at high elevations towards which the flow anomaly is directed. A reduction in melt intensity with global warming might occur locally. However, potential explaining factors at a large scale are unlikely, as increased snowfall at higher elevations has a subordinate impact on the absorbed melt energy (Lenaerts et al., 2020), and reductions in downward longwave radiation contradict the expected increase of liquid clouds and warmer and moister air (Hofer et al., 2019). Rather, as a result of identifying SOM nodes over all three time periods, the composite of $Z500'$ for individual periods slightly differ from one another, and are at least partly able to explain spatial shifts of $\overline{Q}$ from PD to LC, i.e., $\Delta\overline{Q}$. In summary, the increase in melt day frequency over the GrIS is more uniform than the intensification of melt, where further research is needed to confirm and better understand the spatial patterns in 21st century changes found here.

In addition to not accounting for the entire GrIS melt, the methods applied in this chapter are limited in the following ways. First, the decomposition applied here essentially constitutes a linearization of $\overline{m}_s(\overline{A}_i(t), \overline{Q}_i(t), \overline{f}_i(t), ...)$ at $t = \text{PD}$, where the derivatives are approximated by forward differences, e.g. $\Delta\overline{A}_i = \overline{A}_i(LC) - \overline{A}_i(PD)$. Naturally, such a linearization only allows attributing a large fraction in $\Delta\overline{m}_s$ to changes in melt area, melt intensity, and atmospheric circulation as long as these changes are small compared to the respective values in PD. In particular when decomposing the melt increase between PD and LC, $\Delta\overline{A}_i$ relative to $\overline{A}_i^{PD}$ are not small and nonlinear terms such as the concurrent terms including $\Delta\overline{A}_i \cdot \Delta\overline{Q}_i$ attain rather large magnitudes (Fig. 5.4c). Similarly, when considering individual nodes instead of the sum over all nodes, the residual term E_i partially contributes a lot to $\Delta\overline{m}_{s,i}$ as it includes further concurrent changes. Second, we use a single GCM ensemble to model $\Delta\overline{m}_s$. Although CESM2 is among the best-performing GCMs regarding the GrIS climate (van Kampenhout et al., 2020;

Noël et al., 2020), multi-model ensembles better capture the full atmospheric and ice sheet variability in the GrIS region (Belleflamme et al., 2013; Fettweis et al., 2020). Lastly, we highlight that the presented framework of assessing the importance of individual drivers of $\Delta\overline{m}_s$ could be fully exploited when using daily output of higher-resolved RCM coupled to several GCM projections. This data would not only more accurately represent the GrIS melt (Fettweis et al., 2020), but also allow to study the PD ablation area and additional determinants of the GrIS SMB such as refreezing and runoff during individual circulation patterns. The latter is particularly interesting, as we do not separate melt that refreezes from melt that runs off, which is an important hydrological determinant of GrIS mass loss (e.g., Noël et al., 2022). Hence, the limitations of this chapter constitute clear ideas for insightful future research.

5.5 Conclusions

In this chapter, we have used a four-member ensemble of CESM2 simulations (SSP3-7.0) to study the $\Delta\overline{m}_s = +501\,\mathrm{Gt\,JJA^{-1}}$ increase in GrIS summer melt from the upper ($\geq 1'200\,\mathrm{m}$) GrIS from PD (2005–2015) over MC (2045–2055) to LC (2085–2095), and examined how much changes in circulation, in melt area, and in melt intensity contribute to this projected melt increase. We use the SOM method on daily 500 hPa geopotential height anomalies ($Z500'$) to identify 30 atmospheric circulation patterns that serve as a basis for attributing $\Delta\overline{m}_s$ to the three main processes. First, there is a more than twofold acceleration of the melt increase between the first and second half of this century. The overall $\Delta\overline{m}_s$ between PD and LC comes entirely from what is sometimes referred to thermodynamic processes, namely increasing melt area (51%), increasing melt intensity (17%), their concurrent effect (24%), and a stronger covariance of the two measures on the daily timescale (8%). Melt intensification becomes increasingly important over the course of this century. Although there are substantial changes in occurrence frequency of some nodes, the melt increase due to changes in circulation is always smaller than the thermodynamic ones, and the total effect over all nodes almost completely cancels out. While the exact proportions may differ for other models, or for future models that better capture the atmospheric circulation relevant to GrIS melt (Delhasse et al., 2021), the thermodynamic effects are likely to dominate the melt increase in this century regardless of the model used.

Due to the dominance of increasing melt area and melt extent, $\overline{m}_s$ increases during every circulation pattern. However, in flow situations with anticyclonic circulation anomalies, melt increases most strongly in this century, via an intensification of melt at lower elevations and an upward extension of melt frequency. Exceptions are anticyclonic circulation patterns that regionally reach a limit in melt intensity or melt extent already during PD or MC. The highest daily melt in PD occurs when the strong anticyclonic $Z500'$ is located to the south of the GrIS, while a more northerly position of the flow anomaly favors the highest daily melt in LC. During cyclonic circulation anomalies, the melt frequency increases strongly, especially at lower elevations, while the melt intensifies less than averaged over all days. Although the extension of the melt area increases summer melt the most, the inter-node variability in melt is strongly shaped by

the variation in melt intensity.

Our analyses suggest that the long-term trend in $\overline{m}_s$ is driven by an intensification and an extension of melt. In contrast, atmospheric circulation drives the inter-annual variability of m_s, more strongly so towards the end of this century. Due to various feedback mechanisms, a deeper understanding of the drivers of melt intensification as well as of the sequencing of circulation patterns over the summer season is crucial. This chapter provides and applies a framework to a single GCM ensemble, which – ideally combined with RCM data – improves our physical understanding of the accelerating GrIS mass loss.

Chapter 6

Conclusion and outlook

6.1 Highlights

We motivated this thesis in Chapter 1 by highlighting the importance of seasonal atmospheric variability with respect to three aspects of the Earth system: European forest vitality, extremely high vapor pressure deficit (VPD) potentially driving vegetation water stress, and the projected increase in surface melt of the Greenland Ice Sheet (GrIS) that will contribute substantially to global sea-level rise. Amongst others reasons, the profound impact of global warming on terrestrial ecosystems and GrIS melt is due to the fact that seasonal meteorology is rapidly moving out of its historical niche. Therefore, understanding these systems today and how they will change with further global warming is an important step towards developing preparedness and adaptation strategies. A fundamental challenge when studying seasonal timescale climate extremes is that there are only very few meteorological and climatological phenomena at this timescale. We thus adopted, the "weather perspective" to understand how shorter-term variability aggregates over seasons to shape these three components of the Earth system. We highlight the most important findings of each result chapter by answering the three overarching research questions posed in Chapter 1:

1. **What were meteorological precursors of reduced forest vitality in Europe in the summers of the past two decades?**

As an indication of reduced forest vitality, we identified persistent (seasonal) and widespread (50 km) low-forest-greenness events in Europe in the summers of 2002–2022 from the remotely sensed Normalized Difference Vegetation Index (NDVI; Chapter 3). We are the first to quantify the impact of the 2022 European summer (the hottest on record) on forest vitality, which, according to our criteria, negatively affected 37% of temperate and Mediterranean forest regions. The adverse impact on forest greenness was thus more extensive than in any other summer in 2002–2022. Through regionally pooling low-NDVI events of all years across the temperate and Mediterranean biomes, and by accounting for the uneven distribution of events across the study period, we identified so-called meteorological precursors of these events. That is, meteorological

signals in the preceding 3 years that are systematically shared among the low-NDVI events and that deviate in a statistically significant manner from climatology.
The low-NDVI events occurred in particularly dry and hot summers, but their meteorological histories also featured other meteorological precursors, with clear differences between the temperate and Mediterranean biome. A key feature is the anomalous accumulation of dry periods (i.e., periods with a precipitation (P) deficit) over the preceding 26 and 34 months in the temperate and Mediterranean biome, respectively. More specifically, 90-d P was below-normal for approximately 90% of the two years prior to low-NDVI events. In the temperate biome only, positive temperature (T) anomalies were unusually persistent during almost the same 26-month period. While anomalously strong hot-dry conditions were already characteristic of temperate low-NDVI events in the previous summer, we found hardly any other systematic meteorological precursor in the Mediterranean prior to the event year. The identified dry periods went along with reduced cyclone activity in the Mediterranean, and with positive anticyclone frequency in the temperate biome. The occurrence of these two weather systems is locally more nuanced, e.g., showing consistently increased (decreased) cyclone frequency over western (northern) Europe in all event summers.
The low-NDVI events represent an impact-oriented extreme season, in the sense that forest greenness (impact) is significantly adversely affected over large areas and large portions of the summer season. By combining statistical evaluations with the growing body of literature on forest-meteorology interaction, we identified T and P signals that can be seen as precursors of this extreme impact. Moreover, we were able to link these meteorological anomalies at the 90-d timescale to significant anomalies in the occurrence frequency of cyclones and anticyclones, acting on shorter timescales. In the temperate biome, where the four most extensive low-NDVI events occurred within the last five years (except for 2021), the novel systematic understanding of forest–meteorology interactions is of particular relevance for forest dieback in the warming European climate.

2. What is the meteorological composition of extremely high summer mean VPD in the present-day climate?

Extremely high VPD over the course of an entire season in critical for water stress of crops and forest ecosystems, especially in summer. In Chapter 4, we applied and further developed the framework of Röthlisberger et al. (2021) to identify summers with extremely high seasonal mean VPD ($\text{VPD}_{\text{JJA+}}$) in ERA5 in 1979–2020 and in the 1050-year-large set of CESM1 historical climate simulations (Chapter 2). Furthermore, we introduced a decomposition of seasonal VPD anomalies (VPD') to analyze how much seasonal temperature and specific humidity anomalies (T' and q') contribute to the intensity (I) of $\text{VPD}_{\text{JJA+}}$. We identified about 100 $\text{VPD}_{\text{JJA+}}$ in ERA5 and more than 2'500 $\text{VPD}_{\text{JJA+}}$ in the CESM1 simulations with a center of mass in 30–60°N, which enable a systematic investigation of $\text{VPD}_{\text{JJA+}}$.
The two datasets agree extremely well on the meteorological decomposition of I across the Northern Hemisphere mid-latitudes: positive T' contribute about 75% to the average $I \approx 0.3\,\text{kPa}$, but at the same time offset a part of I due to the moistening resulting merely from

the climatological co-variability of T and q. About 31% of I arise due to negative q' related to anomalous circulation dynamics during VPD_{JJA+}. Using the extensive set of VPD_{JJA+} in CESM1, we could robustly analyze spatial variations in this meteorological decomposition. In a few semi-arid and arid regions, all three terms contribute positively to I. In more northern regions, e.g., the UK or parts of Canada and Siberia, the moistening induced by hot T' acts to dampen the very pronounced contributions of the hot and (dynamically induced) dry anomalies during VPD_{JJA+}. Very few regions along the east coasts of North America and Eurasia were identified, where VPD_{JJA+} can also occur in association with negative T' due to exceptionally large negative q'. Moreover, the meteorological substructure of known high-impact VPD_{JJA+}, e.g., in the southern U. S. and Mexico in 2011 or in northern Europe in 2018, underlined the importance of VPD for low soil moisture and a low SPEI drought index.
By thoroughly analyzing and detrending VPD anomalies in both datasets, Chapter 4 has improved our understanding of VPD on the seasonal timescale, and will allow us to assess the response of VPD_{JJA+} to global warming. As a consequence of the nonlinear dependence of VPD on T, VPD is underestimated when estimated from seasonal mean T and q. In the northern mid-latitudes, this underestimation arises due to day-to-day (58%) and sub-daily (42%) VPD variability, and, however, does not contribute to the intensity of VPD_{JJA+}. Altogether, our results have shed light on a how short-term atmospheric variability can lead to VPD_{JJA+} in different mid-latitude regions, and thus help to understand how weather systems can adversely affect terrestrial ecosystems and crops during the summer season. In addition, the findings from ERA5 suggest that the contribution of T' to I will increase with continued global warming. Thanks to the framework developed here, we plan to systematically evaluate this hypothesis in the near future.

3. Which mechanisms govern the summer melt increase of the GrIS in this century?

GrIS summer melt ($\overline{m}_s$) from the upper-elevation zone ($\geq$ 1'200 m) shows an increase from 2005–2015 (PD) to 2085–2095 (LC) equal to $\Delta\overline{m}_s = +501\,\mathrm{Gt\,JJA^{-1}}$, or to a factor of 3.5, assuming the SSP3-7.0 scenario. We extended a decomposition framework (Cassano et al., 2007; Mioduszewski et al., 2016), and applied it to this substantial melt increase derived from the surface energy balance of a CESM2 ensemble (Chapter 5). Furthermore, circulation patterns were classified by applying the Self-Organizing Map (SOM) method to daily 500 hPa geopotential height anomalies ($Z500'$). The $\Delta\overline{m}_s = +501\,\mathrm{Gt\,JJA^{-1}}$ can be attributed to an expansion of the melt area (51%), an intensification of melt (17%), a concurrent change of both (24%), and an increase in the daily covariance between melt area and intensity (8%). Melt accelerates over the course of this century, with melt area expansion contributing more in the first half of the century than in the second half. Furthermore, $\overline{m}_s$ in cyclonic patterns of $Z500'$ increases mainly due to an upward (in orographic terms) expansion of the melt area, while anticyclonic circulation patterns also promote large contributions from melt intensification – especially in the southwestern GrIS. Since substantial circulation changes occur only between flow configurations with similar melt increases, the change in atmospheric circulation patterns has no effect on the projected melt increase in the 21st century.

Despite the strong response of $\overline{m}_s$ to mean climate warming, the impact of intra-seasonal atmospheric variability on the inter-annual variability in $\overline{m}_s$ becomes larger in LC compared to PD. This is because most anticyclonic circulation patterns show a stronger intensification of melt than cyclonic ones. Thus, although the GrIS will contribute continuously and much more strongly to global sea-level rise in a warmer climate, a thorough understanding of the short-term atmospheric variability remains crucial for determining the pace of mass loss as well as its inter-annual variability.

6.2 Caveats

After highlighting the main novelties of this thesis, we state overarching and important limiting aspects of the presented analyses. More specific and more minor caveats are discussed in the Sects. 3.4, 4.6,& 5.4.

It is important to cautiously interpret the meteorological history of low-forest-greenness events in the context of future occurrences thereof, because (i) of the systematic assessment used in Chapter 3, and (ii) forest ecosystems respond dynamically to global warming – i.e., as the climate moves out of its historical niche. First, we considered T and P anomalies based on a relatively short climatology (2002–2022), assuming that the change in mean climate during this period was relatively small compared to the inter-annual variability. However, with further global warming, changes in the mean climate (i.e., climatology) are becoming increasingly relevant to forest dynamics as well (Seidl et al., 2017; Brodribb et al., 2020; McDowell et al., 2020). Therefore, anomalies derived from such a climatology may not have the same significance as the meteorological precursors identified in Chapter 3. The low-NDVI events in 2003 and 2018 underline that forests respond differently to similar meteorological signals (see Sect. 3.4.1). This response depends on the meteorological history in previous years and presumably also on the slowly changing mean climate. Second, although low NDVI is a highly useful indicator of forest dieback (Buras et al., 2021), it does not strictly imply continuously impaired forest vitality as, e.g., indicated by reduced tree growth (Kannenberg et al., 2019). Furthermore, the identified low-NDVI events can lead to improved acclimation to drought (Gessler et al., 2020), but on the other hand, they may reduce tree resilience to subsequent droughts (Bose et al., 2020). The type of response depends on several factors that often operate at finer scales than the analyses in this thesis (see also Sect. 3.4.1), such as site, stand, and tree properties (Etzold et al., 2019; Vitasse et al., 2019; Frei et al., 2022), tree species diversity within a forest (Grossiord et al., 2014), forest microclimate (Buras et al., 2018), and legacies of past forest management (Thom et al., 2018). The co-variability of these factors such as the interaction between host trees and biotic disturbance agents further enhances the complexity of drought-induced tree damage (Trugman et al., 2021). These drought-mediating factors thus also contribute to variations in local meteorological histories, which may differ from those systematically identified at the biome level. While our results contribute to understanding the impact of weather on forests in their current composition and under present climatic conditions, a comprehensive assessment of forests'

future response to multi-seasonal meteorological histories requires further development of our mechanistic understanding of eco-hydraulic processes, drought indicators, and the differential effects of climate change on various tree species and forests.

An additional caveat has to be considered when interpreting the results presented in Chapters 4 & 5, both of which are based on climate simulations of a single general circulation model (GCM). Projections of GrIS melt (Fettweis et al., 2020; Hofer et al., 2020) as well as of q and T (John and Soden, 2007; Dunn et al., 2017) differ strongly between different models, while the mean over several GCM ensembles is often in best agreement with observations (Belleflamme et al., 2013; Fettweis et al., 2020; IPCC, 2021). We have partly evaluated the GCMs and found very high agreement of extreme VPD seasons in CESM1 with those in ERA5 (Sect. 4.5), and the analyzed CESM2 melt estimates are in reasonable agreement with those of the regional climate model (RCM) MAR (Sect. 5.1). Moreover, we use CESM1 and CESM2 micro and macro ensembles to capture a large fraction of internal variability (Sect. 2.2); however, uncertainties associated with the specific GCM used still remain. In particular the mean and variance of q and T point to CESM1 model biases, which are, consequently, also present in the simulated variability and return period of VPD anomalies. In future research, our results should be confronted with those resulting from the application of the frameworks developed here to other GCMs.

The simulation of GrIS melt is further limited by the ability of CESM2 to simulate the polar climate. Compared to CESM1, important aspects relevant for melt could be improved in CESM2, e.g., the representation of liquid clouds (Lenaerts et al., 2020; van Kampenhout et al., 2020) and of the surface snowpack (van Kampenhout et al., 2017). Nevertheless, a higher horizontal resolution still improves the representation of the GrIS climate and topography and thus mass balance in variable-resolution GCMs (van Kampenhout et al., 2019) and RCMs, which are additionally tailored to modeling the polar climate (Fettweis et al., 2020). As such, MAR (Fettweis et al., 2017), RACMO (Noël et al., 2016), and HIRHAM (Christensen et al., 2007) run at close to the kilometer scale and would thus allow to study the substantial ablation area melt, which was excluded from our analyses due to the relatively coarse CESM2 resolution. So the projections of GrIS melt changes could be further improved by using output from high-resolution polar RCMs coupled to multi-model GCM simulations or RCM single model initial-condition large ensembles (SMILEs; Maher et al., 2021). Note that similarly promising projections can be obtained when using output from the coupled 4 km ice sheet model of CESM2 (van Kampenhout et al., 2020; Noël et al., 2020), which was not available at the daily timescale for this thesis.

Furthermore, it is worth revisiting the discussion raised by Belleflamme et al. (2013) and Delhasse et al. (2018) regarding the ability of GCMs to accurately simulate future circulation changes over the Greenland region. During the 2005–2017 period when anticyclonic circulation anomalies over the GrIS in summer, i.e., also negative NAO, have occurred with an intensity and persistence not reproduced by CMIP3 (Belleflamme et al., 2013), CMIP5 (Delhasse et al., 2018;

Hanna et al., 2018), or CMIP6 models (Delhasse et al., 2021). This period went along with strong warming in Greenland, raising the question of whether such dynamic changes are the result of a warming climate or internal climate variability. While the former is underlined by further discrepancies between observed and modeled regional circulation and thus climate anomalies (Shepherd, 2014; Smith et al., 2020), the latter is supported by the extremely uniform circulation projections across CMIP3, CMIP5, and CMIP6 models. Note that these models simulate a slightly decreasing anticyclone occurrence frequency in the GrIS region in this century (e.g., Hanna et al., 2018). Due to the high sensitivity of surface melt to such anticyclonic circulation anomalies (Delhasse et al., 2018), which is expected to increase (Sect. 5.3.3), the importance of circulation changes will remain relevant for GrIS mass loss projections. However, our study does not specifically address this question, emphasizing the importance of considering potential changes in circulation when interpreting the broader implications of our results.

This thesis clearly focused on the short-term atmospheric variability, which we also introduced as the "weather perspective". As emphasized in Chapter 1, a full understanding of seasonal anomalies requires a seamless approach across the timescales of potential driving phenomena in the Earth system. Melt of the GrIS is not only influenced by daily circulation patterns but can also be understood by studying the NAO and the Greenland Blocking Index (GBI; Hanna et al., 2021), which exhibit up to decadal variability (Hurrell, 1995). Likewise, extreme seasons are also related to more slowly varying components of the Earth system such as sea-surface temperature anomalies (e.g., Namias, 1978; Rousi et al., 2023). And as one of the most important teleconnections influencing the extratropical inter-annual variability, ENSO has been mentioned, among others, in the context of the "abnormal winter 1976/77" (Namias, 1978), the globally largest extremely hot summers (Röthlisberger et al., 2021), and anomalous winter seasons in northeastern Europe (Brönnimann et al., 2006). Regarding the external drivers of variability, our analyses mostly studied internal variability separately from global warming due to the relatively short time period of forest greenness anomalies (Chapter 3), by detrending T, q, and VPD anomalies (Chapter 4), and by separately calculating $Z500$ anomalies with respect to each time period in the 21st century (Chapter 5). Undoubtedly, extreme seasons as perceived by the mere magnitude of meteorological anomalies are shaped by a combination of internal climate variability (including weather systems as well as major modes of variability such as ENSO) and external forcing, such as during the extremely cold-wet summer in western Europe following the Tambora volcanic eruption (Brönnimann and Krämer, 2016). In summary, we chose to focus on understanding seasonal climate variability from a weather system perspective. However, we acknowledge that approaching the problem of understanding seasonal climate variability with our understanding of the climate system on longer than seasonal timescales would be complementary and equally valid.

Finally, we used the ERA5 reanalysis to study the observed atmospheric variability (Sect. 2.1), which is not an exact representation of the past atmospheric state. For example, ERA5 is known to have a wet bias over Europe, presumably due to the coarse resolution of orography and

the compensation for smoothed subgrid-scale P peaks (Bandhauer et al., 2022). Mountainous regions with sparse direct observations from weather stations also show the largest disagreement between ERA5 and observed T, where, however, weather station observations are also considered less robust (e.g., Tarek et al., 2020). In the Northern Hemisphere, the ECMWF predecessor of ERA5, ERA-Interim, generally agrees well with other full-input reanalyses on the intensity, frequency, and duration of weather systems, however, spatiotemporal resolution and the identification criteria of weather systems cause some differences between the reanalysis products (Rohrer et al., 2018). Overall, the improvements from ERA-Interim to ERA5 are considerable and have resulted in a spatiotemporally complete dataset, whose major shortcomings are limited locally or to the stratosphere (Hersbach et al., 2020). All in all, the value of ERA5 as a modern full-input reanalysis clearly outweighs its shortcomings, which we do not expect to qualitatively affect the conclusions drawn from Chapters 3–5.

6.3 Outlook

The previous sections have outlined the advances made in this thesis, along with their limitations, which have also revealed relevant research questions for subsequent research at the weather-climate interface. First, as drought and drought-related disturbances are becoming critical for global forests at regionally variable pace, we expect different meteorological precursors of low-NDVI events in different bioclimatic regions. The differences we have found between the event precursors in temperate and Mediterranean forests illustrate that the relevance of meteorological precursors depends at least on the physical environment, the species composition of forests, and the locally relevant weather systems. Considering the potential of low NDVI as an early warning for forest dieback in Europe, it is crucial to identify the meteorological precursors of low forest greenness in other regions, such as the boreal biome of North America and northern Eurasia. Subsequently, the increasing length of satellite records of forest greenness may allow more robust assessments of forest dieback at the local scale. Although in this study, we could aggregate events across a single biome to obtain systematic results applicable to that specific biome, longer observational records will enhance our ability to identify meteorological precursors at a more localized level. Thus, the factors acting at a finer spatial scale mentioned earlier that mediate forest response to seasonal meteorology could successively be accounted for. After considering the dynamic response of ecosystems to global warming, such insights could form the basis for predicting forest dieback similarly to crop failure (Vogel et al., 2021).

The robust framework for the meteorological decomposition of extreme VPD seasons in large-ensemble climate simulations has clearly raised the question of how their intensity and contributions will change in the future. There is a clear hypothesis of increasing contributions from T' in a warming climate, due to the increasing potential of T to cause large VPD in a warmer climate. However, the large variability in the meteorological decomposition across the mid-latitudes (revealed in this thesis), as well as in the current and future distribution of seasonal mean q and T, calls for a thorough investigation of this hypothesis. The flexible nature

of this framework makes it particularly valuable in the light of increasingly available SMILEs (such as the CESM1 used here), which in combination are useful to robustly investigate internal variability separately from global warming and structural, i.e., model-dependent, uncertainty (Deser et al., 2020; Maher et al., 2021). Moreover, applying the framework to identify less (e.g., with a return period of 10 y) or more extreme (e.g., 70 y) VPD seasons could reveal which meteorological conditions make seasonal mean VPD particularly intense – a research question that has not yet been addressed.

As elaborated in the previous two sections, the main limitation of Chapter 5 could be overcome by analyzing GrIS melt in RCM simulations, preferably using input of several GCMs and SMILEs. The advantages of polar RCMs are their higher spatial resolution, which resolves the narrow and steep ablation zone of the GrIS, and a more accurate representation of surface properties such as albedo, both resulting in a better simulation of surface melt and precipitation. Moreover, as GCMs and SMILEs continue to improve from generation to generation in terms of simulating the GrIS climate and mass loss, the role of short-term atmospheric variability in modulating the response of GrIS melt to global warming should be revisited in future research, e.g., by using the framework provided in Chapter 5.

Finally, all three chapters, especially those on extreme VPD seasons (Chapter 4) and GrIS summer melt changes (Chapter 5), assessed daily atmospheric variability and the involved meteorological phenomena rather fundamentally. Indirectly, e.g., in Chapter 5, we have highlighted the potential importance of atmospheric blocking for anticyclonic flow anomalies and of Foehn during cyclonic flow anomalies, while other weather systems such as atmospheric rivers are also highly relevant for GrIS melt (e.g., Mattingly et al., 2016). The specific examination of the weather systems involved, also from a Lagrangian point of view, could, for example, provide answers to the following questions: Given that the projected circulation changes have no effect on the GrIS melt increase, how do weather system dynamics modulate the melt expansion and intensification? Which weather systems and processes lead to the ~31% of the extreme VPD season's intensity that arise from dynamically induced negative q'? These are just two questions whose answers would further deepen our understanding of the seamless interaction of phenomena across the weather-climate interface.

In the quote at the very beginning of this thesis, Callendar (1938) concluded his revolutionary findings with the beneficial consequences of human-caused global warming for crop cultivation, plant growth (CO_2 fertilization), and regarding the retreat of "the deadly glaciers". As it happened, this thesis studied these exact three components of the Earth system, which, however, are responding in a much more alarming than beneficial manner to global warming. Specifically, we have examined how weather matters for forest vitality, extremely high VPD in summer, and GrIS surface melt in the 21st century. Short-term atmospheric variability contributes to seasonal anomalies in regionally and temporally distinct ways, whose evaluation has required particularly systematic approaches throughout this thesis. Moreover, as global warming increas-

ingly alters seasonal meteorology and thus the components of the Earth system studied here, this work has contributed to the understanding needed for timely preparedness strategies. By applying and developing appropriate frameworks to study seasonal meteorological anomalies, this thesis also brought forward tools for further research at the weather-climate interface.

Appendix A

Additional information for Chapter 3

A.1 Sensitivity to threshold parameters

The event identification is based on 3 threshold parameters, namely the minimum affected ratio $AR^{min} = 80\%$, the minimum forest area $FA^{min} = 10\%$, and the minimum number of time steps in JJA with negative NDVI' $c_{ev}^{min} = 4$ (Sect. 3.2.3). Parameter AR^{min} refers to the fraction of forest pixels that has to show persistently negative NDVI per $0.5° \times 0.5°$ grid cell for that grid cell to be identified as low-NDVI grid cell. Persistently here is defined via a lower threshold c_{ev}^{min} for $c_{n,ev}$, where the latter refers to the number of time steps out of a total of six in JJA that show negative NDVI. Lastly, FA^{min} sets a minimum forest cover per grid cell to filter out those with only very few forest NDVI pixels. We vary AR^{min} and FA^{min} by $\pm 5\%$ and test different combinations thereof. We vary c_{ev}^{min} by ± 1 only for the setup "80_10" used in the study ($AR^{min} = 80\%$, $FA^{min} = 10\%$) as the identification scheme depends strongly on this parameter. Table A.1 shows the number of events (n_{tot}), the number of years with at least 10 low-NDVI grid cells in 2002−2022 (n_{yr}), and also the number of events per sub-sample (n_{ev}) that results from varying the threshold parameters. Large n_{yr} is important to the sub-sampling of the low-NDVI grid cells, which is used to retrieve more systematic results, and would optimally be as close to the total years of 21 as possible. The n_{tot} is particularly strongly reduced when increasing AR^{min} to 85%, resulting in $n_{yr} \leq 10$. Aiming to optimize n_{yr} by using looser thresholds, however, would misconceive a typical characteristic of extreme events such as low-NDVI events, namely that they occur concentrated in individual years and not in others. So looser thresholds have the disadvantage of reducing the peculiarity of low-NDVI grid cells. This is illustrated by the ~1.5× increase in n_{tot} when reducing AR^{min} from 80% to 75%. While reducing c_{ev}^{min} in the study setup (80_10) from 4 to 3 has only minor effects, n_{tot} and consequently n_{yr} and n_{ev} are drastically reduced when increasing c_{ev}^{min} to 5 (Table A.1). For example, in the temperate biome, only 3 years would contribute at least ten low-NDVI grid cells if $c_{ev}^{min} = 5$ was used. So while the number of events is not very sensitive to reductions in c_{ev}^{min}, increasing c_{ev}^{min} would render a systematic assessment impossible.

Table A.1: Number of events (n_{tot}), number of years with at least 10 low-NDVI grid cells (n_{yr}), and number of events per sub-sample (n_{ev}) for different combinations of threshold parameters. Values in rows 1–3 and rows 4–6 apply to the temperate and Mediterranean biome, respectively. The column title indicates the setup with $c_{ev}^{min} = 4$ and different AR^{min} and FA^{min} combinations separated by an underscore – except for the last two columns. These denote tuning the threshold parameter c_{ev}^{min} to 3 and 5 while $AR^{min} = 80\%$ and $FA^{min} = 10\%$.

Sensitivity											
	75_5	**75_10**	**75_15**	**80_5**	**80_10**	**80_15**	**85_5**	**85_10**	**85_15**	**3of6 80_10**	**5of6 80_10**
$\mathbf{n_{tot}}$	2294	1998	1744	1580	**1386**	1204	929	809	707	1770	144
$\mathbf{n_{yr}}$	17	17	17	16	**15**	15	10	9	9	16	3
$\mathbf{n_{ev}}$	187	185	183	173	**170**	164	138	132	124	179	35
$\mathbf{n_{tot}}$	1701	1319	1078	1287	**989**	808	861	661	529	1181	195
$\mathbf{n_{yr}}$	18	16	15	16	**14**	14	12	12	11	14	6
$\mathbf{n_{ev}}$	195	187	177	177	**164**	160	155	142	136	177	93

The sensitivity of the main result to these two parameters is illustrated in the example of Fig. 3.5 (Fig. A.1). As in the original Fig. 3.5, we perform a random sub-sampling of up to 10 low-NDVI grid cells per year for each biome and compute an average meteorological history from the resulting samples (Sect. 3.3.3). This sub-sampling is done 10 times for each biome, and Fig. A.1 shows the median of these 10 equivalent average meteorological histories for each of the 11 combinations of AR^{min}, FA^{min}, and c_{ev}^{min} listed in Table A.1. The sub-sampling for each combination of the two threshold parameters is of course dependent on the identified low-NDVI grid cells and, therefore, dependent on n_{tot} and n_{yr} (Table A.1).

Figure A.1 overall highlights low sensitivity of various aspects of the meteorological history to the two threshold parameters. First, the number of events per sub-sample and thus per average meteorological history n_{ev} differs for every setup of threshold parameters depending on variations in n_{tot}. Consequently, setups with more events per sample (loose thresholds) lead to smaller magnitudes of the averaged meteorological anomalies, and, hence, also a more narrow confidence interval than a setup with fewer events per sample (stricter thresholds). The comparison here, therefore, focuses mostly on aspects such as the timing and evolution of significant anomalies instead of their exact magnitude. The statistically significant anomalies highlighted in our study, e.g., negative P'_{90d} in JJA-12m and JJA-ev and positive T'_{90d} that emerged in MAM-3m in temperate forests, would also result from other parameter setups (Fig. A.1a,c). Especially the timing when meteorological anomalies were significantly different from climatology is consistent within almost all 11 setups. Some of the highlighted anomalies persisted longer and emerged more clearly when using stricter thresholds, e.g., $AR^{min} = 85\%$ and $FA^{min} = 15\%$. Positive T'_{90d} followed JJA-12m into SON-9m and also the warm period prior to JJA-ev reached farther into the past (Fig. A.1c). With that setup, also the negative $f'_{90d}(C)$

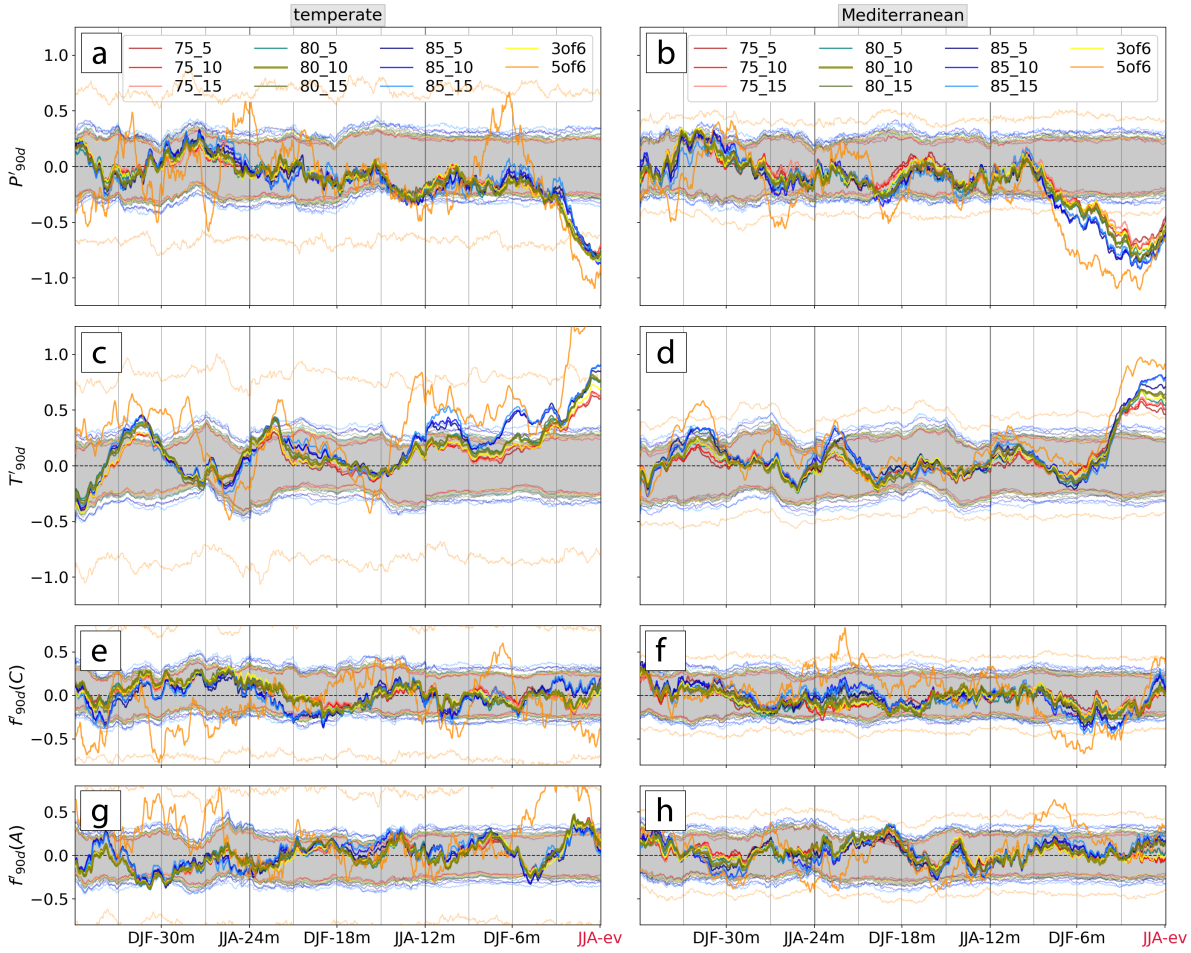

Figure A.1: The same as Fig. 3.5 but for different combinations of AR^{min}, FA^{min}, and c_{ev}^{min}. The bold olive line and the shaded grey 95% confidence interval (CI) correspond to the median setup shown in the study (Fig. 3.5). The other bold lines show the meteorological histories of the other combinations of threshold parameters, and the corresponding CI is shown with thin lines of the same color. The normalized 90 d mean (a,b) precipitation, (c,d) temperature, (e,f) cyclone frequency, and (g,h) anticyclone frequency anomalies, respectively, are shown as line plots. The legend indicates the combination of threshold parameters used as in Table A.1.

in MAM-3m prior to low-NDVI events in the Mediterranean biome was more distinct than for the setup used. With stricter parameter setups, however, n_{ev} is unfavorably reduced as the number of years contributing the maximum of 10 low-NDVI events (n_{yr}) is greatly reduced (Table A.1). This is strongly pronounced when using the setup "5of6", for which, e.g., in the temperate biome, only 3 years (2018, 2019, and 2022) contribute substantially to the average meteorological history shown in Fig. A.1. Considering the numbers in Table A.1 this setup can clearly not provide a meaningful evaluation of low-NDVI events over the study period. Apart from that setup, any larger deviations between the results from the different parameter setups typically occur within the respective confidence intervals – e.g., $f'_{90d}(A)$ in JJA-ev – and are, hence, not highlighted in the analysis and interpretation of Fig. 3.5. To summarize, the sensitivity analysis supports the chosen setup with $AR^{min} = 80\%$, $FA^{min} = 10\%$, and $c_{ev}^{min} = 4$,

and generally demonstrates low sensitivity of the main results to reasonable variations in the 3 parameters.

A.2 Bootstrapping tests

In the bootstrapping test we want to test the null hypothesis $H_{0,EV}$ that a given aspect X of the meteorological history at $t_{ev} - \Delta t$ of low-NDVI events is equal to that of any random meteorological history. For X we use the meteorological fields of T'_{90d}, P'_{90d}, $f'_{90d}(C)$, and $f'_{90d}(A)$, as well as the fraction of Δt where $T'_{90d} > 0$ and $P'_{90d} < 0$, respectively, covering 1999–2022 and the study domain (Fig. 3.1a). The fields are used here for the period 1999–2022, in order to compute 3-year meteorological histories for all low-NDVI events in 2002–2022. Figure A.2 illustrates the procedure of retrieving event mean meteorological histories as well as the way the bootstrapping is constructed.

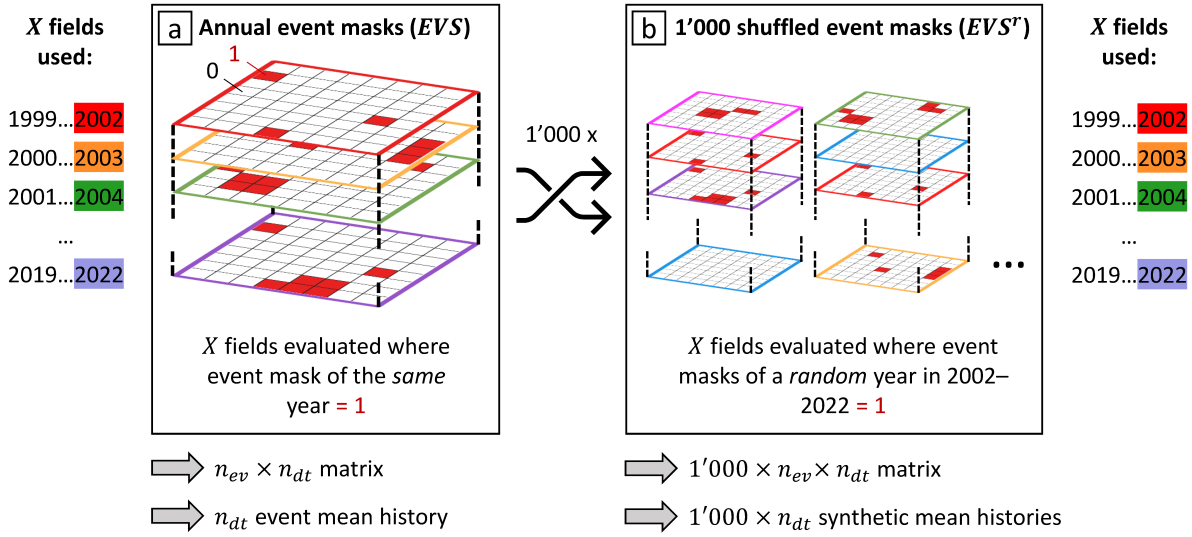

Figure A.2: Schematic of the construction of the event mean meteorological histories (a) of event set EVS and (b) their synthetic analogues EVS^r used for the bootstrapping test. The rows on the side show the order in which fields of X are used to extract the time series for EVS and each EVS^r. The annual binary event masks of EVS in (a) are colored according to the year of occurrence. The shuffled EVS^r sets have a different order of these masks; however, they use the X fields in the same order as EVS.

First, the sub-sampling of all low-NDVI grid cells results in an event set EVS of low-NDVI grid cells that can be represented as 3-dimensional binary $21 \times n_{lat} \times n_{lon}$ event mask, which is equal to 1 at every low-NDVI grid cell (Fig. A.2a). Further, for every X we retrieve an $n_{ev} \times n_{dt}$ matrix – i.e., one with a time series with $n_{dt} = 3 \times 365$ daily time steps for every of the n_{ev} selected low-NDVI grid cells – by extracting the fields of X where EVS equals 1. The average time series of X for one sample results from taking the mean along the first dimension of this matrix, as shown in Fig. 3.5. For the bootstrapping test, we generate 1'000 synthetic event sets (EVS^r) by randomly shuffling the 21 annual masks of EVS 1'000 times (Fig. A.2b). This shuffling process is best visualized by shuffling a deck of cards, whereby each card corresponds to the binary

$n_{lat} \times n_{lon}$ event mask of a specific year. Specifically, when constructing the random event set with number r we assign a randomly selected year y_i^r to all low-NDVI grid cells occurring in year y_i and then repeat the process for all remaining years. Hereby, the random years are chosen such that each year occurs once in every EVS^r. Consequently, each reference event set contains the same number of low-NDVI grid cells as EVS but in a different year-location combination. Afterwards, the synthetic meteorological histories are generated by first retrieving X^r from extracting X fields for EVS^r, i.e., using the shuffled deck of annual binary event masks. Then, the resulting $1'000 \times n_{ev} \times n_{dt}$ matrix is averaged along its second dimension to retrieve a set of 1'000 synthetic event mean time series for every X^r. We, thereby, create 1'000 meteorological histories that are equally plausible in the climatological reference period without the prerequisite of a following low NDVI.

We then compare event mean time series of X of low-NDVI grid cells to the 1'000 synthetic event mean time series of X^r. Values of X outside the range of X^r receive a p value of 0 (Röthlisberger et al., 2016). The remaining p values are estimated from the percentiles of the $1'000 \times n_{dt}$ synthetic matrix along its first dimension. At the significance level of $\alpha = 5\%$, $H_{0,EV}$ is rejected at time lags Δt if the event value of X is outside the 95% confidence interval, i.e., outside the $2.5^{\text{th}} - 97.5^{\text{th}}$ percentile range, of the 1'000 reference values of X^r. Note that the shuffling of years is done prior to extracting the spatial fields of X from the ERA5 data set. This has – in contrast to a random sampling of all forest grid cells – the convenient effect that spatial correlation in these meteorological variables is retained. Thus, synthetic meteorological histories of X^r are constructed from a data set with exactly the same spatial correlation as the original data sets of X.

A.3 Maps of low-NDVI grid cells

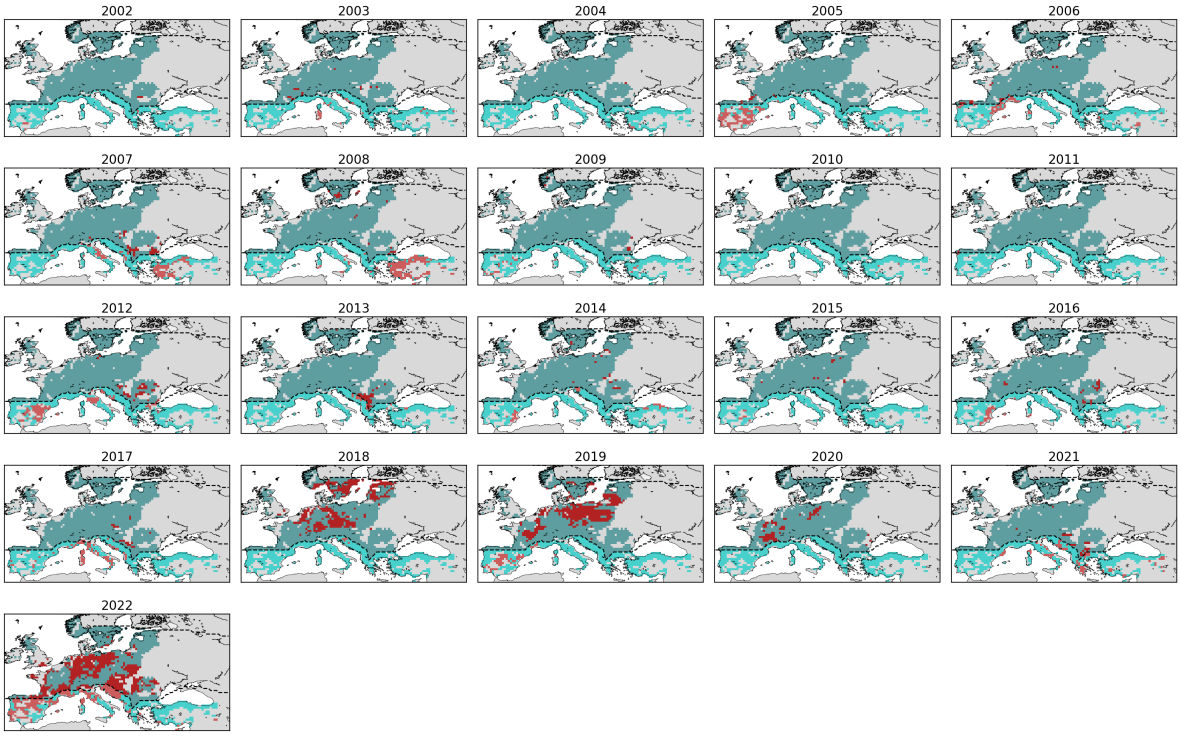

Figure A.3: Low-NDVI grid cells in 2002−2022 (red) in forest grid cells of the temperate (turquoise) and Mediterranean biome (cyan). The dashed lines delineate the two biomes. Data available from Hermann (2022).

A.4 Low-NDVI events and forest disturbance

We provide a brief and qualitative comparison of our set of low-NDVI grid cells with the independent disturbance data set of Senf and Seidl (2021a). The comparison is useful to put the identified low-NDVI events into perspective regarding existing knowledge on forest disturbances.

A.4.1 Forest disturbance data set

We use the forest disturbance data set by Senf and Seidl (2021a) with an original resolution of 30 m. It is based on a time series segmentation approach called LandTrendr (Kennedy et al., 2010) and identifies tree canopy mortality in 1986−2020. The approach uses two spectral bands (shortwave infrared I and II) and two spectral indices (tasselled cap wetness and normalized burn ratio) from Tier 1 Landsat 4, 5, 7, and 8 images in Jun−Sep. For more details see Senf and Seidl (2021a). From this data set we use the annual disturbance area $D_{J,n}$, which is aggregated for every $0.5° \times 0.5°$ forest grid cell. We only use years and grid cells that overlap with our study period and forest grid cells as identified in Sect. 3.2.1. Our event data set overlaps with

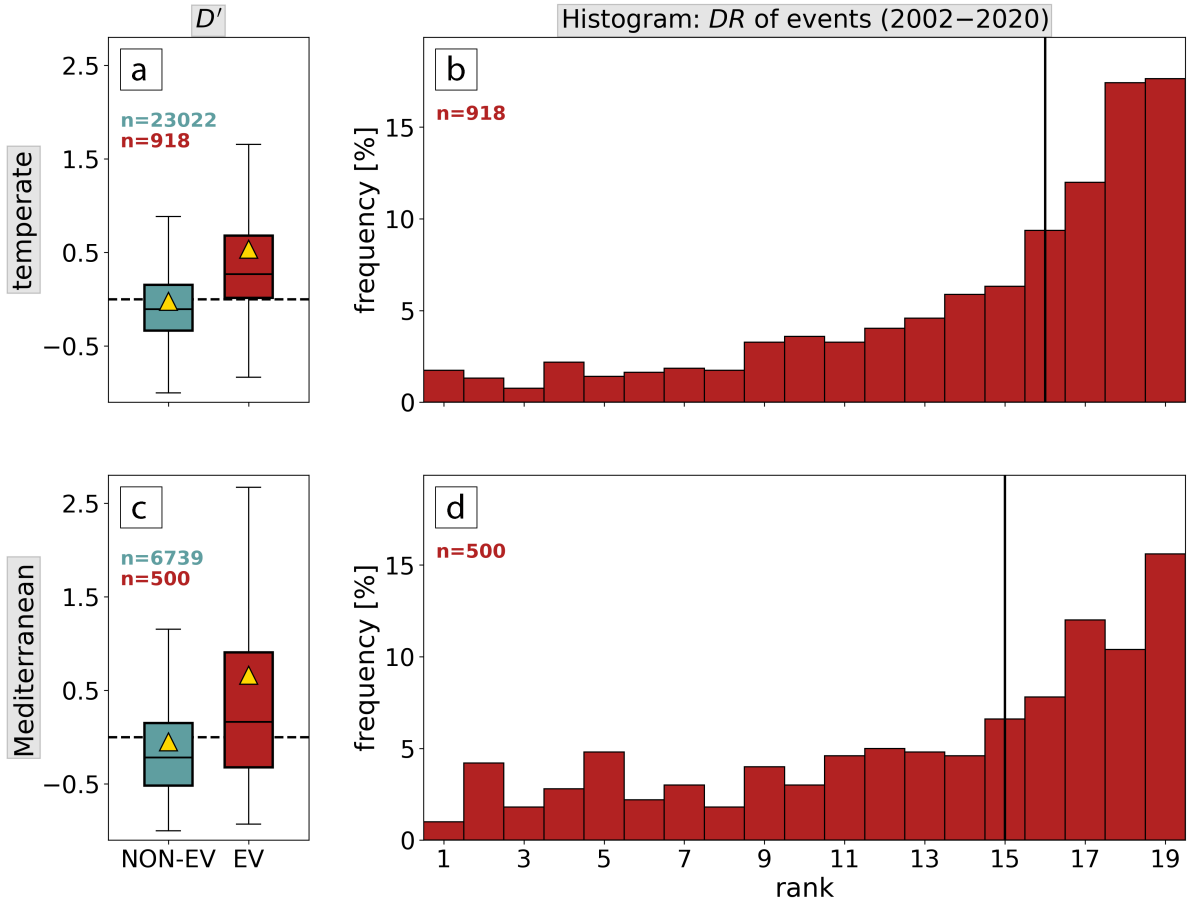

Figure A.4: Event comparison for (a,b) the temperate and (c,d) the Mediterranean biome in the period 2002−2020. (a,c) Boxplots of the disturbance anomaly D' of low-NDVI grid cells (red) and non-event grid cells (turquoise). The distribution mean is shown by a yellow triangle, outliers are omitted. (b,d) Histograms of ranks 1−19 of disturbance area DR of low-NDVI grid cells in 2002−2020. The median is shown by the vertical line.

the disturbance data set in the time period of 2002−2020 at 91% of forest grid cells as D does not cover Turkey. Consequently, 66% and 51% of all low-NDVI grid cells in the temperate and Mediterranean biome are compared to the disturbance data set. More specifically, we use two measures of D: the disturbance anomaly D', and the rank of D among the 19 annual values $DR_{J,n}$ in 2002−2020:

$$D'_{J,n} = \frac{D_{J,n} - \overline{D_J}}{\overline{D_J}} \tag{A.1}$$

$$DR_{J,n} = rank(D_{J,n}) \tag{A.2}$$

at forest grid cell J in year n, with $\overline{D_J}$ denoting the climatological mean disturbance area in 2002−2020. When referring to low-NDVI grid cells in the following, we thereby only address those that spatially overlap with D data in 2002−2020.

A.4.2 Qualitative comparison

In 70% of all low-NDVI grid cells the disturbance area D is larger than on average in 2002−2020 – more often in the temperate (76%) than in the Mediterranean biome (59%; Fig. A.4a,c). The me-

dian disturbed area increases by +27% and +16% during low-NDVI events in the temperate and Mediterranean biome, respectively. Furthermore, non-events typically go along with negative D' in the temperate (61% of non-events) and the Mediterranean biome (66%). Figure A.4b,d additionally shows the disturbance area rank, DR, from 1 (smallest D in 2002−2020) to 19 (largest D). With 1−6 events per affected forest grid cell (Fig. 3.2c) a low-NDVI grid cell would go along with DR 14−19 if the event years were equal to the years of largest disturbed area. The majority of low-NDVI grid cells indeed covers ranks 16−19 and 15−19 in the temperate and Mediterranean biome, respectively. We conclude that low-NDVI grid cells tend to go along with more forest disturbances, i.e., enhanced canopy mortality, and rank among the largest forest disturbances at forest grid cells.

A.5 Weather system anomalies

The following Figures A.5 & A.6 show the spatial pattern of weather system anomalies. For all forest grid cells with at least two low-NDVI events in 2002−2022, we show how many of these events were linked to positive or negative anomalies in f'^{rel}_{90d}. Additionally, we calculate the average anomaly over all events that had the same sign of the anomaly and highlight those with mean changes of at least 25%. For each season of the past year, from JJA-ev backward to SON-9m, we use the value of f'^{rel}_{90d} on the last day of the season, which is approximately equal to the seasonal average over the 3 preceding months.

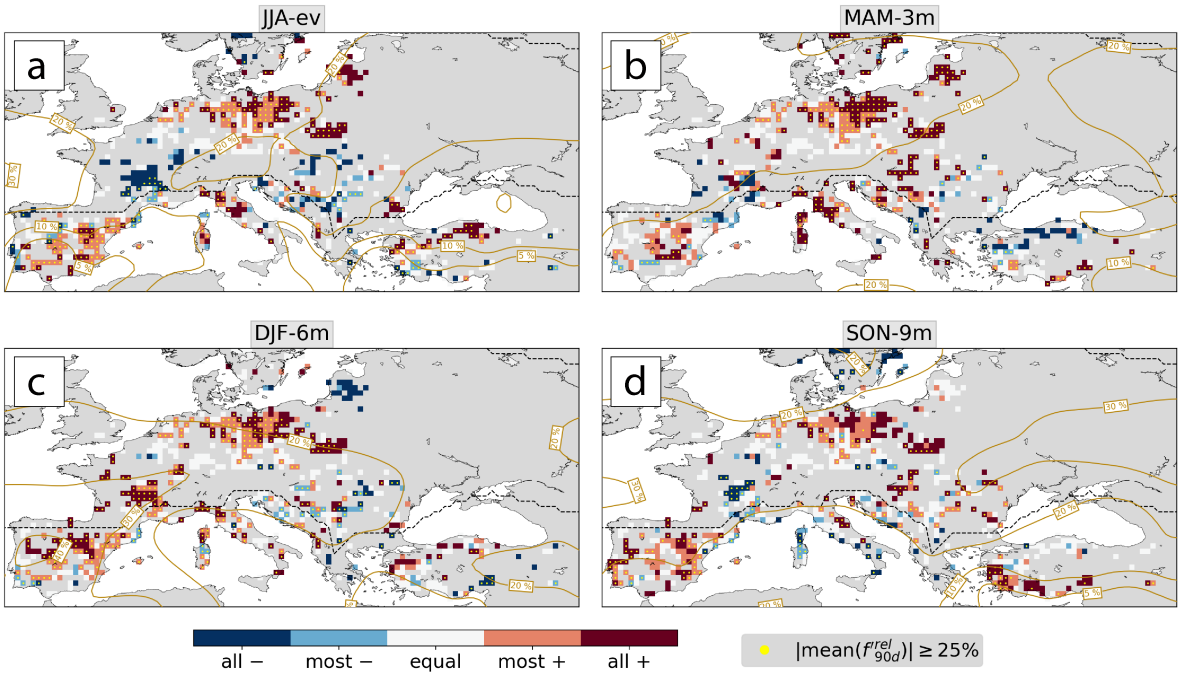

Figure A.5: The same as Fig. 3.7 but for the relative anticyclone frequency anomaly $f'^{rel}_{90d}(A)$ in (a) JJA-ev, (b) MAM-3m, (c) DJF-6m, and (d) SON-9m.

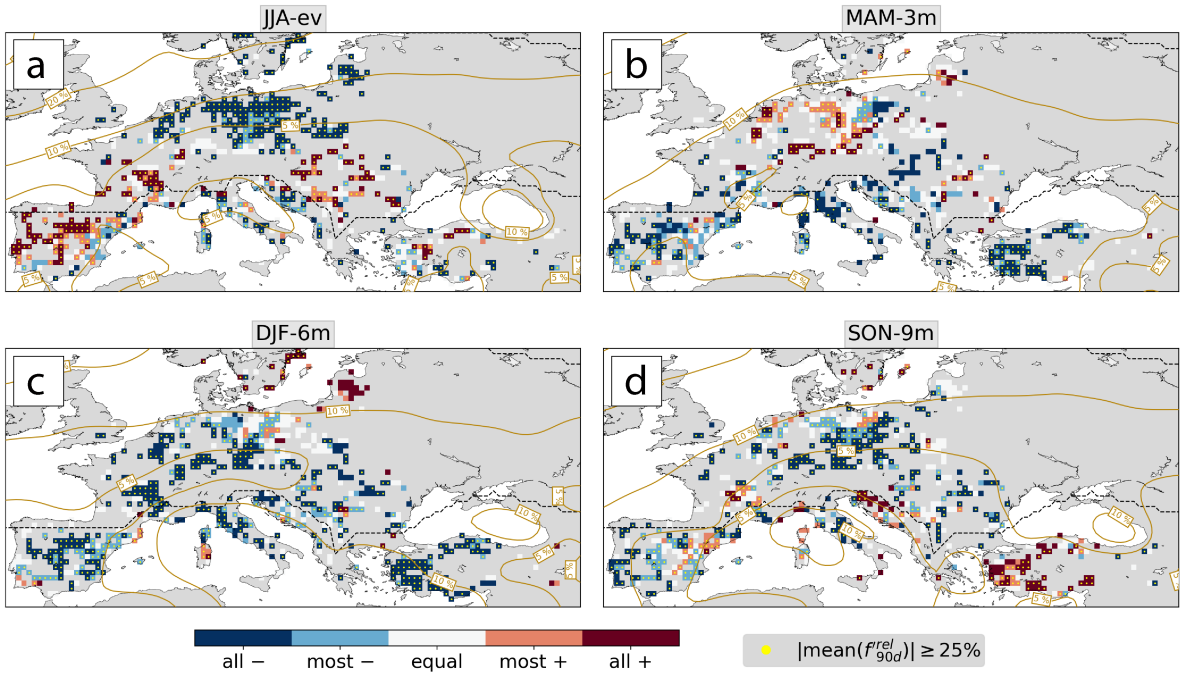

Figure A.6: The same as Fig. 3.7 but for the relative cyclone frequency anomaly $f'^{rel}_{90d}(C)$ in (a) JJA-ev, (b) MAM-3m, (c) DJF-6m, (d) SON-9m.

Appendix B

Additional information for Chapter 4

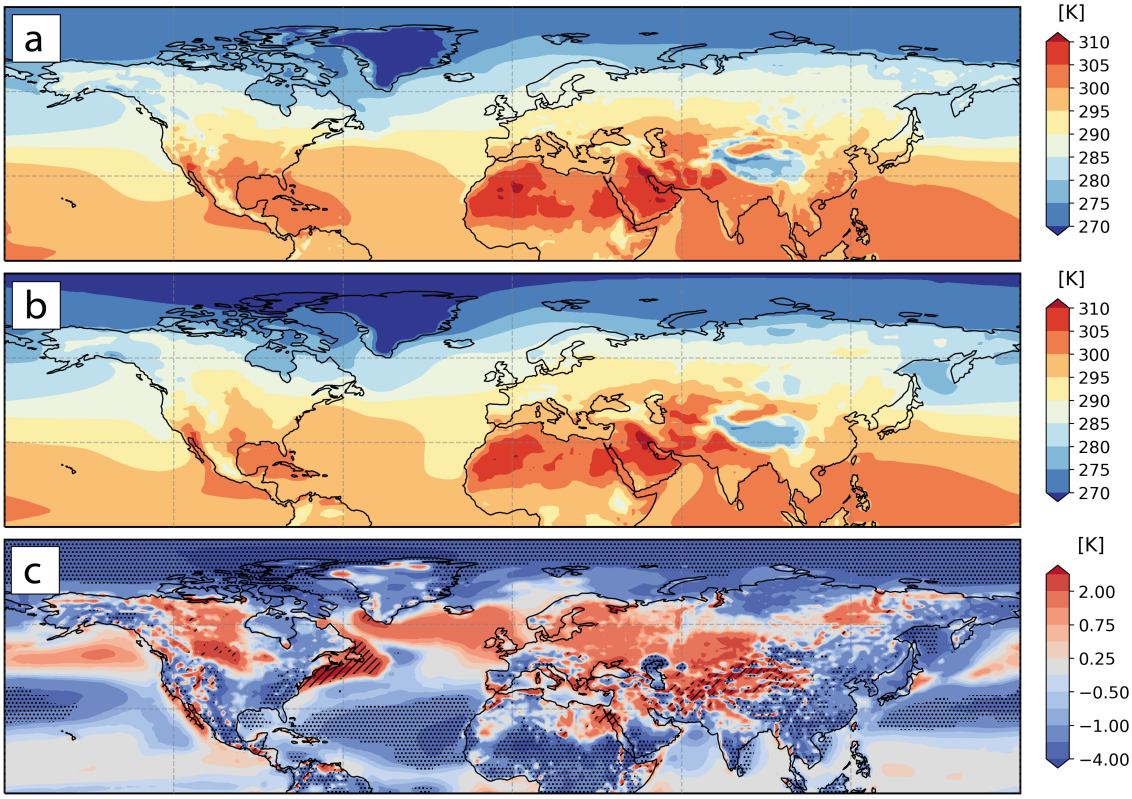

Figure B.1: Mean T (a) in ERA5 in JJA 1979–2020, and (b) averaged over all 25 CESM subsets in JJA 1990–1999. (c) The difference of (b) minus (a), where stippling (hatching) indicates where the ERA5 value lies above (below) the values of all CESM subsets.

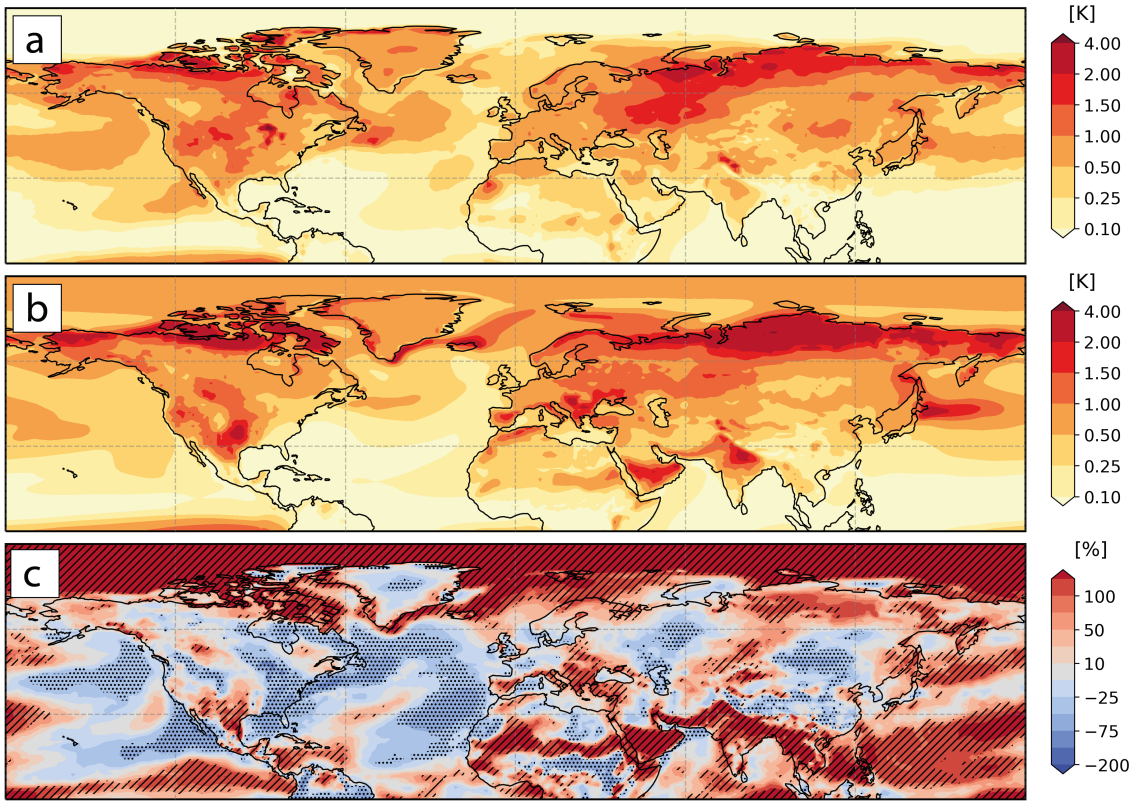

Figure B.2: Variance of seasonal T' (a) in ERA5 in JJA 1979–2020, and (b) averaged over all 25 CESM subsets in JJA 1990–1999. (c) The difference of (b) minus (a) relative to (a). Stippling (hatching) indicates where ERA5 variance lies above (below) the values of all CESM subsets.

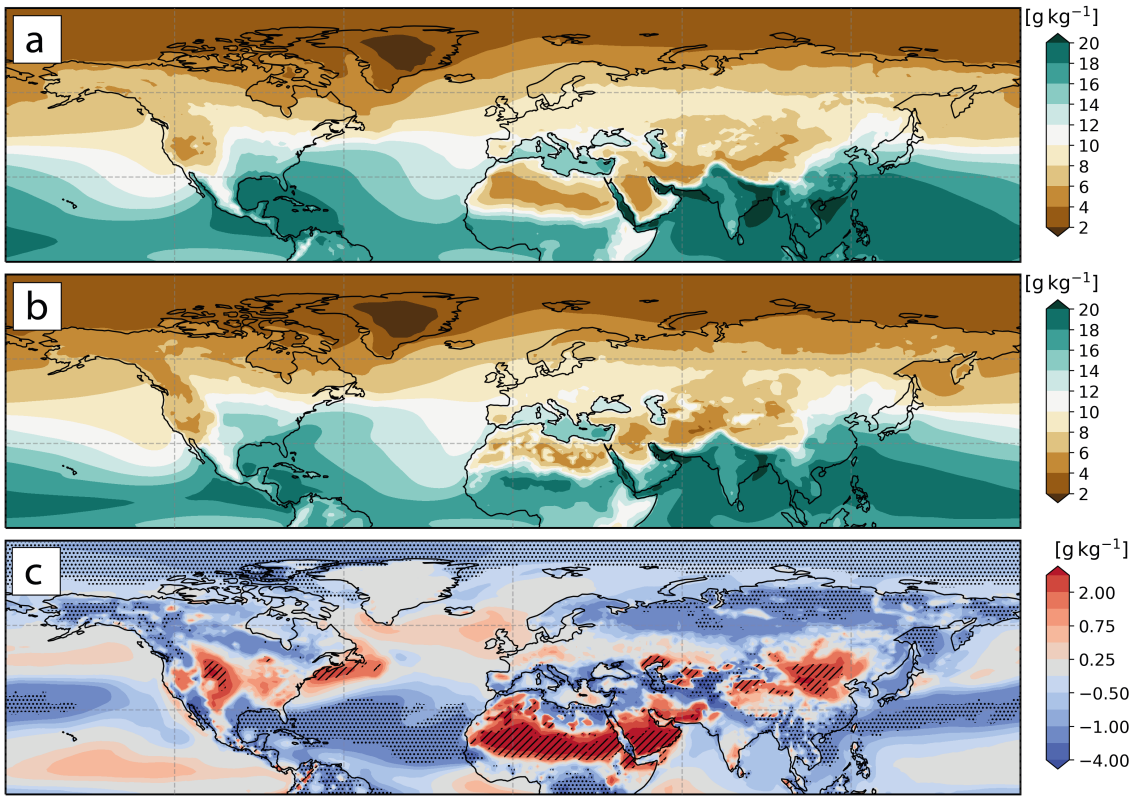

Figure B.3: The same as Fig. B.1 but for seasonal q.

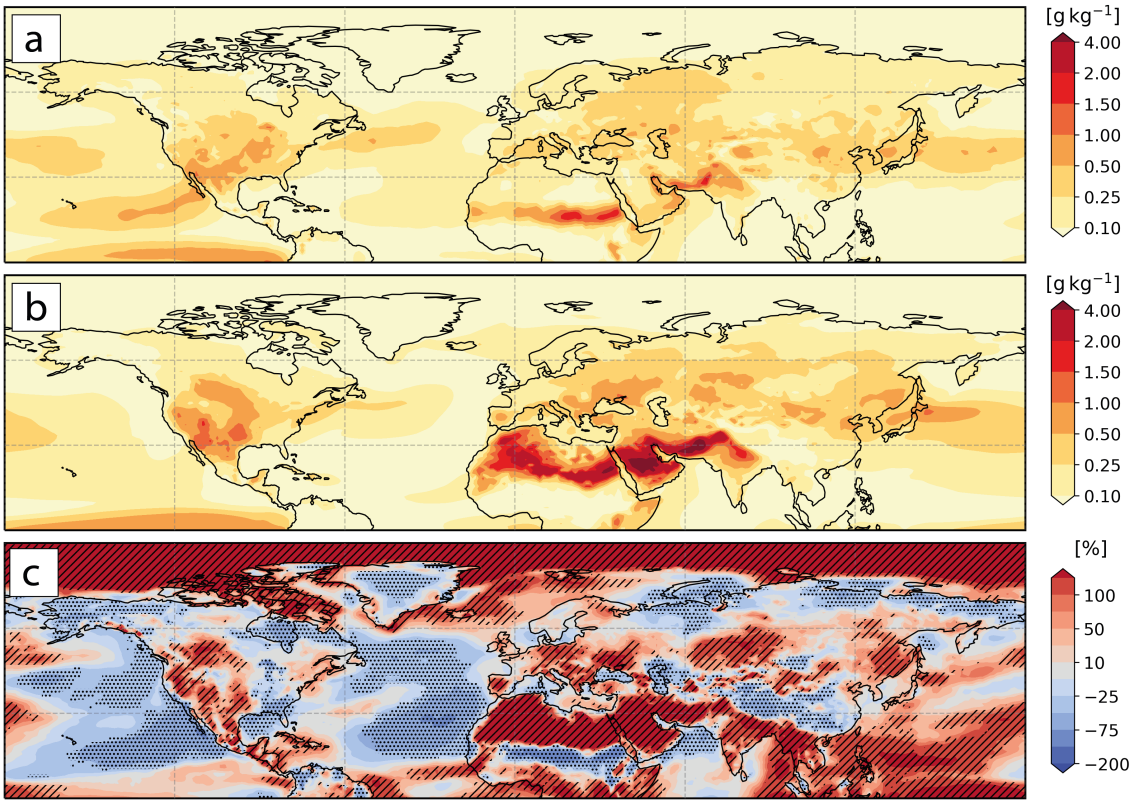

Figure B.4: The same as Fig. B.2 but for seasonal q'.

Table B.1: The same as in Table 4.1 but ranked according to the season's rarity (R).

Year	Region	A [10^5 km^2]	I [kPa]	R [years]
2008	China/Kazakhstan	5.8	0.33	158
2011	Southern U. S./Mexico	14.6	0.78	104
2008	Iran/Afghanistan	5.3	0.39	102
2003	Central Europe	12.5	0.32	99
2010	Western Russia	30.2	0.60	99
1984	Central Asia	19.8	0.37	98
2004	Russia/Japan	1.5	0.09	94
1997	Alaska	1.3	0.11	91
1994	Western U. S./Mexico	15.3	0.52	91
2012	Pakistan	1.5	0.59	89

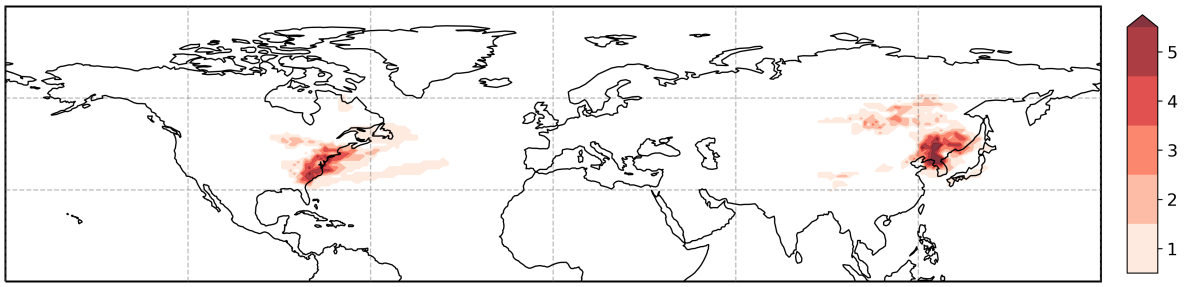

Figure B.5: The number of mid-latitude VPD_{JJA+} with a negative T' in CESM (66 in total).

Appendix C

Additional information for Chapter 5

Table C.1: The map size (nx×ny), radius (r), number of training iterations (I), quantization error (QE), and topographic error (TE) for different tested SOM setups. The chosen setup is highlighted in red.

nx	ny	r	I	QE	TE	nx	ny	r	I	QE	TE
5	4	2	1'000	20.396	0.279	6	5	2	1'000	19.419	0.397
5	4	2	3'000	20.319	0.344	6	5	2	3'000	19.415	0.410
5	4	2	5'000	20.312	0.359	6	5	2	5'000	19.385	0.401
5	4	2	10'000	20.303	0.362	6	5	2	10'000	19.403	0.376
5	4	3	1'000	20.405	0.307	6	5	3	1'000	19.428	0.386
5	4	3	3'000	20.355	0.372	6	5	3	3'000	19.428	0.394
5	4	3	5'000	20.328	0.391	6	5	3	5'000	19.428	0.400
5	4	3	10'000	20.306	0.437	6	5	3	10'000	19.402	0.422
5	4	4	1'000	20.433	0.274	6	5	4	1'000	19.457	0.369
5	4	4	3'000	20.363	0.362	6	5	4	3'000	19.457	0.383
5	4	4	5'000	20.346	0.378	6	5	4	5'000	19.439	0.409
5	4	4	10'000	20.318	0.399	6	5	4	10'000	19.418	0.425
6	4	2	1'000	19.917	0.363	6	4	3	5'000	19.930	0.390
6	4	2	3'000	19.891	0.359	6	4	3	10'000	19.930	0.392
6	4	2	5'000	19.911	0.376	6	4	4	1'000	19.958	0.348
6	4	2	10'000	19.906	0.388	6	4	4	3'000	19.936	0.370
6	4	3	1'000	19.957	0.355	6	4	4	5'000	19.932	0.372
6	4	3	3'000	19.932	0.378	6	4	4	10'000	19.931	0.376

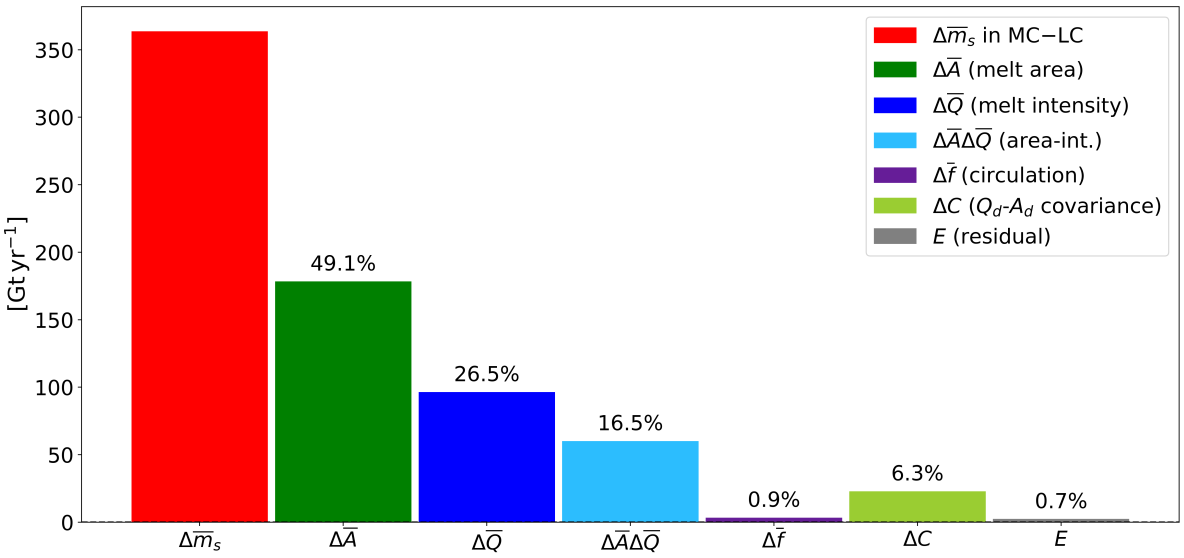

Figure C.1: The same as Fig. 5.4c but from MC to LC. That is, we compute changes from MC to LC (as shown in Fig. 5.4b) but by using the decomposition (Eq. 5.8) with MC as P1 and LC as P2, instead of subtracting changes between PD to MC from those between PD and LC (see Sect. 5.2.5).

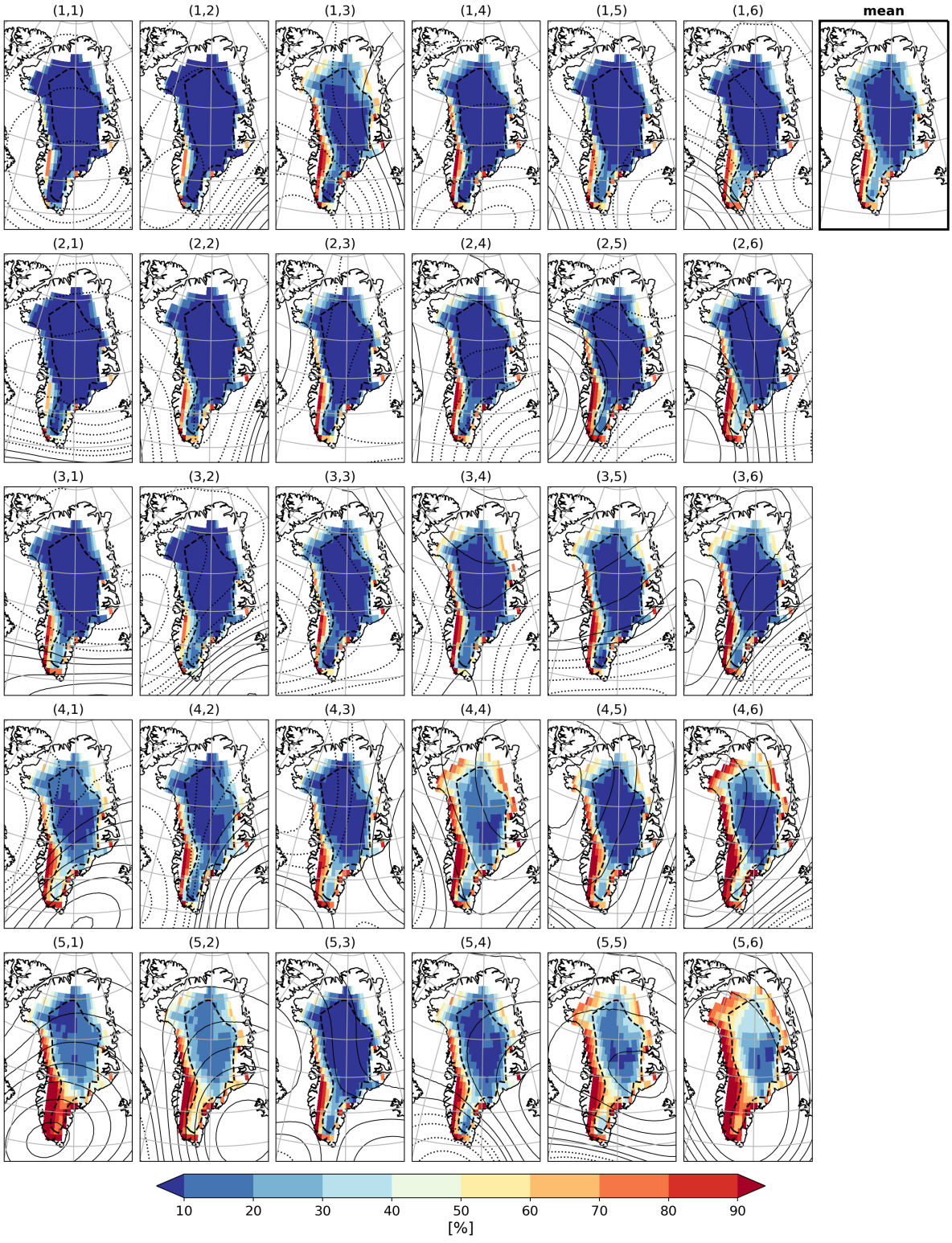

Figure C.2: The top right panel shows the mean daily melt frequency in PD ($\overline{\omega}^{PD}$). The other panels illustrate the mean daily melt frequency during each SOM node ($\overline{\omega}_i^{PD}$). Dotted (solid) black lines show negative (positive) $Z500'$ contours according to Fig. 5.2. The dashed line denotes the 2'200 m elevation contour.

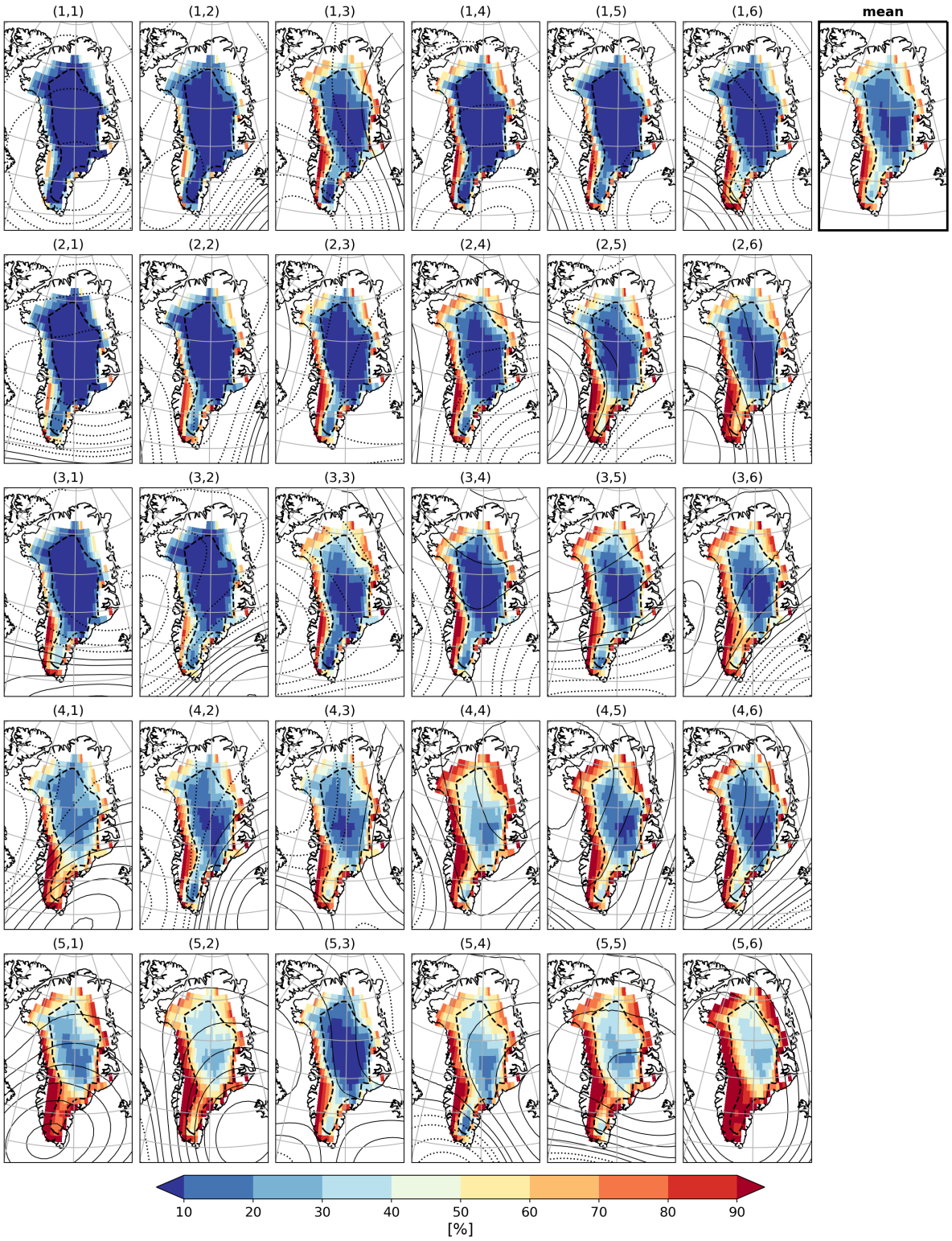

Figure C.3: The same as Fig. C.2 but for $\overline{\omega}^{MC}$ (top right panel) and $\overline{\omega}_i^{MC}$.

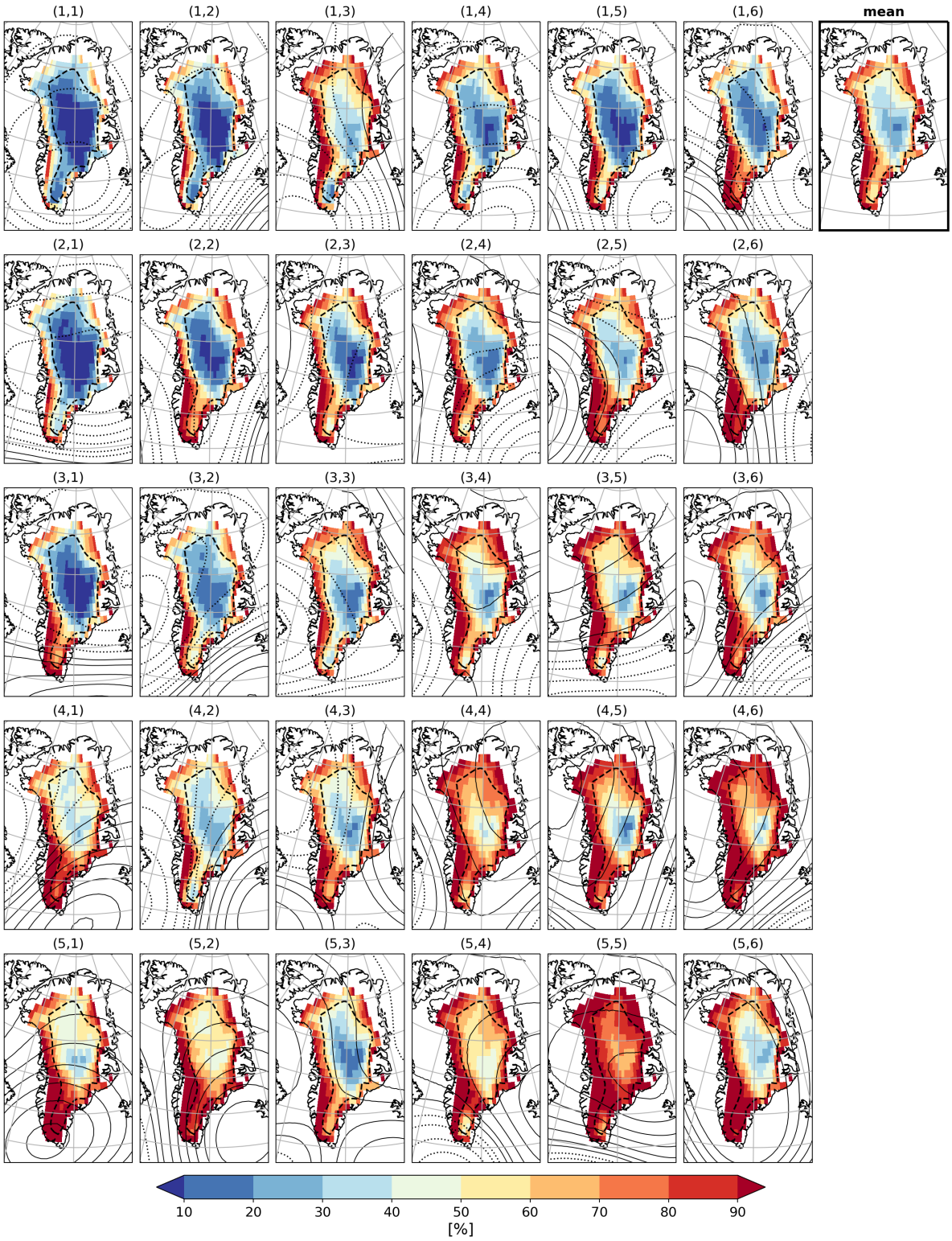

Figure C.4: The same as Fig. C.2 but for $\overline{\omega}^{LC}$ (top right panel) and $\overline{\omega}_i^{LC}$.

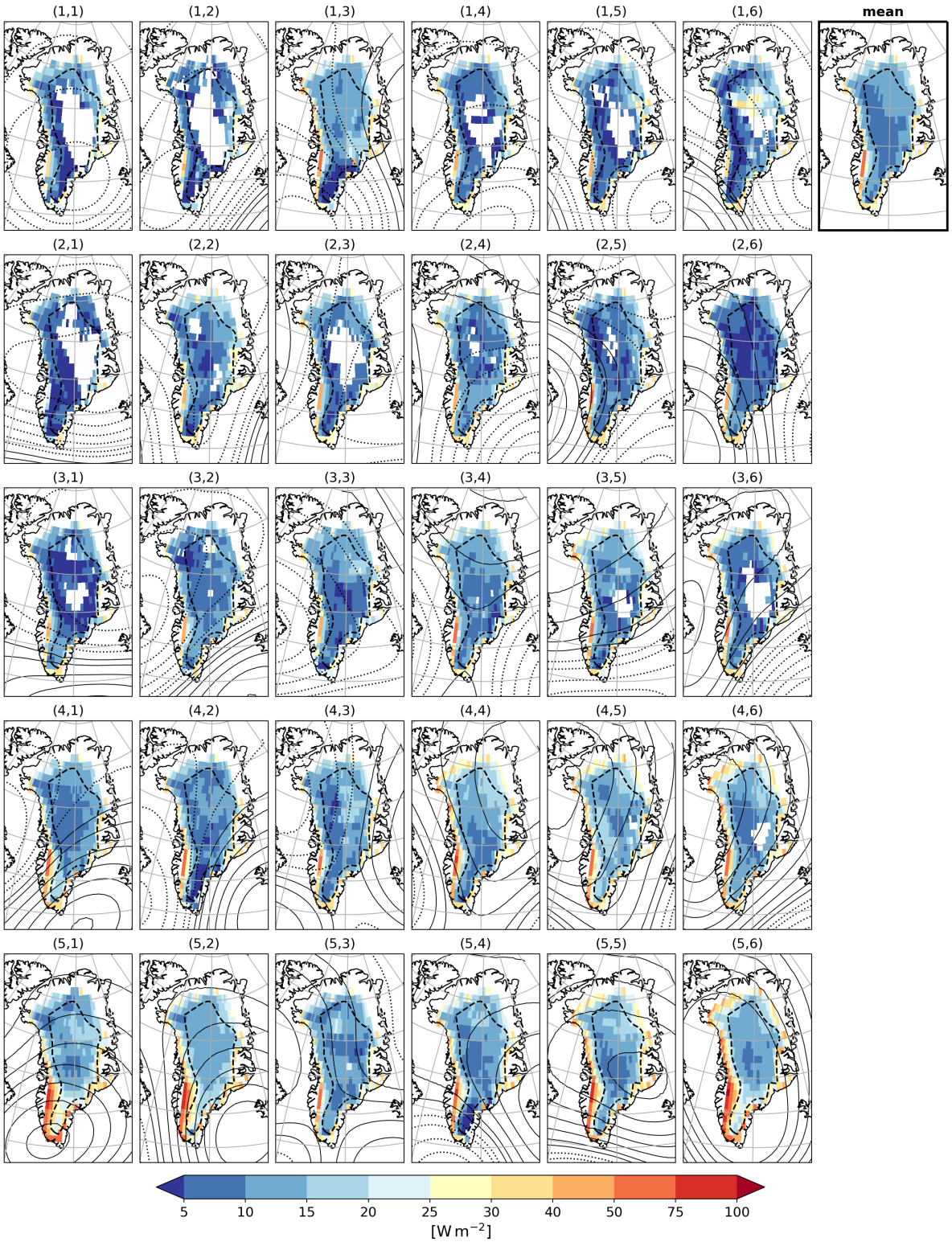

Figure C.5: The same as Fig. C.2 but for melt intensity $\overline{Q}^{PD}$ (top right panel) and $\overline{Q}_i^{PD}$.

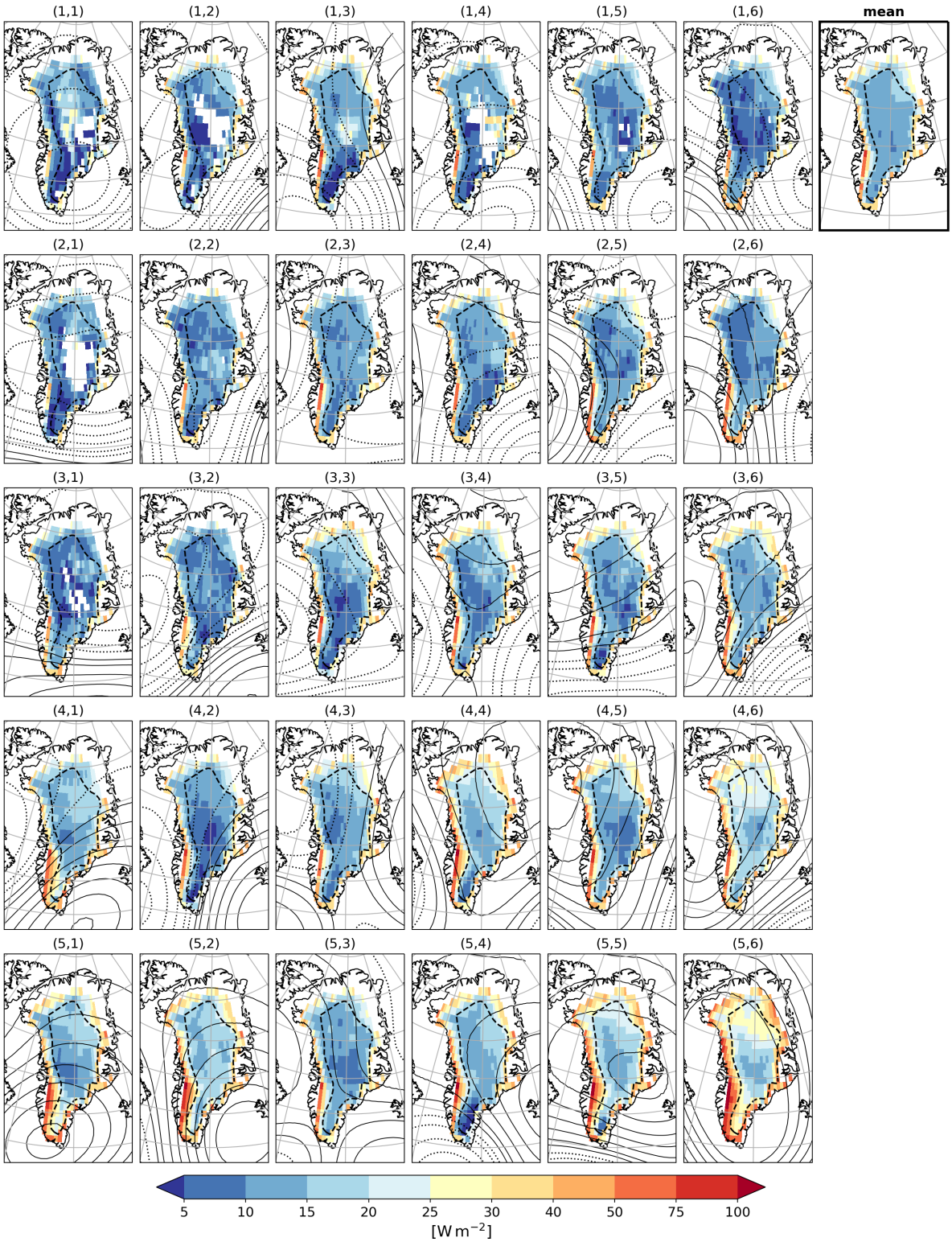

Figure C.6: The same as Fig. C.5 but for $\overline{Q}^{MC}$ (top right panel) and $\overline{Q}_i^{MC}$.

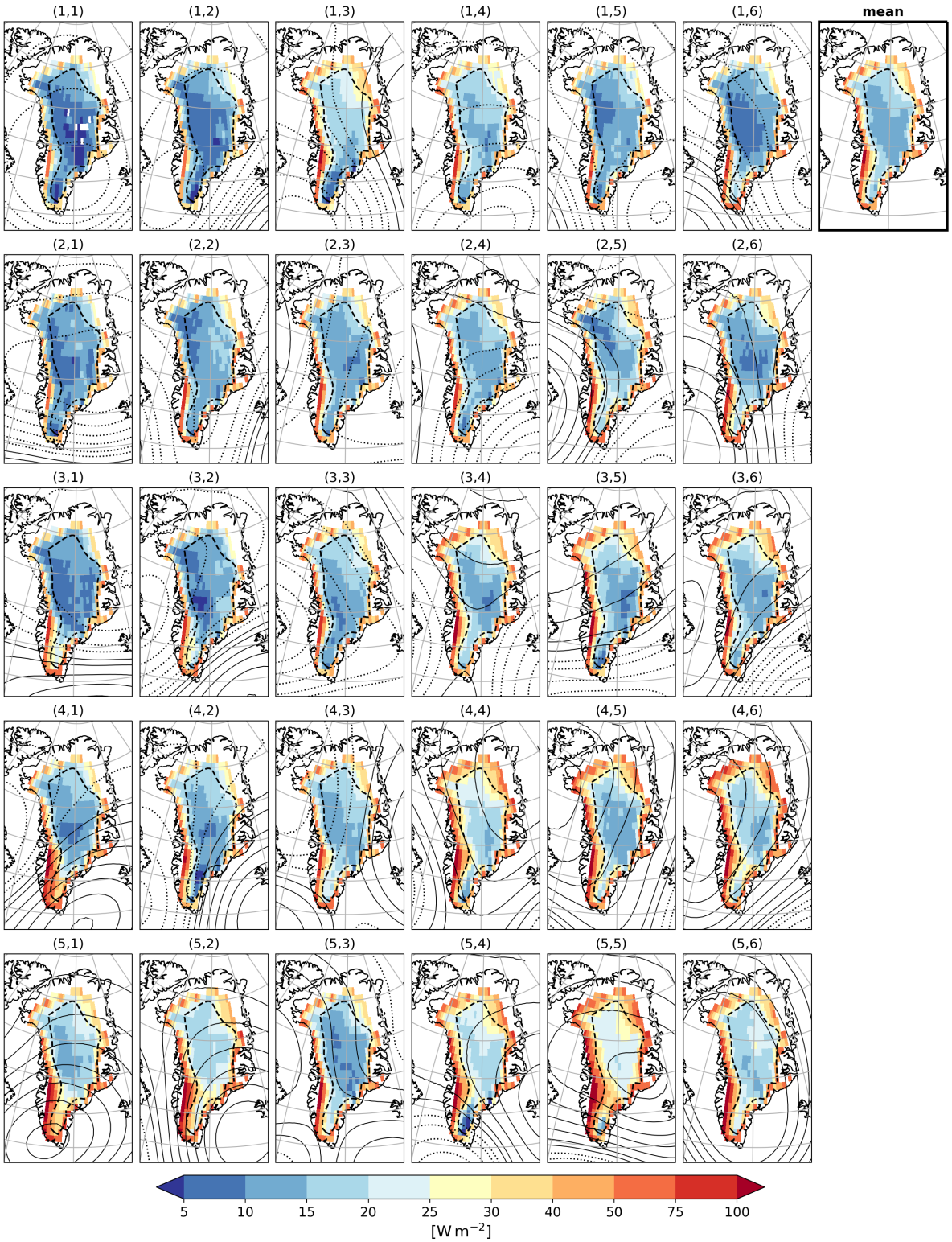

Figure C.7: The same as Fig. C.5 but for $\overline{Q}^{LC}$ (top right panel) and $\overline{Q}_i^{LC}$.

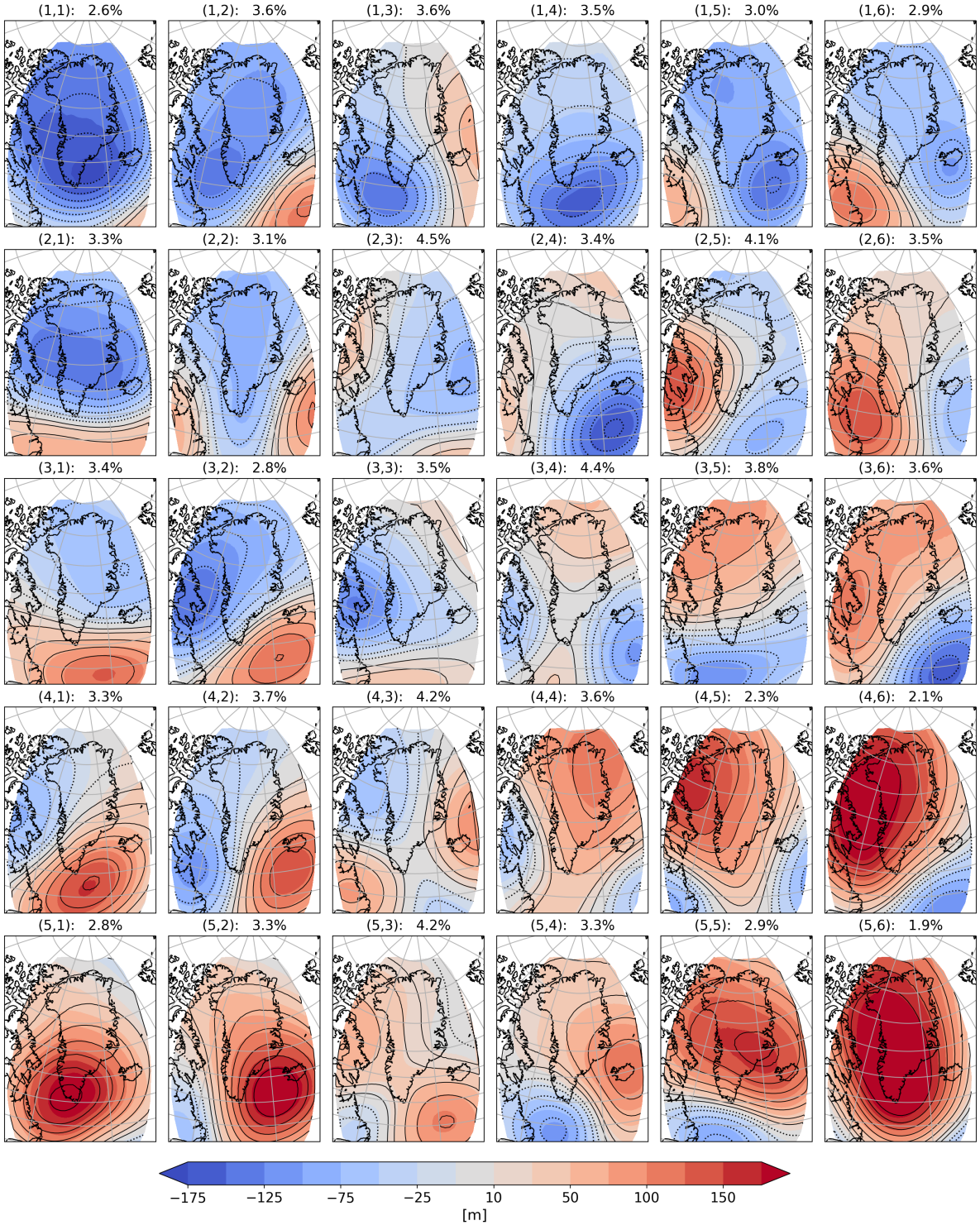

Figure C.8: Composites of $Z500'$ for all days attributed to the respective SOM nodes in PD (shading). Dotted (solid) black lines show the same negative (positive) $Z500'$ contours of the 30 SOM nodes according to Fig. 5.2. The title indicates the node frequency in PD.

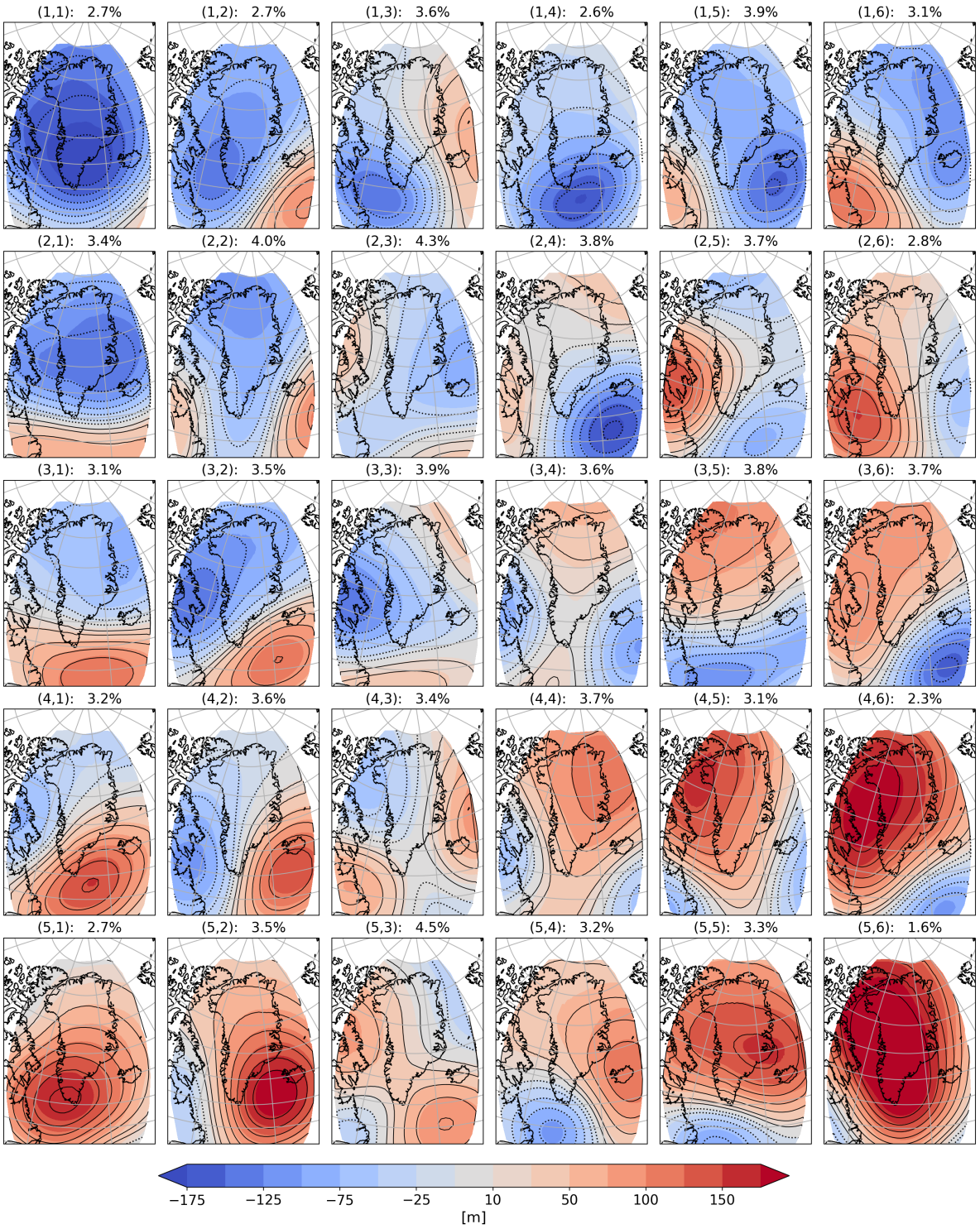

Figure C.9: The same as Fig. C.8 but for all days in LC.

References

Ali, S. M., O. Martius, and M. Röthlisberger, 2021: Recurrent Rossby wave packets modulate the persistence of dry and wet spells across the globe. *Geophys. Res. Lett.*, **48 (5)**, e2020GL091 452, doi:10.1029/2020GL091452.

Allen, C. D., D. D. Breshears, and N. G. McDowell, 2015: On underestimation of global vulnerability to tree mortality and forest die-off from hotter drought in the Anthropocene. *Ecosphere*, **6 (8)**, 129, doi:10.1890/ES15-00203.1.

Allen, C. D., and Coauthors, 2010: A global overview of drought and heat-induced tree mortality reveals emerging climate change risks for forests. *For. Ecol. Manag.*, **259 (4)**, 660–684, doi:10.1016/j.foreco.2009.09.001.

Anderegg, W. R. L., A. T. Trugman, G. Badgley, A. G. Konings, and J. Shaw, 2020: Divergent forest sensitivity to repeated extreme droughts. *Nat. Clim. Change*, **10 (12)**, 1091–1095, doi:10.1038/s41558-020-00919-1.

Anderegg, W. R. L., C. Schwalm, F. Biondi, J. J. Camarero, G. Koch, M. Litvak, K. Ogle, J. D. Shaw, E. Shevliakova, A. P. Williams, A. Wolf, E. Ziaco, and S. Pacala, 2015: Pervasive drought legacies in forest ecosystems and their implications for carbon cycle models. *Science*, **349 (6247)**, 528–532, doi:10.1126/science.aab1833.

Angélil, O., D. Stone, S. Perkins-Kirkpatrick, L. V. Alexander, M. Wehner, H. Shiogama, P. Wolski, A. Ciavarella, and N. Christidis, 2018: On the nonlinearity of spatial scales in extreme weather attribution statements. *Clim. Dyn.*, **50 (7–8)**, 2739–2752, doi:10.1007/s00382-017-3768-9.

Anyamba, A., and C. J. Tucker, 2012: Historical perspective of AVHRR NDVI and vegetation drought monitoring. *Remote Sensing of Drought: Innovative Monitoring Approaches*, B. D. Wardlow, M. C. Anderson, and J. P. Verdin, Eds., CRC Press/Taylor & Francis, Boca Raton, Florida, USA, 23–50.

Bachmair, S., M. Tanguy, J. Hannaford, and K. Stahl, 2018: How well do meteorological indicators represent agricultural and forest drought across Europe? *Environ. Res. Lett.*, **13 (3)**, 034 042, doi:10.1088/1748-9326/aaafda.

Balting, D., S. Michel, V. Nagavciuc, G. Helle, M. Freund, G. H. Schleser, D. Steger, G. Lohmann, and M. Ionita, 2022: A past, present and future perspective on the European summer vapour pressure deficit. *Earth Syst. Sci. Data Disc.*, 1–32, doi:10.5194/essd-2022-47.

Bandhauer, M., F. Isotta, M. Lakatos, C. Lussana, L. Båserud, B. Izsák, O. Szentes, O. E. Tveito, and C. Frei, 2022: Evaluation of daily precipitation analyses in E-OBS (v19.0e) and ERA5 by comparison to regional high-resolution datasets in European regions. *Int. J. Climatol.*, **42 (2)**, 727–747, doi:10.1002/joc.7269.

Barnett, T. P., and M. E. Schlesinger, 1987: Detecting changes in global climate induced by greenhouse gases. *J. Geophys. Res.*, **92 (D12)**, 14 772, doi:10.1029/JD092iD12p14772.

Barriopedro, D., E. M. Fischer, J. Luterbacher, R. M. Trigo, and R. García-Herrera, 2011: The hot summer of 2010: Redrawing the temperature record map of Europe. *Science*, **332 (6026)**, 220–224, doi:10.1126/science.1201224.

Bascietto, M., S. Bajocco, F. Mazzenga, and G. Matteucci, 2018: Assessing spring frost effects on beech forests in Central Apennines from remotely-sensed data. *Agric. For. Meteorol.*, **248**, 240–250, doi:10.1016/j.agrformet.2017.10.007.

Bastos, A., P. Ciais, T. Park, J. Zscheischler, C. Yue, J. Barichivich, R. B. Myneni, S. Peng, S. Piao, and Z. Zhu, 2017: Was the extreme Northern Hemisphere greening in 2015 predictable? *Environ. Res. Lett.*, **12 (4)**, 044 016, doi:10.1088/1748-9326/aa67b5.

Bastos, A., and Coauthors, 2020a: Direct and seasonal legacy effects of the 2018 heat wave and drought on European ecosystem productivity. *Sci. adv.*, **6 (24)**, eaba2724, doi:10.1126/sciadv.aba2724.

Bastos, A., and Coauthors, 2020b: Impacts of extreme summers on European ecosystems: a comparative analysis of 2003, 2010 and 2018. *Philos. Trans. R. Soc. B: Biol. Sci.*, **375 (1810)**, 20190 507, doi:10.1098/rstb.2019.0507.

Belleflamme, A., X. Fettweis, C. Lang, and M. Erpicum, 2013: Current and future atmospheric circulation at 500 hpa over Greenland simulated by the CMIP3 and CMIP5 global models. *Clim. Dyn.*, **41 (7-8)**, 2061–2080, doi:10.1007/s00382-012-1538-2.

Benassi, M., 2008: Drought and climate change in Morocco. analysis of precipitation field and water supply. *Options Méditerranéennes*, **80**, 83–87, accessed at 28-June-2023, http://om.ciheam.org/article.php?IDPDF=800423.

Bennartz, R., M. D. Shupe, D. D. Turner, V. P. Walden, K. Steffen, C. J. Cox, M. S. Kulie, N. Miller, and C. Pettersen, 2013: July 2012 Greenland melt extent enhanced by low-level liquid clouds. *Nature*, **496 (7443)**, 83–86, doi:10.1038/nature12002.

Berg, A., and J. Sheffield, 2018: Soil moisture–evapotranspiration coupling in CMIP5 models: Relationship with simulated climate and projections. *J. Clim.*, **31 (12)**, 4865–4878, doi:10.1175/JCLI-D-17-0757.1.

Betts, A. K., J. H. Ball, A. C. M. Beljaars, M. J. Miller, and P. A. Viterbo, 1996: The land surface-atmosphere interaction: A review based on observational and global modeling perspectives. *J. Geophys. Res.: Atmos.*, **101 (D3)**, 7209–7225, doi:10.1029/95JD02135.

Biedermann, P. H., and Coauthors, 2019: Bark beetle population dynamics in the Anthropocene: Challenges and solutions. *Trends Ecol. Evol.*, **34 (10)**, 914–924, doi:10.1016/j.tree.2019.06.002.

Bigler, C., and Y. Vitasse, 2021: Premature leaf discoloration of European deciduous trees is caused by drought and heat in late spring and cold spells in early fall. *Agric. For. Meteorol.*, **307**, 108 492, doi:10.1016/j.agrformet.2021.108492.

Blunden, J., and T. Boyer, 2021: State of the Climate in 2020. *Bull. Am. Meteorol. Soc.*, **102 (8)**, 1–475, doi:10.1175/2021BAMSStateoftheClimate.1.

Boers, N., and M. Rypdal, 2021: Critical slowing down suggests that the western Greenland Ice Sheet is close to a tipping point. *Proc. Natl. Acad. Sci. U. S. A.*, **118 (21)**, e2024192 118, doi:10.1073/pnas.2024192118.

Boettcher, M., M. Röthlisberger, R. Attinger, J. Rieder, and H. Wernli, 2023: The ERA5 extreme seasons explorer as a basis for research at the weather and climate interface. *Bull. Am. Meteorol. Soc.*, **104 (3)**, E631–E644, doi:10.1175/BAMS-D-21-0348.1.

Bose, A. K., and Coauthors, 2020: Growth and resilience responses of Scots pine to extreme droughts across Europe depend on predrought growth conditions. *Glob. Chang. Biol.*, **26 (8)**, 4521–4537, doi:10.1111/gcb.15153.

Bose, A. K., and Coauthors, 2021: Climate sensitivity and drought seasonality determine post-drought growth recovery of Quercus petraea and Quercus robur in Europe. *Sci. Total Environ.*, **784**, 147 222, doi:10.1016/j.scitotenv.2021.147222.

Box, J. E., X. Fettweis, J. C. Stroeve, M. Tedesco, D. K. Hall, and K. Steffen, 2012: Greenland ice sheet albedo feedback: Thermodynamics and atmospheric drivers. *Cryosphere*, **6 (4)**, 821–839, doi:10.5194/tc-6-821-2012.

Box, J. E., A. Wehrlé, D. As, R. S. Fausto, K. K. Kjeldsen, A. Dachauer, A. P. Ahlstrøm, and G. Picard, 2022a: Greenland Ice Sheet rainfall, heat and albedo feedback impacts from the mid-August 2021 atmospheric river. *Geophys. Res. Lett.*, **49 (11)**, e2021GL097 356, doi:10.1029/2021GL097356.

Box, J. E., A. Hubbard, D. B. Bahr, W. T. Colgan, X. Fettweis, K. D. Mankoff, A. Wehrlé, B. Noël, M. R. van den Broeke, B. Wouters, A. A. Bjørk, and R. S. Fausto, 2022b: Greenland ice sheet climate disequilibrium and committed sea-level rise. *Nat. Clim. Change*, **12 (9)**, 808–813, doi:10.1038/s41558-022-01441-2.

Breshears, D. D., H. D. Adams, D. Eamus, N. G. McDowell, D. J. Law, R. E. Will, A. P. Williams, and C. B. Zou, 2013: The critical amplifying role of increasing atmospheric moisture demand on tree mortality and associated regional die-off. *Front. Plant Sci.*, **4**, doi:10.3389/fpls.2013.00266.

Brodribb, T. J., J. Powers, H. Cochard, and B. Choat, 2020: Hanging by a thread? Forests and drought. *Science*, **368 (6488)**, 261–266, doi:10.1126/science.aat7631.

Brönnimann, S., and D. Krämer, 2016: Tambora and the "Year Without a Summer" of 1816. A perspective on Earth and Human Systems Science. *Geogr. Bern.*, **90**, 48 pp, doi:10.4480/GB2016.G90.01.

Brönnimann, S., E. Xoplaki, C. Casty, A. Pauling, and J. Luterbacher, 2006: ENSO influence on Europe during the last centuries. *Clim. Dyn.*, **28 (2–3)**, 181–197, doi:10.1007/s00382-006-0175-z.

Buras, A., A. Rammig, and C. S. Zang, 2020: Quantifying impacts of the 2018 drought on European ecosystems in comparison to 2003. *Biogeosciences*, **17 (6)**, 1655–1672, doi:10.5194/bg-17-1655-2020.

Buras, A., A. Rammig, and C. S. Zang, 2021: The European Forest Condition Monitor: Using remotely sensed forest greenness to identify hot spots of forest decline. *Front. Plant Sci.*, **12**, 2355, doi:10.3389/fpls.2021.689220.

Buras, A., C. Schunk, C. Zeiträg, C. Herrmann, L. Kaiser, H. Lemme, C. Straub, S. Taeger, S. Gößwein, H.-J. Klemmt, and A. Menzel, 2018: Are Scots pine forest edges particularly prone to drought-induced mortality? *Environ. Res. Lett.*, **13 (2)**, 025 001, doi:10.1088/1748-9326/aaa0b4.

Byrne, M. P., and P. A. O'Gorman, 2016: Understanding decreases in land relative humidity with global warming: Conceptual model and GCM simulations. *J. Clim.*, **29 (24)**, 9045–9061, doi:10.1175/JCLI-D-16-0351.1.

Büttner, G., J. Feranec, G. Jaffrain, L. Mari, G. Maucha, and T. Soukup, 2004: The CORINE Land Cover 2000 project. *EARSeL eProceedings*, 331–346, accessed at 26-September-2022, http://eproceedings.uni-oldenburg.de/website/vol03_3/03_3_buttner2.pdf.

Callendar, G. S., 1938: The artificial production of carbon dioxide and its influence on temperature. *Q. J. R. Meteorol. Soc.*, **64 (275)**, 223–240, doi:10.1002/qj.49706427503.

Camarero, J. J., Álvaro Rubio-Cuadrado, and A. Gazol, 2021: Climate windows of intra-annual growth and post-drought recovery in Mediterranean trees. *Agric. For. Meteorol.*, **308-309**, 108 606, doi:10.1016/j.agrformet.2021.108606.

Cassano, J. J., P. Uotila, A. H. Lynch, and E. N. Cassano, 2007: Predicted changes in synoptic forcing of net precipitation in large Arctic river basins during the 21st century. *J. Geophys. Res.: Biogeosci.*, **112 (G4)**, G04S49, doi:10.1029/2006JG000332.

Cattiaux, J., and A. Ribes, 2018: Defining single extreme weather events in a climate perspective. *Bull. Am. Meteorol. Soc.*, **99 (8)**, 1557–1568, doi:10.1175/BAMS-D-17-0281.1.

Christensen, O. B., M. Drews, J. H. Christensen, K. Dethloff, K. Ketelsen, I. Hebestadt, and A. Rinke, 2007: The HIRHAM regional climate model version 5 (beta). Tech. rep., Danish Climate Centre, Danish Meteorological Institute, Copenhagen, Denmark, 22 pp. Accessed at 28-June-2023: https://backend.orbit.dtu.dk/ws/portalfiles/portal/51950450/HIRHAM.pdf.

Ciais, P., and Coauthors, 2005: Europe-wide reduction in primary productivity caused by the heat and drought in 2003. *Nature*, **437 (7058)**, 529–533, doi:10.1038/nature03972.

Cindrić, K., M. T. Prtenjak, I. Herceg-Bulić, D. Mihajlović, and Z. Pasarić, 2016: Analysis of the extraordinary 2011/2012 drought in Croatia. *Theor. Appl. Climatol.*, **123 (3-4)**, 503–522, doi:10.1007/s00704-014-1368-8.

Coleman, J. S. M., and D. Budikova, 2013: Eastern U.S. summer streamflow during extreme phases of the North Atlantic Oscillation. *J. Geophys. Res.: Atmos.*, **118 (10)**, 4181–4193, doi:10.1002/jgrd.50326.

Compo, G. P., and Coauthors, 2011: The Twentieth Century Reanalysis Project. *Q. J. R. Meteorol. Soc.*, **137 (654)**, 1–28, doi:10.1002/qj.776.

Copernicus Atmosphere Monitoring Service, 2022: Europe's summer wildfire emissions highest in 15 years. Copernicus, accessed at 21-October-2022, https://atmosphere.copernicus.eu/europes-summer-wildfire-emissions-highest-15-years.

Copernicus Climate Change Service, 2022: Copernicus: Summer 2022 Europe's hottest on record. Copernicus, accessed at 10-October-2022, https://climate.copernicus.eu/copernicus-summer-2022-europes-hottest-record.

Dai, A., 2006: Recent climatology, variability, and trends in global surface humidity. *J. Clim.*, **19 (15)**, 3589–3606, doi:10.1175/JCLI3816.1.

Danabasoglu, G., and Coauthors, 2020: The Community Earth System Model Version 2 (CESM2). *J. Adv. Model. Earth Syst.*, **12 (2)**, doi:10.1029/2019MS001916.

Davies, H. C., 2015: Weather chains during the 2013/2014 winter and their significance for seasonal prediction. *Nat. Geosci.*, **8 (11)**, 833–837, doi:10.1038/ngeo2561.

Delhasse, A., X. Fettweis, C. Kittel, C. Amory, and C. Agosta, 2018: Brief communication: Impact of the recent atmospheric circulation change in summer on the future surface mass balance of the Greenland Ice Sheet. *Cryosphere*, **12**, 3409–3418, doi:10.5194/tc-12-3409-2018.

Delhasse, A., E. Hanna, C. Kittel, and X. Fettweis, 2021: Brief communication: CMIP6 does not suggest any atmospheric blocking increase in summer over Greenland by 2100. *Int. J. Climatol.*, **41 (4)**, 2589–2596, doi:10.1002/joc.6977.

Demirtaş, M., 2017: High impact heat waves over the Euro-Mediterranean region and Turkey – In concert with atmospheric blocking and large dynamical and physical anomalies. *Anadolu Univ. J. Sci. Technol. A - Appl. Sci. Eng.*, **18 (1)**, 97–97, doi:10.18038/aubtda.300426.

Deser, C., and Coauthors, 2020: Insights from Earth system model initial-condition large ensembles and future prospects. *Nat. Clim. Chang.*, **10 (4)**, 277–286, doi:10.1038/s41558-020-0731-2.

Didan, K., 2015: MOD13Q1 MODIS/Terra Vegetation Indices 16-Day L3 Global 250m SIN Grid V006. NASA EOSDIS Land Processes DAAC, accessed at 26-September-2022, https://doi.org/10.5067/MODIS/MOD13Q1.006.

Dios, V. R. D., J. Hedo, Àngel Cunill Camprubí, P. Thapa, E. M. del Castillo, J. M. de Aragón, J. A. Bonet, R. Balaguer-Romano, R. Díaz-Sierra, M. Yebra, and M. M. Boer, 2021: Climate change induced declines in fuel moisture may turn currently fire-free Pyrenean mountain forests into fire-prone ecosystems. *Sci. Total Environ.*, **797**, 149 104, doi:10.1016/j.scitotenv.2021.149104.

Dole, R., M. Hoerling, J. Perlwitz, J. Eischeid, P. Pegion, T. Zhang, X.-W. Quan, T. Xu, and D. Murray, 2011: Was there a basis for anticipating the 2010 Russian heat wave? *Geophys. Res. Lett.*, **38 (6)**, L06 702, doi:10.1029/2010GL046582.

Dunn, R. J. H., K. M. Willett, A. Ciavarella, and P. A. Stott, 2017: Comparison of land surface humidity between observations and CMIP5 models. *Earth Sci. Dyn.*, **8 (3)**, 719–747, doi:10.5194/esd-8-719-2017.

ECMWF, 2016: Part IV: Physical Processes. *IFS Documentation CY41R2*, ECMWF, chap. 4, 213 pp., doi:10.21957/tr5rv27xu.

EFFIS, 2022: EFFIS estimates for European Union. Copernicus, accessed at 21-October-2022, https://effis.jrc.ec.europa.eu/apps/effis.statistics/estimates.

Enderlin, E. M., I. M. Howat, S. Jeong, M.-J. Noh, J. H. Van Angelen, and M. R. Van Den Broeke, 2014: An improved mass budget for the Greenland ice sheet. *Geophys. Res. Lett.*, **41 (3)**, 866–872, doi:10.1002/2013GL059010.

Etzold, S., J. Wunder, S. Braun, B. Rohner, C. Bigler, M. Abegg, and A. Rigling, 2016: Mortalität von Waldbäumen: Ursache und Trends [in German]. *Wald im Klimawandel. Grundlagen für Adaptationsstrategien*, A. R. Pluess, S. Augustin, and P. Brang, Eds., Haupt Verlag, Bern, Stuttgart, Wien, 177–197.

Etzold, S., K. Ziemińska, B. Rohner, A. Bottero, A. K. Bose, N. K. Ruehr, A. Zingg, and A. Rigling, 2019: One century of forest monitoring data in Switzerland reveals species- and site-specific trends of climate-induced tree mortality. *Front. Plant Sci.*, **10**, 307, doi:10.3389/fpls.2019.00307.

Fausto, R. S., D. van As, J. E. Box, W. Colgan, P. L. Langen, and R. H. Mottram, 2016: The implication of nonradiative energy fluxes dominating Greenland ice sheet exceptional ablation area surface melt in 2012. *Geophys. Res. Lett.*, **43 (6)**, 2649–2658, doi:10.1002/2016GL067720.

Feichtinger, L. M., B. Eilmann, N. Buchmann, and A. Rigling, 2014: Growth adjustments of conifers to drought and to century-long irrigation. *For. Ecol. Manag.*, **334**, 96–105, doi:10.1016/j.foreco.2014.08.008.

Feichtinger, L. M., B. Eilmann, N. Buchmann, and A. Rigling, 2015: Trait-specific responses of Scots pine to irrigation on a short vs long time scale. *Tree Physiol.*, **35 (2)**, 160–171, doi:10.1093/treephys/tpu114.

Fettweis, X., 2007: Reconstruction of the 1979–2006 Greenland ice sheet surface mass balance using the regional climate model MAR. *Cryosphere*, **1 (1)**, 21–40, doi:10.5194/tc-1-21-2007.

Fettweis, X., 2020: Modèle atmosphérique régional v3.11. University of Liège, accessed at 20-October-20202, ftp://ftp.climato.be/fettweis/MARv3.11/Greenland/.

Fettweis, X., B. Franco, M. Tedesco, J. H. van Angelen, J. T. M. Lenaerts, M. R. van den Broeke, and H. Gallée, 2013a: Estimating the Greenland ice sheet surface mass balance contribution to future sea level rise using the regional atmospheric climate model MAR. *Cryosphere*, **7 (2)**, 469–489, doi:10.5194/tc-7-469-2013.

Fettweis, X., E. Hanna, C. Lang, A. Belleflamme, M. Erpicum, and H. Gallée, 2013b: Important role of the mid-tropospheric atmospheric circulation in the recent surface melt increase over the Greenland Ice Sheet. *Cryosphere*, **7**, 241–248, doi:10.5194/tc-7-241-2013.

Fettweis, X., J. E. Box, C. Agosta, C. Amory, C. Kittel, C. Lang, D. van As, H. Machguth, and H. Gallée, 2017: Reconstructions of the 1900-2015 Greenland ice sheet surface mass balance using the regional climate MAR model. *Cryosphere*, **11 (2)**, 1015–1033, doi:10.5194/tc-11-1015-2017.

Fettweis, X., and Coauthors, 2020: GrSMBMIP: Intercomparison of the modelled 1980–2012 surface mass balance over the Greenland Ice Sheet. *Cryosphere*, **14 (11)**, 3935–3958, doi:10.5194/tc-14-3935-2020.

Ficklin, D. L., and K. A. Novick, 2017: Historic and projected changes in vapor pressure deficit suggest a continental-scale drying of the United States atmosphere. *J. Geophys. Res.: Atmos.*, **122 (4)**, 2061–2079, doi:10.1002/2016JD025855.

Fischer, E. M., U. Beyerle, and R. Knutti, 2013: Robust spatially aggregated projections of climate extremes. *Nat. Clim. Change*, **3 (12)**, 1033–1038, doi:10.1038/nclimate2051.

Fischer, E. M., and R. Knutti, 2013: Robust projections of combined humidity and temperature extremes. *Nat. Clim. Change*, **3 (2)**, 126–130, doi:10.1038/nclimate1682.

Fischer, E. M., and R. Knutti, 2015: Anthropogenic contribution to global occurrence of heavy-precipitation and high-temperature extremes. *Nat. Clim. Chang.*, **5 (6)**, 560–564, doi:10.1038/nclimate2617.

Fischer, E. M., S. I. Seneviratne, P. L. Vidale, D. Lüthi, and C. Schär, 2007: Soil moisture-atmosphere interactions during the 2003 European summer heat wave. *J. Clim.*, **20 (20)**, 5081–5099, doi:10.1175/JCLI4288.1.

Flaounas, E., M. Röthlisberger, M. Boettcher, M. Sprenger, and H. Wernli, 2021: Extreme wet seasons – their definition and relationship with synoptic-scale weather systems. *Weather Clim. Dyn.*, **2 (1)**, 71–88, doi:10.5194/wcd-2-71-2021.

Forzieri, G., M. Girardello, G. Ceccherini, J. Spinoni, L. Feyen, H. Hartmann, P. S. A. Beck, G. Camps-Valls, G. Chirici, A. Mauri, and A. Cescatti, 2021: Emergent vulnerability to climate-driven disturbances in European forests. *Nat. Commun.*, **12 (1)**, 1081, doi:10.1038/s41467-021-21399-7.

Franco, B., X. Fettweis, and M. Erpicum, 2013: Future projections of the Greenland ice sheet energy balance driving the surface melt. *Cryosphere*, **7 (1)**, 1–18, doi:10.5194/tc-7-1-2013.

Franks, P. J., I. R. Cowan, and G. D. Farquhar, 1997: The apparent feedforward response of stomata to air vapour pressure deficit: information revealed by different experimental procedures with two rainforest trees. *Plant Cell Environ.*, **20 (1)**, 142–145, doi:10.1046/j.1365-3040.1997.d01-14.x.

Frei, E. R., M. M. Gossner, Y. Vitasse, V. Queloz, V. Dubach, A. Gessler, C. Ginzler, F. Hagedorn, K. Meusburger, M. Moor, E. S. Vives, A. Rigling, I. Uitentuis, G. von Arx, and T. Wohlgemuth, 2022: European beech dieback after premature leaf senescence during the 2018 drought in northern Switzerland. *Plant Biol.*, **24**, 1132–1145, doi:10.1111/plb.13467.

Fujiwara, M., and Coauthors, 2017: Introduction to the SPARC Reanalysis Intercomparison Project (S-RIP) and overview of the reanalysis systems. *Atmos. Chem. Phys.*, **17 (2)**, 1417–1452, doi:10.5194/acp-17-1417-2017.

Fyke, J. G., M. Vizcaíno, W. Lipscomb, and S. Price, 2014: Future climate warming increases Greenland ice sheet surface mass balance variability. *Geophys. Res. Lett.*, **41 (2)**, 470–475, doi:10.1002/2013GL058172.

Gallagher, M. R., M. D. Shupe, H. Chepfer, and T. L'Ecuyer, 2022: Relating snowfall observations to Greenland ice sheet mass changes: an atmospheric circulation perspective. *Cryosphere*, **16 (2)**, 435–450, doi:10.5194/tc-16-435-2022.

Gamelin, B. L., J. Feinstein, J. Wang, J. Bessac, E. Yan, and V. R. Kotamarthi, 2022: Projected U.S. drought extremes through the twenty-first century with vapor pressure deficit. *Sci. Rep.*, **12 (1)**, 8615, doi:10.1038/s41598-022-12516-7.

Gessler, A., A. Bottero, J. Marshall, and M. Arend, 2020: The way back: recovery of trees from drought and its implication for acclimation. *New Phytol.*, **228 (6)**, 1704–1709, doi:10.1111/nph.16703.

Gouveia, C., R. M. Trigo, and C. C. DaCamara, 2009: Drought and vegetation stress monitoring in Portugal using satellite data. *Nat. Hazards Earth Syst. Sci.*, **9 (1)**, 185–195, doi:10.5194/nhess-9-185-2009.

Grossiord, C., T. N. Buckley, L. A. Cernusak, K. A. Novick, B. Poulter, R. T. W. Siegwolf, J. S. Sperry, and N. G. McDowell, 2020: Plant responses to rising vapor pressure deficit. *New Phytol.*, **226 (6)**, 1550–1566, doi:10.1111/nph.16485.

Grossiord, C., A. Granier, S. Ratcliffe, O. Bouriaud, H. Bruelheide, E. Checko, D. I. Forrester, S. M. Dawud, L. Finer, M. Pollastrini, M. Scherer-Lorenzen, F. Valladares, D. Bonal, and A. Gessler, 2014: Tree diversity does not always improve resistance of forest ecosystems to drought. *Proc. Natl. Acad. Sci. U. S. A.*, **111 (41)**, 14 812–14 815, doi:10.1073/pnas.1411970111.

Hanna, E., X. Fettweis, and R. J. Hall, 2018: Brief communication: Recent changes in summer Greenland blocking captured by none of the CMIP5 models. *Cryosphere*, **12 (10)**, 3287–3292, doi:10.5194/tc-12-3287-2018.

Hanna, E., J. Cappelen, X. Fettweis, S. H. Mernild, T. L. Mote, R. Mottram, K. Steffen, T. J. Ballinger, and R. J. Hall, 2021: Greenland surface air temperature changes from 1981 to 2019 and implications for ice-sheet melt and mass-balance change. *Int. J. Climatol.*, **41 (S1)**, doi:10.1002/joc.6771.

Hansen, M. C., P. V. Potapov, R. Moore, M. Hancher, S. A. Turubanova, A. Tyukavina, D. Thau, S. V. Stehman, S. J. Goetz, T. R. Loveland, A. Kommareddy, A. Egorov, L. Chini, C. O. Justice, and J. R. G. Townshend, 2013: High-resolution global maps of 21st-century forest cover change. *Science*, **342 (6160)**, 850–853, doi:10.1126/science.1244693.

Hansen, W. D., N. B. Schwartz, A. P. Williams, K. Albrich, L. M. Kueppers, A. Rammig, C. P. O. Reyer, A. C. Staver, and R. Seidl, 2022: Global forests are influenced by the legacies of past inter-annual temperature variability. *Environ. Res.: Ecol.*, **1 (1)**, 011 001, doi:10.1088/2752-664X/ac6e4a.

Harpold, A. A., N. P. Molotch, K. N. Musselman, R. C. Bales, P. B. Kirchner, M. Litvak, and P. D. Brooks, 2015: Soil moisture response to snowmelt timing in mixed-conifer subalpine forests. *Hydrol. Process.*, **29 (12)**, 2782–2798, doi:10.1002/hyp.10400.

Hartmuth, K., M. Boettcher, H. Wernli, and L. Papritz, 2022: Identification, characteristics and dynamics of Arctic extreme seasons. *Weather Clim. Dyn.*, **3 (1)**, 89–111, doi:10.5194/wcd-3-89-2022.

Hartmuth, K., L. Papritz, M. Boettcher, and H. Wernli, 2023: Arctic seasonal variability and extremes, and the role of weather systems in a changing climate. *Geophys. Res. Lett.*, **50 (8)**, e2022GL102 349, doi:10.1029/2022GL102349.

Hasselmann, K., 1979: On the signal-to-noise problem in atmospheric response studies. *Meteorology over the tropical oceans*, D. B. Shaw, Ed., Royal Meteorological Society, Bracknell, United Kingdom, 251–259, accessed at 28-June-2023, https://hdl.handle.net/21.11116/0000-0003-12C3-C.

Hawkins, E., and R. Sutton, 2012: Time of emergence of climate signals. *Geophys. Res. Lett.*, **39 (1)**, L01 702, doi:10.1029/2011GL050087.

Hegerl, G. C., H. von Storch, K. Hasselmann, B. D. Santer, U. Cubasch, and P. D. Jones, 1996: Detecting greenhouse-gas-induced climate change with an optimal fingerprint method. *J. Clim.*, **9 (10)**, 2281–2306, doi:10.1175/1520-0442(1996)009<2281:DGGICC>2.0.CO;2.

Held, I. M., and B. J. Soden, 2006: Robust responses of the hydrological cycle to global warming. *J. Clim.*, **19 (21)**, 5686–5699, doi:10.1175/JCLI3990.1.

Hermann, M., 2022: Normalized difference vegetation index (NDVI) based low forest greenness events in europe in 2002–2022 (1.0) [dataset]. ETH Zurich Research Collection, https://doi.org/10.3929/ethz-b-000505559.

Hermann, M., L. Papritz, and H. Wernli, 2020: A Lagrangian analysis of the dynamical and thermodynamic drivers of large-scale Greenland melt events during 1979–2017. *Weather Clim. Dyn.*, **1 (2)**, 497–518, doi:10.5194/wcd-1-497-2020.

Hermann, M., M. Röthlisberger, A. Gessler, A. Rigling, C. Senf, T. Wohlgemuth, and H. Wernli, 2023: Meteorological history of low-forest-greenness events in Europe in 2002–2022. *Biogeosciences*, **20 (6)**, 1155–1180, doi:10.5194/bg-20-1155-2023.

Hersbach, H., and Coauthors, 2020: The ERA5 global reanalysis. *Q. J. R. Meteorol. Soc.*, **146 (730)**, 1999–2049, doi:10.1002/qj.3803.

Hlásny, T., J. Trombik, M. Bošeľa, J. Merganič, R. Marušák, V. Šebeň, P. Štěpánek, J. Kubišta, and M. Trnka, 2017: Climatic drivers of forest productivity in Central Europe. *Agric. For. Meteorol.*, **234-235**, 258–273, doi:10.1016/j.agrformet.2016.12.024.

Hofer, S., C. Lang, C. Amory, C. Kittel, A. Delhasse, A. Tedstone, and X. Fettweis, 2020: Greater Greenland Ice Sheet contribution to global sea level rise in CMIP6. *Nat. Commun.*, **11 (1)**, 6289, doi:10.1038/s41467-020-20011-8.

Hofer, S., A. J. Tedstone, X. Fettweis, and J. L. Bamber, 2017: Decreasing cloud cover drives the recent mass loss on the Greenland ice sheet. *Sci. Adv.*, **3 (6)**, e1700 584, doi:10.1126/sciadv.1700584.

Hofer, S., A. J. Tedstone, X. Fettweis, and J. L. Bamber, 2019: Cloud microphysics and circulation anomalies control differences in future Greenland melt. *Nat. Clim. Chang.*, **9 (7)**, 523–528, doi:10.1038/s41558-019-0507-8.

Hoskins, B., 2013: The potential for skill across the range of the seamless weather-climate prediction problem: A stimulus for our science. *Quart. J. Roy. Meteor. Soc.*, **139 (672)**, 573–584, doi:10.1002/qj.1991.

Hsiao, J., A. L. Swann, and S.-H. Kim, 2019: Maize yield under a changing climate: The hidden role of vapor pressure deficit. *Agric. For. Meteorol.*, **279**, 107 692, doi:10.1016/j.agrformet.2019.107692.

Hurrell, J. W., 1995: Decadal trends in the North Atlantic Oscillation: Regional temperatures and precipitation. *Science*, **269 (5224)**, 676–679, doi:10.1126/science.269.5224.676.

Hurrell, J. W., and Coauthors, 2013: The Community Earth System Model: A framework for collaborative research. *Bull. Am. Meteorol. Soc.*, **94 (9)**, 1339–1360, doi:10.1175/BAMS-D-12-00121.1.

IMBIE Team, 2020: Mass balance of the Greenland Ice Sheet from 1992 to 2018. *Nature*, **579 (7798)**, 233–239, doi:10.1038/s41586-019-1855-2.

IPCC, 2021: Climate Change 2021: The physical science basis. Contribution of Working Group I to the Sixth Assessment Report of the Intergovernmental Panel on Climate Change. *IPCC*, 2391 pp., doi:10.1017/9781009157896.

Izeboud, M., S. Lhermitte, K. van Tricht, J. T. M. Lenaerts, N. P. M. van Lipzig, and N. Wever, 2020: The spatiotemporal variability of cloud radiative effects on the Greenland Ice Sheet surface mass balance. *Geophys. Res. Lett.*, **47 (12)**, e2020GL087 315, doi:10.1029/2020GL087315.

Jakoby, O., H. Lischke, and B. Wermelinger, 2019: Climate change alters elevational phenology patterns of the European spruce bark beetle (Ips typographus). *Glob. Chang. Biol.*, **25 (12)**, 4048–4063, doi:10.1111/gcb.14766.

John, V. O., and B. J. Soden, 2007: Temperature and humidity biases in global climate models and their impact on climate feedbacks. *Geophys. Res. Lett.*, **34 (18)**, L18 704, doi:10.1029/2007GL030429.

Kannenberg, S. A., K. A. Novick, M. R. Alexander, J. T. Maxwell, D. J. P. Moore, R. P. Phillips, and W. R. L. Anderegg, 2019: Linking drought legacy effects across scales: From leaves to tree rings to ecosystems. *Glob. Chang. Biol.*, **25 (9)**, 2978–2992, doi:10.1111/gcb.14710.

Kautz, L.-A., O. Martius, S. Pfahl, J. G. Pinto, A. M. Ramos, P. M. Sousa, and T. Woollings, 2022: Atmospheric blocking and weather extremes over the Euro-Atlantic sector – a review. *Weather Clim. Dyn.*, **3 (1)**, 305–336, doi:10.5194/wcd-3-305-2022.

Kay, J. E., and Coauthors, 2015: The Community Earth System Model (CESM) Large Ensemble Project: A community resource for studying climate change in the presence of internal climate variability. *Bull. Am. Meteorol. Soc.*, **96 (8)**, 1333–1349, doi:10.1175/BAMS-D-13-00255.1.

Kennedy, R. E., Z. Yang, and W. B. Cohen, 2010: Detecting trends in forest disturbance and recovery using yearly landsat time series: 1. LandTrendr temporal segmentation algorithms. *Remote Sens. Environ.*, **114 (12)**, 2897–2910, doi:10.1016/j.rse.2010.07.008.

Kirchmeier-Young, M. C., H. Wan, X. Zhang, and S. I. Seneviratne, 2019: Importance of framing for extreme event attribution: The role of spatial and temporal scales. *Earth's Future*, **7 (10)**, 1192–1204, doi:10.1029/2019EF001253.

Kittl, B., 2022: Drought 2018: Beech trees with early discoloured foliage tend to die in subsequent years. Swiss Federal Institute for Forest, Snow and Landscape Research WSL, accessed at 25-October-2022, https://www.wsl.ch/en/newsseiten/2022/09/drought-2018-beech-trees-with-early-discoloured-foliage-tend-to-die-in-subsequent-years.html.

Kohonen, T., 1982: Self-organized formation of topologically correct feature maps. *Biol. Cybern.*, **43 (1)**, 59–69, doi:10.1007/BF00337288.

Lawrence, D. M., and Coauthors, 2019: The Community Land Model version 5: Description of new features, benchmarking, and impact of forcing uncertainty. *J. Adv. Model. Earth Syst.*, **11 (12)**, 4245–4287, doi:10.1029/2018MS001583.

Le clec'h, S., S. Charbit, A. Quiquet, X. Fettweis, C. Dumas, M. Kageyama, C. Wyard, and C. Ritz, 2019: Assessment of the Greenland ice sheet–atmosphere feedbacks for the next century with a regional atmospheric model coupled to an ice sheet model. *Cryosphere*, **13 (1)**, 373–395, doi:10.5194/tc-13-373-2019.

Lenaerts, J. T. M., M. D. Camron, C. R. Wyburn-Powell, and J. E. Kay, 2020: Present-day and future Greenland Ice Sheet precipitation frequency from CloudSat observations and the Community Earth System Model. *Cryosphere*, **14 (7)**, 2253–2265, doi:10.5194/tc-14-2253-2020.

Lesk, C., W. Anderson, A. Rigden, O. Coast, J. Jägermeyr, S. McDermid, K. F. Davis, and M. Konar, 2022: Compound heat and moisture extreme impacts on global crop yields under climate change. *Nat. Rev. Earth Environ.*, **3 (12)**, 872–889, doi:10.1038/s43017-022-00368-8.

Liu, Y., and R. H. Weisberg, 2011: A review of Self-Organizing Map – Applications in meteorology and oceanography. *Self Organizing Maps*, J. I. Mwasiagi, Ed., IntechOpen, Rijeka, Croatia, chap. 13, 253–272, doi:10.5772/13146.

Liu, Y., R. H. Weisberg, and C. N. K. Mooers, 2006: Performance evaluation of the self-organizing map for feature extraction. *J. Geophys. Res.: Oceans*, **111 (C5)**, C05 018, doi:10.1029/2005JC003117.

Lloret, F., D. Siscart, and C. Dalmases, 2004: Canopy recovery after drought dieback in holm-oak Mediterranean forests of Catalonia (NE Spain). *Glob. Chang. Biol.*, **10 (12)**, 2092–2099, doi:10.1111/j.1365-2486.2004.00870.x.

Lobell, D. B., M. J. Roberts, W. Schlenker, N. Braun, B. B. Little, R. M. Rejesus, and G. L. Hammer, 2014: Greater sensitivity to drought accompanies maize yield increase in the U.S. Midwest. *Science*, **344 (6183)**, 516–519, doi:10.1126/science.1251423.

Lorenz, E. N., 1963: Deterministic nonperiodic flow. *J. Atmos. Sci.*, **20 (2)**, 130–141, doi:10.1175/1520-0469(1963)020<0130:DNF>2.0.CO;2.

Luterbacher, J., and C. Pfister, 2015: The year without a summer. *Nat. Geosci.*, **8 (4)**, 246–248, doi:10.1038/ngeo2404.

Maher, N., S. Milinski, and R. Ludwig, 2021: Large ensemble climate model simulations: introduction, overview, and future prospects for utilising multiple types of large ensemble. *Earth Syst. Dyn.*, **12 (2)**, 401–418, doi:10.5194/esd-12-401-2021.

Mahlstein, I., R. Knutti, S. Solomon, and R. W. Portmann, 2011: Early onset of significant local warming in low latitude countries. *Environ. Res. Lett.*, **6 (3)**, 034 009, doi:10.1088/1748-9326/6/3/034009.

Mattingly, K. S., T. L. Mote, and X. Fettweis, 2018: Atmospheric river impacts on Greenland Ice Sheet surface mass balance. *J. Geophys. Res.: Atmos.*, **123 (16)**, 8538–8560, doi:10.1029/2018JD028714.

Mattingly, K. S., C. A. Ramseyer, J. J. Rosen, T. L. Mote, and R. Muthyala, 2016: Increasing water vapor transport to the Greenland Ice Sheet revealed using self-organizing maps. *Geophys. Res. Lett.*, **43 (17)**, 9250–9258, doi:10.1002/2016GL070424.

McDowell, N. G., and Coauthors, 2016: Multi-scale predictions of massive conifer mortality due to chronic temperature rise. *Nat. Clim. Change*, **6 (3)**, 295–300, doi:10.1038/nclimate2873.

McDowell, N. G., and Coauthors, 2020: Pervasive shifts in forest dynamics in a changing world. *Science*, **368 (6494)**, eaaz9463, doi:10.1126/science.aaz9463.

Meehl, G. A., R. Lukas, G. N. Kiladis, K. M. Weickmann, A. J. Matthews, and M. Wheeler, 2001: A conceptual framework for time and space scale interactions in the climate system. *Clim. Dyn.*, **17 (10)**, 753–775, doi:10.1007/s003820000143.

Meehl, G. A., and C. Tebaldi, 2004: More intense, more frequent, and longer lasting heat waves in the 21st century. *Science*, **305 (5686)**, 994–997, doi:10.1126/science.1098704.

Mekonnen, Z. A., R. F. Grant, and C. Schwalm, 2017: Carbon sources and sinks of North America as affected by major drought events during the past 30 years. *Agric. For. Meteorol.*, **244-245**, 42–56, doi:10.1016/j.agrformet.2017.05.006.

Messori, G., M. Wu, G. Vico, and V. M. Galfi, 2022: Atmospheric jet stream variability reflects vegetation activity in Europe. *Agric. For. Meteorol.*, **322**, 109 008, doi:10.1016/j.agrformet.2022.109008.

Mioduszewski, J. R., A. K. Rennermalm, A. Hammann, M. Tedesco, E. U. Noble, J. C. Stroeve, and T. L. Mote, 2016: Atmospheric drivers of Greenland surface melt revealed by self-organizing maps. *J. Geophys. Res.: Atmos.*, **121 (10)**, 5095–5114, doi:10.1002/2015JD024550.

Miralles, D. G., P. Gentine, S. I. Seneviratne, and A. J. Teuling, 2019: Land-atmospheric feedbacks during droughts and heatwaves: state of the science and current challenges. *Ann. N. Y. Acad. Sci.*, **1436 (1)**, 19–35, doi:10.1111/nyas.13912.

Mohr, S., J. Wilhelm, J. Wandel, M. Kunz, R. Portmann, H. J. Punge, M. Schmidberger, J. F. Quinting, and C. M. Grams, 2020: The role of large-scale dynamics in an exceptional sequence of severe thunderstorms in Europe May–June 2018. *Weather Clim. Dyn.*, **1 (2)**, 325–348, doi:10.5194/wcd-1-325-2020.

Mora, C., A. G. Frazier, R. J. Longman, R. S. Dacks, M. M. Walton, E. J. Tong, J. J. Sanchez, L. R. Kaiser, Y. O. Stender, J. M. Anderson, C. M. Ambrosino, I. Fernandez-Silva, L. M. Giuseffi, and T. W. Giambelluca, 2013: The projected timing of climate departure from recent variability. *Nature*, **502 (7470)**, 183–187, doi:10.1038/nature12540.

Mouginot, J., E. Rignot, A. A. Bjørk, M. van den Broeke, R. Millan, M. Morlighem, B. Noël, B. Scheuchl, and M. Wood, 2019: Forty-six years of Greenland ice sheet mass balance from 1972 to 2018. *Proc. Natl. Acad. Sci. U. S. A.*, **116 (19)**, 9239–9244, doi:10.1073/pnas.1904242116.

Muntjewerf, L., M. Petrini, M. Vizcaino, C. E. da Silva, R. Sellevold, M. D. W. Scherrenberg, K. Thayer-Calder, S. L. Bradley, J. T. M. Lenaerts, W. H. Lipscomb, and M. Lofverstrom, 2020: Greenland ice sheet contribution to 21st century sea level rise as simulated by the coupled CESM2.1-CISM2.1. *Geophys. Res. Lett.*, **47 (9)**, doi:10.1029/2019GL086836.

Murray, F. W., 1967: On the computation of saturation vapor pressure. *J. Appl. Meteorol. Climatol.*, **6 (1)**, 203–204, doi:10.1175/1520-0450(1967)006<0203:OTCOSV>2.0.CO;2.

Muñoz-Sabater, J., and Coauthors, 2021: ERA5-Land: a state-of-the-art global reanalysis dataset for land applications. *Earth Syst. Sci. Data*, **13 (9)**, 4349–4383, doi:10.5194/essd-13-4349-2021.

Nagel, T. A., S. Mikac, M. Dolinar, M. Klopcic, S. Keren, M. Svoboda, J. Diaci, A. Boncina, and V. Paulic, 2017: The natural disturbance regime in forests of the Dinaric Mountains: A synthesis of evidence. *For. Ecol. Manag.*, **388**, 29–42, doi:10.1016/j.foreco.2016.07.047.

Namias, J., 1978: Multiple causes of the North American abnormal winter 1976–77. *Mon. Weather Rev.*, **106 (3)**, 279–295, doi:10.1175/1520-0493(1978)106<0279:MCOTNA>2.0.CO;2.

National Academies of Science Engineering and Medicine, 2016: *Attribution of Extreme Weather Events in the Context of Climate Change*. National Academies Press, Washington, D.C., USA, doi:10.17226/21852.

Neumann, M., V. Mues, A. Moreno, H. Hasenauer, and R. Seidl, 2017: Climate variability drives recent tree mortality in Europe. *Glob. Chang. Biol.*, **23 (11)**, 4788–4797, doi:10.1111/gcb.13724.

Nghiem, S. V., D. K. Hall, T. L. Mote, M. Tedesco, M. R. Albert, K. Keegan, C. Shuman, N. E. DiGirolamo, and G. Neumann, 2012: The extreme melt across the Greenland ice sheet in 2012. *Geophys. Res. Lett.*, **39 (20)**, L20 502, doi:10.1029/2012GL053611.

NOAA Global Monitoring Laboratory, 2023: Carbon Cycle Greenhouse Gases. National Oceanic and Atmospheric Administration, accessed at 21-June-2023, https://gml.noaa.gov/ccgg/.

Nojarov, P., and M. Nikolova, 2022: Heat waves and forest fires in Bulgaria. *Nat. Hazards*, **114 (2)**, 1879–1899, doi:10.1007/s11069-022-05451-3.

Noël, B., W. Jan van De Berg, H. Machguth, S. Lhermitte, I. Howat, X. Fettweis, and M. R. Van Den Broeke, 2016: A daily, 1 km resolution data set of downscaled Greenland ice sheet surface mass balance (1958–2015). *Cryosphere*, **10 (5)**, 2361–2377, doi:10.5194/tc-10-2361-2016.

Noël, B., J. T. M. Lenaerts, W. H. Lipscomb, K. Thayer-Calder, and M. R. van den Broeke, 2022: Peak refreezing in the Greenland firn layer under future warming scenarios. *Nat. Commun.*, **13 (1)**, 6870, doi:10.1038/s41467-022-34524-x.

Noël, B., L. van Kampenhout, J. T. M. Lenaerts, W. J. van de Berg, and M. R. van den Broeke, 2021: A 21st century warming threshold for sustained Greenland Ice Sheet mass loss. *Geophys. Res. Lett.*, **48 (5)**, doi:10.1029/2020GL090471.

Noël, B., L. van Kampenhout, W. J. van de Berg, J. T. M. Lenaerts, B. Wouters, and M. R. van den Broeke, 2020: Brief communication: CESM2 climate forcing (1950–2014) yields realistic Greenland ice sheet surface mass balance. *Cryosphere*, **14 (4)**, 1425–1435, doi:10.5194/tc-14-1425-2020.

Ogaya, R., D. Liu, A. Barbeta, and J. Peñuelas, 2020: Stem mortality and forest dieback in a 20-years experimental drought in a Mediterranean holm oak forest. *Front. For. Glob. Chang.*, **2**, eaaz9463, doi:10.3389/ffgc.2019.00089.

Oren, R., J. S. Sperry, G. G. Katul, D. E. Pataki, B. E. Ewers, N. Phillips, and K. V. R. Schäfer, 1999: Survey and synthesis of intra- and interspecific variation in stomatal sensitivity to vapour pressure deficit. *Plant Cell Environ.*, **22 (12)**, 1515–1526, doi:10.1046/j.1365-3040.1999.00513.x.

Orth, R., J. Zscheischler, and S. I. Seneviratne, 2016: Record dry summer in 2015 challenges precipitation projections in Central Europe. *Sci. Rep.*, **6**, 28 334, doi:10.1038/srep28334.

O'Neill, B. C., E. Kriegler, K. Riahi, K. L. Ebi, S. Hallegatte, T. R. Carter, R. Mathur, and D. P. van Vuuren, 2014: A new scenario framework for climate change research: the concept of shared socioeconomic pathways. *Clim. Chang.*, **122 (3)**, 387–400, doi:10.1007/s10584-013-0905-2.

Pausas, J. G., and E. Ribeiro, 2013: The global fire-productivity relationship. *Glob. Ecol. Biogeogr.*, **22 (6)**, 728–736, doi:10.1111/geb.12043.

Peters, W., A. Bastos, P. Ciais, and A. Vermeulen, 2020: A historical, geographical and ecological perspective on the 2018 European summer drought. *Philos. Trans. R. Soc. B: Biol. Sci.*, **375 (1810)**, 20190 505, doi:10.1098/rstb.2019.0505.

Peñuelas, J., F. Lloret, and R. Montoya, 2001: Severe drought effects on Mediterranean woody flora in Spain. *For. Sci.*, **47**, 214–218, doi:10.1093/forestscience/47.2.214.

Pfahl, S., and H. Wernli, 2012a: Quantifying the relevance of atmospheric blocking for co-located temperature extremes in the Northern Hemisphere on (sub-)daily time scales. *Geophys. Res. Lett.*, **39 (12)**, L12 807, doi:10.1029/2012GL052261.

Pfahl, S., and H. Wernli, 2012b: Quantifying the relevance of cyclones for precipitation extremes. *J. Clim.*, **25 (19)**, 6770–6780, doi:10.1175/JCLI-D-11-00705.1.

Preece, J. R., L. J. Wachowicz, T. L. Mote, M. Tedesco, and X. Fettweis, 2022: Summer Greenland blocking diversity and its impact on the surface mass balance of the Greenland Ice Sheet. *J. Geophys. Res.: Atmos.*, **127 (4)**, doi:10.1029/2021JD035489.

Rigling, A., H. Brühlhart, O. U. Bräker, T. Forster, and F. H. Schweingruber, 2003: Effects of irrigation on diameter growth and vertical resin duct production in Pinus sylvestris l. on dry

sites in the central Alps, Switzerland. *For. Ecol. Manag.*, **175 (1-3)**, 285–296, doi:10.1016/S0378-1127(02)00136-6.

Rita, A., J. J. Camarero, A. Nolè, M. Borghetti, M. Brunetti, N. Pergola, C. Serio, S. M. Vicente-Serrano, V. Tramutoli, and F. Ripullone, 2020: The impact of drought spells on forests depends on site conditions: The case of 2017 summer heat wave in southern Europe. *Glob. Chang. Biol.*, **26 (2)**, 851–863, doi:10.1111/gcb.14825.

Rodgers, K. B., and Coauthors, 2021: Ubiquity of human-induced changes in climate variability. *Earth Sci. Dyn.*, **12 (4)**, 1393–1411, doi:10.5194/esd-12-1393-2021.

Rohrer, M., S. Brönnimann, O. Martius, C. C. Raible, M. Wild, and G. P. Compo, 2018: Representation of extratropical cyclones, blocking anticyclones, and alpine circulation types in multiple reanalyses and model simulations. *J. Clim.*, **31 (8)**, 3009–3031, doi:10.1175/JCLI-D-17-0350.1.

Rousi, E., and Coauthors, 2023: The extremely hot and dry 2018 summer in central and northern Europe from a multi-faceted weather and climate perspective. *Nat. Hazards Earth Syst. Sci.*, **23 (5)**, 1699–1718, doi:10.5194/nhess-23-1699-2023.

Russo, A., C. M. Gouveia, E. Dutra, P. M. M. Soares, and R. M. Trigo, 2019: The synergy between drought and extremely hot summers in the Mediterranean. *Environ. Res. Lett.*, **14 (1)**, 014 011, doi:10.1088/1748-9326/aaf09e.

Röthlisberger, M., M. Hermann, C. Frei, F. Lehner, E. M. Fischer, R. Knutti, and H. Wernli, 2021: A new framework for identifying and investigating seasonal climate extremes. *J. Clim.*, **34 (19)**, doi:10.1175/JCLI-D-20-0953.1.

Röthlisberger, M., and O. Martius, 2019: Quantifying the local effect of Northern Hemisphere atmospheric blocks on the persistence of summer hot and dry spells. *Geophys. Res. Lett.*, **46 (16)**, 10 101–10 111, doi:10.1029/2019GL083745.

Röthlisberger, M., and L. Papritz, 2023: Quantifying the physical processes leading to atmospheric hot extremes at a global scale. *Nat. Geosci.*, **16 (3)**, 210–216, doi:10.1038/s41561-023-01126-1.

Röthlisberger, M., S. Pfahl, and O. Martius, 2016: Regional-scale jet waviness modulates the occurrence of midlatitude weather extremes. *Geophys. Res. Lett.*, **43 (20)**, 10 989–10 997, doi:10.1002/2016GL070944.

Röthlisberger, M., M. Sprenger, E. Flaounas, U. Beyerle, and H. Wernli, 2020: The substructure of extremely hot summers in the Northern Hemisphere. *Weather Clim. Dyn.*, **1 (1)**, 45–62, doi:10.5194/wcd-1-45-2020.

Rüdisühli, S., M. Sprenger, D. Leutwyler, C. Schär, and H. Wernli, 2020: Attribution of precipitation to cyclones and fronts over Europe in a kilometer-scale regional climate simulation. *Weather Clim. Dyn.*, **1 (2)**, 675–699, doi:10.5194/wcd-1-675-2020.

Salomón, R. L., and Coauthors, 2022: The 2018 European heatwave led to stem dehydration but not to consistent growth reductions in forests. *Nat. Commun.*, **13 (1)**, 28, doi:10.1038/s41467-021-27579-9.

Santos, J. A., S. Pfahl, J. G. Pinto, and H. Wernli, 2015: Mechanisms underlying temperature extremes in Iberia: a Lagrangian perspective. *Tellus A: Dyn. Meteorol.*, **67 (1)**, 26 032, doi:10.3402/tellusa.v67.26032.

Scherrer, D., M. K.-F. Bader, and C. Körner, 2011: Drought-sensitivity ranking of deciduous tree species based on thermal imaging of forest canopies. *Agric. For. Meteorol.*, **151 (12)**, 1632–1640, doi:10.1016/j.agrformet.2011.06.019.

Schubert, S. D., and Coauthors, 2016: Global meteorological drought: A synthesis of current understanding with a focus on SST drivers of precipitation deficits. *J. Clim.*, **29 (11)**, 3989–4019, doi:10.1175/JCLI-D-15-0452.1.

Schuldt, B., and Coauthors, 2020: A first assessment of the impact of the extreme 2018 summer drought on Central European forests. *Basic Appl. Ecol.*, **45**, 86–103, doi:10.1016/j.baae.2020.04.003.

Schultz, J., 2005: *The Ecozones of the World*. Springer, Berlin and Heidelberg, Germany, 252 pp., doi:10.1007/3-540-28527-X.

Seager, R., A. Hooks, A. P. Williams, B. Cook, J. Nakamura, and N. Henderson, 2015: Climatology, variability, and trends in the U.S. vapor pressure deficit, an important fire-related meteorological quantity. *J. Appl. Meteorol. Climatol.*, **54 (6)**, 1121–1141, doi:10.1175/JAMC-D-14-0321.1.

Seager, R., N. Pederson, Y. Kushnir, J. Nakamura, and S. Jurburg, 2012: The 1960s drought and the subsequent shift to a wetter climate in the Catskill Mountains region of the New York City watershed. *J. Clim.*, **25 (19)**, 6721–6742, doi:10.1175/JCLI-D-11-00518.1.

Seftigen, K., D. C. Frank, J. Björklund, F. Babst, and B. Poulter, 2018: The climatic drivers of normalized difference vegetation index and tree-ring-based estimates of forest productivity are spatially coherent but temporally decoupled in Northern Hemispheric forests. *Glob. Ecol. Biogeogr.*, **27 (11)**, 1352–1365, doi:10.1111/geb.12802.

Seidl, R., M.-J. Schelhaas, W. Rammer, and P. J. Verkerk, 2014: Increasing forest disturbances in Europe and their impact on carbon storage. *Nat. Clim. Change*, **4 (9)**, 806–810, doi:10.1038/nclimate2318.

Seidl, R., and Coauthors, 2017: Forest disturbances under climate change. *Nat. Clim. Change*, **7 (6)**, 395–402, doi:10.1038/nclimate3303.

Seidl, R., and Coauthors, 2020: Globally consistent climate sensitivity of natural disturbances across boreal and temperate forest ecosystems. *Ecography*, **43 (7)**, 967–978, doi:10.1111/ecog.04995.

Seneviratne, S. I., T. Corti, E. L. Davin, M. Hirschi, E. B. Jaeger, I. Lehner, B. Orlowsky, and A. J. Teuling, 2010: Investigating soil moistureclimate interactions in a changing climate: A review. *Earth-Sci. Rev.*, **99 (3-4)**, 125–161, doi:10.1016/j.earscirev.2010.02.004.

Senf, C., A. Buras, C. S. Zang, A. Rammig, and R. Seidl, 2020: Excess forest mortality is consistently linked to drought across Europe. *Nat. Commun.*, **11 (1)**, 6200, doi:10.1038/s41467-020-19924-1.

Senf, C., and R. Seidl, 2021a: Mapping the forest disturbance regimes of Europe. *Nat. Sustain.*, **4 (1)**, 63–70, doi:10.1038/s41893-020-00609-y.

Senf, C., and R. Seidl, 2021b: Persistent impacts of the 2018 drought on forest disturbance regimes in Europe. *Biogeosciences*, **18 (18)**, 5223–5230, doi:10.5194/bg-18-5223-2021.

Senf, C., and R. Seidl, 2021c: Storm and fire disturbances in Europe: Distribution and trends. *Glob. Chang. Biol.*, **27 (15)**, 3605–3619, doi:10.1111/gcb.15679.

Shepherd, T. G., 2014: Atmospheric circulation as a source of uncertainty in climate change projections. *Nat. Geosci.*, **7 (10)**, 703–708, doi:10.1038/ngeo2253.

Simmons, A. J., K. M. Willett, P. D. Jones, P. W. Thorne, and D. P. Dee, 2010: Low-frequency variations in surface atmospheric humidity, temperature, and precipitation: Inferences from reanalyses and monthly gridded observational data sets. *J. Geophys. Res.: Atmos.*, **115 (D1)**, D01 110, doi:10.1029/2009JD012442.

Smith, D. M., and Coauthors, 2020: North Atlantic climate far more predictable than models imply. *Nature*, **583 (7818)**, 796–800, doi:10.1038/s41586-020-2525-0.

Sommerfeld, A., and Coauthors, 2018: Patterns and drivers of recent disturbances across the temperate forest biome. *Nat. Commun.*, **9 (1)**, 4355, doi:10.1038/s41467-018-06788-9.

Sousa, P. M., R. M. Trigo, D. Barriopedro, P. M. M. Soares, and J. A. Santos, 2018: European temperature responses to blocking and ridge regional patterns. *Clim. Dyn.*, **50 (1-2)**, 457–477, doi:10.1007/s00382-017-3620-2.

Spensberger, C., E. Madonna, M. Boettcher, C. M. Grams, L. Papritz, J. F. Quinting, M. Röthlisberger, M. Sprenger, and P. Zschenderlein, 2020: Dynamics of concurrent and sequential Central European and Scandinavian heatwaves. *Q. J. R. Meteorol. Soc.*, **146 (732)**, 2998–3013, doi:10.1002/qj.3822.

Sprenger, M., G. Fragkoulidis, H. Binder, M. Croci-Maspoli, P. Graf, C. M. Grams, P. Knippertz, E. Madonna, S. Schemm, B. Škerlak, and H. Wernli, 2017: Global climatologies of Eulerian and Lagrangian flow features based on ERA-Interim. *Bull. Am. Meteorol. Soc.*, **98 (8)**, 1739–1748, doi:10.1175/BAMS-D-15-00299.1.

Stewart, J., 2012: *Multivariable calculus*. Brooks/Cole, Belmont, US, 600 pp.

Stigler, S. M., 1997: Regression towards the mean, historically considered. *Stat. Methods Med. Res.*, **6 (2)**, 103–114, doi:10.1177/096228029700600202.

Stott, P. A., 2003: Attribution of regional-scale temperature changes to anthropogenic and natural causes. *Geophys. Res. Lett.*, **30 (14)**, doi:10.1029/2003GL017324.

Stott, P. A., D. A. Stone, and M. R. Allen, 2004: Human contribution to the European heatwave of 2003. *Nature*, **432 (7017)**, 610–614, doi:10.1038/nature03089.

Stuart-Haëntjens, E., and Coauthors, 2018: Mean annual precipitation predicts primary production resistance and resilience to extreme drought. *Sci. Total Environ.*, **636**, 360–366, doi:10.1016/j.scitotenv.2018.04.290.

Sulman, B. N., D. T. Roman, K. Yi, L. Wang, R. P. Phillips, and K. A. Novick, 2016: High atmospheric demand for water can limit forest carbon uptake and transpiration as severely as dry soil. *Geophys. Res. Lett.*, **43 (18)**, 9686–9695, doi:10.1002/2016GL069416.

Sun, W., D. Fleisher, D. Timlin, C. Ray, Z. Wang, S. Beegum, and V. Reddy, 2023: Projected long-term climate trends reveal the critical role of vapor pressure deficit for soybean yields in the US Midwest. *Sci. Total Environ.*, **878**, 162 960, doi:10.1016/j.scitotenv.2023.162960.

Sutton, R., E. Suckling, and E. Hawkins, 2015: What does global mean temperature tell us about local climate? *Philos. Trans. R. Soc. A: Math. Phys. Eng. Sci.*, **373 (2054)**, 20140 426, doi:10.1098/rsta.2014.0426.

Tague, C. L., M. Moritz, and E. Hanan, 2019: The changing water cycle: The eco-hydrologic impacts of forest density reduction in Mediterranean (seasonally dry) regions. *WIREs Water*, **6 (4)**, e1350, doi:10.1002/wat2.1350.

Tan, X., T. Y. Gan, and D. E. Horton, 2018: Projected timing of perceivable changes in climate extremes for terrestrial and marine ecosystems. *Glob. Chang. Biol.*, **24 (10)**, 4696–4708, doi:10.1111/gcb.14329.

Tarek, M., F. P. Brissette, and R. Arsenault, 2020: Evaluation of the ERA5 reanalysis as a potential reference dataset for hydrological modelling over North America. *Hydrol. Earth Syst. Sci.*, **24 (5)**, 2527–2544, doi:10.5194/hess-24-2527-2020.

Tedesco, M., and X. Fettweis, 2020: Unprecedented atmospheric conditions (1948-2019) drive the 2019 exceptional melting season over the Greenland ice sheet. *Cryosphere*, **14**, 1209–1223, doi:10.5194/tc-14-1209-2020.

Temperli, C., H. Bugmann, and C. Elkin, 2013: Cross-scale interactions among bark beetles, climate change, and wind disturbances: a landscape modeling approach. *Ecol. Monogr.*, **83 (3)**, 383–402, doi:10.1890/12-1503.1.

Thom, D., W. Rammer, R. Garstenauer, and R. Seidl, 2018: Legacies of past land use have a stronger effect on forest carbon exchange than future climate change in a temperate forest landscape. *Biogeosciences*, **15 (18)**, 5699–5713, doi:10.5194/bg-15-5699-2018.

Trenberth, K. E., G. W. Branstator, and P. A. Arkin, 1988: Origins of the 1988 North American Drought. *Science*, **242 (4886)**, 1640–1645, doi:10.1126/science.242.4886.1640.

Trenberth, K. E., A. Dai, G. van der Schrier, P. D. Jones, J. Barichivich, K. R. Briffa, and J. Sheffield, 2014: Global warming and changes in drought. *Nat. Clim. Change*, **4 (1)**, 17–22, doi:10.1038/nclimate2067.

Trotsiuk, V., and Coauthors, 2020: Assessing the response of forest productivity to climate extremes in Switzerland using modeldata fusion. *Glob. Chang. Biol.*, **26 (4)**, 2463–2476, doi:10.1111/gcb.15011.

Trugman, A. T., L. D. Anderegg, W. R. Anderegg, A. J. Das, and N. L. Stephenson, 2021: Why is tree drought mortality so hard to predict? *Trends Ecol. Evol.*, **36 (6)**, 520–532, doi:10.1016/j.tree.2021.02.001.

Tucker, C. J., 1979: Red and photographic infrared linear combinations for monitoring vegetation. *Remote Sens. Environ.*, **8 (2)**, 127–150, doi:10.1016/0034-4257(79)90013-0.

Turco, M., J. von Hardenberg, A. AghaKouchak, M. C. Llasat, A. Provenzale, and R. M. Trigo, 2017: On the key role of droughts in the dynamics of summer fires in Mediterranean Europe. *Sci. Rep.*, **7 (1)**, 81, doi:10.1038/s41598-017-00116-9.

Ulbrich, U., A. H. Fink, M. Klawa, and J. G. Pinto, 2001: Three extreme storms over Europe in December 1999. *Weather*, **56 (3)**, 70–80, doi:10.1002/j.1477-8696.2001.tb06540.x.

van den Broeke, M. R., E. M. Enderlin, I. M. Howat, P. Kuipers Munneke, B. P. Noël, W. Jan Van De Berg, E. Van Meijgaard, and B. Wouters, 2016: On the recent contribution of the Greenland ice sheet to sea level change. *Cryosphere*, **10 (5)**, 1933–1946, doi:10.5194/tc-10-1933-2016.

van Kampenhout, L., J. T. M. Lenaerts, W. H. Lipscomb, S. Lhermitte, B. Noël, M. Vizcaíno, W. J. Sacks, and M. R. van den Broeke, 2020: Present-day Greenland ice sheet climate and surface mass balance in CESM2. *J. Geophys. Res.: Earth Surf.*, **125 (2)**, doi:10.1029/2019JF005318.

van Kampenhout, L., J. T. M. Lenaerts, W. H. Lipscomb, W. J. Sacks, D. M. Lawrence, A. G. Slater, and M. R. van den Broeke, 2017: Improving the representation of polar snow and firn in the Community Earth System Model. *J. Adv. Model. Earth Syst.*, **9 (7)**, 2583–2600, doi:10.1002/2017MS000988.

van Kampenhout, L., A. M. Rhoades, A. R. Herrington, C. M. Zarzycki, J. T. M. Lenaerts, W. J. Sacks, and M. R. van den Broeke, 2019: Regional grid refinement in an Earth system model: impacts on the simulated Greenland surface mass balance. *Cryosphere*, **13 (6)**, 1547–1564, doi:10.5194/tc-13-1547-2019.

van Oldenborgh, G. J., S. Drijfhout, A. van Ulden, R. Haarsma, A. Sterl, C. Severijns, W. Hazeleger, and H. Dijkstra, 2009: Western Europe is warming much faster than expected. *Clim. Past*, **5 (1)**, 1–12, doi:10.5194/cp-5-1-2009.

Vanoni, M., H. Bugmann, M. Nötzli, and C. Bigler, 2016: Quantifying the effects of drought on abrupt growth decreases of major tree species in Switzerland. *Ecol. Evol.*, **6 (11)**, 3555–3570, doi:10.1002/ece3.2146.

Varol, T., and M. Ertuğrul, 2016: Analysis of the forest fires in the Antalya region of Turkey using the Keetch–Byram drought index. *J. For. Res.*, **27 (4)**, 811–819, doi:10.1007/s11676-016-0235-0.

Velicogna, I., Y. Mohajerani, G. A, F. Landerer, J. Mouginot, B. Noel, E. Rignot, T. Sutterley, M. van den Broeke, M. van Wessem, and D. Wiese, 2020: Continuity of ice sheet mass loss in Greenland and Antarctica from the GRACE and GRACE Follow-On missions. *Geophys. Res. Lett.*, **47 (8)**, e2020GL087 291, doi:10.1029/2020GL087291.

Vesanto, J., J. Himberg, E. Alhoniemi, and J. Parhankangas, 2000: SOM Toolbox for Matlab 5, in Report A57. Tech. rep., Helsinki University of Technology, Helsinki, Finland, 60 pp.

Vicente-Serrano, S. M., S. Beguería, and J. I. López-Moreno, 2010: A multiscalar drought index sensitive to global warming: The Standardized Precipitation Evapotranspiration Index. *J. Clim.*, **23 (7)**, 1696–1718, doi:10.1175/2009JCLI2909.1.

Vicente-Serrano, S. M., R. Nieto, L. Gimeno, C. Azorin-Molina, A. Drumond, A. E. Kenawy, F. Dominguez-Castro, M. Tomas-Burguera, and M. Peña-Gallardo, 2018: Recent changes of relative humidity: regional connections with land and ocean processes. *Earth Sci. Dyn.*, **9 (2)**, 915–937, doi:10.5194/esd-9-915-2018.

Vicente-Serrano, S. M., T. R. McVicar, D. G. Miralles, Y. Yang, and M. Tomas-Burguera, 2020: Unraveling the influence of atmospheric evaporative demand on drought and its response to climate change. *WIREs Climate Change*, **11 (2)**, e632, doi:10.1002/wcc.632.

Vicente-Serrano, S. M., F. Domínguez-Castro, F. Reig, M. Tomas-Burguera, D. Peña-Angulo, B. Latorre, S. Beguería, I. Rabanaque, I. Noguera, J. Lorenzo-Lacruz, and A. E. Kenawy, 2022: A global drought monitoring system and dataset based on ERA5 reanalysis: A focus on crop-growing regions. *Geosci. Data J.*, **00**, 1–14, doi:10.1002/gdj3.178.

Vitasse, Y., A. Bottero, M. Cailleret, C. Bigler, P. Fonti, A. Gessler, M. Lévesque, B. Rohner, P. Weber, A. Rigling, and T. Wohlgemuth, 2019: Contrasting resistance and resilience to extreme drought and late spring frost in five major European tree species. *Glob. Chang. Biol.*, **25 (11)**, 3781–3792, doi:10.1111/gcb.14803.

Vogel, J., P. Rivoire, C. Deidda, L. Rahimi, C. A. Sauter, E. Tschumi, K. van der Wiel, T. Zhang, and J. Zscheischler, 2021: Identifying meteorological drivers of extreme impacts: an application to simulated crop yields. *Earth Sci. Dyn.*, **12 (1)**, 151–172, doi:10.5194/esd-12-151-2021.

Wallace, J. M., and P. V. Hobbs, 2006: *Atmospheric Science*, Vol. 92. 2nd ed., Elsevier, Amsterdam, Netherlands, doi:10.1016/C2009-0-00034-8.

Wang, W., C. S. Zender, D. van As, R. S. Fausto, and M. K. Laffin, 2021: Greenland surface melt dominated by solar and sensible heating. *Geophys. Res. Lett.*, **48 (7)**, doi:10.1029/2020GL090653.

Wang, W., C. S. Zender, D. van As, and N. B. Miller, 2019: Spatial distribution of melt season cloud radiative effects over Greenland: evaluating satellite observations, reanalyses, and model simulations against in situ measurements. *J. Geophys. Res.: Atmos.*, **124 (1)**, 57–71, doi:10.1029/2018JD028919.

Wernli, H., and C. Schwierz, 2006: Surface cyclones in the ERA-40 dataset (1958–2001). Part I: Novel identification method and global climatology. *J Atmos. Sci.*, **63 (10)**, 2486–2507, doi:10.1175/JAS3766.1.

Williams, A. P., J. T. Abatzoglou, A. Gershunov, J. Guzman-Morales, D. A. Bishop, J. K. Balch, and D. P. Lettenmaier, 2019: Observed impacts of anthropogenic climate change on wildfire in California. *Earth's Future*, **7 (8)**, 892–910, doi:10.1029/2019EF001210.

Williams, A. P., B. I. Cook, J. E. Smerdon, D. A. Bishop, R. Seager, and J. S. Mankin, 2017: The 2016 southeastern U.S. Drought: An extreme departure from centennial wetting and cooling. *J. Geophys. Res.: Atmos.*, **122 (20)**, doi:10.1002/2017JD027523.

Williams, A. P., C. D. Allen, A. K. Macalady, D. Griffin, C. A. Woodhouse, D. M. Meko, T. W. Swetnam, S. A. Rauscher, R. Seager, H. D. Grissino-Mayer, J. S. Dean, E. R. Cook, C. Gangodagamage, M. Cai, and N. G. McDowell, 2013: Temperature as a potent driver of regional forest drought stress and tree mortality. *Nat. Clim. Change*, **3 (3)**, 292–297, doi:10.1038/nclimate1693.

Williams, A. P., R. Seager, M. Berkelhammer, A. K. Macalady, M. A. Crimmins, T. W. Swetnam, A. T. Trugman, N. Buenning, N. Hryniw, N. G. McDowell, D. Noone, C. I. Mora, and T. Rahn, 2014: Causes and implications of extreme atmospheric moisture demand during the record-breaking 2011 wildfire season in the southwestern United States. *J. Appl. Meteorol. Climatol.*, **53 (12)**, 2671–2684, doi:10.1175/JAMC-D-14-0053.1.

Williams, J. W., S. T. Jackson, and J. E. Kutzbach, 2007: Projected distributions of novel and disappearing climates by 2100 AD. *Proc. Natl. Acad. Sci. U. S. A.*, **104 (14)**, 5738–5742, doi:10.1073/pnas.0606292104.

Wolf, G., D. J. Brayshaw, N. P. Klingaman, and A. Czaja, 2018: Quasi-stationary waves and their impact on European weather and extreme events. *Q. J. R. Meteorol. Soc.*, **144 (717)**, 2431–2448, doi:10.1002/qj.3310.

Wolf, S., W. Eugster, C. Ammann, M. Häni, S. Zielis, R. Hiller, J. Stieger, D. Imer, L. Merbold, and N. Buchmann, 2013: Contrasting response of grassland versus forest carbon and water fluxes to spring drought in Switzerland. *Environ. Res. Lett.*, **8 (3)**, 035 007, doi:10.1088/1748-9326/8/3/035007.

Yeo, I.-K., and R. A. Johnson, 2000: A new family of power transformations to improve normality or symmetry. *Biometrika*, **87 (4)**, 954–959, doi:10.1093/biomet/87.4.954.

Yuan, W., and Coauthors, 2019: Increased atmospheric vapor pressure deficit reduces global vegetation growth. *Sci. adv.*, **5 (8)**, eaax1396, doi:10.1126/sciadv.aax1396.

Zang, C. S., A. Buras, A. Esquivel-Muelbert, A. S. Jump, A. Rigling, and A. Rammig, 2020: Standardized drought indices in ecological research: Why one size does not fit all. *Glob. Chang. Biol.*, **26 (2)**, 322–324, doi:10.1111/gcb.14809.

Zhang, Y., T. F. Keenan, and S. Zhou, 2021: Exacerbated drought impacts on global ecosystems due to structural overshoot. *Nat. Ecol. Evol.*, **5 (11)**, 1490–1498, doi:10.1038/s41559-021-01551-8.

Zheng-Bin, Y., L. Zhao-Hui, and Z. He, 2014: The relationship between the East Asian Subtropical Westerly Jet and summer precipitation over East Asia as simulated by the IAP AGCM4.0. *Atmos. Ocean. Sci. Lett.*, **7 (6)**, 487–492, doi:10.1080/16742834.2014.11447212.

Zschenderlein, P., A. H. Fink, S. Pfahl, and H. Wernli, 2019: Processes determining heat waves across different European climates. *Q. J. R. Meteorol. Soc.*, **145 (724)**, 2973–2989, doi:10.1002/qj.3599.

Zschenderlein, P., S. Pfahl, H. Wernli, and A. H. Fink, 2020: A Lagrangian analysis of upper-tropospheric anticyclones associated with heat waves in Europe. *Weather Clim. Dyn.*, **1 (1)**, 191–206, doi:10.5194/wcd-1-191-2020.

Zschenderlein, P., and H. Wernli, 2022: How intense daily precipitation depends on temperature and the occurrence of specific weather systems – an investigation with ERA5 reanalyses in the extratropical Northern Hemisphere. *Weather Clim. Dyn.*, **3 (2)**, 391–411, doi:10.5194/wcd-3-391-2022.

Acknowledgements

I would like to express my gratitude to all those who have supported and guided me throughout this dissertation journey.

First and foremost, I thank my supervisors Heini Wernli and Matthias Röthlisberger for their guidance, patience, and expertise. I thank Heini not only for his support during the past four years, but also for guiding me through my initial research explorations (BSc and MSc theses), as well as for stimulating my interest in atmospheric dynamics during his truly enjoyable lectures. I sincerely admire his dedication to high-quality research, personal and fair leadership, supervision and teaching, and commitment for the greater good, all of which he devotes seemingly endless time to. I also want to acknowledge all that he does behind the scenes to keep this group and institute thriving. My great thanks to Matthias, who stepped in when I was looking for personal and scientific support during my dissertation. I appreciated his extremely valuable scientific input, which underlines his broad expertise in this field of research, as well as his great ability and willingness to communicate and share. His ideas were crucial for the development of the presented research, and I could learn a lot from him. Both of them have been truly understanding and helpful during some of the most difficult times of my life. I am very fortunate to have had such capable mentors, both socially and scientifically, which is anything but usual.

I would also like to thank my collaborators Andreas Rigling, Arthus Gessler, and Thomas Wohlgemuth for the time they invested in our collaboration and for sharing their extensive knowledge on forest dynamics, disturbances, and ecology. Many thanks for your positive feedback and invaluable support during this unexpected and arduous publication process.

On a related note, I extend my gratitude to Cornelius Senf for providing disturbance data and an invaluable outside perspective on this project in short notice.

Stefan Brönnimann is my external examiner and, therefore, takes his time to read my thesis and attend my doctoral exam in Zurich, for which I thank him very much.

My appreciation goes to the entire Dynamo group, which provided an open and liberal working environment, especially my fellow PhD students, with whom I could share the ups and downs of our daily lives. I enjoyed our conversations to learn more about scientific careers, and to

discuss on anything related to global warming. Our group retreats, the Dynamo beers, and social gatherings outside the office will be fondly remembered.

I extend my gratitude to Michael Sprenger and Urs Beyerle, who provided the technical foundation for this thesis by extracting and processing ERA5 data and running the CESM model simulations used in this thesis. I would like to thank Urs Beyerle also for providing temperature data from the weather station on the roof of the CHN building (used in Fig. 1.1a,b).

In addition, Urs Beyerle together with Mathias Hauser, Hans-Heini Vogel and Peter Isler maintains an impeccable IT environment from which I have been fortunate to benefit.

I am grateful to Bianca Wagenbach for her administrative support, handling our time sheets, and managing my employment.

I would like to thank Timo Schmid, who I supervised during his impressive master thesis, for his help in implementing the Self-Organizing Map method.

I acknowledge funding from the European Research Council within the INTEXseas project.

Moreover, I acknowledge the freely available NDVI data from NASA, ERA5 data from ECMWF and surface land cover observations from Copernicus.

I am grateful to NCAR, particularly Isla Simpson and Gunter Leguy, for sharing the CESM1 and CESM2 restart files together with technical information on CESM2.

I would also like to thank Xavier Fettweis for making present-day MAR climate model simulations available online.

The deepest appreciation goes to my family, Pap, Mam, Amanda, Sophie, Manu, Lukas, and many more. Words cannot express how grateful I am for the love and sense of home you provide. Your support and care have been and will continue to be the most important pillars that empower me to follow my aspirations. The past few months have been extremely rough and infinitely sad, and the end of this thesis marks another event that Mam would have made extra special. I appreciate and thank you to the moon and back for your presence in my life.